





(i)

INDUCED CHARGES

IN

X-RAY PROPORTIONAL DETECTORS

A thesis submitted to  
The University of Leicester

by

Trevor J. Harris

in partial fulfilment of the regulations  
for the degree of Doctor of Philosophy.

May 1979

UMI Number: U333303

All rights reserved

INFORMATION TO ALL USERS

The quality of this reproduction is dependent upon the quality of the copy submitted.

In the unlikely event that the author did not send a complete manuscript and there are missing pages, these will be noted. Also, if material had to be removed, a note will indicate the deletion.



UMI U333303

Published by ProQuest LLC 2015. Copyright in the Dissertation held by the Author.  
Microform Edition © ProQuest LLC.

All rights reserved. This work is protected against  
unauthorized copying under Title 17, United States Code.



ProQuest LLC  
789 East Eisenhower Parkway  
P.O. Box 1346  
Ann Arbor, MI 48106-1346

THESIS  
642672

(ii)

ABSTRACT

A brief description is given of gas proportional detectors, with emphasis on the development and behaviour of multiwire proportional counters (MWPC's). In particular, the behaviour of MWPC's as position sensitive detectors is discussed and a description given of the various techniques employed in obtaining and processing positional information.

A theoretical analysis of a recently discovered phenomenon, known as angular localisation of the electron avalanche, is presented and a study is made of induced charges, due to this avalanche, on nearby anodes and cathodes. Formulae are developed which allow the calculation of the induced charges, and theoretical predictions are given of how the effect may be used to provide position signals.

An experimental system is described from which evidence has been obtained that a high degree of angular localisation does indeed exist. Comparisons are made between these experimental measurements and the predictions of the theoretical model. Various fundamental limitations are discussed which indicate the feasibility of using the localisation effect for positional interpolation between anode wires.

The experimental work is extended to observe the effects of using several common counter gas mixtures and also of varying the chamber geometry.

Finally some applications are discussed and suggestions are made for future research.

(iii)

ACKNOWLEDGMENTS

I am grateful to Professor J. L. Beeby and formerly to Professor J. E. Enderby, who have permitted the facilities of the Physics Department to be used, often out of normal hours, for this research.

Thanks are especially due to my supervisor, Dr. E. Mathieson, to whom I have always been able to turn for encouragement and stimulating discussion.

I wish to thank Mrs. P. J. V. Harris and Mrs. P. M. Jayes for their part in typing this thesis so efficiently.

Finally I am indebted to my wife and children, who have patiently supported me during this research project.

CONTENTS

CHAPTER 1      INTRODUCTION - GAS PROPORTIONAL DETECTORS

- 1.1      The Single Wire Proportional Counter
- 1.2      The Development of Multiwire Proportional Counters
- 1.3      Resolution Considerations
- 1.4      The Efficiency of Multiwire Proportional Counters
- 1.5      Applications of the Multiwire Proportional Counter

CHAPTER 2      POSITION SENSITIVE DETECTORS

- 2.1      Introduction
- 2.2      Techniques Employed in Obtaining Positional Information
  - 2.2.1      Individual wire readout
  - 2.2.2      The resistive anode
  - 2.2.3      The resistance-capacitance line
  - 2.2.4      Delay line readout
  - 2.2.5      Digital processing
- 2.3      Drift Techniques
- 2.4      Discussion

CHAPTER 3      LOCALISATION OF THE AVALANCHE

- 3.1      Initial Observations
- 3.2      Basic Description of the System
- 3.3      Theoretical Considerations
- 3.4      Time Development of the Induced Pulse
- 3.5      Effects of Pulse Shaping
- 3.6      Effect of Finite Distribution of Charge
- 3.7      Theoretical Predictions

CHAPTER 4      EXPERIMENTAL DETAILS

- 4.1      The Experimental Proportional Chambers
- 4.2      The Electronic System
  - 4.2.1    General overview
  - 4.2.2    Chamber connections
  - 4.2.3    The charge-sensitive preamplifiers
  - 4.2.4    Pulse shaping
  - 4.2.5    Pulse stretchers
  - 4.2.6    The divider
  - 4.2.7    Methods of readout
- 4.3      Radiation Sources
- 4.4      Collimators

CHAPTER 5      THE INDUCED ANODE PULSE-EXPERIMENTAL RESULTS IN P.10

- 5.1      Experimental Conditions
- 5.2      Anode Pulse Shapes
- 5.3      Gas Gain and Choice of Operating Point
- 5.4      Traversing the Chamber
- 5.5      Beyond the Cell Boundary
- 5.6      The Position Signal
- 5.7      Resolution
- 5.8      Increased Gas Gain
- 5.9      Discussion

CHAPTER 6      THE INDUCED CATHODE PULSE-EXPERIMENTAL RESULTS IN P.10

- 6.1      Experimental Conditions
- 6.2      Cathode Pulse Shapes
- 6.3      Spectra of Cathode Pulse Heights

- 6.4 Traversing the Chamber
- 6.5 Discussion
  - 6.5.1 Experimental limitations
  - 6.5.2 The choice of mobility value
  - 6.5.3 The angular spread
  - 6.5.4 Resolution

CHAPTER 7      EXPERIMENTAL RESULTS IN OTHER GASES

- 7.1 Introduction - Choice of Gas Mixtures
- 7.2 Induced Anode Signals
  - 7.2.1 Measurements in Ar/75%CH<sub>4</sub> (P.75)
  - 7.2.2 Measurements in Ne/10%CH<sub>4</sub>
  - 7.2.3 Measurements in Ne/10%CO<sub>2</sub>
  - 7.2.4 Measurements in Ar/10%CO<sub>2</sub>
- 7.3 Discussion - Induced Anode Signals
  - 7.3.1 Limitations
  - 7.3.2 Comparison of gas mixtures
- 7.4 Induced Cathode Signals
  - 7.4.1 Photographs of induced cathode pulses
  - 7.4.2 Induced cathode signals in Ar/75%CH<sub>4</sub>
  - 7.4.3 Induced cathode signals in Ne/10%CH<sub>4</sub>
  - 7.4.4 Induced cathode signals in Ne/10%CO<sub>2</sub>
  - 7.4.5 Induced cathode signals in Ar/10%CO<sub>2</sub>
- 7.5 Discussion - Induced Cathode Signals

CHAPTER 8      CHAMBER GEOMETRY

- 8.1 Introduction
- 8.2 Effects of Varying the Anode Wire Spacing

- 8.2.1 Induced cathode signals
- 8.2.2 Induced anode signals
- 8.3 Effects of Varying Anode Wire Diameter
- 8.4 Resolution
- 8.5 The Single Wire Chamber
- 8.6 Discussion

CHAPTER 9      CONCLUDING DISCUSSION

- 9.1 Summary
- 9.2 Major Experimental Limitations
  - 9.2.1 Cell boundaries
  - 9.2.2 Positive ion mobility
  - 9.2.3 Diffusion
  - 9.2.4 Radioactive sources
- 9.3 Future Research
  - 9.3.1 Count rate limitations
  - 9.3.2 Further work with the Al-K source
  - 9.3.3 Greater chamber depths
  - 9.3.4 Use of heavier gases
  - 9.3.5 Rise-time and crossover detection
- 9.4 Applications
  - 9.4.1 Background reduction
  - 9.4.2 Left-right discrimination
  - 9.4.3 Absorption depth discrimination
  - 9.4.4 X-ray imaging

- APPENDIX 1 The Chamber Response due to a Slit Collimator
- APPENDIX 2 Reprint from Nature, Vol.272, No. 5655, p. 709,  
20 April 1978 'Angular Localisation of Proportional  
Chamber Avalanche', - E.Mathieson, T.J.Harris and  
G.C.Smith.
- APPENDIX 3 Paper read at 3rd Int. Conf. on "Drift and Proportional  
Chambers", Dubna, U.S.S.R., June 1978.  
'Induced Cathode Signals in Multiwire Chambers' -  
T.J.Harris and E.Mathieson.
- APPENDIX 4 Reprint from Nucl. Instr. and Meth. 154(1978)183  
'Angular Localisation of Proportional Chamber Avalanche' -  
T.J.Harris and E.Mathieson.
- APPENDIX 5 Reprint from Nucl. Instr. and Meth. 154(1978)189 'Induced  
Charges in a Multiwire Proportional Chamber ' -  
E.Mathieson and T.J.Harris.
- APPENDIX 6 Reprint from Nucl. Instr. and Meth. 157(1978)563  
'Modulation of Anode Signal in Multiwire Proportional  
Chambers' - E.Mathieson and T.J.Harris.
- APPENDIX 7 Reprint from Nucl. Instr. and Meth. 159(1979)483  
'Evaluation of the Initial Angular Width of the Avalanche  
in a Proportional Chamber' - E.Mathieson and T.J.Harris.

REFERENCES

ILLUSTRATIONS

- Fig. 1.1      The field distribution in a multiwire chamber
- Fig. 2.1      The resistive anode system
- 2.2      The R - C line system
- 2.3      The two dimensional resistive cathode system
- 2.4      The resistive chain system
- 2.5      The delay line system
- 2.6      The two dimensional R - C line system
- 2.7      The digitally processed system
- 2.8a     The spherical drift chamber
- 2.8b     Particle location by drift time measurement
- 2.8c     Interpolation between wires
- Fig. 3.1      Schematic diagram of a conventional multiwire chamber
- 3.2      Theoretical ratio of anode pulse heights against source  
              position
- 3.3      Effects of finite avalanche spreading
- 3.4      The ratio of cathode pulse heights against source position
- 3.5      Isometric plot of induced cathode charges
- 3.6      Isometric plot of induced anode charge
- Fig. 4.1      Chamber plate detail
- 4.2      The experimental chamber
- 4.3      The screening and mechanical assembly
- 4.3a     Photograph of the experimental apparatus
- 4.4      The electronic system
- 4.5      Photograph of the laboratory
- 4.6      Configuration of anode/cathode connections for observing  
              induced anode pulses

ILLUSTRATIONS cont.

- 4.7 Configuration of anode/cathode connections for observing cathode signals
- 4.8 Pulse shaping amplifier
- 4.9 Stretcher linearity
- 4.10 Dual stretcher
- 4.11 Theoretical times to maximum of induced cathode pulses
- 4.12 Photograph of induced cathode pulses
- 4.13 The divider
- 4.14 The  $^{55}\text{Fe}$  source mounting
- 4.15 The Al-K source and housing
- 4.16 Collimator dimensions
- 4.17 Dimensions of the source-collimator assembly
- Fig. 5.1 Induced anode pulse photographs
- 5.2 The variation of potential P along the y/s axis
- 5.3 Gas gain variation with anode voltage
- 5.4a Change in count rate across the centre wire
- 5.4b Gain variation across a single wire
- 5.5 Gain variation over central three anodes
- 5.6 The experimental induced anode pulse ratio compared with theory for two sources of radiation
- 5.7 Comparison of experimental and theoretical values for  $-v_B/v_A$  for values of  $x_0$  extending beyond the cell boundary
- 5.8a Experimental values of the position signal r as a function of X-ray beam position  $x_0$

ILLUSTRATIONS cont.

- 5.8b Pulse height distribution of position signal  $r$  at  $x_0/s = .2$ .
- 5.9 Experimental measurements of  $-v_B/v_A$  plotted against  $x_0/s$  for various values of gas gain
- 5.10 Theoretical preamplifier noise against time-constant characteristics
- 5.11 Field pattern near the centre of the chamber
- Fig. 6.1 Induced cathode pulses in Ar/10%CH<sub>4</sub>.
- 6.2 Induced cathode pulses showing effects of unilateral absorption
- 6.3 Pulse height spectrum from upper cathode -  $x_0/s = 0$
- 6.4 Pulse height spectrum from lower cathode -  $x_0/s = 0$
- 6.5 Pulse height spectrum from upper cathode -  $x_0/s = .3$
- 6.6 Spectra of the ratio of cathode signals -  $v_C/v_C'$
- 6.7 Values of  $v_C/v_C'$  as a function of  $x_0/s$  compared with theoretical predictions -  $T = 10\mu s$
- 6.8 Values of  $v_C/v_C'$  as a function of  $x_0/s$  compared with theoretical predictions -  $T = 25\mu s$
- 6.9 Photograph of individual cathode pulses taken from the top cathode
- Fig. 7.1 The ratio of  $-v_B/v_A$  in Ar/75%CH<sub>4</sub> compared with theoretical predictions
- 7.2 Spectra of  $(v_B - v_A')/(v_B + v_A')$  in Ar/75%CH<sub>4</sub> for several values of  $x_0/s$
- 7.3 The ratio of  $-v_B/v_A$  in Ne/10%CH<sub>4</sub> compared with theoretical predictions

ILLUSTRATIONS cont.

- 7.4 The ratio of  $-v_B/v_A$  in Ne/10%CO<sub>2</sub> compared with theoretical predictions
- 7.5 The ratio of  $-v_B/v_A$  in Ar/10%CO<sub>2</sub> compared with theoretical predictions
- 7.6 Photograph of induced cathode pulses after 10 $\mu$ s shaping
- 7.7 Cathode pulse ratios in Ar/75%CH<sub>4</sub>
- 7.8 Cathode pulse ratios in Ne/10%CH<sub>4</sub>
- 7.9 Cathode pulse ratios in Ne/10%CO<sub>2</sub>
- 7.10 Cathode pulse ratios in Ar/10%CO<sub>2</sub>
- Fig. 8.1 The ratio  $v_C/v_C'$  as a function of  $x_0/s$
- 8.2 The ratio of anode signals against source position for three anode wire spacings
- 8.3 The ratio of anode signals against source position for several anode wire radii
- 8.4 Spectra of the position signal  $r$  for different anode spacings and wire diameters
- Fig. 9.1 Photograph of the induced cathode pulse after bipolar shaping
- 9.2 Spectra of  $(v_C - v_C')/(v_C + v_C') + K$
- 9.3 Experimental curve to show the effects of discriminating against background upon an uncollimated source of 6 keV X-rays.

CHAPTER 1.INTRODUCTION - GAS PROPORTIONAL DETECTORS1.1 The Single Wire Proportional Counter.

The gas proportional counter, basically so simple in its construction, continues to present itself in new roles to suit the demands of modern technology. The proportional counter was a natural development of the ionisation chamber and was first introduced in 1908 by Rutherford and Geiger<sup>(1)</sup>.

For many years work continued with Geiger counters but it was some time after the initial work by Rutherford and Geiger, particularly during the years of World War II, that the behaviour of the proportional counter became better understood and these counters were used more extensively when greater effort was being made to apply atomic energy to military projects. The behaviour of proportional counters and similar gas detectors, as it was then understood, and typical construction details, are given in some detail by Rossi and Staub<sup>(2)</sup> who used counters of many shapes and sizes and with a variety of differing anode structures.

The counter operates in a region of strictly controlled potential where gas multiplication takes place (the region often termed the 'saturation' region of an ionisation chamber), yet below the region of uncontrollable discharge known as the Geiger-Müller region.

In basic terms, the operation of gas proportional counters is such that electrons, liberated by some form of initial ionisation process in a gas filled region between a cathode and an anode, drift under the influence of an electric field, towards the anode and at

some point attain sufficient energy (i.e. greater than or equal to the ionisation potential of the gas atoms) to liberate further electrons. The process is cumulative and a controlled avalanche commences until ultimately all electrons are collected by the anode. In the wake of the drifting electron cloud are the positive ions which immediately commence to drift relatively slowly towards the cathode, and as they do so, the anode pulse develops.

Generally coaxial geometry, or a form of geometry using a circular section anode, such that the field immediately surrounding the anode is radial, is favoured. In this case the avalanche is confined to the intense field region immediately surrounding the anode. With the majority of secondary electrons being produced within one or two wire radii of the anode, the final pulse is almost independent of the position of initial interaction of the incoming radiation, and the pulse formation is more rapid.

Perhaps because of its extreme geometrical flexibility and its constructional simplicity the proportional counter still remains a useful instrument in all fields of science where detection of radiation of various types (including particles and electromagnetic radiation) is required. In particular the proportional counter is best suited to low energy work below 100 keV, where, with a careful choice of filling gas mixture, high efficiencies of detection can be achieved. It finds application where the much longer resolving time of the Geiger-Müller counter becomes prohibitive.

In early attempts, presumably to increase the sensitive area of counters, the multiple-wire proportional counter was introduced (see for example Rossi and Staub<sup>(3)</sup>) in which the anode structure was a grid of equally spaced, parallel anode wires.

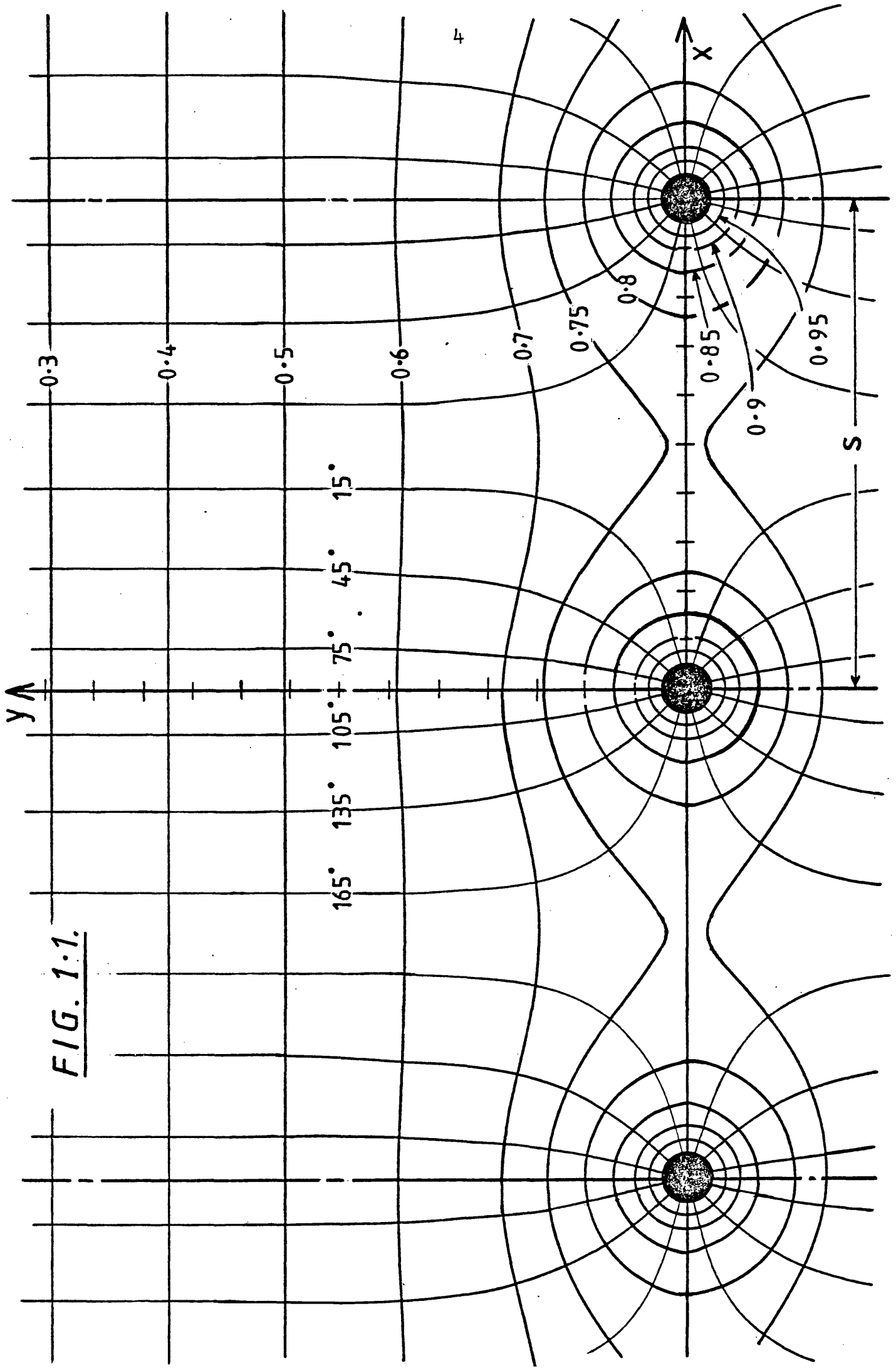
## 1.2 The Development of Multiwire Proportional Counters

Little work was carried out on multiwire proportional counters until 1968 when the behaviour of multiwire anode planes was investigated more fully by Charpak et al, at CERN<sup>(4,5)</sup>. Charpak pointed out that the equipotential lines immediately surrounding the anodes remained circular and the more remote equipotentials gradually blended with those due to adjacent anodes, until they became planar as the cathode was approached. The field distribution in a multiwire chamber has been determined and is plotted in Fig.1.1 where the geometrical proportions were  $h/s = 2$  and  $r_a/s = 1/20$ . (This rather high value for  $r_a/s$  has been chosen for convenience of illustration; in a typical chamber  $r_a/s$  would be much smaller than this; i.e.  $1/50 - 1/200$ ). Equipotentials have been plotted for values of  $P$  ranging from .35 to .95 using the formula for  $P$  given in Eqn.11, Chapter 3. The stream lines have been determined using Eqn.12 and are shown for values of  $\alpha$  from  $15^\circ$  to  $165^\circ$  by  $30^\circ$  intervals.

Thus Charpak found, under certain conditions of anode and cathode spacing, each anode and its surrounding volume behaved as an individual proportional counter, with normal multiplication taking place near the anode, but with reduced gas gain due to the reduced potential gradient in the multiplication region. Higher anode potentials were therefore needed to restore the gain, and this in turn placed greater demands upon the chamber construction to avoid electrical breakdown. (Some constructional details are discussed by Charpak et al<sup>(6,7)</sup>).

Consequently a new field of counter research was opened up, new techniques were developed, and proportional chambers were produced which were to provide considerable new information about the characteristics and trajectories of incident radiations. Furthermore,

FIG. 1:1.



the large amount of research done in developing gas proportional counters since 1968 has led to a greater understanding of the behaviour of electrons and positive ions, as they move within the chamber.

In the following sections some operating characteristics of multiwire proportional counters will be discussed and some typical applications briefly outlined.

### 1.3 Resolution Considerations

Events giving rise to the same amount of initial ionisation will inevitably produce a spread in the output pulse height of a proportional counter. A measurement of this spread in terms of full-width, half-maximum of the resulting distribution is normally termed the resolution of the proportional counter. Some factors contributing to the resolution are : statistical fluctuations in the number of initial electrons, electron attachment, diffusion, non-uniformity in wire diameter and counter geometry, counter end effect, unhygenic construction and electronegative impurities in the filling gas. A typical value for the resolution of a coaxial cylindrical counter would be about 17%, but the resolution may deteriorate for other counter geometries and for multiwire chambers, and values of resolution in excess of this are not uncommon.

### 1.4 The Efficiency of Multiwire Proportional Counters

Multiwire proportional counters are often more efficient than single wire counters because of their larger sensitive areas. In single wire counters, pockets of low and perturbed field often exist causing inefficient detection.

Efficiencies close to 100% have been claimed for multiwire counters<sup>(4)</sup>, but clearly, efficiency depends upon so many variables such

as the source solid angle, the counter area and thickness, the filling gas, the type and energy of the detected radiation, the setting of discrimination levels, etc., that it is difficult at this stage to make comparisons. Nevertheless, the fact that nearly 100% of the incident radiation can be effectively detected in a well designed chamber is indeed encouraging. High efficiencies are normally realised with minimum ionising radiations and with X-radiation in the region of 2 - 20 keV, but special precautions need to be taken to reduce absorption in the window material for sub-keV X-ray energies and to ensure that the gas filling has adequate stopping power for energies in the range 20 - 50 keV used in medical work<sup>(8)</sup>.

### 1.5 Applications of the Multiwire Proportional Counter

Multiwire chambers have found many uses in high energy physics, often replacing more cumbersome scintillation detectors in such applications as anticoincidence counters and telescopes<sup>(6)</sup>, and in spark chamber applications where more than one chamber can be used to determine the track location and orientation of an incident particle prior to making a decision whether or not to initiate the spark. The rapid response time of multiwire proportional chambers is of course an important factor here, where fast decisions are required.

In applications such as that described above, the large sensitive area of the multiwire proportional chamber is a distinct advantage. It is often necessary, however, to have a constant gain pattern over the whole area and Parker et al<sup>(9)</sup> have developed such a chamber with dimensions 20 cm. x 20 cm. and a gain uniformity within 2% rms over the entire area.

Apart from the high energy particle trajectory measurement applications typified above, multiwire proportional chambers are finding

very important low energy application in biomedical research for X-ray and neutron imaging and as isotope cameras in nuclear medicine<sup>(10)</sup>.

Typical X-ray energies used for this work are 5keV to about 30keV<sup>(11),(12)</sup> and<sup>(13)</sup>, and often it is necessary to resort to long drift regions and/or heavy gases to realise high efficiencies.

An application in molecular biological research has been described by Faruqi<sup>(14)</sup> where X-radiation of about 8keV (the characteristic K-radiation of copper) is commonly used with X-ray diffraction techniques for studying biological structures in, for example, protein crystallography and fibre diffraction experiments.

Slow neutron imaging, which offers the advantage of great depths of tissue penetration, requires the use of a converter screen in front of the multiwire proportional chamber or a converting gas filling mixture containing He<sup>3</sup> or BF<sub>3</sub>, which will emit ionising particles. Conversion efficiencies of 70% and 50% have been reported<sup>(15),(16)</sup>.

Proportional chambers are, of course, being used now in the research field of X-ray astronomy for the detection and mapping of soft X-radiation from extended sources. Chambers can be constructed of lightweight materials, and they offer considerable flexibility of geometrical design and lend themselves to the high packaging densities encountered in space vehicles and rocket payloads<sup>(17),(18)</sup>. For example Rappaport et al<sup>(19)</sup> and Levine et al<sup>(20)</sup> have successfully used multiwire proportional chamber two dimensional imaging systems on board sounding rockets for the X-ray imaging of supernova remnants in the X-ray energy range 0.2 - 1.5keV.

In the above applications several methods have been developed for reading-out the positional information in one or two dimensions, and these are described in the following chapter.

## CHAPTER 2.

### POSITION SENSITIVE DETECTORS

#### 2.1 Introduction

In the preceding chapter but a few of the more common applications of gas proportional chambers are mentioned. All exploit the ability of the proportional chamber to provide accurate positional information and all utilise some form of conversion to permit data to be processed and read out.

It is the purpose of this chapter to look in more detail at some positional information systems as they have been applied to proportional detectors and to discuss the various advantages and limitations which have been experienced by workers over the last ten years or so.

Interest in position sensitive proportional detectors was aroused following the success of using semiconductor detectors for this purpose<sup>(21),(22),(23),(24),(25),(26)</sup> and some of the readout techniques involved could be similarly applied to proportional detectors. Since then much has been written on this subject and it is beyond the scope of this thesis to look into all variations and combinations of methods. Only the more common methods will be discussed.

#### 2.2 Techniques Employed in Obtaining Positional Information

##### 2.2.1 Individual wire readout

The most obvious method of extracting positional information uses one amplifier and discriminator per wire. Whilst recent technology has made this possible in terms of size and cost per amplifier through the use of integrated circuits<sup>(27)</sup>, it still remains a prohibitive technique for larger chambers. Charpak, for example, has reported the

use of a system having 70,000 wires<sup>(28)</sup>.

Low-cost integrated circuit amplifiers tend to be noisy and may impose a limitation where low output proportional chambers are used. A further fundamental limitation and possible restriction of this method is that the best resolution obtainable is that of the wire spacing (i.e. typically 2mm.). Generally it is felt that better methods are now in existence which are far less laborious to install, are less costly and consume a fraction of the electronics space. A point in favour of this method is that the outputs are in a suitable form for digital manipulation.

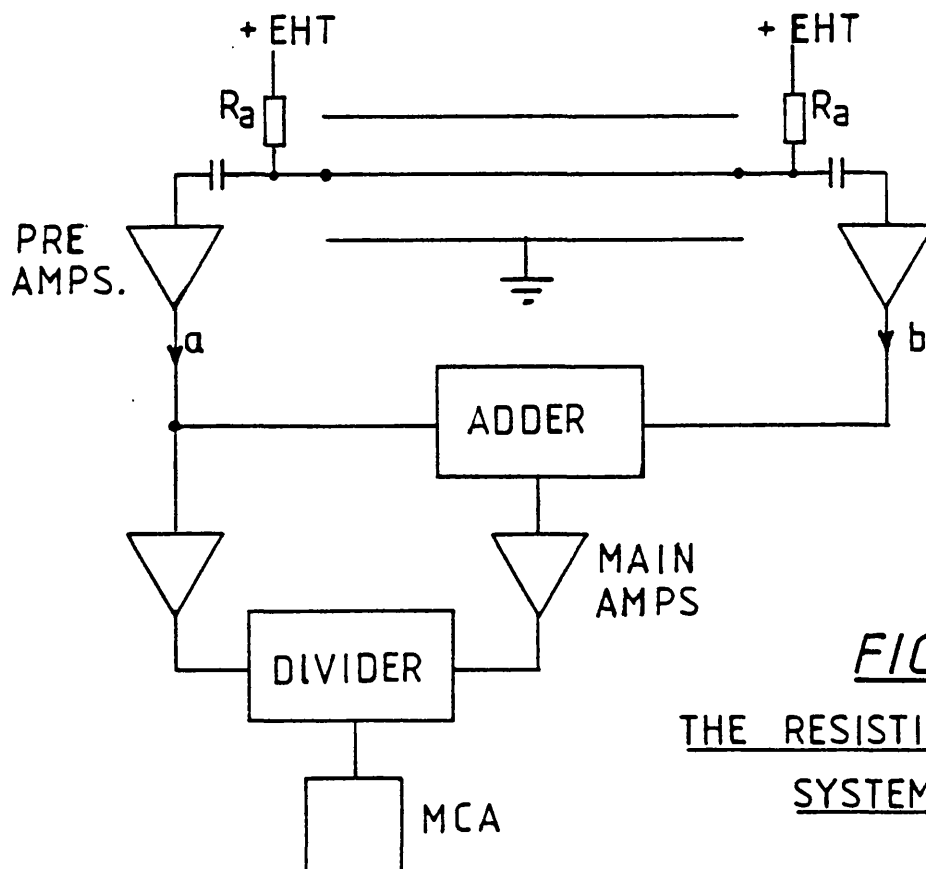


FIG. 2.1-  
THE RESISTIVE ANODE  
SYSTEM, ref. 22.

### 2.2.2 The resistive anode

The earliest position sensitive proportional counter was introduced by Kuhlmann et al<sup>(29)</sup> in 1966. This work was based on that of earlier workers with semiconductor detectors, Kuhlmann<sup>(22)</sup> and Lauterjung et al<sup>(21)</sup>. Shown in Fig. 2.1 their apparatus consisted of a proportional counter with a resistive anode 30 cm. long with voltage amplifiers connected to each end. By electronically dividing  $a/(a + b)$ , the energy component was removed from the output leaving only positional information for analysis by the multichannel analyser. The positional uncertainty reported was 1.2 mm. over the 30 cm. length.

A similar method has been applied to a Geiger counter with an expected increase in positional uncertainty (2 cm. in 70 cm. length),<sup>(72)</sup>.

### 2.2.3 The resistance-capacitance line

In 1968 Borkowski and Kopp introduced a readout method for single wire counters<sup>(30)</sup>, which has since been applied in various forms to multiwire chambers<sup>(16)</sup>. Their counter used a highly resistive anode made from quartz fibre with a pyrolytic carbon coating having a resistance of about 40k $\Omega$ /mm. The operation was such that a charge deposited on the anode caused a current to flow through the anode, and into the terminating capacitance, developing a voltage whose rise time was dependent upon the position of charge deposition, the anode acting as a distributed resistance-capacitance transmission line. Fig. 2.2 shows the method of processing the information. A time reference pick-up was used, after fast shaping, crossover detection and some delay, to start a time-to-amplitude converter. The stop signal was similarly obtained in a slow channel from the anode voltage pulse developed across C. The crossover time is dependent only on pulse rise time and not on pulse height and hence the energy of the ionising radiation is not important.

A similar electronics system has been described by Mathieson

and Harris<sup>(31),(32)</sup> and in more detail by Harris<sup>(33)</sup>. The spatial resolution of .5 mm.fwhm in 400 mm. which was claimed for this technique compares favourably with present day achievements.

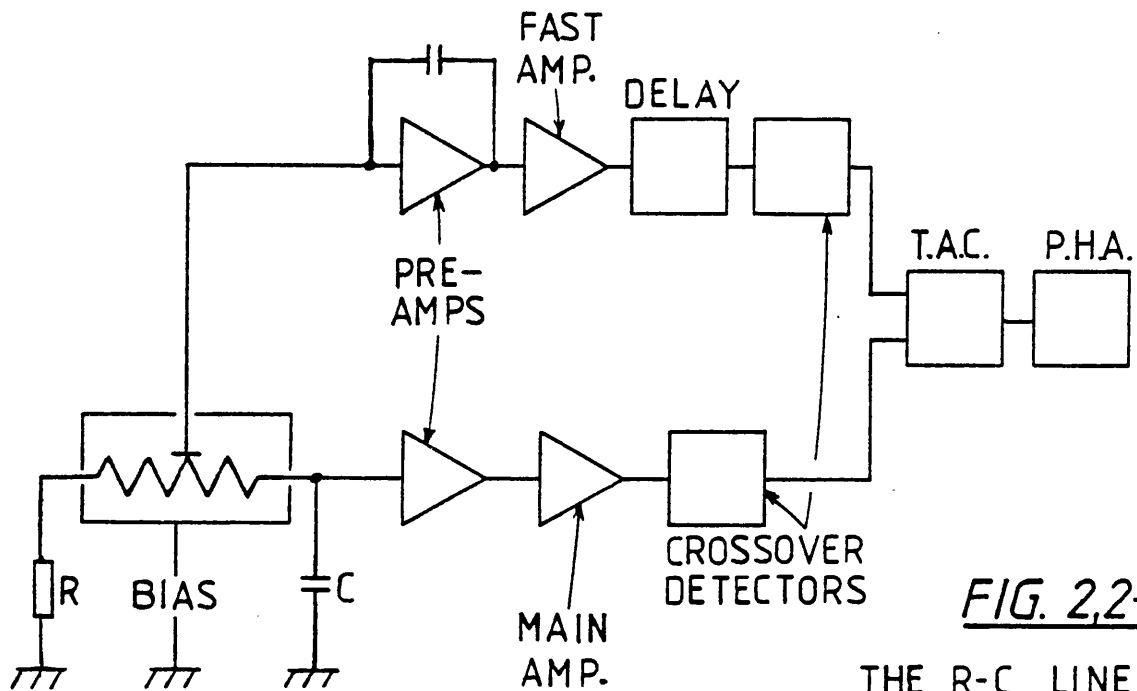
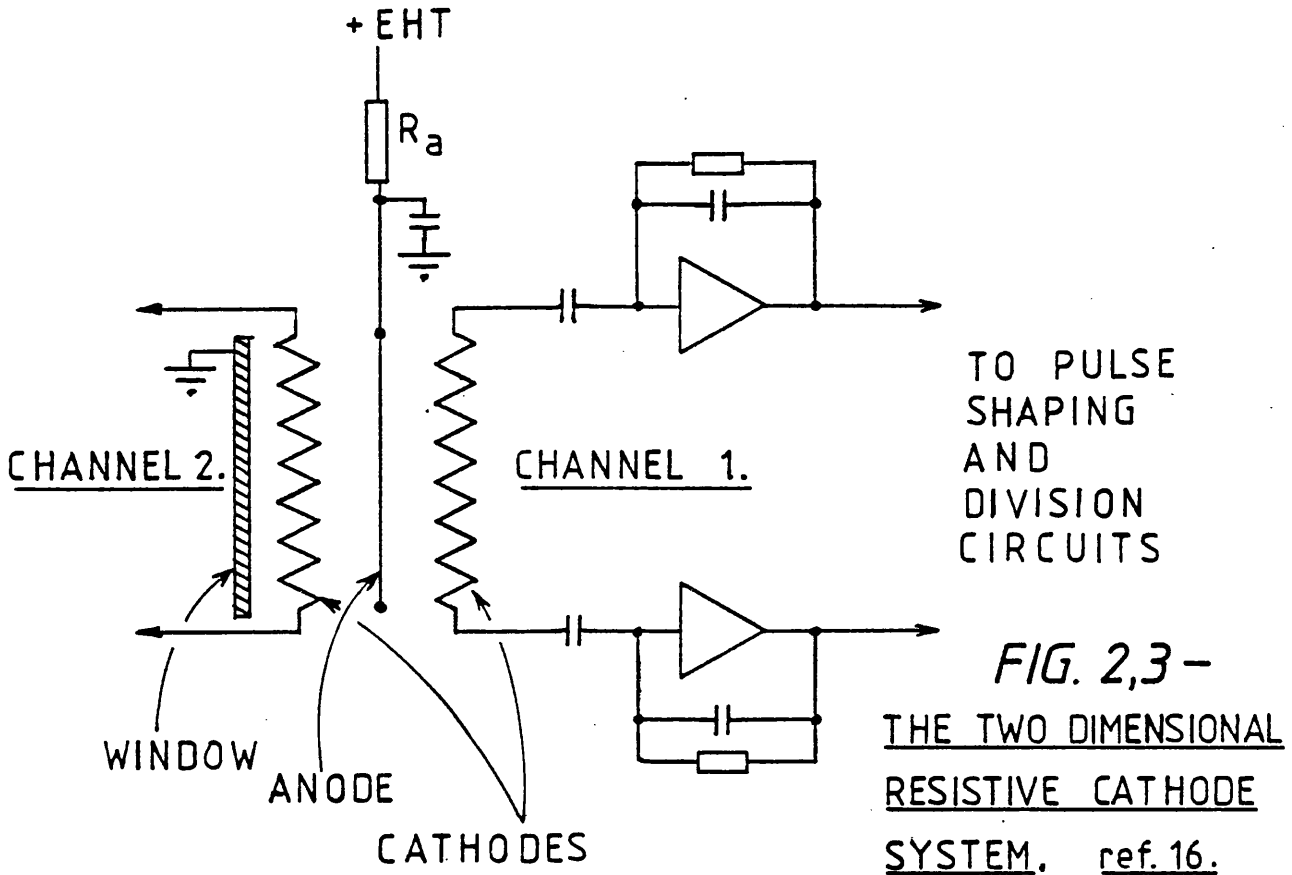


FIG. 2,2-

THE R-C LINE  
SYSTEM, ref. 30.

Several variations of Borkowski's and Kopp's method have since been introduced; for example, Alberi et al<sup>(16)</sup>, (see Fig. 2.3) have used a charge sensitive division method in a two dimensional, resistive cathode chamber.



This method differs from that above in that charge induced in the cathode wire is sensed at each end of the cathode, and the ratio taken (the energy dependent terms cancel out). The electronics system compares the charge collected at one end with the total charge summed from both ends of the cathode. The system was developed to detect thermal neutrons and the spatial resolution of 3.1 mm. seems to have been determined mainly by the physical path length of the reaction products and not by the electronics.

Becker et al<sup>(34)</sup> have described a resistive chain readout system for obtaining positional information in a direction orthogonal to the anodes. The system, shown in Fig. 2.4, again uses a charge division method of data extraction.

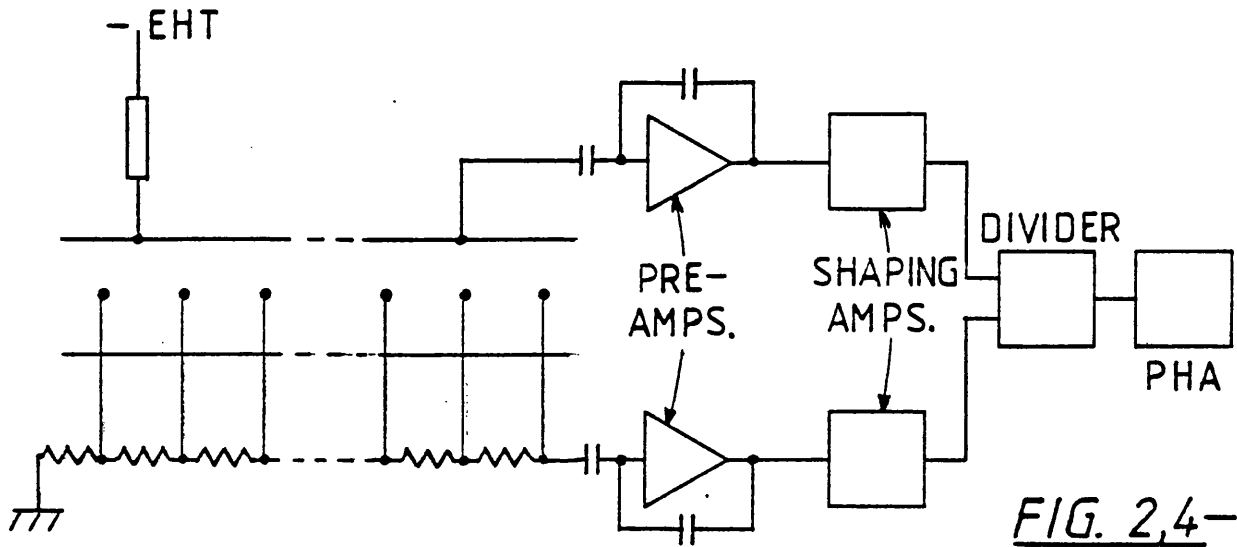


FIG. 2,4-  
THE RESISTIVE  
CHAIN SYSTEM. ref. 34.

This system has a disadvantage in that the resolution for radiation giving rise to local ionisation, is simply the wire spacing, whereas for oblique incidence particles, generating distributed ionisation tracks, more than one anode will respond and some interpolation is carried out. Under these latter conditions a somewhat better resolution was claimed of between .5 and 1.5 mm.fwhm depending on the type of radiation, with an integral non-linearity of less than .5%.

The use of resistance-capacitance readout systems requires careful consideration of noise which is the major resolution degrading factor. Not only does noise cause amplitude fluctuations in pulse height division methods, but it also introduces time jitter in leading edge and crossover timing methods.

Mathieson<sup>(35)</sup> and Mathieson et al<sup>(36),(37)</sup> have provided a detailed analysis of both shorted and open circuit resistance-

capacitance lines for use in the rise time mode of operation and have considered the effects of system noise on positional resolution. They have shown that there is an optimum value of time constant, T, for equal C-R, R-C, C-R filters in the electronic system, which reduces the rms positional uncertainty (over the central 85% of the line) to a minimum, and also an optimum value of T which reduces the rms non-linearity to a minimum. Values of T were not too different and a suitable compromise value could be chosen for each line configuration.

#### 2.2.4 Delay line readout

In more recent years, delay line readout has become perhaps the most popular. It was first used by Rindi et al<sup>(38)</sup> and Grove et al<sup>(39)</sup> (Fig. 2.5), who have tried both a ferrite loaded delay line and a ceramic cored line. They preferred the latter which gave a greater sensitivity to position and hence a much lower positional uncertainty; the positional uncertainty quoted was less than 150 $\mu$ m. for readout in the orthogonal direction. By this method, anode or cathode wires are uniformly coupled to the delay line along its length and the electronic detector system is normally of the zero-cross, time-to-amplitude conversion type. It is important to note that overcoupling of the signal into the line will upset its delay characteristics but light coupling, of course, reduces the signal level. The technique is therefore best employed in high energy proportional chamber or spark chamber situations, where signal levels are sufficiently large that low-capacity, wrap-around strips may be used for coupling with the delay line. There have been variations of this approach in attempts to obtain direct coupling by integrating the chamber electrical characteristics with those of the delay line<sup>(40),(41)</sup>, but more recently Beardsworth et al<sup>(42)</sup> have shown that by choosing a line of low

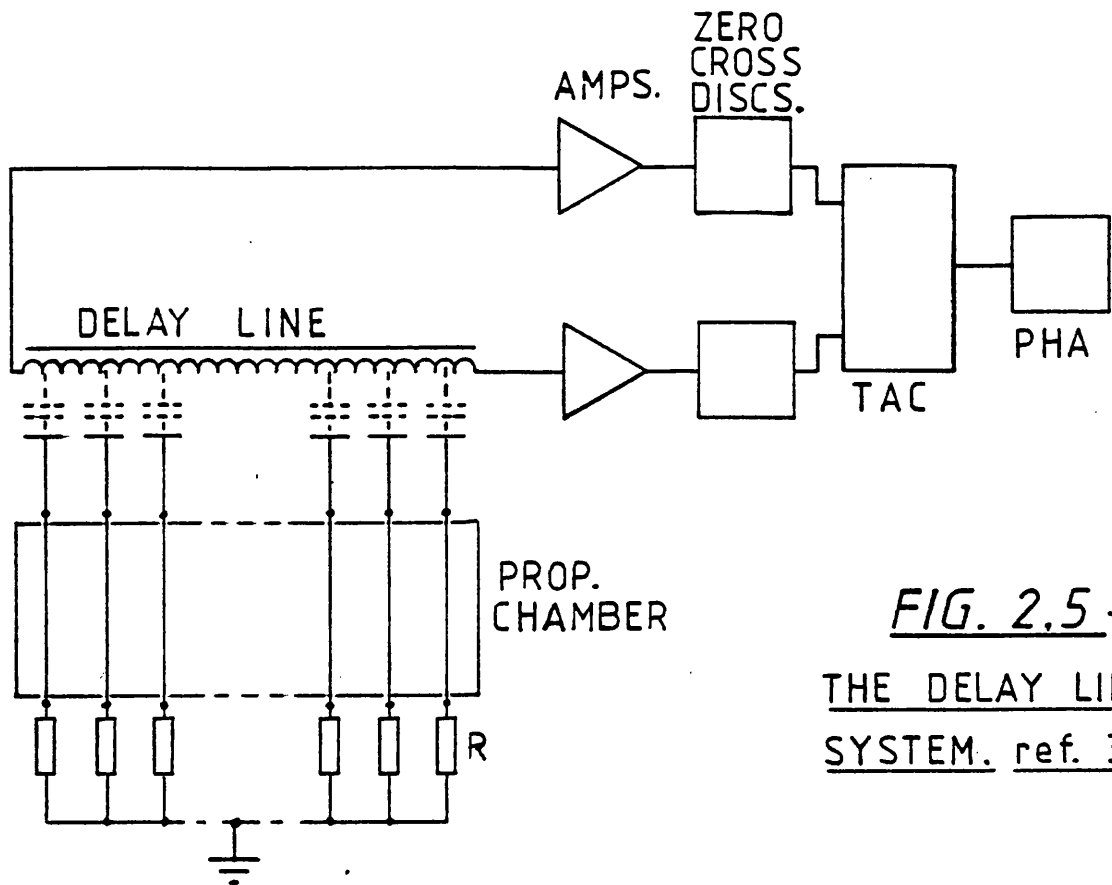


FIG. 2.5 —  
THE DELAY LINE  
SYSTEM. ref. 39.

characteristic impedance and by paying due regard to the noise introduced by using such low impedance lines, it is possible to directly couple the cathode wires to the line without serious modification to its performance. A positional uncertainty of less than .2 mm. was achieved with an rms non-linearity of .08 mm.

A limitation of this method would be the cost of specially designed tapped delay lines.

### 2.2.5 Digital processing

Simultaneous readout in two dimensions from anode signals by the analogue methods outlined above introduces complex networks of components and preamplifiers around the chamber, and whilst excellent results have been achieved, for example, by the R.C. line system of Borkowski and Kopp<sup>(43)</sup>, (Fig. 2.6), the obvious limitation has been the

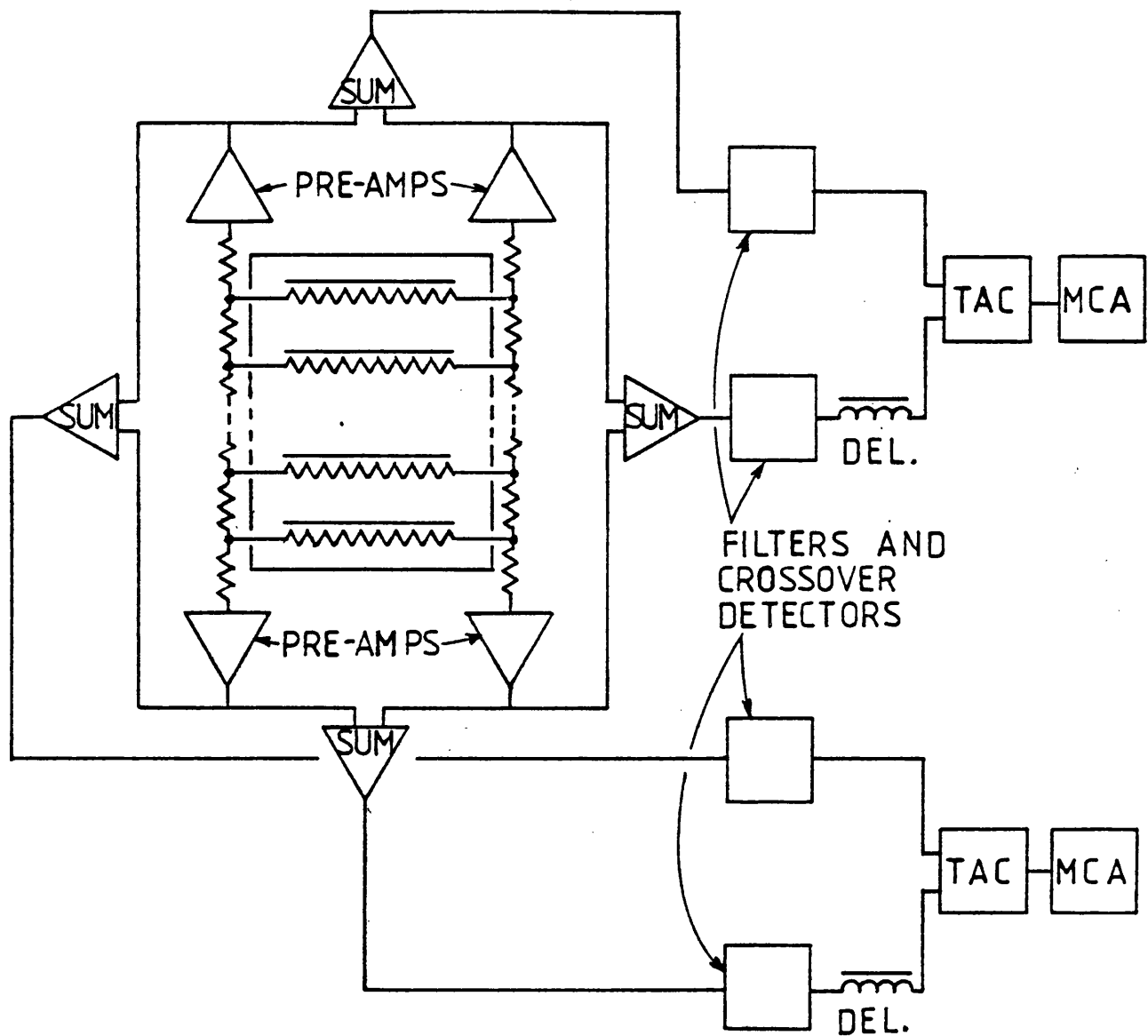


FIG. 2,6-

THE TWO DIMENSIONAL  
R C LINE SYSTEM. ref. 43.

resolution in the direction orthogonal to the anodes, which is limited by the wire spacing for radiation producing confined ionisation. It has been found recently that there is some considerable advantage in using a wire cathode readout, and by interpolation, much better resolution is possible in the orthogonal direction. The reason for this forms the basis of this thesis and will be discussed in detail in later chapters.

At the time of writing the most recent published results are those of Sauli<sup>(44)</sup> (see also<sup>(45),(46)</sup>), whose method was to use two mutually orthogonal sets of cathode wires, each set being divided into groups (Fig. 2.7).

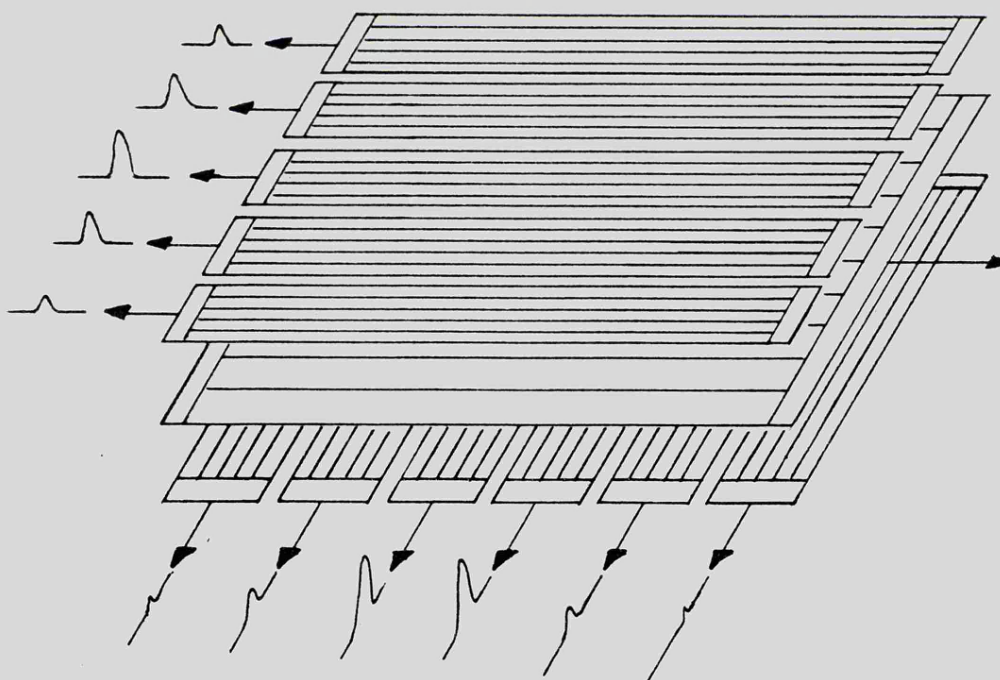


FIG. 2.7- THE DIGITALLY PROCESSED SYSTEM. ref. 44.

The groups of wires were each equipped with a charge sensitive preamplifier and an analogue to digital converter. By digital

computation to provide positional information based on the centre of gravity of the induced charge distribution, a positioning accuracy of around  $150\mu\text{m.rms}$  was obtained for a  $1.5\text{ keV X-ray}$  beam in a xenon isobutane filling, in the direction orthogonal to the anode wires, and  $35\mu\text{m.rms}$  was obtained in the direction along the anode wires, which was better than one tenth of the wire spacing. At the present time, with inexpensive local microcomputing systems, integrated circuit preamplifiers and analogue-to-digital converters readily available for a few pounds each, the cost of such a system is certainly not prohibitive.

### 2.3 Drift Techniques

Many configurations of drift chambers have been described in the past decade, all serving rather different purposes, but generally their function is to provide information concerning the position location of incident radiation by measuring the drift time of electrons, formed during the initial ionisation process, as they move from the point of ionisation to the collecting anode. Electron drift regions have also been used in a passive nature to improve the performance of multiwire proportional chambers. Some applications are outlined in Fig. 2.8.

Fig.2.8a shows a spherical drift space used in front of a multiwire proportional chamber as an efficiency improver. The drift space provides a large absorption volume intended for the efficient absorption of X-rays up to  $50\text{keV}$  often encountered in medical physics. The spherical field removes any interdependence between absorption depth and final imaging position, by causing electrons to drift along radial lines focussed on the source. This technique has been successfully employed here in the Physics Department by Christie and Mathieson<sup>(11)</sup> and at CERN by Charpak<sup>(13),(47)</sup>.

A secondary effect of drifting prior to detection is that the

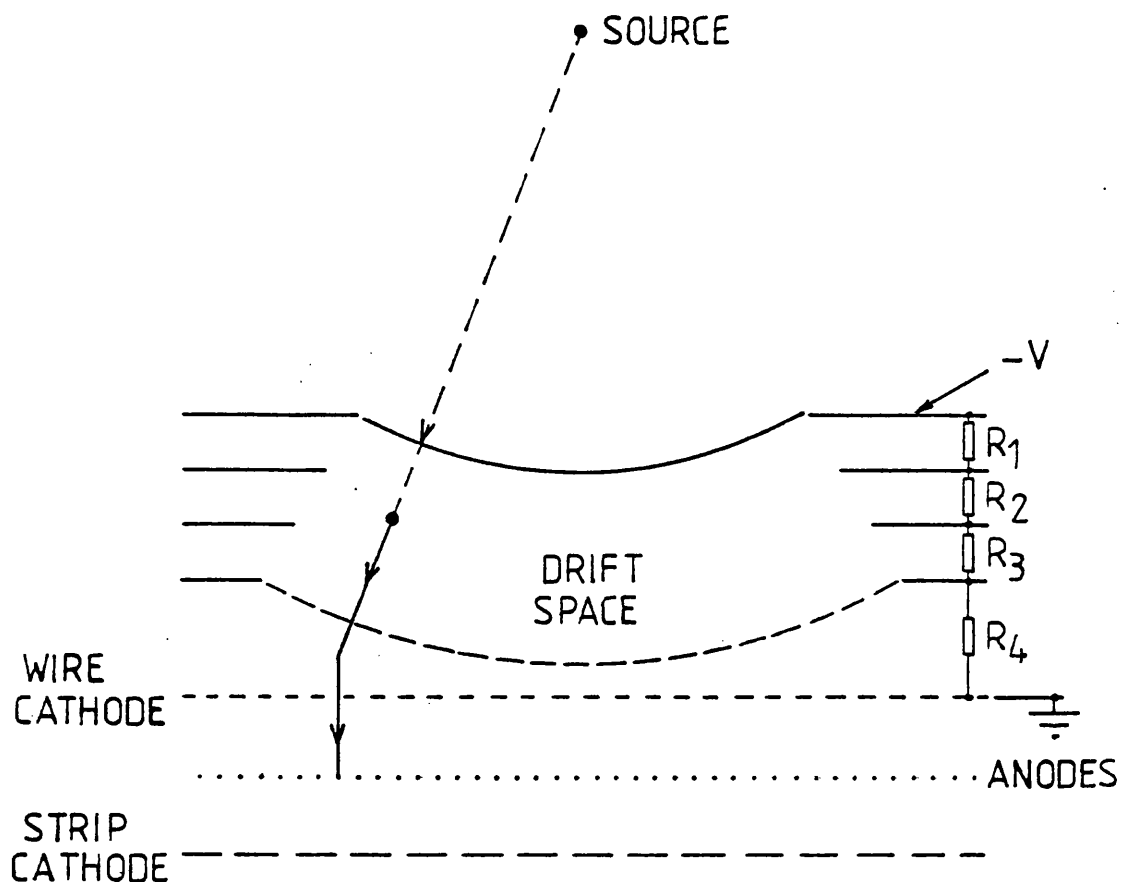


FIG. 2,8a — THE SPHERICAL DRIFT CHAMBER.  
refs. 11, 13, 47.

diffusion process causes the cloud of electrons to spread to a diameter similar to the wire spacing, so that the final avalanche may be shared by two or more anodes. This effect is often beneficial in improving the resolution by reducing 'binning' effects<sup>(48)</sup>.

A method of locating particles by drift time measurement has been developed by Bressani et al<sup>(49)</sup> (Charpak et al<sup>(6)</sup>) and further developed by Saudinos et al<sup>(50)</sup> for practical application to localise 1GeV protons. A uniform field drift space and proportional detector were so arranged that electrons liberated during the initial ionisation process drifted at constant velocity towards the detector, and passed

through a grid into the non-linear detector field. Thus the time spent in the drift region was a measure of the position of the particle. Fig.2.8b is an illustration of the chamber.

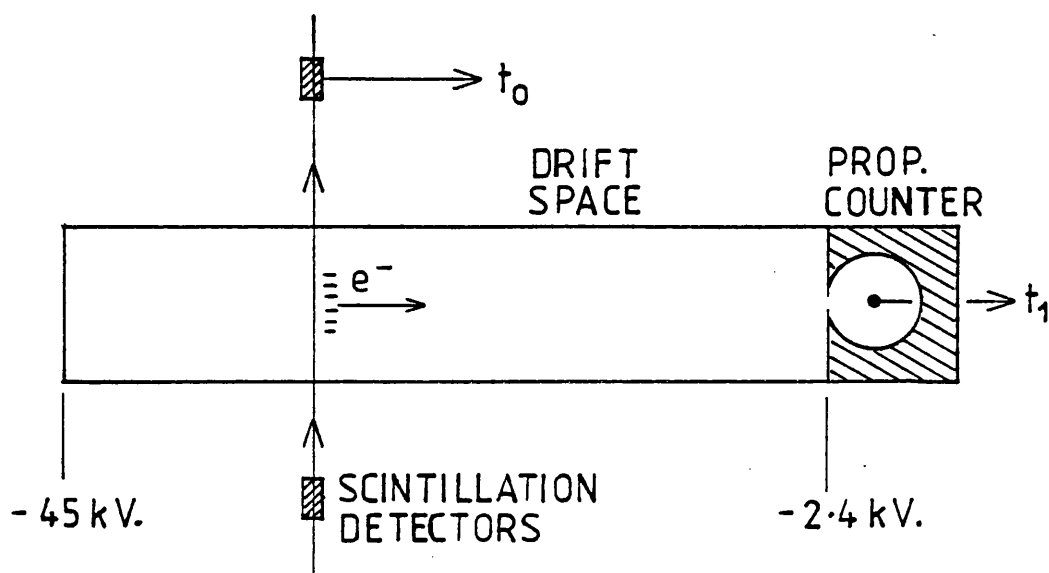


FIG. 2,8b — PARTICLE LOCATION BY DRIFT TIME MEASUREMENT. ref. 50.

The particle track was defined by scintillation detectors in coincidence which also gave a time-zero pulse. Data was processed by conventional time-to-amplitude-to-digital conversion electronics. The spatial resolution of such a system clearly depends upon the time spent by the electron cloud in the drift space, and it has been shown that the best resolution obtainable near the grid is about 200 $\mu$ m. whilst at about 50cm. from the grid a resolution of 1.6 mm.fwhm has been achieved. It should be noted that linear drift chambers are not suitable for radiation which is totally absorbed within the gas. The radiation must pass through the chamber to operate the time zero probe.

Certain important limitations must be considered when using drift chambers:

Gas composition: we have noticed from previous work carried

out in this department that gas impurities and small variations in gas mixtures can cause the drift velocity,  $W$ , to change rather more than might be expected. This has been reported and discussed by El Hakeem<sup>(51)</sup>, who found that normal outgassing from various organic components in his system was responsible for up to 25% reduction in  $W$ . Water vapour is indeed the most serious of likely impurities. It has been shown by experiment<sup>(51)</sup> that .2% water vapour may be responsible for up to 30% reduction in drift velocity near the saturation region.

Temperature: drift velocity is temperature dependent to such an extent that normal room temperature changes may severely influence results. El Hakeem reports a change in drift velocity  $dW/W = .2\%/^{\circ}C$  in Ar/10%CH<sub>4</sub>. The effect varies with gas mixture but as an example, Sauli<sup>(44)</sup> states that a 10<sup>o</sup>C rise in temperature produces an error of around 100 $\mu$ m. in a 3 cm. drift space filled with an argon isobutane and methylal mixture.

Furthermore, the importance of avoiding or compensating for the effects of local magnetic fields should always be considered wherever drifting electrons are present.

An interesting method of interpolation between wires by drift time measurements shown in Fig.2.8c, was described by Walenta et al<sup>(52)</sup>, who used fewer anode wires than normal with 1 cm. spacing and were able to localise the incoming particle by measurement of the drift time. They compared the electron arrival time with a time-zero pulse obtained from a scintillation detector outside the chamber. The success of this technique depends upon the constancy of electron drift velocity with changing electric field strength, and care was taken to choose a gas such as pure ethylene or argon/10%methane (P.10) where this condition nearly applies. Information was translated into digital form by a gated 60MHz. scaler and data handling was accomplished by a PDP.9 computer.

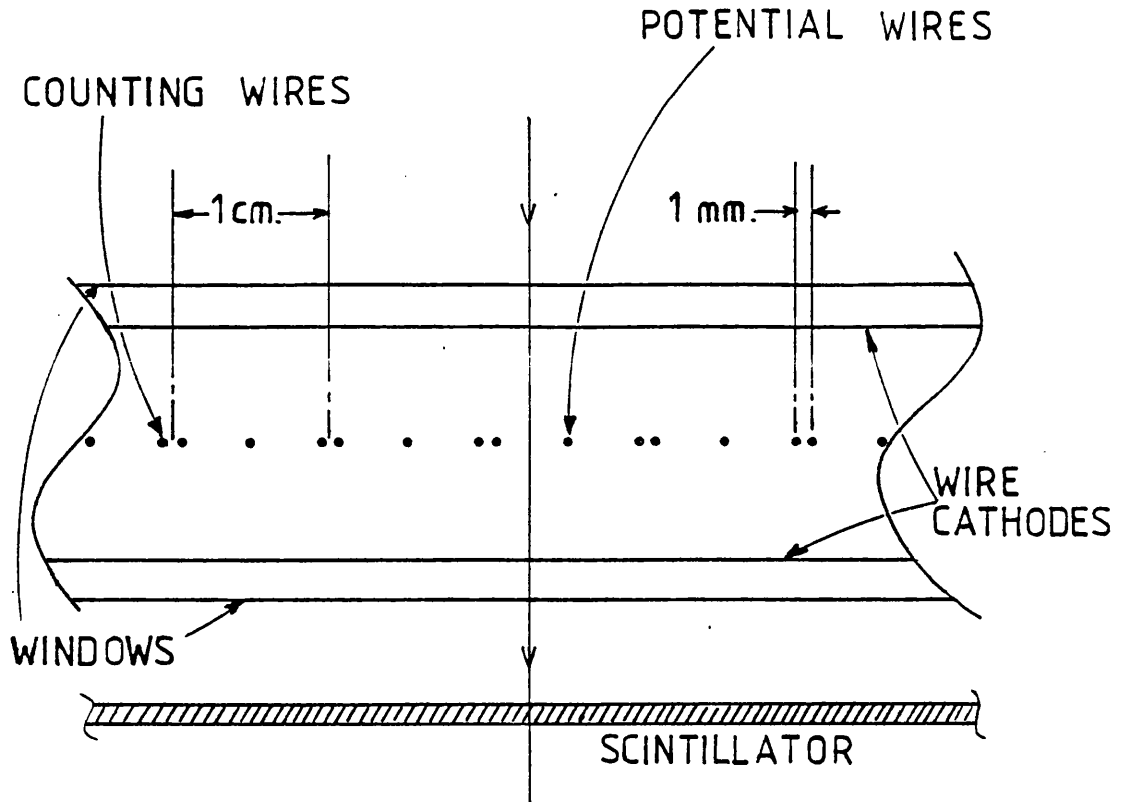


FIG. 2,8c — INTERPOLATION BETWEEN WIRES  
BY DRIFT TIME MEASUREMENT. ref. 52.

Published results indicate that ethylene is the better filling gas for this work giving a more linear drift time versus drift length curve than P.10, and the positional accuracy obtained was .47 mm. A practical chamber of this nature is somewhat more complicated by the need to differentiate between events to the left and right of the anode. This has been accomplished by replacing the anode with two wires 1 mm. apart, each being active to those events on its own side of the cell.

Between the pairs of anodes were inserted single wires termed potential wires which were connected to the cathode plane and served to define the boundary associated with each anode pair, and also to improve the cylindrical field. Further solutions to left-right ambiguity using charge induction effects on cathode wires or neighbouring anodes (chapters 3 and 4 discuss this phenomenon in detail), have since been

given<sup>(53,54,55)</sup>, whereby left-right assignment could be given to minimum ionising particles as close as 50 $\mu$ m. to either side of the anode. Improvements on the method of Walenta et al<sup>(52)</sup> in terms of positional accuracy and time resolution<sup>(56)</sup> have resulted in a positional accuracy of .26 mm.fwhm and a time resolution of 6.4 ns.

#### 2.4 Discussion

There has naturally been some improvement over the years in the positional accuracy that can be obtained with position sensitive detectors. Clearly, the best accuracy has been achieved by the recent centre-of-gravity digital methods but the major disadvantage here could be the cost. The earlier analogue systems give very good results and should still be considered for low cost systems.

Resulting accuracies and linearities have been obtained under extremely varied conditions of gas filling pressure, gas gain, incoming radiation etc. and are not necessarily directly comparable, but they serve to give an indication of the effectiveness of methods.

The type of incoming radiation is of particular importance when choosing a system. It should be borne in mind that systems with anode readout cannot be expected to give better spatial resolution than the anode wire spacing in the orthogonal direction, except for inclined tracks of minimum ionising radiation. It is now generally accepted that anode wire spacing cannot be less than 1 mm. without introducing severe gain loss or accompanying high voltage breakdown problems associated with increased e.h.t.

Readout from cathode planes offers certain advantages for two dimensional chambers. Firstly, cathode wires can be arranged mutually orthogonal, and identical electronics can be used on each channel. Secondly, the electronics system is generally less complex than that required for two dimensional readout from the anode plane, where

information from two coordinates is mixed and requires separation at the anode terminations. Finally, to some degree, interpolation between anodes is automatically provided by cathode readout systems, which can provide up to an order of magnitude improvement in spatial resolution over the anode wire separation.

It should be noted that linear drift chambers or chambers employing drift techniques as a means of interpolating between wire spacing are only suitable for minimum ionising particle detection where a trail of ionisation is formed across the chamber. Totally absorbed radiation would, of course, not be able to operate the time-zero scintillation detector, and would also create uncertainty in the drift path length.

CHAPTER 3.LOCALISATION OF THE AVALANCHE3.1 Initial Observations

Perhaps influenced by the behaviour of the avalanche in the Geiger counter, which is thought to spread around and along the anode wire, one has always assumed that in proportional counters and chambers the avalanche similarly surrounds the anode, but is localised longitudinally. This concept was not questioned until recently, when during various experimental investigations in this department on imaging multiwire chambers<sup>(57)</sup>, it was noticed that, under certain conditions, the pulses in the two cathode position-sensing planes differed in a surprising manner. Under conditions where absorption normally occurred in one half of the chamber due to soft X-radiation, or where electrons liberated in a drift space were drifted in from one side of the anode plane, a comparison of the pulses induced in each cathode suggested that the avalanche was to some degree angularly localised. The difference in cathode pulses also indicated an angular localisation directed towards the active side of the chamber.

An experiment was set up to examine this effect, which it was thought could provide additional useful information from position sensitive detectors. In the experiment a simple multi-anode chamber was used, and a collimated soft X-ray source was moved across the anode 'cell', whilst the pulse height on a neighbouring anode was observed. The results of this exploratory run were indeed favourable, indicating a strong localisation of the avalanche. A more detailed description of the apparatus is given later in chapter 4.

It was soon apparent, from publications which appeared during

the course of our investigations at Leicester, that other workers were independently considering this phenomenon<sup>(28, (46, (58, (59</sup>, but no satisfactory theoretical survey had been forthcoming. An earlier reference to angular localisation which has recently come to the writer's attention was by Charpak and Sauli<sup>(68</sup>. They were able to show experimentally that some non-uniformity existed in the way the ion cloud surrounded the anode wire, but again, no theoretical analysis was given. Obviously a more detailed experimental exploration was required, but more urgently, some theoretical explanations were necessary.

### 3.2 Basic Description of the System.

A conventional multiwire proportional chamber is shown schematically in Fig. 3.1. The anodes are drawn perpendicular to the  $x - y$  plane with the particular anode A, at which the avalanche takes place, situated at the  $x - y$  origin, between two neighbouring anode wires with spacing  $s$ . The anode to cathode distance is  $h$ . The angle  $\alpha$ , measured from the  $x$  axis, indicates the angular position of the avalanche at the anode surface due to an incoming X-ray at position  $x_0$ .

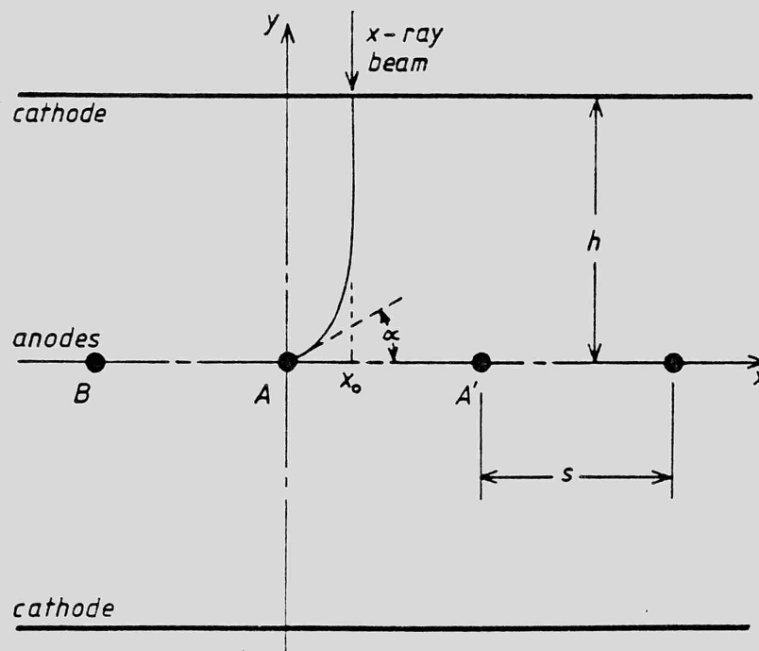


FIG. 3,1.

With normal chamber geometry, where the anode radius is small compared with  $h$ , the field near the surface of the anode is very accurately radial and providing  $s$  is also small compared with  $h$ , the field at the cathode is spatially uniform and probably remains so for some distance into the chamber. Thus a set of equidistant field lines leave the cathode and terminate at the anode as equiangular field lines. Ideally then, electrons produced by an ionising event near the cathode drift along a particular field line and eventually create an avalanche whose centre-of-charge has an angular position directly proportional to the  $x$ -coordinate of the event.

Positive ions, formed during the avalanche, drift back towards the cathode along the same field line and as they do so, charges are induced on the anodes and cathodes. The magnitude of these induced charges may be calculated from formulae given later in this chapter, and from these formulae, if one assumes a constant positive ion mobility, the time development of the induced charges may be calculated.

In practice, of course, the initial electron group is of finite size, and diffusion occurs during the drifting process. The avalanche will therefore encompass many field lines and will, to some extent, spread itself around the anode.

### 3.3 Theoretical Considerations

As a basis for the theory that follows, we have used a theorem due to James Clerk Maxwell<sup>(60)</sup>, which states, in terms appropriate to the present applications, that if a conductor is raised to unit potential and produces at an external point a potential  $P$ , then a unit charge placed at that point will induce on the conductor a charge  $-P$ . This may be proved in the following manner:

Standard electrostatic theory states that in a system of

conductors, the charges  $q_i$  and the potentials  $v_i$  may be conveniently expressed in terms of the capacitance coefficients thus:

$$q_i = \sum_{j=1}^n C_{ij} v_j .$$

Therefore in a system of conductors 1 and 2,

$$q_1 = C_{12} v_2 + C_{11} v_1 \quad \text{and} \quad q_2 = C_{21} v_1 + C_{22} v_2 .$$

If we now consider a unit charge placed on conductor 2, with all other conductors, including 1, grounded, we may calculate the charge  $q_1$  induced on conductor 1.

The equations above then reduce to

$$q_1 = C_{12} v_2 \quad \text{and} \quad 1 = C_{22} v_2 ,$$

and hence 
$$q_1 = C_{12}/C_{22} .$$

Consider now that conductor 1 is raised to unit potential.

Assuming all other conductors are grounded except conductor 2 which is insulated and uncharged allowing it to rise to a potential which we shall call  $P$ ,

then 
$$0 = C_{21} + C_{22} P ,$$

or 
$$C_{21}/C_{22} = -P ,$$

but according to Green's reciprocation theorem,

$$C_{21} = C_{12} .$$

Thus 
$$\underline{q_1 = -P}$$

The conductor 2 may be physically very small; that is, we may regard a positive ion mathematically as conductor 2.

In the following theoretical studies we shall derive an expression for potential  $P$ , at coordinates  $x, y$  in the  $z$  plane, under three conditions:

- a) when all anodes, connected together, are raised to unit potential and both cathodes are grounded.
- b) when one particular anode is raised to unit potential and both cathodes are grounded.

c) when one cathode is raised to unit potential and the other cathode and all the anodes are grounded.

Thus we may calculate the value of induced charge  $q_i$  on either the anode plane, on one particular anode or on one cathode as

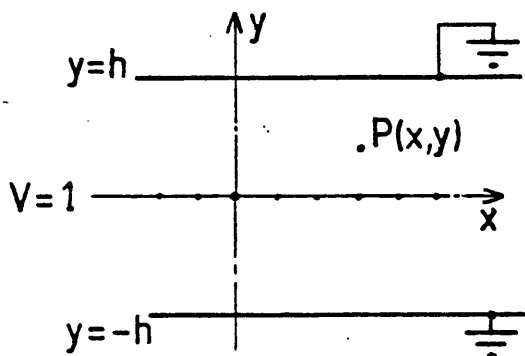
$$q_i = -QP.$$

where  $Q$  is the total charge due to the positive ion cloud at position  $x, y$ . The movement of the positive ion cloud along a field line from the avalanche anode to the cathode, will cause the induced charge to develop with time and this situation will also be considered.

Referring to Fig. 3.1 we shall simplify the analysis by imposing the conditions  $s \gg r_a$  and  $h \gg s$ , where  $s$  is the wire spacing,  $r_a$  is the wire radius and  $h$  is the anode-cathode spacing. It is also assumed that both the anode wire length and the lateral width of the anode plane are large compared with the anode-cathode spacing. In a normal fine-wire chamber, these conditions are not unreasonable.

With these conditions in mind, the first situation may now be considered:

a) Induced charge at connected anode wires.



The equipotential and field lines in a symmetric multi-wire chamber may be described by the complex potential  $W$ <sup>(6)</sup> given by:

$$W = -K \log \sin \pi z/s + V_0, \quad \text{Eqn. 1.}$$

where  $K$  and  $V_0$  are real constants determined by the electrode potentials.

Substituting  $x + jy$  for  $z$  and expanding the sine term, one obtains:

$$W = -K \log (\sin \pi x/s \cosh \pi y/s + j \cos \pi x/s \sinh \pi y/s) + V_0. \text{ Eqn. 2.}$$

Under boundary conditions, at the cathode,  $y=h$  and  $h \gg s$ ,

therefore  $\pi h/s \gg 1$ , and the following approximation results:

$$W = -K \log \sin \pi (x+jh)/s + V_0 \simeq -K (\pi h/s - \log 2 + j \pi x/s) + V_0.$$

The potential P is the real part of this equation and at the cathode

$P = 0$ , hence:

$$0 = -K (\pi h/s - \log 2) + V_0. \text{ Eqn. 3.}$$

The complex potential W may also be written

$$W = -K \log (A e^{j\theta}) + V_0,$$

where A is the modulus of the expression in parenthesis in Eqn. 2. and

$\theta$  is its argument.

It can be shown that  $A^2 = \frac{1}{2} (\cosh 2\pi y/s - \cos 2\pi x/s)$ . Eqn. 4.

$$\text{Now } W = -K \log A - Kj\theta + V_0. \text{ Eqn. 5.}$$

Equating the real terms to P we have,

$$P = -K \log A + V_0. \text{ Eqn. 6.}$$

Since we are considering unit potential on the anodes, then at the surface  $P = 1$ .

Now, substituting for A, expanding, and applying the boundary conditions

at the anode surface where  $x, y \ll s$ ,  $x^2 + y^2 = r_a^2$ :

$$1 = -K \log \pi r_a/s + V_0. \text{ Eqn. 7.}$$

Equations 3 and 7 may be solved simultaneously for K and  $V_0$ .

$$\text{hence } K = \frac{1}{\pi h/s - \log 2\pi r_a/s}, \text{ Eqn. 8.}$$

$$\text{and } V_0 = \frac{\pi h/s + \log 1/2}{\pi h/s - \log 2\pi r_a/s}. \text{ Eqn. 9.}$$

Substituting these for K and  $V_0$  in equation 1, an expression for the complex potential W results:

$$W = \frac{\pi h/s - \log 2 \sin \pi z/s}{\pi h/s - \log 2\pi r_a/s}. \text{ Eqn. 10.}$$

Also substituting for  $K$  and  $V_0$  in equation 5 together with the expression for  $A$  from equation 4, the real part  $P$  of the complex potential  $W$  may be written:

$$P = \frac{\pi h/s - \log \left\{ 2 (\cosh 2\pi y/s - \cos 2\pi x/s) \right\}^{\frac{1}{2}}}{\pi h/s - \log 2\pi r_a/s} \quad \text{Eqn. 11.}$$

The imaginary term  $-Kj\theta$ , of equation 5 describes the stream-lines of the system,

$$\text{where } \tan \theta = \cot \pi x/s \cdot \tanh \pi y/s.$$

Equating the imaginary terms and substituting for  $\theta$  in equation 5, an expression develops which describes a stream-line starting at the anode wire and terminating at the cathode thus:

$$\tanh \pi y/s = \tan \alpha \cdot \tan \pi x/s, \quad \text{Eqn. 12.}$$

where  $r_a \cos \alpha$  and  $r_a \sin \alpha$  are the cartesian coordinates of the intersection of the stream-line with the anode surface.

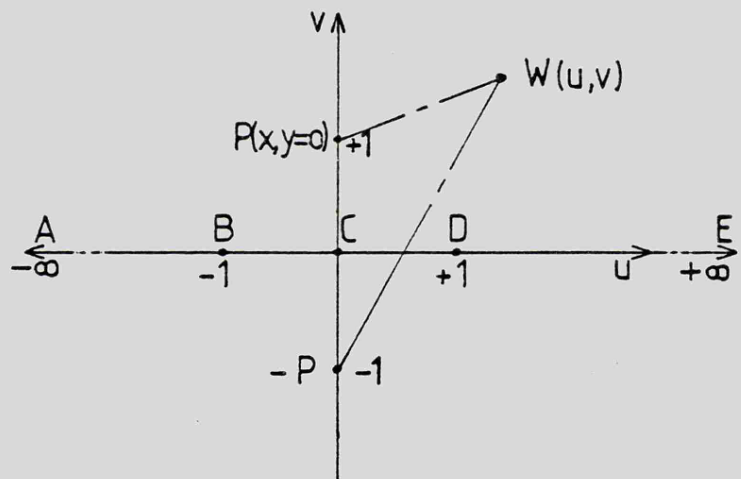
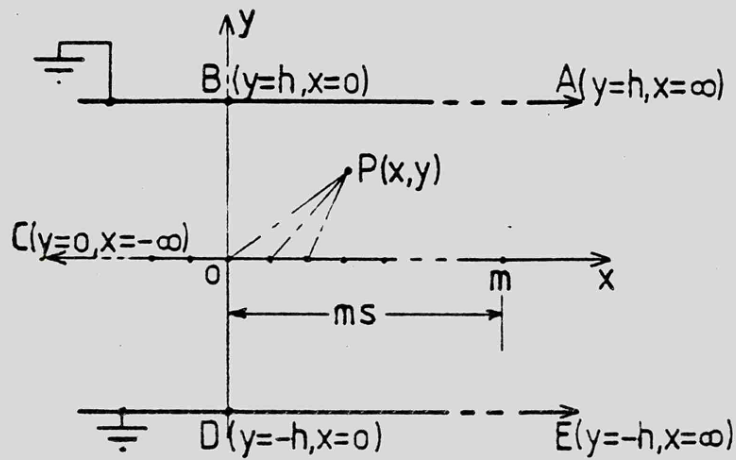
For regions away from the anode plane where  $y > s$ , the  $\tanh$  term in equation 12 becomes near unity and equation 12 may be simply rewritten as

$$\alpha = \frac{\pi}{2} \left( 1 - \frac{2x}{s} \right). \quad \text{Eqn. 13.}$$

As  $\tanh \pi y/s$  nears unity, the relationship between  $\alpha$  and  $x$  becomes independent of  $y$  and the stream-line runs parallel to the  $y$  axis.

Equation 13 shows clearly the linear relationship between the angle  $\alpha$  at the anode surface, and the lateral position of the field line near the cathode (Fig.3.1).

b) Induced charge at individual anode wire



This problem is rather more complicated since the potential  $P$  is due to an array of line charges which are not necessarily of equal magnitude, but are of equal spacing,  $s$ , along the  $x$ -axis. The analysis may be simplified by using the mapping function:

$$w = u + jv = j e^{\pi z / 2h}$$

Eqn. 14.

Substituting  $x + jy$  for  $z$ , we obtain

$$\begin{aligned} \omega &= -e^{\pi x/2h} \sin \pi y/2h + j e^{\pi x/2h} \cos \pi y/2h . \\ &= u + jv . \end{aligned} \quad \text{Eqn. 15.}$$

In equation 15 it can be seen that by inserting  $y = \pm h$  that all zero potential points on the upper cathode plane, map into the  $-u$  axis and all zero potential points on the lower cathode plane, map into the  $+u$  axis, with the particular points,  $y = h, x = 0$  and  $y = -h, x = 0$  occurring at  $u = -1$  and  $u = +1$  respectively.

Similarly, by inserting  $y = 0$ , points along the  $x$  axis map into the  $v$  axis, with the  $x, y$  origin occurring at  $v = 1$ .

A situation now exists to which standard image theory may be applied, and by considering  $P$  at the origin  $x, y = 0$ , a complex potential,  $W$ , may now be written:

$$W = -C_1 \log(\omega - j) + C_1 \log(\omega + j), \quad \text{Eqn. 16.}$$

where  $C_1$  is a constant determined by the line charge magnitude.

We may now revert to the  $z$  plane by substituting  $j e^{\pi z/2h}$  for  $w$  in equation 16 and manipulating.

$$\text{Thus, } W = \log \coth \pi z/4h . \quad \text{Eqn. 17.}$$

By substituting  $x + jy$  for  $z$  and by further manipulation,

$$W = C_1 \log \left\{ \frac{\cosh \pi x/2h + \cos \pi y/2h}{\cosh \pi x/2h - \cos \pi y/2h} \right\}^{1/2} + j C_1 \phi, \quad \text{Eqn. 18.}$$

where  $\tan \phi = -\sin \pi y/2h / \sinh \pi x/2h$ .

At the anode surface where  $x, y \ll h$ , the field lines are nearly radial and the expression for  $W$  may be simplified to the following:

$$W = C_1 \log 4h/\pi r - j C_1 \theta, \quad \text{Eqn. 19.}$$

where  $r = (x^2 + y^2)^{1/2}$  and  $\tan \theta = y/x$ .

We may now consider the potential  $P$  due to an array of  $(2l + 1)$  line charges, which is given by

$$P = \sum_{n=-l}^l C_n L_n, \quad \text{Eqn. 20.}$$

where

$$L_n = \log \left\{ \frac{\cosh \pi (x - ns) / 2h + \cos \pi y / 2h}{\cosh \pi (x - ns) / 2h - \cos \pi y / 2h} \right\}^{1/2}. \quad \text{Eqn. 21.}$$

Now, the constants  $C_n$  may be determined by the potentials of the anode wires. Provided  $r_a \ll s$ , the wire surfaces may be considered as equipotential cylinders, coaxial with the line charges. Thus the potential of the  $m^{\text{th}}$  wire is given by letting  $x = ms$  and  $y = 0$

$$\text{then } P_m = \sum C_n L_{nm} \quad \text{Eqn. 22}$$

$$\text{where } L_{nm} = \log \left\{ \frac{\cosh \pi s (m-n) / 2h + 1}{\cosh \pi s (m-n) / 2h - 1} \right\}^{1/2}. \quad \text{Eqn. 23.}$$

The special case for  $L_{mm}$  where  $n = m$  must be considered differently,

$$L_{mm} = \log \left\{ \frac{\cosh \pi (x - ms) / 2h + \cos \pi y / 2h}{\cosh \pi (x - ms) / 2h - \cos \pi y / 2h} \right\}. \quad \text{Eqn. 24.}$$

Now, by expanding the cosh and cos terms and putting  $x - ms = \Delta x$ ,

$$\text{then when } (\Delta x^2 + y^2)^{1/2} = r_a,$$

$$L_{mm} = \log 4h / \pi r_a. \quad \text{Eqn. 25.}$$

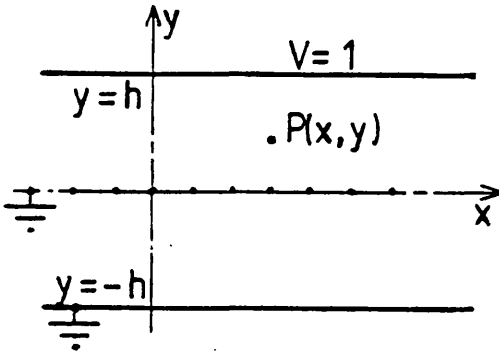
In order now to calculate the charge induced on the  $k^{\text{th}}$  anode wire, say, we must apply the original theorem by placing  $P_k = 1$  and  $P_m = 0$ , for  $m \neq k$ . Thus the constants  $C_n$  are obtained as the solution vector of the matrix equation

$$P_m = \sum C_n L_{nm}, \quad \text{Eqn. 26.}$$

with the input vector  $P_m$  as given above. The charge induced on the  $k^{\text{th}}$  wire is then

$$-P = -\sum C_n L_n. \quad \text{Eqn. 27.}$$

c) Induced charge at the cathode



This case can be treated in a similar manner to case a). A suitable complex potential,  $W$ , has been chosen as

$$W = -K \log \sin \pi z/s - jE_0 z + V_0. \quad \text{Eqn. 28.}$$

where  $K$ ,  $E_0$  and  $V_0$  are real constants determined by the electrode potentials. The additional constant  $E_0$  has been added such that the equation 28 may fit this slightly more complicated situation.

By similar manipulations to those in a) above, it is possible to equate the real terms of equation 28, to the potential  $P$ . Then in general terms the following equations may be written:

$$P = -K (\log 1/2 + \pi y/s) + E_0 y + V_0, \quad \text{Eqn. 29.}$$

$$\text{for } \pi y/s \gg 1,$$

$$\text{and } P = -K \log(\pi/s)(x^2 + y^2) + E_0 y + V_0, \quad \text{Eqn. 30.}$$

$$\text{for } x, y \ll s.$$

Now by applying the boundary conditions, the constants may be evaluated. Thus if one cathode, at  $y = h$ , is at unit potential and the other cathode and the anode wires are grounded, three equations can be formed,

$$1 = -K (\log 1/2 + \pi h/s) + E_0 h + V_0 \quad \text{Eqn. 31.}$$

$$(P=1 \text{ when } y=h).$$

$$0 = -K (\log 1/2 + \pi h/s) - E_0 h + V_0 \quad \text{Eqn. 32.}$$

$$(P=0 \text{ when } y=-h).$$

$$0 = -K \log \pi r_a/s + V_0 \quad \text{Eqn. 33.}$$

$$(P=0 \text{ at } (x^2 + y^2)^{1/2} = r_a).$$

In equation 33 the term  $E_0 r_a$  has been removed. This is in order, provided  $E_0 r_a \ll V_0$ , and this condition is equivalent to  $r_a/h \ll V_0$ . Substitution of normal values shows this to be adequately justified.

By solving equations 31, 32 and 33 simultaneously for  $K$ ,  $E_0$  and  $V_0$  and substituting in the expression for  $W$  (equation 28) we find that the real part  $P$  is given by

$$P = y/2h - \frac{\log 2\pi r_a/s - \log \{2(\cosh 2\pi y/s - \cos 2\pi x/s)\}^{1/2}}{2(\pi h/s - \log 2\pi r_a/s)} \quad \text{Eqn. 34.}$$

### 3.4 Time Development of the Induced Pulse

As the positive ion cloud moves away from the avalanche region, the induced charge will develop with time. If we consider a chamber with anode potential  $V_a$  and cathode potential zero, then from equation 10 the expression for the complex potential  $W$  is

$$W = V_a \frac{\pi h/s - \log 2 \sin \pi z/s}{\pi h/s - \log 2\pi r_a/s} \quad \text{Eqn. 35.}$$

The real part of this equation which defines the equipotential surfaces is given in equation 11 and by differentiating this with respect to  $x$  and  $y$ , the resultant field intensity  $E$  may be obtained.

Thus,

$$E = \frac{V_a}{h} \cdot \frac{1}{1 - s/\pi h \cdot \log 2\pi r_a/s} \cdot \left\{ \frac{\cosh 2\pi y/s + \cos 2\pi x/s}{\cosh 2\pi y/s - \cos 2\pi x/s} \right\}^{1/2} \quad \text{Eqn. 36.}$$

Now a positive ion created near the  $x, y$  origin at the surface of the anode wire at coordinates  $r_a \cos \alpha$ ,  $r_a \sin \alpha$ , will drift along the field line given by

$$\tanh \pi y/s = \tan \alpha \tan \pi x/s, \quad (\text{Equation 12})$$

and the  $x, y$  coordinates as a function of time  $t$  can be calculated progressively, numerically by solving simultaneously the differential equations:

$$1/s \left\{ \left( \frac{dx}{dt} \right)^2 + \left( \frac{dy}{dt} \right)^2 \right\}^{1/2} = \mu \frac{E}{s}, \quad \text{Eqn. 37.}$$

where  $\mu$  is the positive ion mobility,

and

$$\frac{dy}{dx} = \tan \alpha \left\{ \frac{\cosh \pi y/s}{\cos \pi x/s} \right\}^2, \quad \text{Eqn. 38.}$$

with initial conditions that at  $t = 0$ ,  $x = r_a \cos \alpha$  and  $y = r_a \sin \alpha$ .

When substituting  $E$  in the velocity expression  $\mu E/s$ , there emerges a natural unit for time  $s^2/\mu V_a = T_0$ , say. For convenience in calculations, all times have been normalised to this unit. For similar reasons, all distances have been normalised to the anode spacing  $s$ .

### 3.5 Effects of Pulse Shaping

Throughout this theoretical discussion it has been assumed that when a charge was induced on a chamber electrode, this electrode did not change in potential. Any change in potentials would introduce direct capacitive interelectrode coupling and would render invalid the present arguments. It has been assumed therefore that charge sensitive pre-amplifiers would be used wherever signals were taken from the chamber. Thus all useful electrodes would be virtually earthed, and other electrodes, not used for signal pickoff, would be either directly earthed or heavily decoupled.

The output of a charge sensitive preamplifier of conversion gain  $1/C$  is a voltage signal  $v(t)$ , and

$$v(t) = -q/C, \quad \text{Eqn. 39.}$$

where  $q$  is the input charge and  $C$  is the feedback capacitor.

Calculations have been extended to include the effects of pulse shaping in a main amplifier. Here non-interacting single integrating and single differentiating filters, of equal time constant  $T$ , have been assumed, and the final output  $v_0(t)$  of such filter network can be shown to be

$$v_0(t) = \int_0^t v(t') h(t-t') dt', \quad \text{Eqn. 40.}$$

where  $h(t)$  is the impulse response of the system. The peak height  $v_c$ , of the output signal may be obtained from this formula.

The impulse response for the simple filters above is given by

$$h(t) = e^{-t/\tau} (1 - t/\tau) \tau. \quad \text{Eqn. 41.}$$

Similar networks have been analysed in more detail in a previous thesis<sup>(33)</sup>.

Calculations and graphical illustrations have been simplified by using the normalised filter time constant  $T/T_0$  where  $T_0 = s^2/\mu V_a$ , the natural unit of time previously mentioned.

### 3.6 Effect of Finite Distribution of Charge

The calculations for induced charge on an individual anode wire were extended to take account of the finite angular distribution of charge which will inevitably occur in a practical system. This extension was not difficult to include, although it was laborious, involving the summation of the individual induced charges due to a range of positive ion trajectories centred upon the mean initial angular position  $\alpha$ . To compute one point on a curve relating angular position to induced charge for these extended calculations took about ten minutes, and we were indeed fortunate in being on line to a Cyber 72 computer which could be used during off-peak periods.

A uniform distribution spreading around a fraction  $f$  of  $2\pi$  of the anode wire circumference has been assumed, and as  $f$  increases, the dependence of the induced charge magnitude upon the angular position  $\alpha$  of the centre of charge (and hence the lateral position  $x$  of the ionising radiation) becomes weaker until at  $f = 1$ , where the avalanche completely surrounds the wire, the two are no longer interdependent.

In later calculations, when considering the induced charge on the cathodes, a Gaussian angular distribution, which was perhaps more realistic, was assumed. By this method computations were performed

for several points about  $\alpha$  (the initial angular centre of charge) for various weightings of  $q_0$  (the positive ion charge), according to the formula

$$\rho(\alpha') = \frac{q_0}{\sqrt{(2\pi\sigma_\alpha^2)}} \cdot e^{-\frac{(\alpha' - \alpha)^2}{2\sigma_\alpha^2}} \quad \text{Eqn. 42.}$$

where  $\rho(\alpha')d\alpha'$  represents the initial positive ion charge in the angular range  $d\alpha'$ , and  $\sigma_\alpha$  is the standard deviation of the distribution.

In addition to the angular spread there must also be some radial spread in the initial positive ion distribution, since the ions are not all produced at the surface of the anode wire. However, one can visualise this effect to be quite small. Even longitudinal spread in the electron cloud, due perhaps to the initial photoelectron range and further diffusion effects, would cause a greatly reduced spread of positive ions in the avalanche region because of the very much lower positive ion mobility. Calculations show that for an electron drift velocity of 4 cm./ $\mu$ s.<sup>(66)</sup> and a typical electron cloud spread of .5 mm. after diffusion (section 5.9), then the electron collection time will be about 12 ns, and this will result in a radial spread of positive ions near the anode of only 40  $\mu$ m. (assuming  $V_a = 2.5$  kV and  $\mu = 1.6$  cm<sup>2</sup>/Vs - See Chapter 5). In fact calculations with the present model for induced cathode pulses have shown that the ratio of cathode signals is very insensitive to the radial position of the ions at the anode.

### 3.7 Theoretical Predictions

In later chapters, when experimental results are illustrated, it is intended wherever possible to compare these with theoretical predictions calculated for the same system parameters. For the moment, however, it is useful to look at some specific examples of the effects of localised avalanche on the induced charge on the anodes and cathodes of a chamber, and to show how in theory, these results are affected by

shaping time constants and by differing amounts of avalanche spreading. Theoretical results will be shown for a chamber having  $h/s = 2.22$  and  $r_a/s = 2.5 \cdot 10^{-3}$ .

The signal amplitude from the preamplifier connected to the sense anode will be termed  $v_B$ , whilst that from the preamplifier connected to the avalanche anode will be termed  $v_A$ .

$v_B$  will of course be dependent upon the positive ion charge magnitude  $Q$  and therefore, for the purpose of comparing experimental and theoretical results, we have chosen to calculate the ratio  $v_B/v_A$ , which is energy independent.  $v_A$  is nearly an order of magnitude larger than  $v_B$  because it is mostly due to the full electron charge  $-Q$  collected from the avalanche. The output from the A preamplifier is then  $v_A(t) = (-Q - q_k)/C$ , whilst that of the B preamplifier connected to the  $k^{\text{th}}$  anode is  $v_B(t) = -q_k/C$ . Inspection of these equations together with that for  $q_k$  (equation 27,  $q_k = -QP_k$ ) now shows clearly that the ratio of  $v_B/v_A$  does not contain  $Q$ .

In Fig. 3.2 the theoretical ratio of pulse heights,  $v_B/v_A$ , is shown for a chamber 'cell' spanning from  $x_0 = -.5s$  to  $x_0 = +.5s$ , for three values of time constant  $T/T_0$  and zero angular spread. The sensitivity of  $-v_B/v_A$  with  $x_0$  can be seen to increase as the shaping time constant  $T$  is increased, but this is accompanied by increasing non-linearity and assymetry.

The effects of finite angular spreading of the avalanche can be seen in Fig. 3.3 where, for a time constant  $T/T_0 = 1.5 \cdot 10^{-1}$  (corresponding to  $\mu = 1.5 \text{ cm}^2/\text{Vs}$  at  $V = 2.5 \text{ kV}$  and  $s = 5 \text{ mm}$ .), curves of  $-v_B/v_A$  are shown for rectangular distributions spreading around 0%, 50% and 100% of the anode wire circumference. It is interesting to note that some considerable positional sensitivity exists even when 50% spreading occurs.

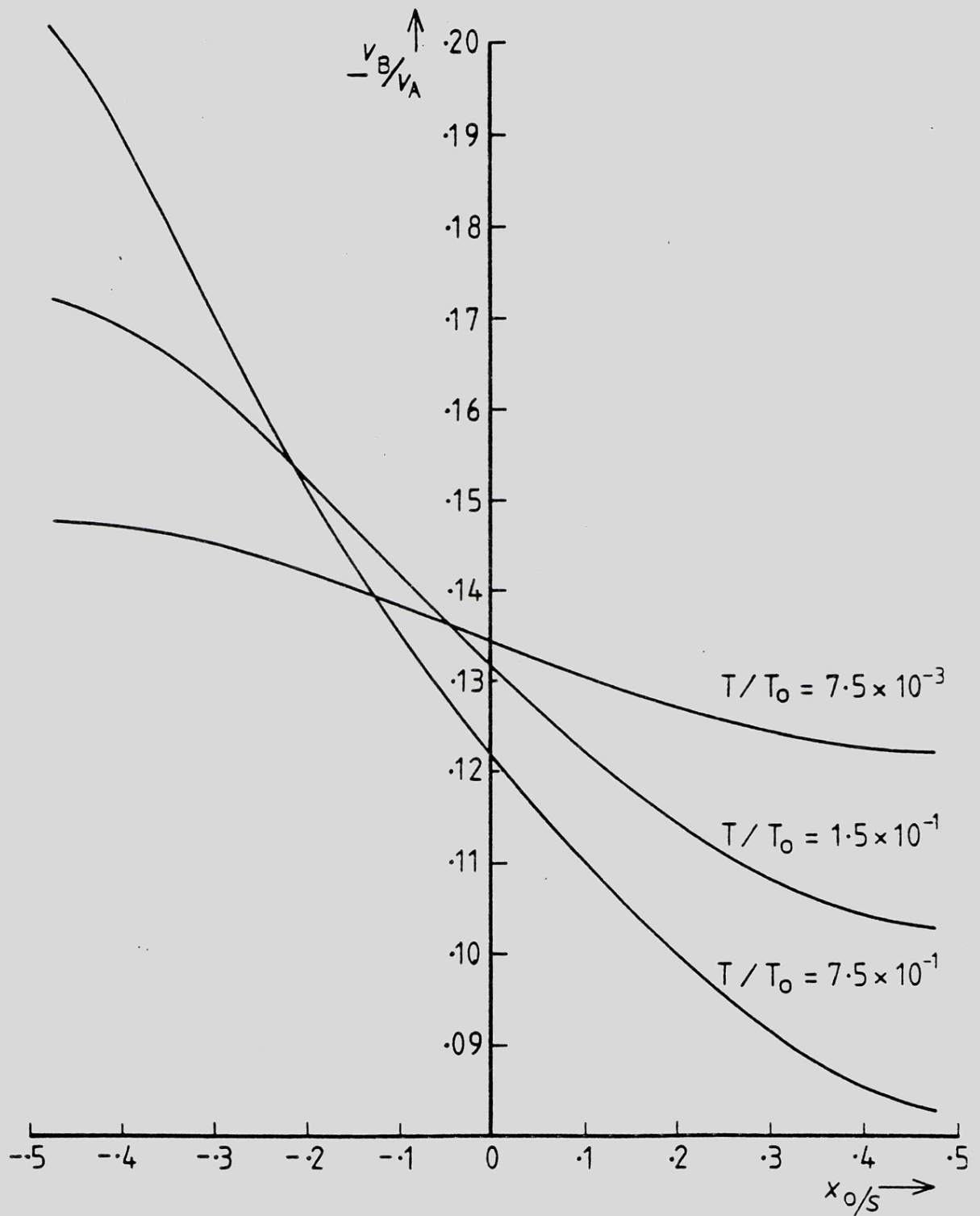


FIG. 3,2— THEORETICAL RATIO OF ANODE PULSE HEIGHTS AGAINST SOURCE POSITION.

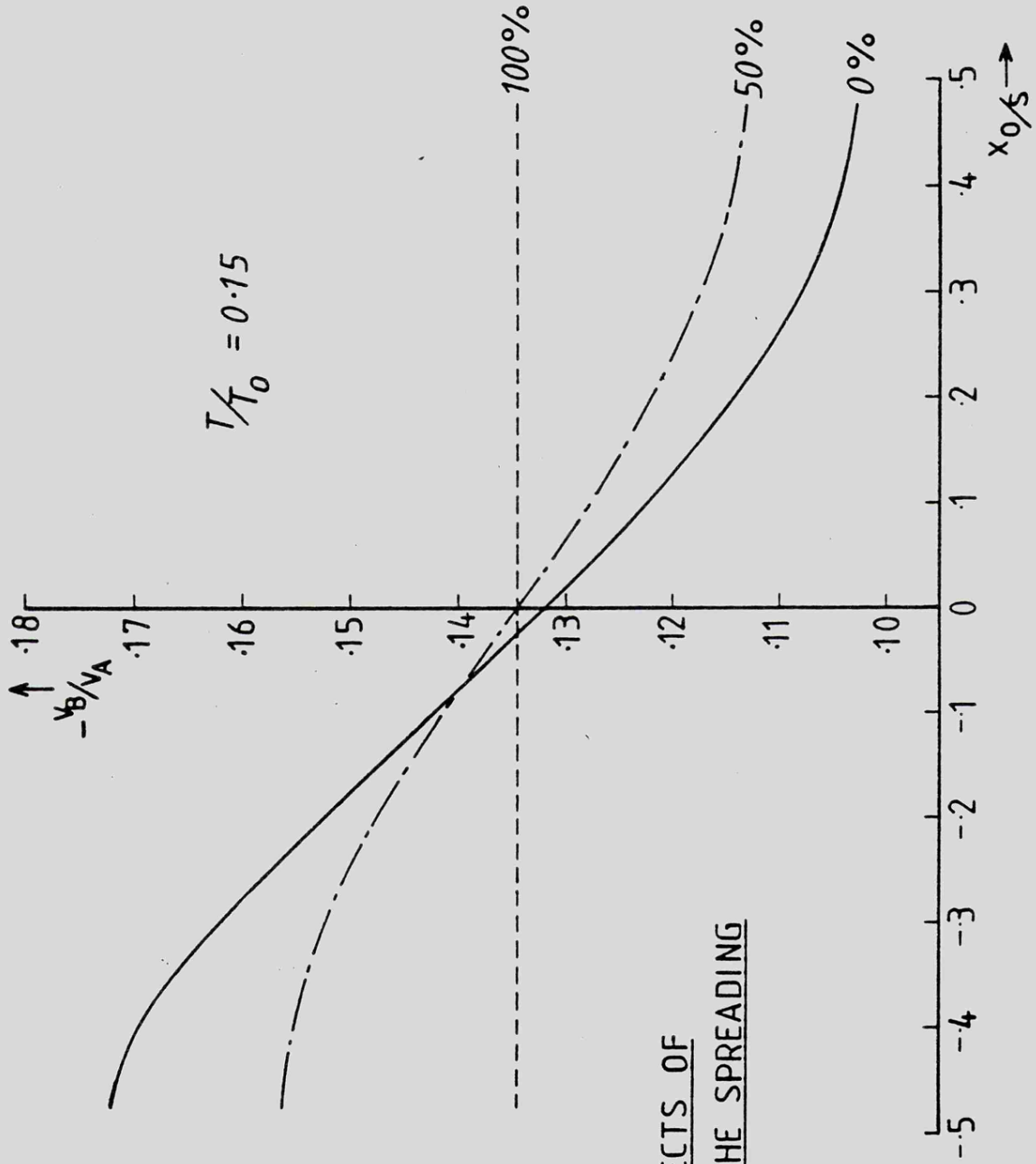


FIG. 3,3-  
EFFECTS OF  
FINITE AVALANCHE SPREADING

The ratio of cathode pulse heights plotted against  $x_0/s$  is shown in Fig. 3.4. The set of curves illustrates the dependence of this ratio upon the initial Gaussian angular distribution of positive ions. Standard deviations of  $0^\circ$ ,  $33^\circ$  and  $60^\circ$  are represented. Absorption may take place above or below the wire and so two curves are drawn for each value of  $\sigma_\alpha$ .

The isometric plot of the charge induced on a cathode P (x,y), as a function of the position x/s, y/s, of the inducing charge is reproduced in Fig. 3.5, and a similar isometric plot for charges induced on a neighbouring anode is reproduced in Fig. 3.6. These provide an interesting visual indication of the way the induced charge builds up as the positive ions commence their journey near the anode.

It should be noted that the induced charge is always positive, regardless of the direction of travel of the positive ions. Early workers<sup>(6)</sup>, expected to see negative charges induced in a sensing electrode when the positive ion cloud was moving away from that electrode. Since positive signals were observed everywhere, it was incorrectly assumed that angular localisation did not occur. A reversal of induced charge polarity could be expected in linear fields, but in fields highly concentrated around the anodes, such as we have here, some 10 to 15% of the positive induced charge has developed before the positive ions have moved very far, and this positive charge is induced on all neighbouring electrodes. Soon after this, the positive ions are moving in a more linear field, and then we see a slow increase in charge as ions move towards the sensing cathode, but a slow reduction in the positive charge when ions are moving away. We can therefore expect the pulse shape also to be quite markedly dependent upon the position of initial absorption.

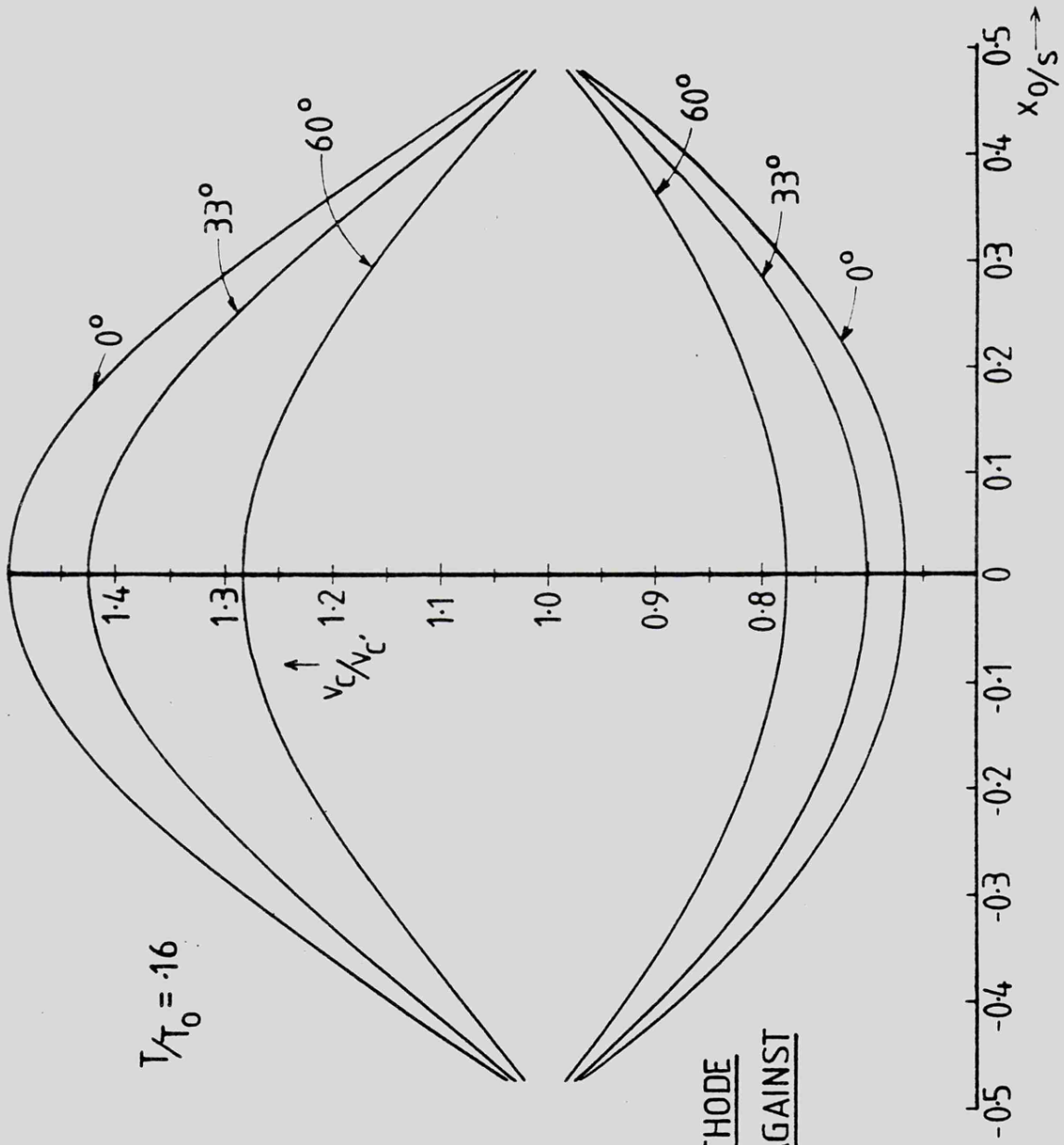


FIG. 3,4-

THE RATIO OF CATHODE  
PULSE HEIGHTS AGAINST  
SOURCE POSITION.

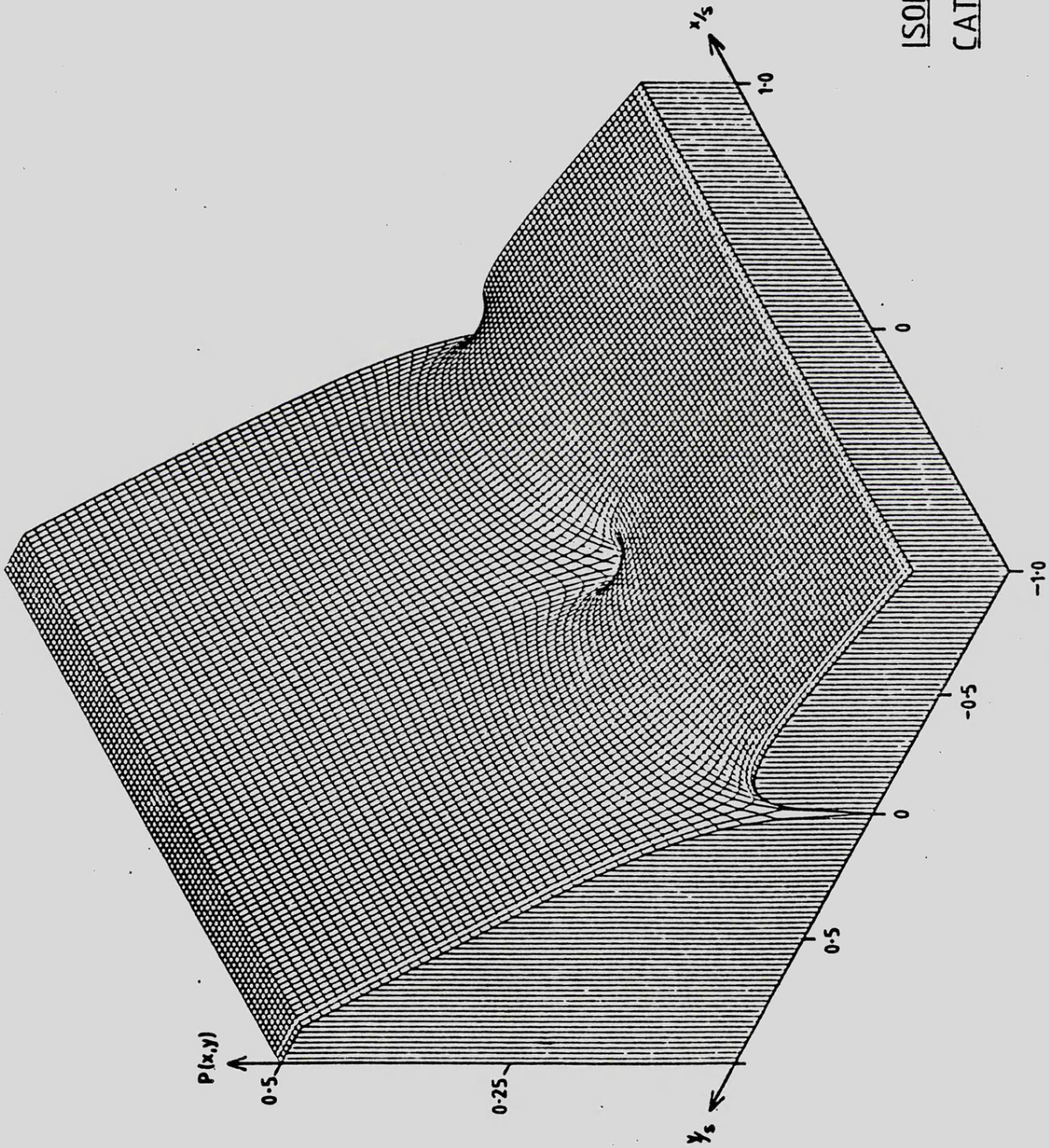
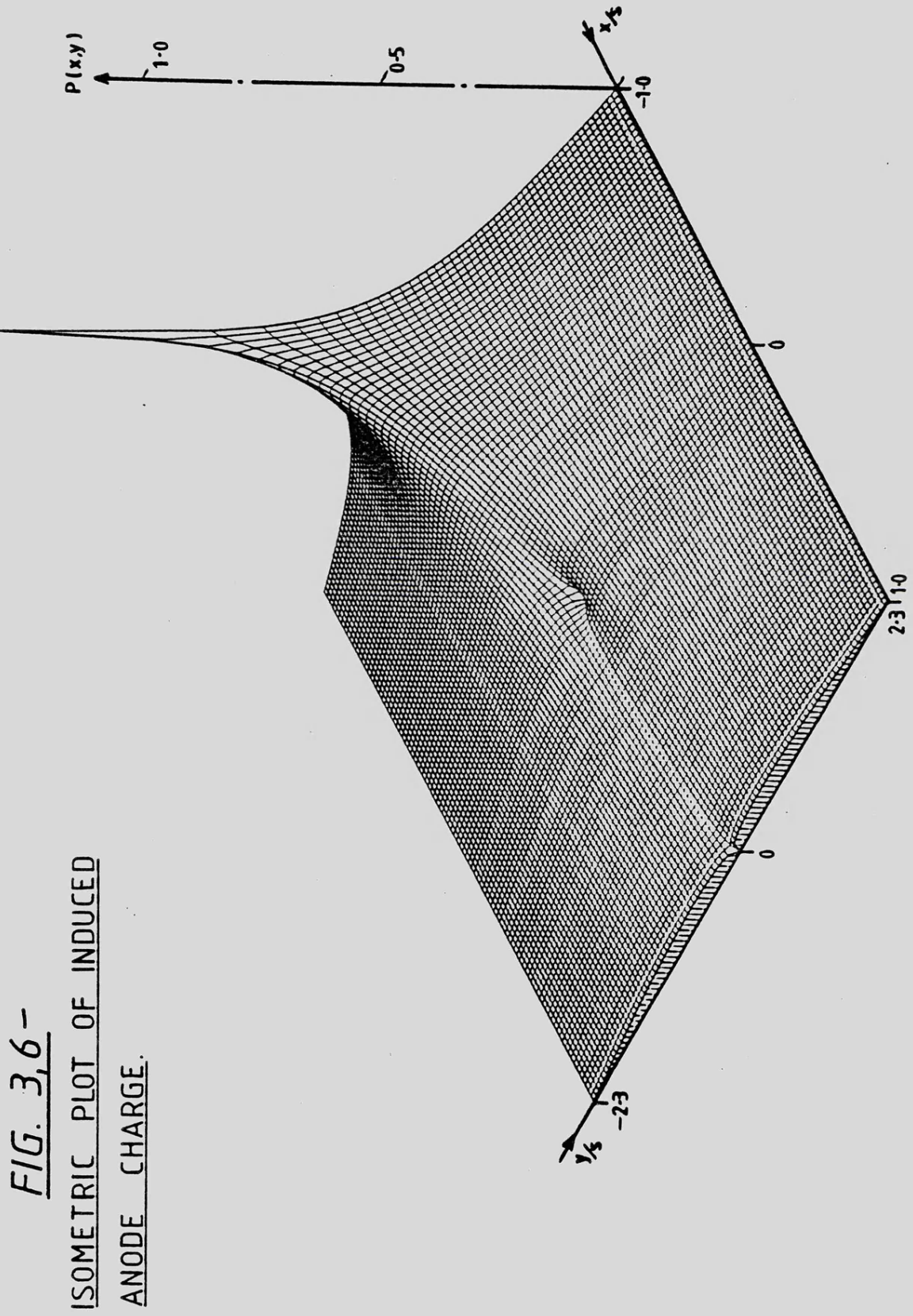


FIG 3,5--  
ISOMETRIC PLOT OF INDUCED  
CATHODE CHARGES.



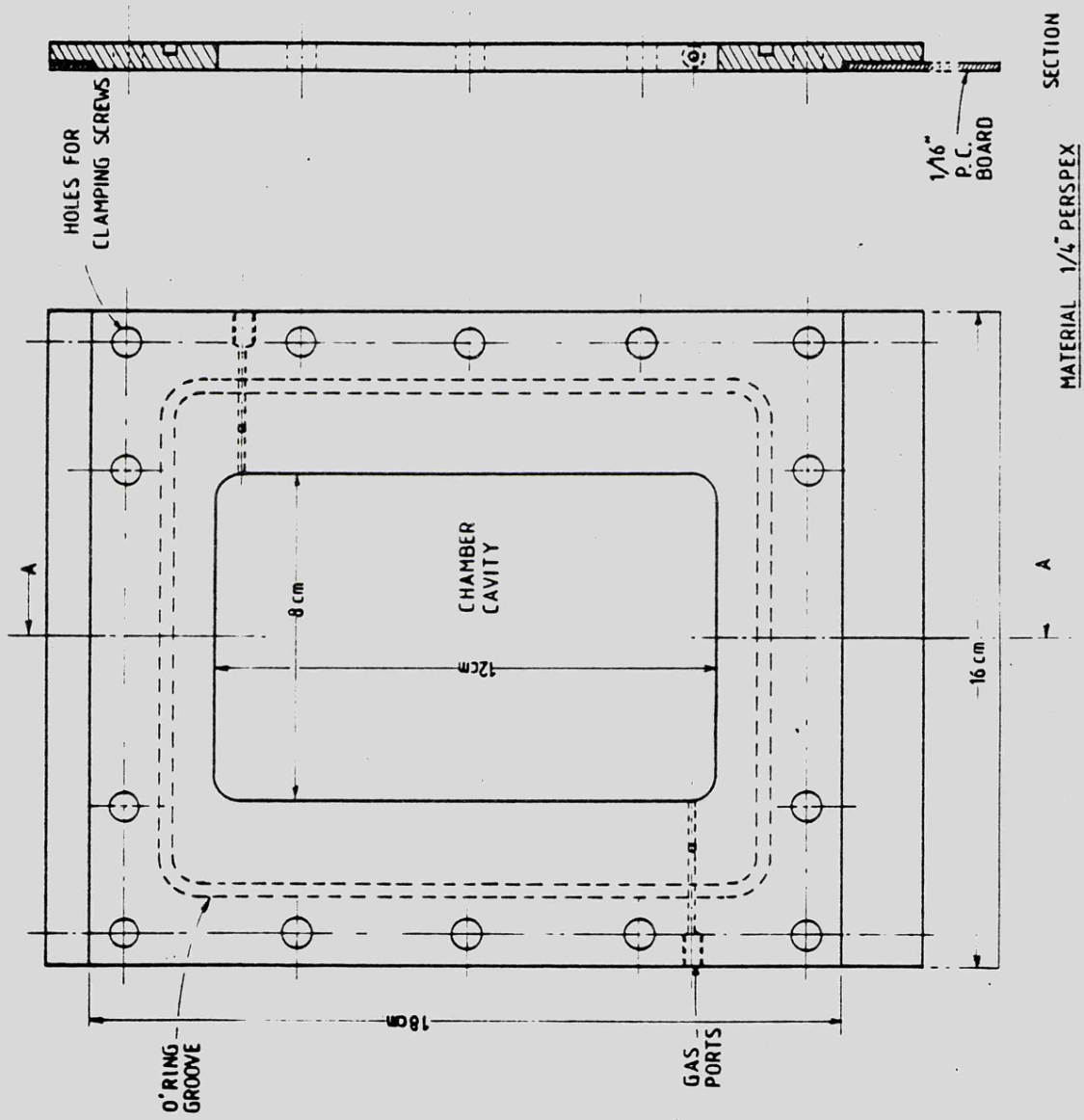
CHAPTER 4.EXPERIMENTAL DETAILS4.1 The Experimental Proportional Chambers

Several small multiwire chambers were used throughout the course of this work, and these were all of similar construction but with differing anode and cathode structures. The chamber walls were built up of clear perspex plates each with the centre machined out to form a chamber cavity 8 cm. by 12 cm. and machined where necessary to accommodate 'o' ring seals and gas ports as shown in Fig. 4.1. The centre section was milled to accept the anode support boards which were made from single-sided, copper-clad fibreglass printed-circuit board. The copper was etched away where necessary to provide isolation for the anodes and to accept the high voltage resistors and coupling capacitors.

In the prototype chamber, the anode plane consisted of seven gold-plated tungsten anodes,  $15\mu\text{m}$ . diameter, the inner five spaced 5 mm. and the outer two spaced 2.5 mm. Beyond these outer anodes were two field reducing anodes also spaced 2.5 mm. and made from stainless steel,  $125\mu\text{m}$ . diameter.

In practice only the three inner anode wires were used to provide information. The remainder were incorporated in an attempt to remove side effects and to ensure that the field around the three active anodes resembled to some extent that of an infinite array. The increase in diameter and smaller spacing served to reduce the field around the ends of the array and thus prevent breakdown. This is now an accepted technique with multiwire chambers, where breakdown so readily commences around the outer wires at the higher voltages necessary with multi-anode arrays. Electrical breakdown normally

FIG. 4,1—  
CHAMBER PLATE  
DETAIL.



manifests itself, not in the catastrophic sense, but as a 'noisy' background which is quite troublesome when operating at gas gains of around  $10^4$ .

In the prototype chamber the cathodes were spaced 8 mm. from the anode, each cathode being wound with a grid of  $125\mu\text{m}$ . diameter copper wires with 2 mm. inter-spacing. Both sets of cathode wires were at right angles to the anodes.

The chamber was made gas-tight with the addition of two windows of  $6\mu\text{m}$ . aluminised melinex secured to the perspex by double-sided adhesive tape and mounted with the conducting surface inwards. In all cases, chambers were connected to a gas flow system in which the output flow rate was measured by a GEC-Elliott flowmeter and the input flow was governed by a flow controller (G.A. Platon, Flostat). From previous experience, the need for a well sealed chamber and gas flow system was considered important. Small amounts of atmospheric contamination cause a rapid deterioration in the resolution and inconsistent performance. A non-leaking system also enables the use of extremely low flow rates, an important consideration when an expensive gas such as neon is used. The flow rate for these experiments was 10cc./min.

Later, the cathode plane was completely removed and the outer windows were used as cathodes. This increased the anode-cathode spacing, and better resembled the theoretical conditions of large  $h/s$  ratio, but bulging of the cathodes due to the slight internal gas pressure caused a distortion of the field.

A large proportion of the experimental work was carried out with the chamber of Fig. 4.2. This had an increased anode-cathode spacing of 11.1 mm. Wire cathodes were replaced with plane cathodes of aluminised melinex, thickness  $6\mu\text{m}$ ., and the outer windows were of

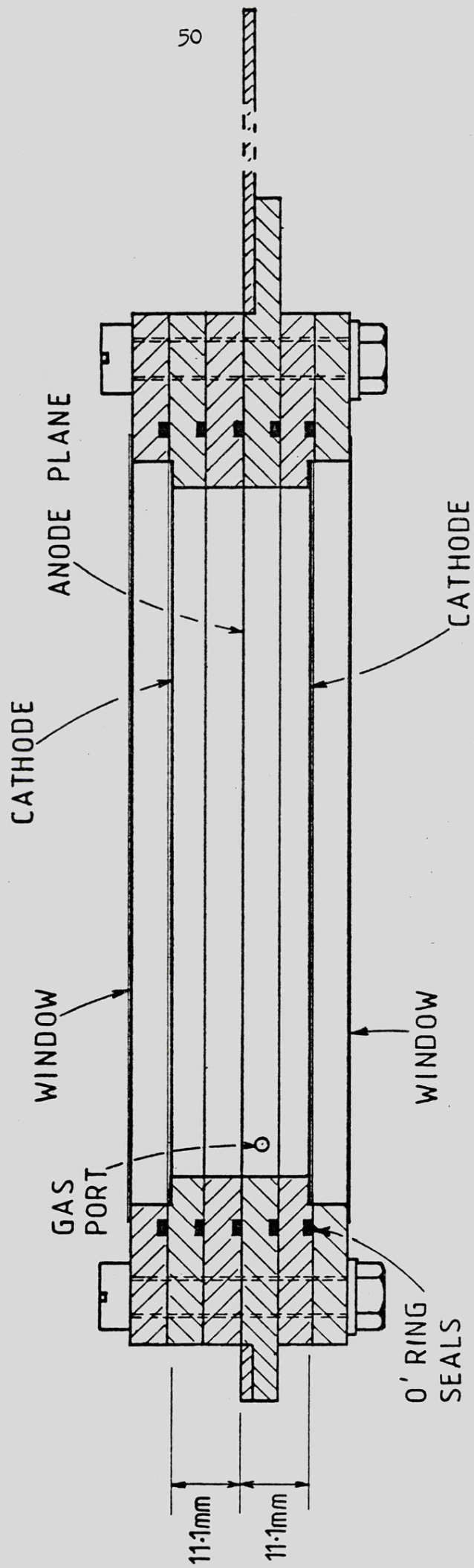


**FIG. 4,2-- THE EXPERIMENTAL CHAMBER**

6 $\mu$ m. clear melinex. Gas bypass holes were drilled in the cathode frame to release gas pressure on the cathodes. Thus the outer windows bulged but the cathodes remained flat. An inter-anode spacing of 5 mm. made it possible to include nine anodes to give a better approximation to an infinite plane.

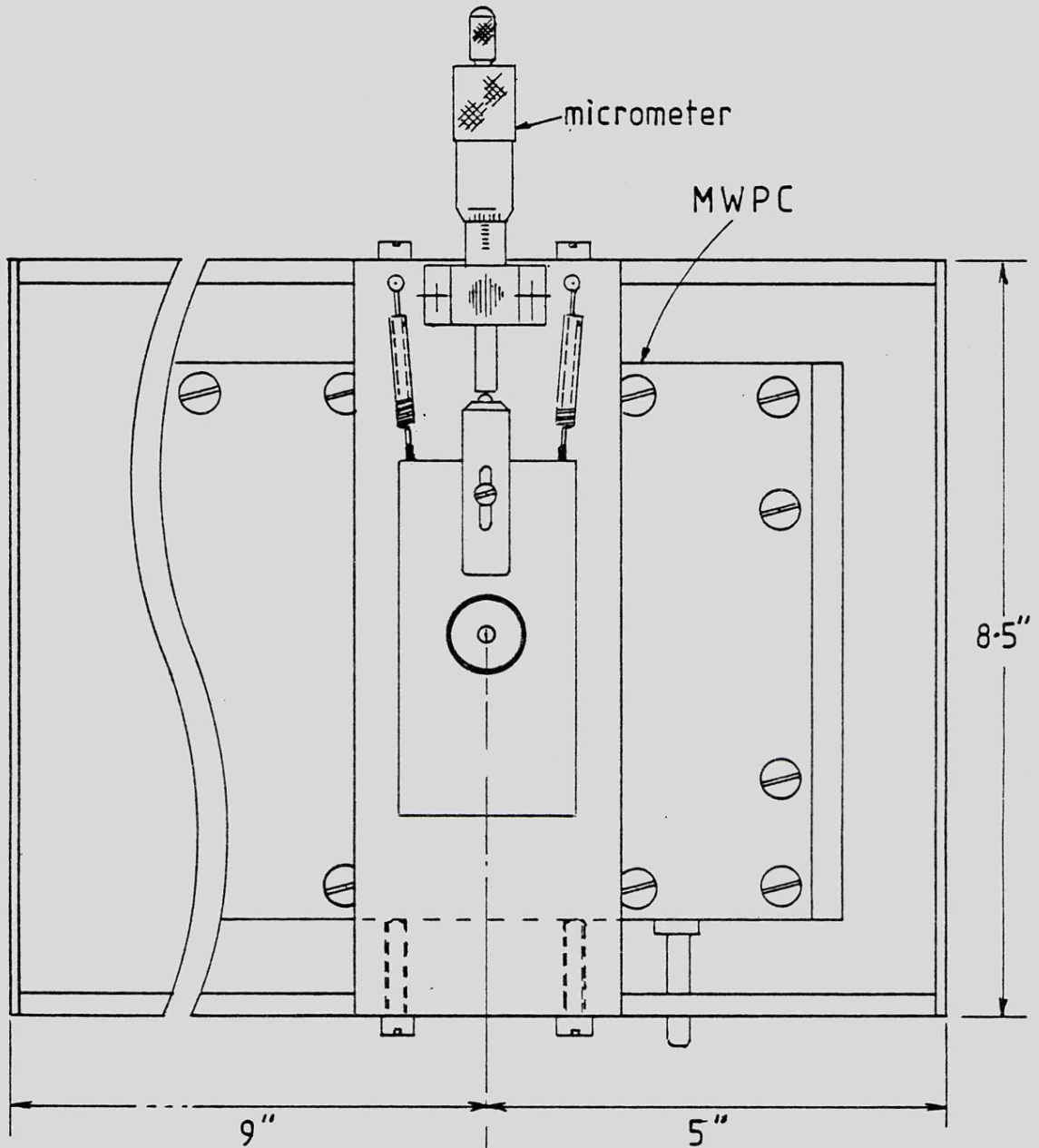
With the prototype chamber some difficulty had been experienced with gain variations along the anodes, probably due to uneven stretching of these very fine wires, or possibly due to impurity deposits, and so with the final chamber, the anode diameter was increased to 25 $\mu$ m. (gold plated tungsten). Winding of the anode plane was then carried out under more hygienic, clean-room conditions and all parts were thoroughly cleaned in iso-propyl-alcohol prior to final assembly. No problems of gain variation were then apparent.

The proportional chamber was finally enclosed in a rigid aluminium container, shown in Fig. 4.3 and in the photograph, Fig. 4.3a, which provided essential screening and supported the micrometer scanning arrangement. The source could then be scanned across the chamber on a sliding carriage in a direction perpendicular to the anodes. The source position could be set to an accuracy of 10 $\mu$ m. The whole screening assembly was electrically earthed and mounted on resilient pads to reduce microphony due to anode vibration.

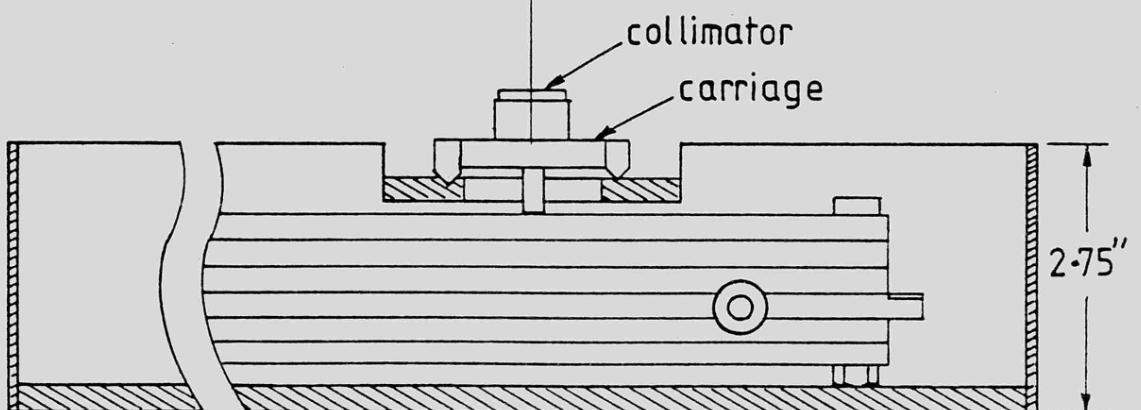
Several different operating gas mixtures were used at atmospheric pressure. These were argon + 10% methane, argon + 75% methane, argon + 10% carbon dioxide, neon + 10% methane and neon + 10% carbon dioxide. Argon mixtures were of high purity (H.P. grade  $\equiv$  99.998% purity), whilst neon mixtures were of counter purity (C.P. grade  $\equiv$  99.97% purity). All were supplied ready mixed by British Oxygen Co. Ltd.

FIG. 4,3-  
SCREENING & MECHANICAL ASSEMBLY

52



SCALE - X .5



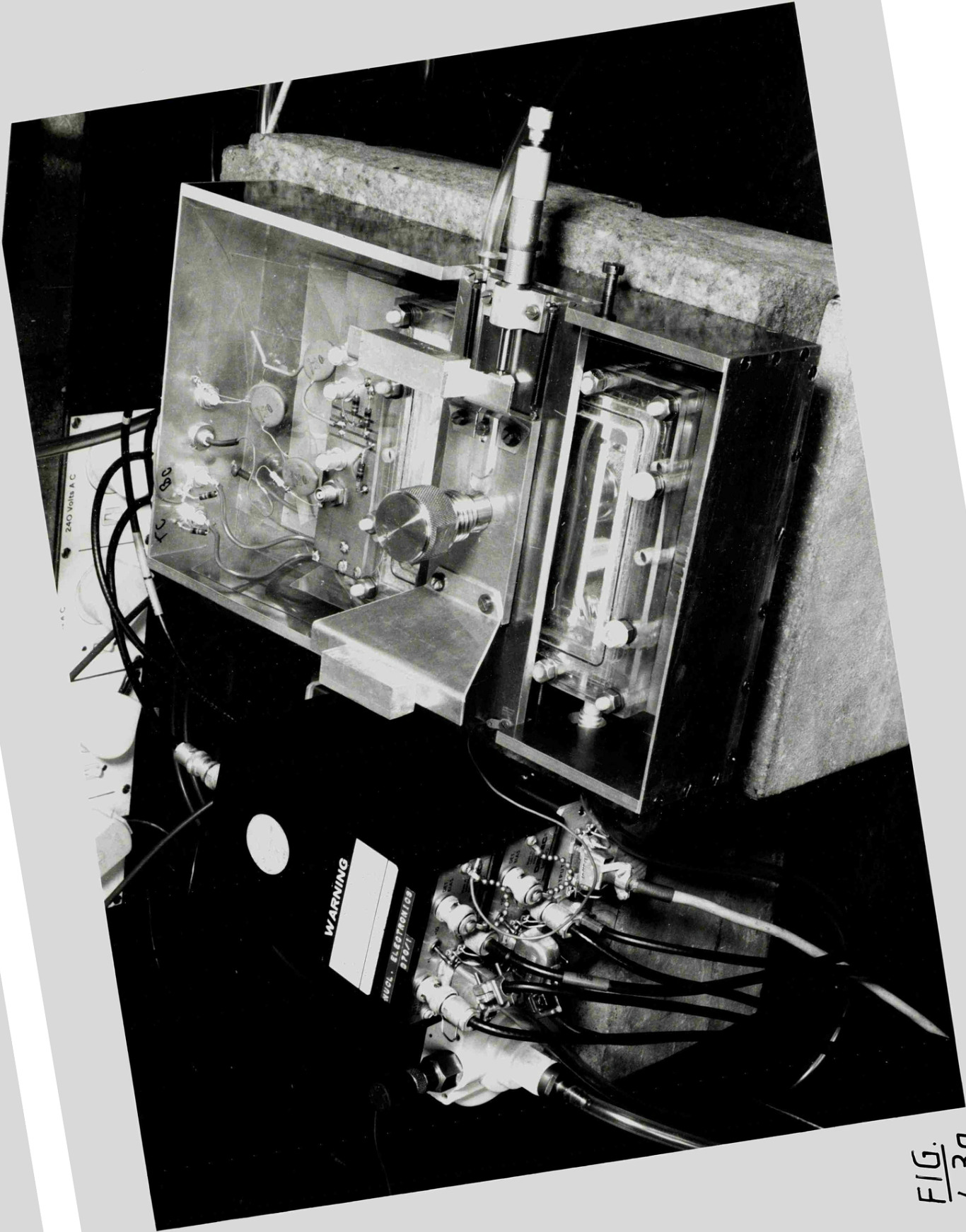


FIG.  
4,3a.

## 4.2 The Electronic System

### 4.2.1 General overview

A block diagram of the apparatus is shown in Fig. 4.4. Normally, three chamber electrodes were monitored; the outer two channels provided information from either the 'sense' anodes or the cathodes, whilst the centre channel, which was always connected to the 'avalanche' anode, was used in an energy cancelling capacity (section 3.7) and also as an energy selection channel.

Charge sensitive preamplifiers were used in all channels and were followed by pulse-shaping amplifiers from which, pulses in the 'sense' channels could be stretched prior to entering the dividing circuit. The avalanche channel, connected through a single channel analyser was used to provide a coincidence signal to gate a multi-channel analyser, used to store data from the divider.

A NIM system of packaging was used to house and power the electronic circuits. A photograph of the laboratory, showing the complete apparatus, is given in Fig. 4.5.

### 4.2.2 Chamber connections

Two configurations of anode-cathode connections were used:-

a) The configuration shown in Fig. 4.6 was used for looking at induced anode pulses. To obviate the need for high voltage components, the anodes were at earth potential with negative e.h.t. applied to the cathodes via an R.C. filtering network to remove e.h.t. ripple. The three central anodes were earthed through  $100M\Omega$  carbon resistors and coupled directly to the charge sensitive preamplifiers. All other anodes were directly earthed.

b) When observing cathode signals, the configuration became that of Fig. 4.7, where the two cathodes were earthed through  $100M\Omega$  resistors and connected to charge-sensitive preamplifiers. All anodes, with the

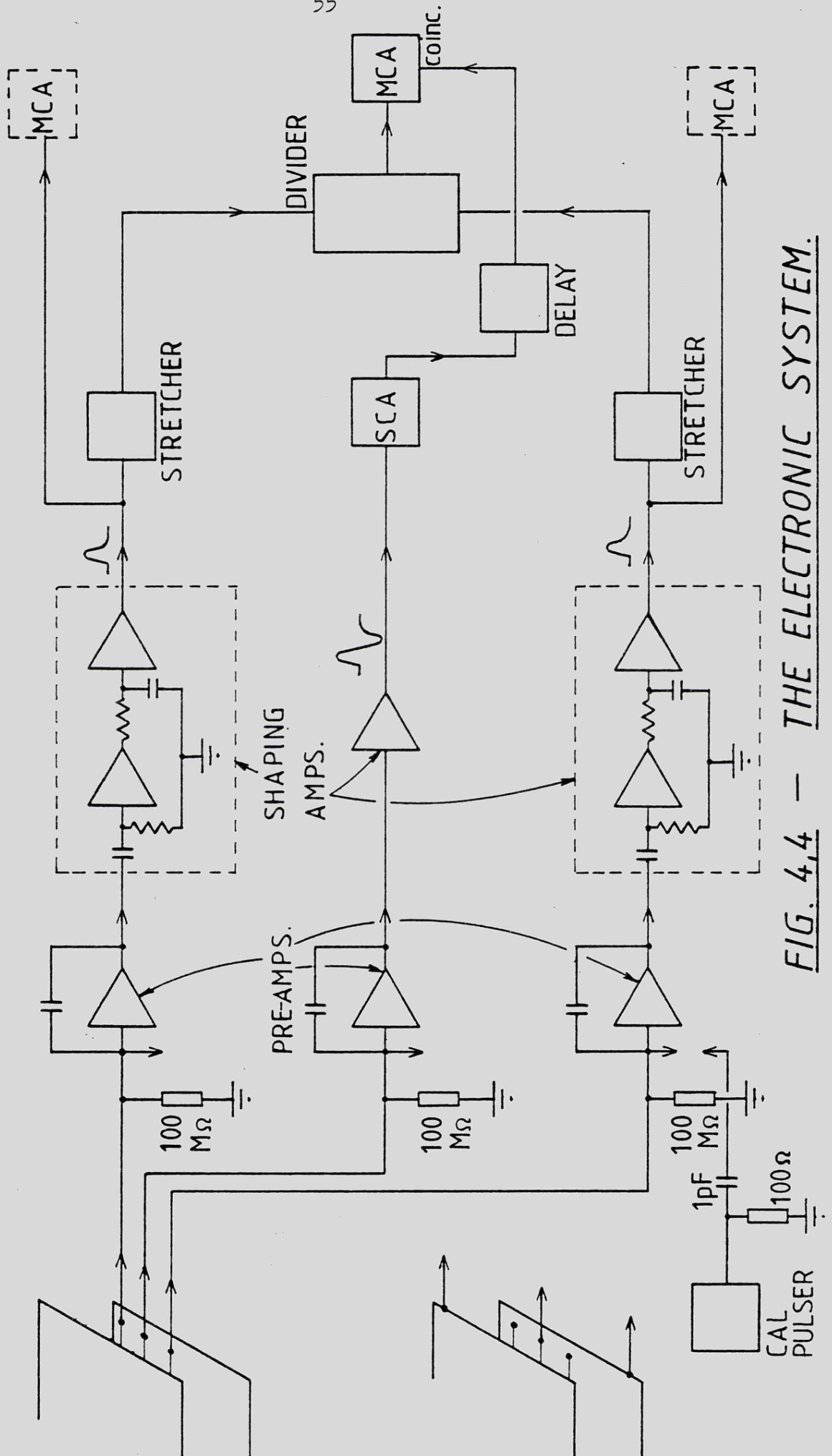
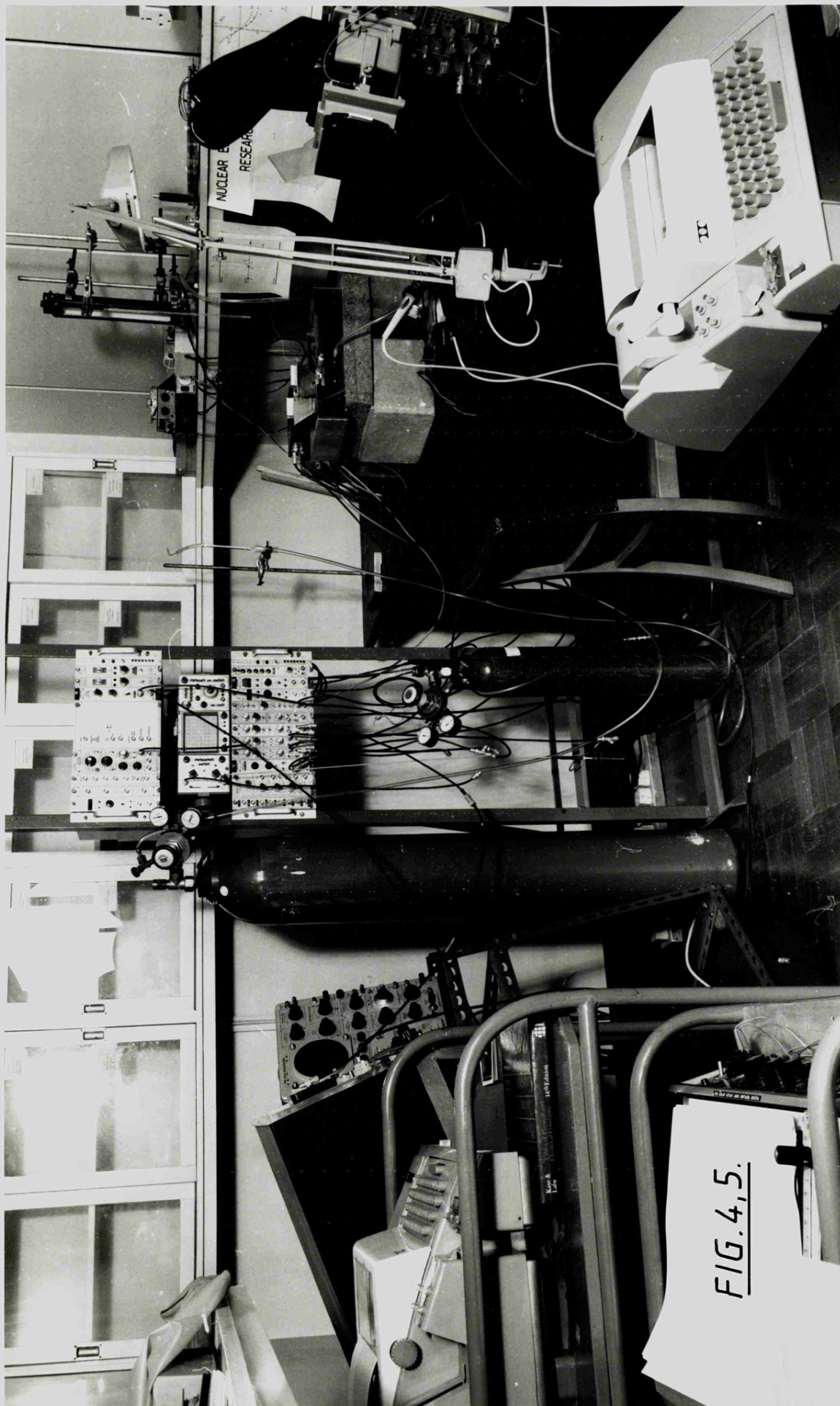
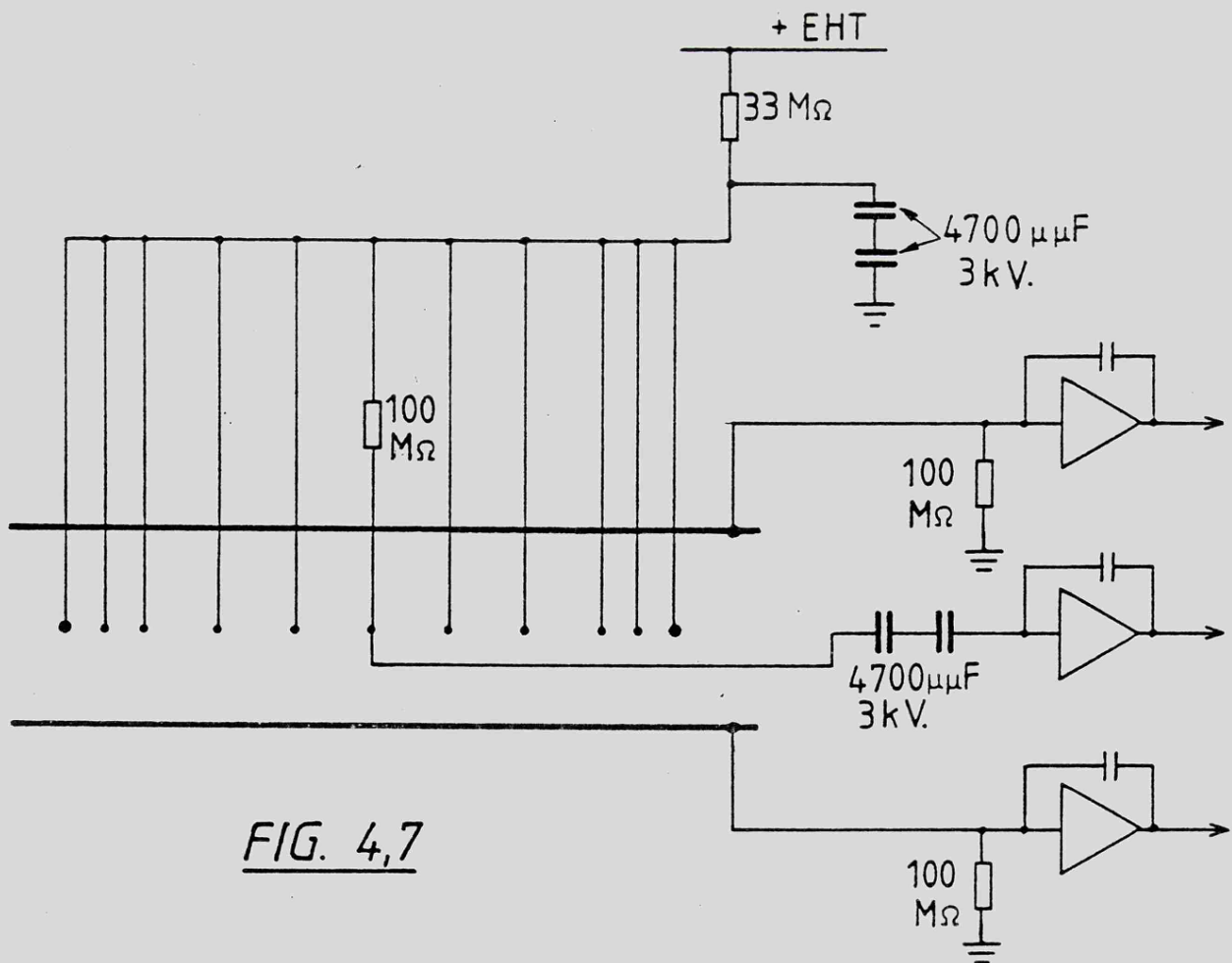
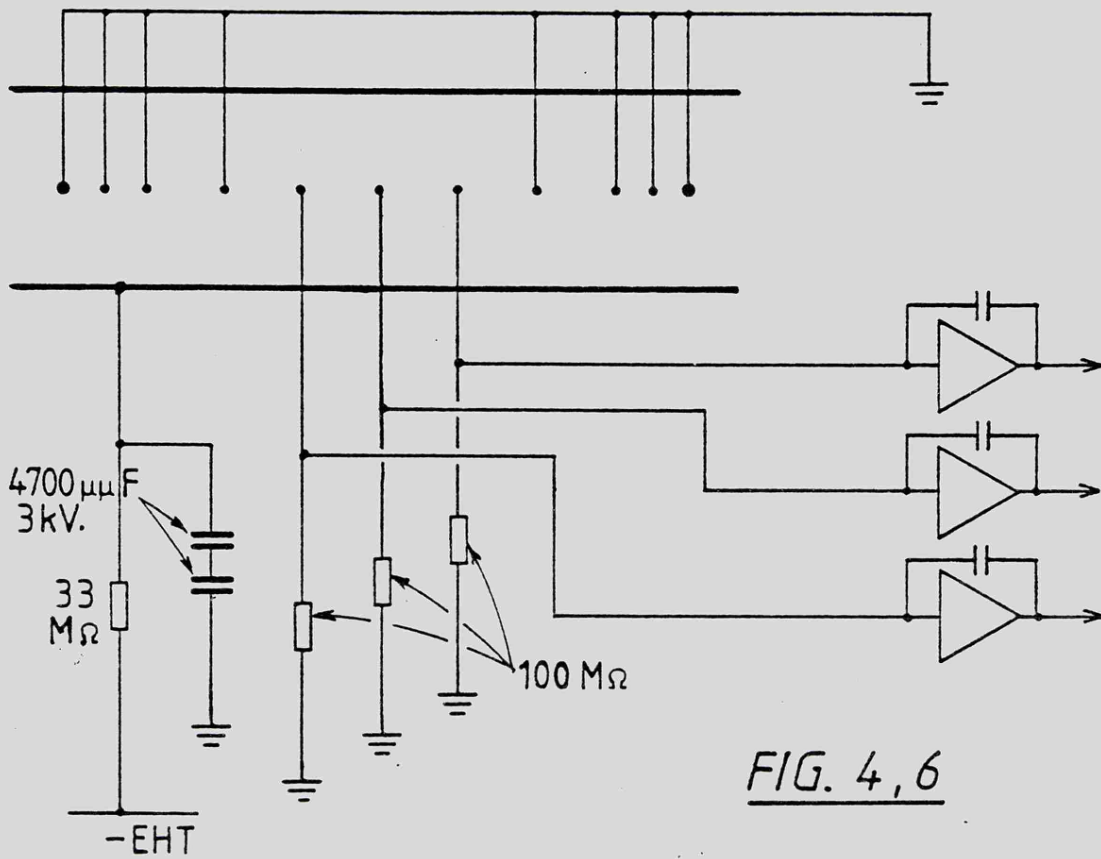


FIG. 4.4 - THE ELECTRONIC SYSTEM.





exception of the 'avalanche' anode, were taken to positive e.h.t. through the ripple filtering network. The central 'avalanche' anode was connected to positive e.h.t. via a  $100M\Omega$  resistor and coupled to the charge-sensitive preamplifier with high voltage capacitors (2350pF, 6kV.).

#### 4.2.3 The charge-sensitive preamplifiers

The lowest signal level to be encountered in this work occurred when looking at induced charges on the anodes situated at  $x_0 = \pm 2s$  where the corresponding signal level was found to be about twenty times lower than that of the avalanche anode. For 6keV. incident radiation energy and for a gas gain of  $10^4$ , this was equivalent to about  $10^5$  electrons. With the choice of reasonably low noise preamplifiers, noise was clearly not a problem and no unusual precautions were necessary to reduce the noise below normal working levels.

The preamplifiers used were Ortec type 118A. The typical equivalent noise charge, when used with a  $2\mu s$  shaping amplifier, was specified as 175 rms electrons with about 4 additional electrons per pF of external capacitance. The coaxial cables coupling the chamber to the preamplifiers were made as short as possible (12") to keep the external capacitance to a minimum and the total anode wire and cable capacitance was then  $\sim 40pF$ , resulting in an anticipated noise performance of 335 electrons. When using cathode readout, the total capacitance increased to  $\sim 80pF$  and a noise performance of 495 electrons was expected.

Measurements showed that the preamplifiers were in fact rather worse than this but were just within the Ortec basis of warranty of 220 rms electrons + 4.4 electrons/pF (396 electrons and 572 electrons for anode and cathode couplings respectively).

Absolute measurement of charge, and chamber pulse simulation was by means of a precision mercury relay pulser and charge termination

(Fig. 4.4), the output of which could be set accurately ( $<1\%$ ) against a digital voltmeter and which was linear throughout its range to within  $.25\%$  of full scale.

#### 4.2.4 Pulse shaping

Normally, commercially available pulse shaping amplifiers contain a rather complicated system of filtering, containing one or two differentiating filters and a series of integrating filters. The effect is to produce a pseudo-Gaussian response, which, whilst giving a slightly better noise filtering characteristic, is more difficult to accurately analyse than the simple case of a single differentiating, single integrating pair of non-interacting R.C. filters, for which the impulse response is described in section 3.5. The shaping amplifiers used here have been specially designed to have this latter impulse response and a circuit diagram is given in Fig. 4.8. The circuit includes a pole-zero cancellation network to compensate for the preamplifier roll-off characteristic. The facility was included for switching over a range of time constants from  $.5\mu\text{s}$  to  $25\mu\text{s}$ .

#### 4.2.5 Pulse stretchers

The times to maximum of the induced pulses differ between various pickoff points in the chamber, and strictly, pulse stretchers should be used prior to division, in order that the maximum amplitudes may coincide. The function of the pulse stretcher is to sample the rising edge of the induced pulse up to its maximum, and then to accurately hold this maximum for as long as it takes the divider circuitry to function. There are two important yet conflicting requirements in the stretcher design. Firstly it is important to preserve good linearity and it is therefore desirable to use a design employing high gain operational amplifiers. Secondly it is necessary that the stretcher should have a fast rise time, so that the pre-shaped

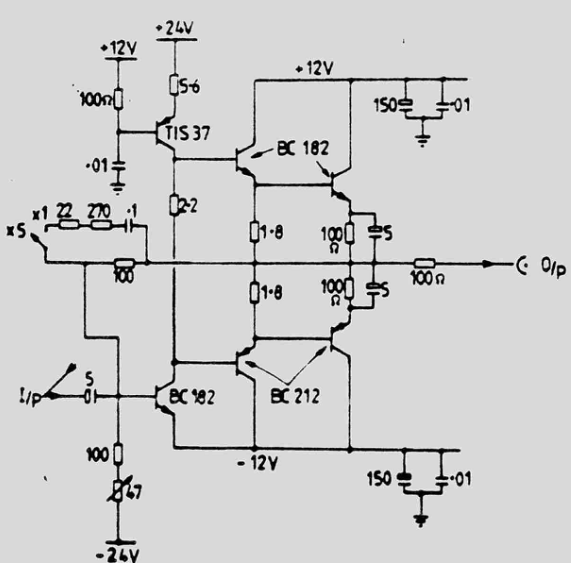
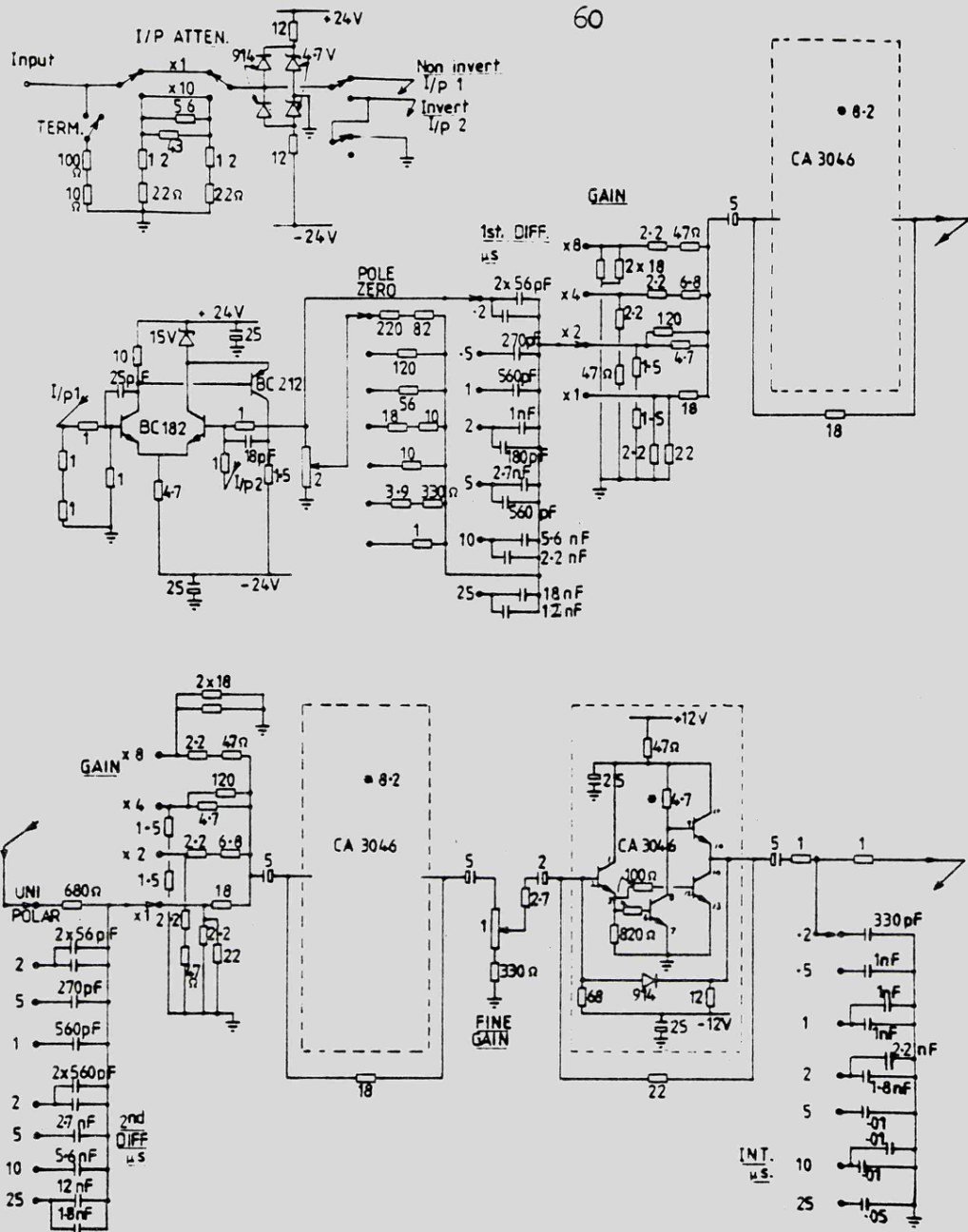


FIG. 4.8—  
PULSE SHAPING  
AMPLIFIER.

CAPACITORS -  $\mu$ F  
RESISTORS - k $\Omega$   
UNLESS STATED

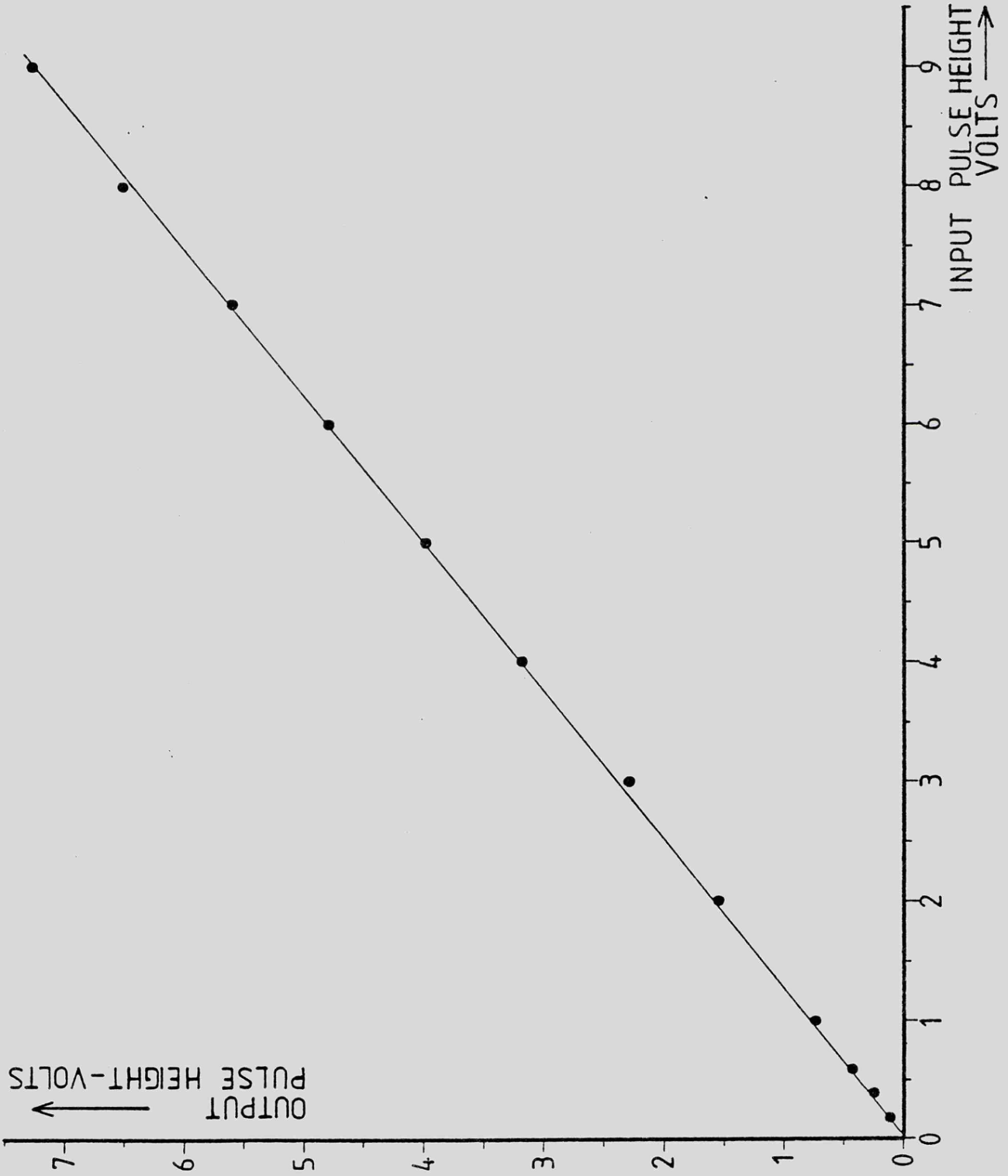
pulse is not distorted.

By the use of moderately priced high slew-rate operational amplifiers, it was possible to achieve excellent linearity, Fig. 4.9, but the rise time was  $0.7\mu\text{s}$ . Further improvements in rise time were at the expense of degraded linearity. However, this was certainly adequately fast when using  $> 5\mu\text{s}$  shaping, where the modification to the rise time would be less than 1%.

The circuit diagram of the dual stretcher is shown in Fig. 4.10. The second stage ( $OA_2$ ) performs the stretching operation by charging the feedback capacitor  $C_2$  through resistor  $R_2$  and diode  $D_2$ . As the waveform goes through its maximum,  $D_2$  cuts off, leaving  $C_2$  charged.  $D_1$  prevents reverse saturation of  $OA_2$ . The voltage across  $C_2$  is buffered and presented to the output by the high input resistance voltage follower  $OA_3$ . To preserve a 1:1 gain relationship it was necessary that the input differentiating stage  $OA_1$  should be equal in time constant to the integrating stage  $OA_2$ ; i.e.  $R_1C_1 = R_2C_2$ . The natural decay time of  $C_2$  due to circuit loading effects was about 50 ms., but this was cut short by the FET switch across  $C_2$ , so that the final output was a flat-topped pulse of adjustable duration 3 - 30 $\mu\text{s}$ . The gating pulse delay was generated by the dual monostable (74221) fed from the comparator  $OA_5$  and the amplifier/inverter  $OA_4$  which sensed both inputs.

In practical use, the benefits of using the stretchers are very small. The pulse shape has been computed for induced cathode signals with two extreme values of  $\alpha = \pm 90^\circ$ . The calculations were for a chamber having  $s = 5\text{mm}$ ,  $h/s = 2.2$ , e.h.t. = 2.5kV, and filled with 90% argon/10% methane ( $\mu = 1.6 \text{ cm}^2/\text{Vs}$ <sup>(62)</sup>). From Fig. 4.11, where normalised times and amplitudes of the induced cathode pulses at maximum are shown, it can be calculated that the true ratio of

FIG. 4,9—  
STRETCHER LINEARITY.





maximum pulse heights, assuming that stretchers were used to permit the times to coincide, is 1.426, whereas the direct ratios at the two points of maximum are 1.397 and 1.460. The differences are - 2.0% and + 2.4%. Experimental evidence in the photograph of Fig. 4.12 shows the differences to be rather less than those calculated above for the same conditions. It is interesting to note, however, that experimental times to maximum are in good agreement with the theoretical times shown in Fig. 4.11, which have been calculated assuming that  $T_0 = 62.5 \mu\text{s}$ .

In fact the stretchers were not developed until quite late in this work program, and many of the earlier results are therefore subject to an approximate error of  $\pm 2\%$ .

#### 4.2.6 The divider

For the experimental work that follows it was necessary for the divider to perform two functions. When processing information from the anodes, the function  $(A - B)/(A + B)$  was sometimes desirable in order to provide a symmetrical response about the central anode axis, whilst for all other conditions the ratio  $A/B$  was used.

Addition, subtraction and inversion were performed by a switchable combination of LM318 operational amplifiers (Fig. 4.13), chosen for their high slew rate ( $50\text{V}/\mu\text{s}$ ), which would not appreciably modify the input pulse shape. The divider was an Intersil 8013 integrated circuit multiplier/divider, which performed the function  $E_{\text{out}} = 10Z/X$ . This was found to be an excellent low cost device which divided with a typical mean accuracy (including non-linearity and offset errors) of 1% of full output. The output was able to respond rapidly ( $< .5\mu\text{s}$  rise-time from  $-10\text{V}$  to  $+10\text{V}$ ) but was subject to a settling time of  $1\mu\text{s}$ .

To avoid feedthrough of transients which occurred during the

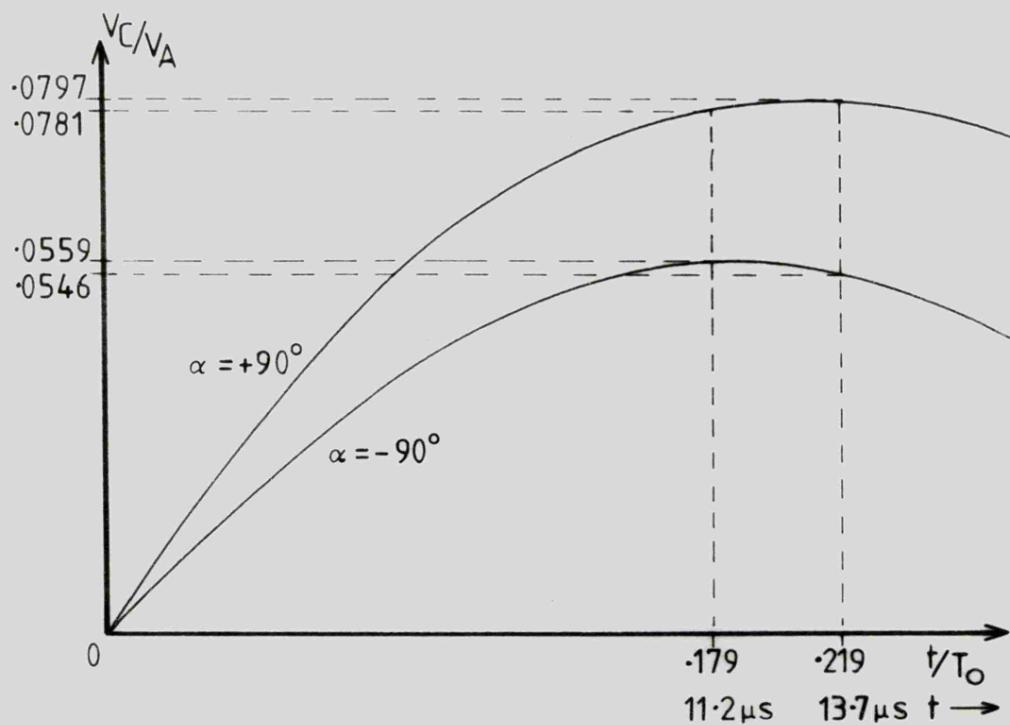


FIG. 4,11.

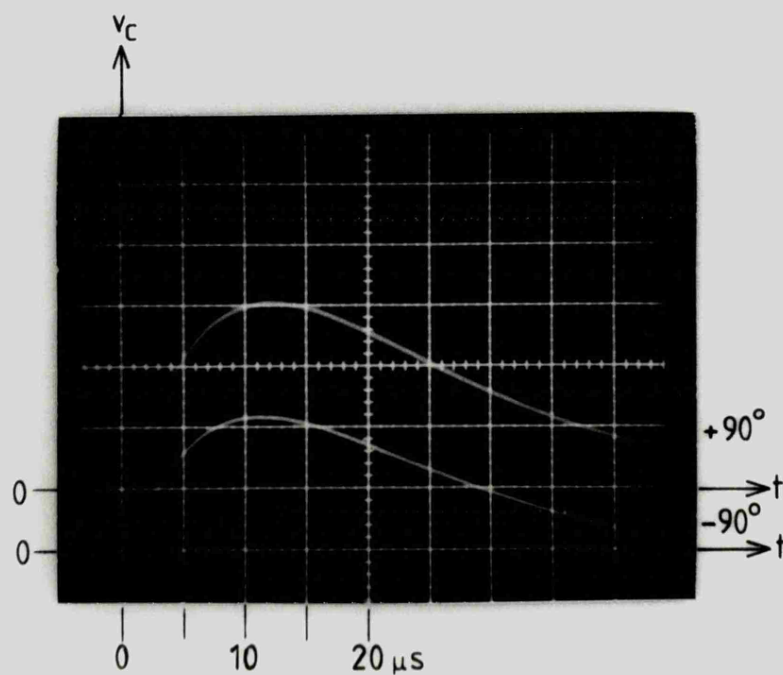


FIG. 4,12.

INDUCED CATHODE PULSES.

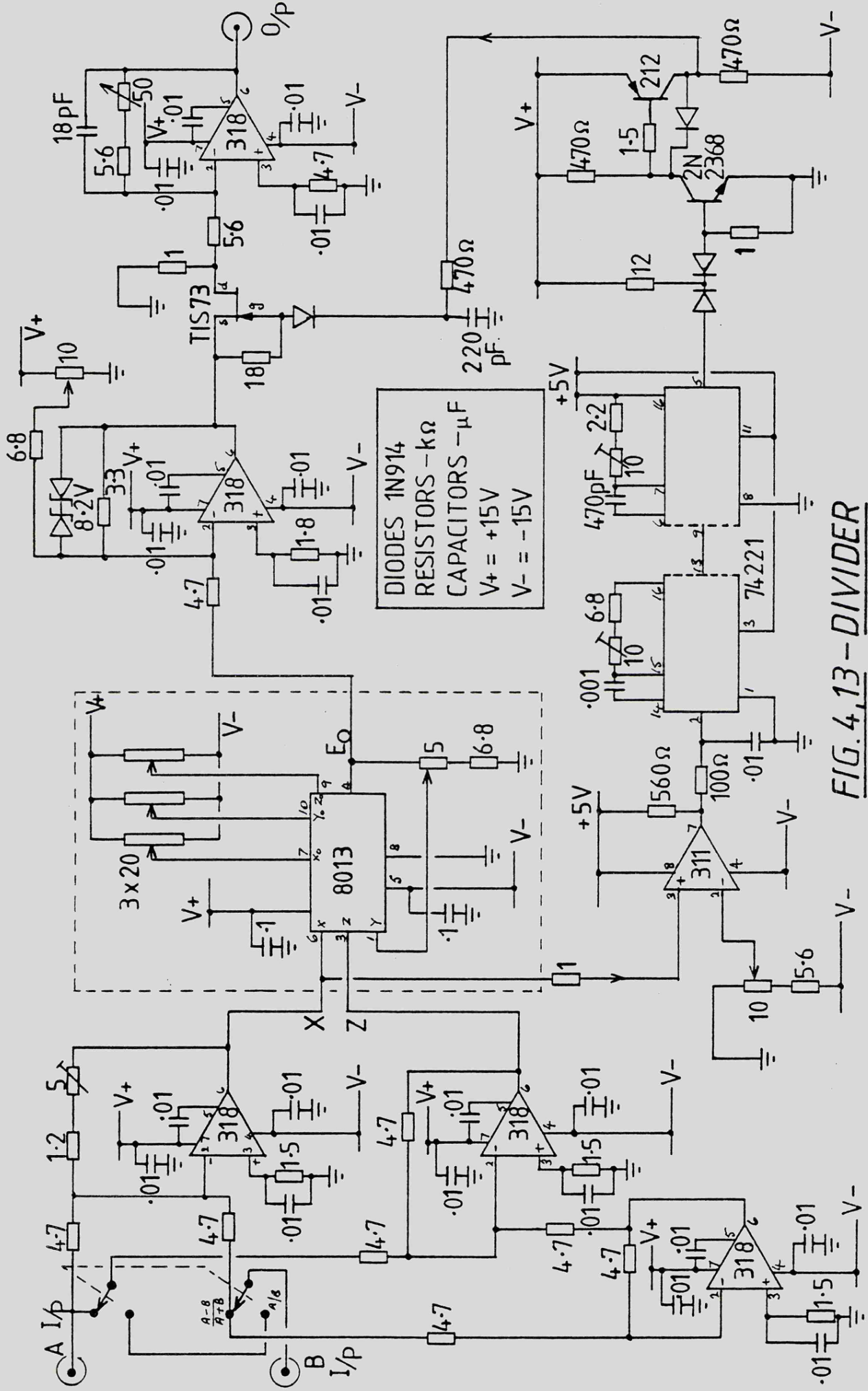


FIG. 4.13 - DIVIDER

settling time of the divider it was necessary to strobe the output some time after the inputs had been applied. An LM311 comparator was used to sample the X input and, above a certain threshold level, to produce an output which would trigger the first delaying stage of an SN 74221 dual TTL monostable. The strobe pulse was generated then by the second stage of this device which was interfaced by two discrete stages to a TIS73L f.e.t. switch, situated between two LM318 buffering stages. The operation of the circuit was simply that two pulses presented to inputs X and Z would be divided, and the ratio  $10Z/X$  would appear at the divider output and therefore at the first buffer output. Assuming now that the level conditions demanded by the comparator were met, then after some delay, the first buffer output would be allowed through the f.e.t. gate and presented to the final output by way of the second buffer. The delay and strobe width could be adjusted according to the shaping time constant so that a brief sample was taken as the input pulses reached their maximum.

#### 4.2.7 Methods of readout

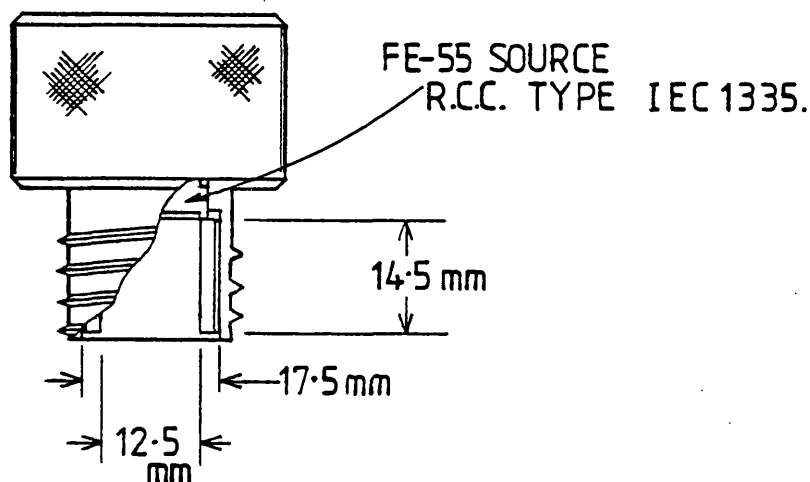
Information was recorded by several means, the most useful being a Northern type NS602 256 channel analyser. For hard copy numerical readout, this was coupled to a Teletype ASR33, and for a pictorial copy of the CRT display, a Moseley type 2D2 X - Y recorder was used in conjunction with a Hewlett-Packard G2B null detector. The NS602 linearity was set to be within 1 channel in 256.

Waveforms were generally observed by means of a Telequipment type D75 or a Tektronix type 7403N/7A15/7B50 oscilloscope. Pulse shapes were recorded photographically using a Shackman Super 7 Mk II oscilloscope camera fitted with a Polaroid M2 film module and adapted for use with the Tektronix 7403N. All recorded times were taken from the Tektronix 7403N which had been calibrated and was accurate to better

than 1% of full scale of the time-base ranges of interest.

#### 4.3 Radiation Sources

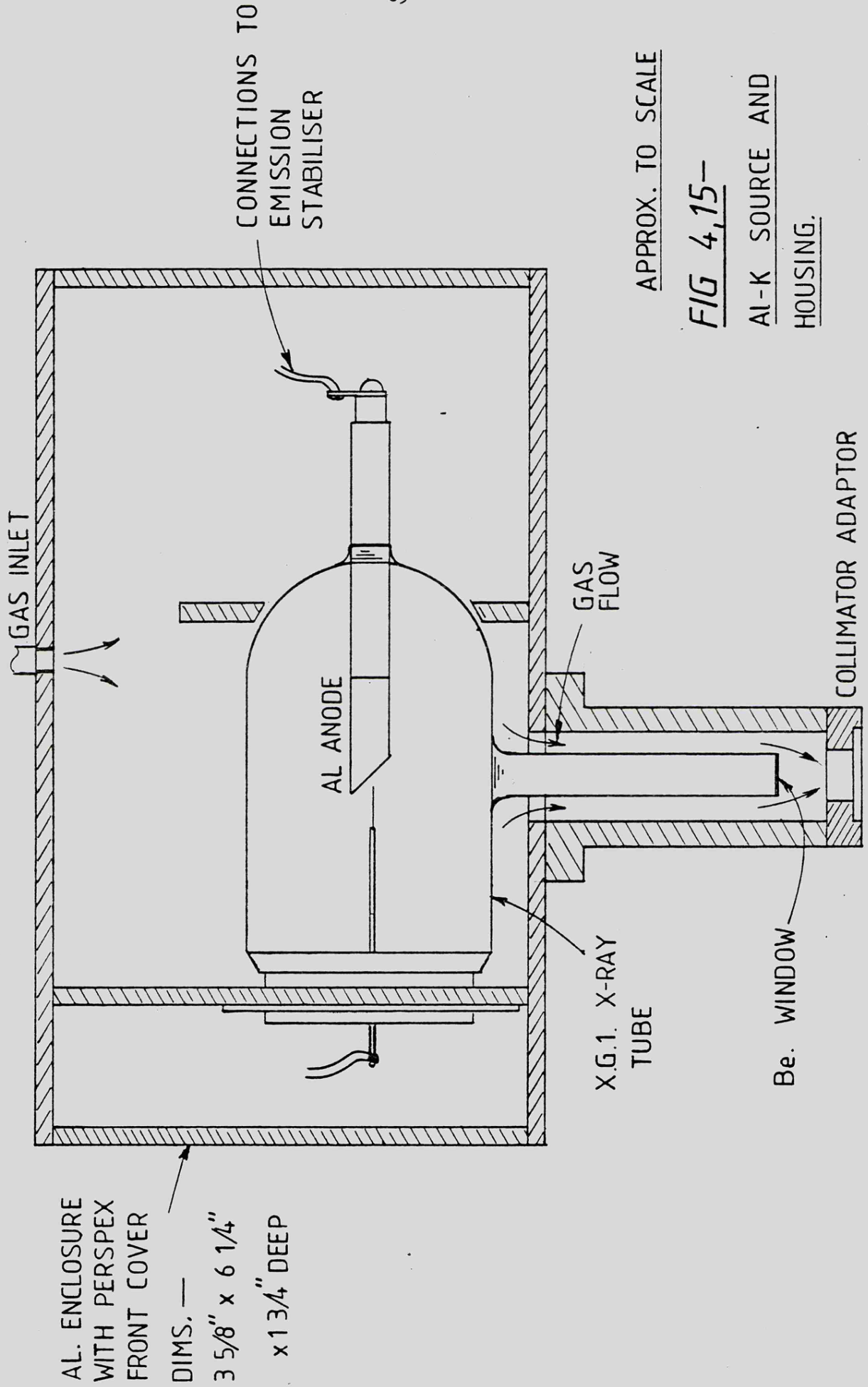
Most measurements were taken using an  $^{55}\text{Fe}$  source of Mn.K X-radiation (5.9keV.). A source of strength 20mCi was chosen to give a useful count rate after quite restrictive collimation. The source was deposited on a copper disc of about 12.5 mm. diameter which was supplied, sealed in a container with a .625 mm. thick beryllium window, by the Radiochemical Centre. A stainless-steel mounting was made (Fig. 4.14) to give protection from the source and to facilitate attachment to the collimator.



MATL.-ST. STEEL  
SCALE - X1

FIG. 4,14.- FE 55 SOURCE  
MOUNTING.

A second source of radiation was a Centronic (20th Century) sealed X-ray tube fitted with a pure aluminium target which emitted characteristic radiation at 1.5keV. through a 75 $\mu\text{m}$  thick, 3 mm. diameter beryllium window. The source was mounted above the collimator in a sealed aluminium and perspex container, and helium was flowed around the tube and through the collimator to improve the X-ray transmission to the chamber. Fig. 4.15 gives more detail of this assembly. The source was operated at 1.9 kV. and 500 $\mu\text{A}$  emission current from an emission stabilised power supply.



APPROX. TO SCALE

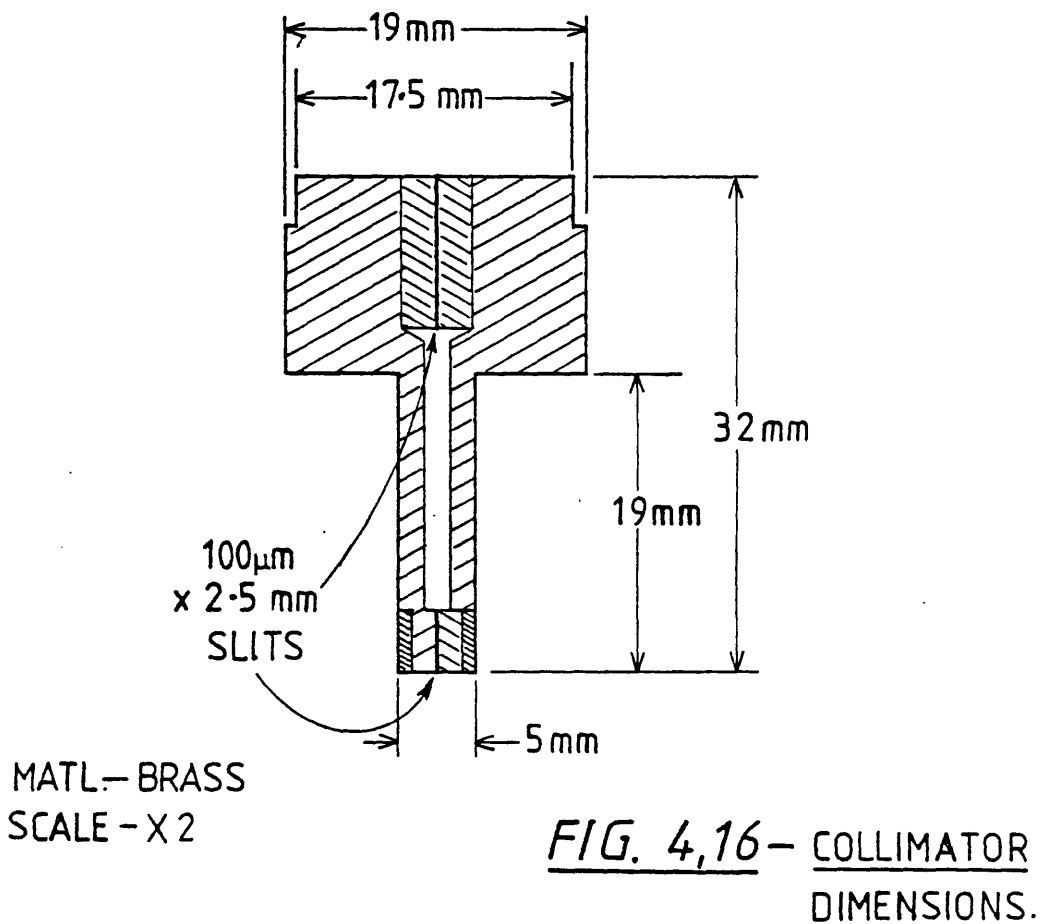
FIG 4,15--

AL-K SOURCE AND HOUSING.

#### 4.4 Collimators

The phenomena of angular localisation may only be observed with effective collimation; the effect is quickly overshadowed as the beam is broadened. It is therefore important to use as small a collimator hole as possible, consistent with preserving a workable count rate.

Several collimators were manufactured in brass to the outside dimensions shown in Fig. 4.16, but with differing hole diameters in the range 1.5 mm. to 100 $\mu$ m. Machining problems and hole alignment difficulties were becoming significant at very small diameters and 100 $\mu$ m



diameter was the smallest achievable with the available workshop equipment. There were also difficulties of very low count rate, below background level, associated with holes of this diameter, and so a  $100\mu\text{m.} \times 2.5 \text{ mm.}$  slit collimator was finally adopted, which when aligned accurately with the anode wires, overcame this latter problem without broadening the beam along the working axis. Fig. 4.17 shows the pertinent dimensions of the source-collimator assembly and its location with respect to the chamber.

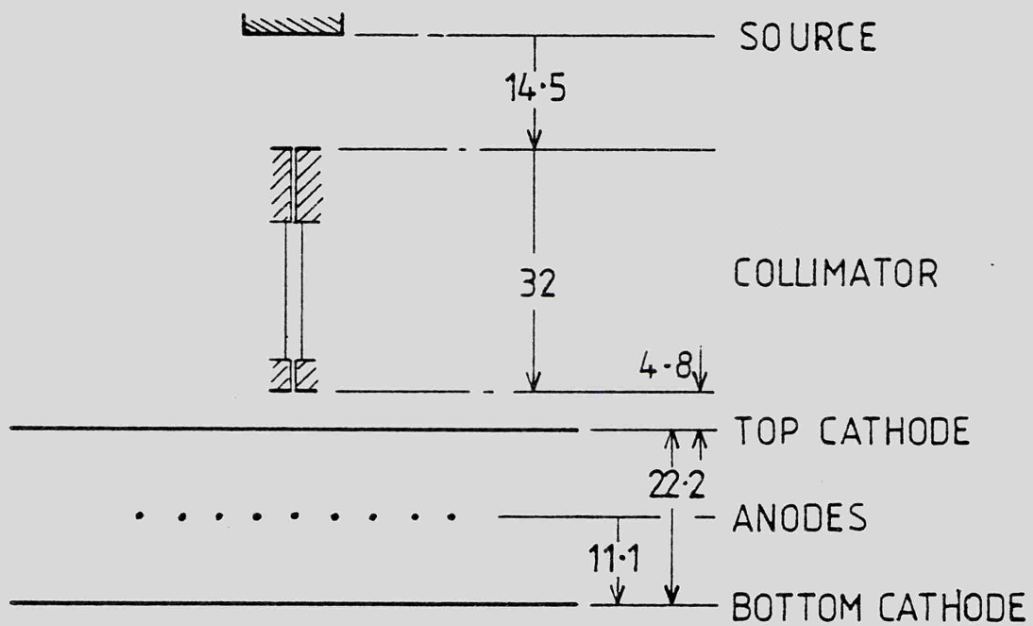


FIG 4,17

DIMENSIONS -mm.

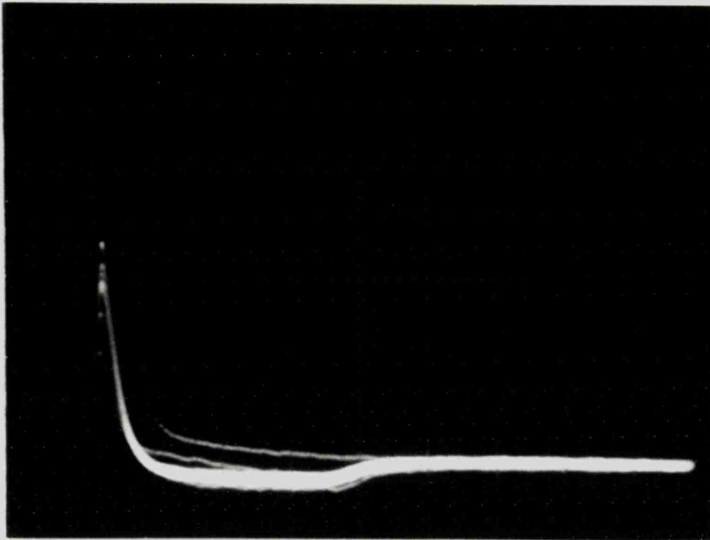
The modification of the collimator transmission pattern due to non-linear absorption within the chamber is accounted for in appendix I and the results have been applied in chapter 5.

CHAPTER 5.THE INDUCED ANODE PULSE - EXPERIMENTAL RESULTS IN P10.5.1 Experimental Conditions

All results reproduced in this chapter were taken using the chamber with 5 mm. anode spacing and 11.1 mm. anode-cathode spacing. The anode radius was 12.5 $\mu$ m. The chamber electrical connections are described in section 4.2.2(a). The flow gas was Ar/10%CH<sub>4</sub> at atmospheric pressure and normal room temperature. Measurements were taken using the .004 in. slit collimator.

5.2 Anode Pulse Shapes

After the induced anode pulse has reached its maximum, its behaviour is of little importance so far as avalanche localisation is concerned, but it is of academic interest to note the pulse shape which is rather strikingly different from pulse shapes previously encountered in proportional counters. This yields some interesting information concerning the positive ion mobility during the later stages of pulse development. With the 1.5keV source situated directly above an anode, the induced pulses in a neighbouring anode were observed and photographed from the oscilloscope with  $T = 10\mu$ s and  $T = 25\mu$ s, and the photographs are shown in Fig. 5.1. The prolonged constant voltage negative region is indicative of a long period of constant negative slope prior to differentiation, which may be explained by noting on the isometric plot of induced anode charges Fig. 3.6, the effect of a group of positive ions moving from the centre anode along the most direct field line which runs perpendicular to the cathode. The induced charge undergoes a gentle linear negative slope, and finally remains constant when all positive ions are collected at the cathode. From the photographs, the



10  $\mu$ s SHAPING

$V_A = 2.7$  kV

TIME CAL. = 100  $\mu$ s / DIV

POSN.  $X_0 = 0$

25  $\mu$ s SHAPING

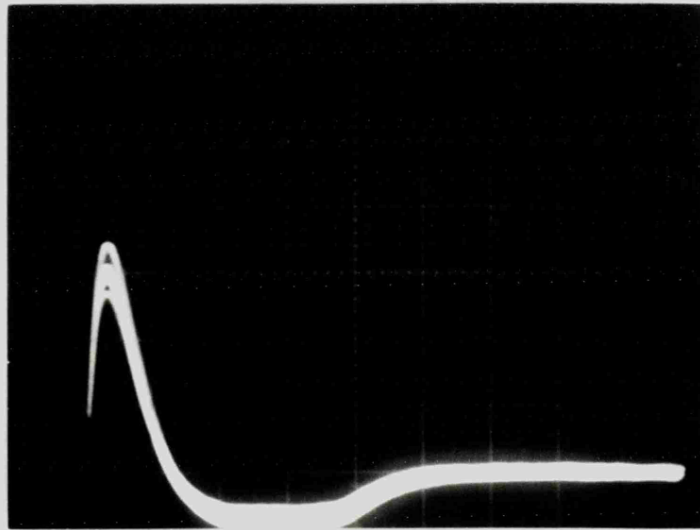


FIG 5,1 — THE INDUCED ANODE PULSE

collection time is about 360 $\mu$ s.

The variation of potential P along the field line at  $x/s = 0$ , for  $y/s = 0$  to  $y/s = 2.22$  has been plotted from Eqn. 3 for the present chamber, and is shown in Fig. 5.2

The near linear field region can be regarded as extending from  $y/s = .22$  to  $y/s = 2.22$ . In real terms  $\Delta y = 90\%$  of  $h$  ( $=1$  cm., for  $s = 5$  mm.). Since the field in the remaining 10% of  $h$  near the anode is extremely non-linear and high ion drift velocities will occur, then considerably less than 10% of the total collection time will be spent in this region, and in order to obtain an estimate of the ion mobility, it is necessary to develop further the theory of section 3.4.

From Eqn. 36, at  $x = 0$ ,

$$E = \frac{V_a}{s} \cdot K_1 \cdot \left\{ \frac{\cosh 2\pi y/s + 1}{\cosh 2\pi y/s - 1} \right\}^{1/2},$$

$$\text{where } K_1 = s/h / (1 - s/\pi h \cdot \log 2\pi r_a/s).$$

$$\text{Now } 1/s \frac{dy}{dt} = \frac{\mu E}{s} = \frac{\mu V_a}{s^2} \cdot K_1 \left\{ \frac{\cosh 2\pi y/s + 1}{\cosh 2\pi y/s - 1} \right\}^{1/2}$$

In normalised terms, i.e. time normalised to  $s^2/\mu V_a$  and distance normalised to  $s$ ,

$$\frac{dy}{dt} = K_1 \coth \pi y$$

$$\therefore \int_{r_a}^h \tanh \pi y \, dy = \int K_1 \, dt$$

$$\therefore \log \cosh \pi h - \log \cosh \pi r_a = \pi K_1 t_c,$$

where  $t_c$  is the ion collection time.

Now for  $\pi h \gg 1 \gg \pi r_a$ ,

$$t_c = 1/\pi K_1 (\pi h - \log 2).$$

Therefore at  $x = 0$ ,  $\alpha = 90^\circ$ ,

$$t_c = 1/K_1 (h - \log 2/\pi).$$

Inserting actual values,  $h/s = 2.22$ ,  $r_a/s = 2.5$

then  $K_1 = .282$

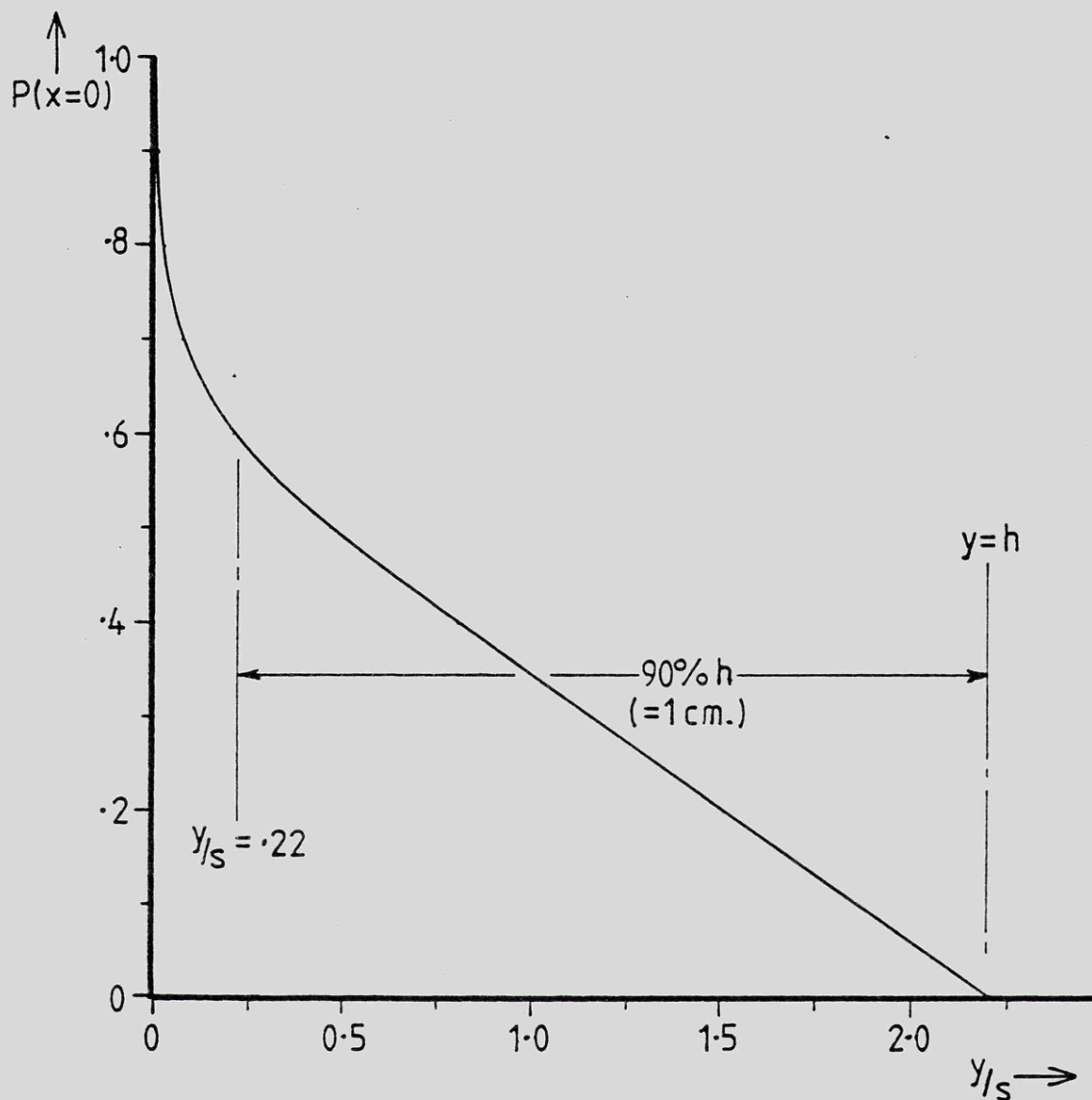


FIG 5,2 — THE VARIATION OF POTENTIAL  $P$   
 ALONG THE  $y/s$  AXIS, WHERE  $x/s = 0$ ,  
 $h/s = 2.2$ ,  $r_{a/s} = 2.5 \cdot 10^{-3}$

and  $t_c/T_0 = 7.08$ .

If  $t_c = 360\mu s$ . (from Fig. 5.1)

then  $T_0 = 50.8\mu s$ .,

therefore for  $V_a = 2.7kV$ ,

$$\mu = 1.82 \text{ cm.}^2/Vs.$$

This value is in reasonably good agreement with the mobility determined by Gott and Charles<sup>(62)</sup> i.e.  $1.6 \pm 0.2 \text{ cm.}^2/Vs$ , but is in rather better agreement with that obtained by Schultz et al.<sup>(69)</sup>, whose experimental measurements indicate a value for  $\mu$  of 1.9. This would indicate that charge transfer has taken place quite early in the pulse formation and the carrier is methane.

It is therefore not altogether clear from these rather insensitive measurements what the nature of the ion is, but for the purpose of comparing experimental results with theory, the mobility figures of Gott and Charles, listed in table 5.1, will be applied wherever possible.

Since the field is known to be very nearly uniform over most of the chamber, the flatness of the differentiated pulse must be an indication of the constancy of the positive ion mobility during this time.

As one would expect, a change in time constant of the shaping amplifiers affects the initial pulse shape and also the decay time after total collection, but does not, of course, affect the collection time.

Table 5.1

Gas	$\mu - \text{cm} \cdot \text{s}^{-1} \text{V}^{-1}$	Carrier
A/CH <sub>4</sub> 90/10	1.6 ± .2	A <sup>+</sup>
A/CH <sub>4</sub> 25/75	2.3 ± .4	
Ne/CH <sub>4</sub> 90/10	4.0 ± 1	Ne <sup>+</sup>

### 5.3 Gas Gain and Choice of Operating Point.

The gas gain has been determined for several values of  $V_a$  and the curve is given in Fig. 5.3. The onset of saturation occurred at a gain of about  $7 \cdot 10^4$  where the 2:1 ratio between photopeak and escape peak of an <sup>55</sup>Fe spectrum began to reduce noticeably. When using <sup>55</sup>Fe as a source of radiation (5.9keV) a normal operating gain of about  $10^4$  was chosen, ( $V_a = 2.5\text{kV}$ ). Under this condition electronic noise was not troublesome (see section 3.2.3) and the operating point was well below any signs of saturation. Where aluminium-K X-rays were used, (1.5keV), the gain was increased by a factor almost 4 ( $V_a = 2.7\text{kV}$ ) to remain well above noise, and this condition was also clear of saturation. Hence the two limiting criteria were met; to stay well clear of electronic noise and to avoid gas gain saturation, which it was thought would cause the avalanche to spread around the wire.

### 5.4 Traversing the Chamber.

The position of each wire was located with respect to the micrometer scale, by observing the count rate from that particular wire whilst scanning across the chamber with the source and .004 slit collimator. Typical results are shown in Fig. 5.4(a) where the rapid fall off in count rate on either side shows the sensitivity with which

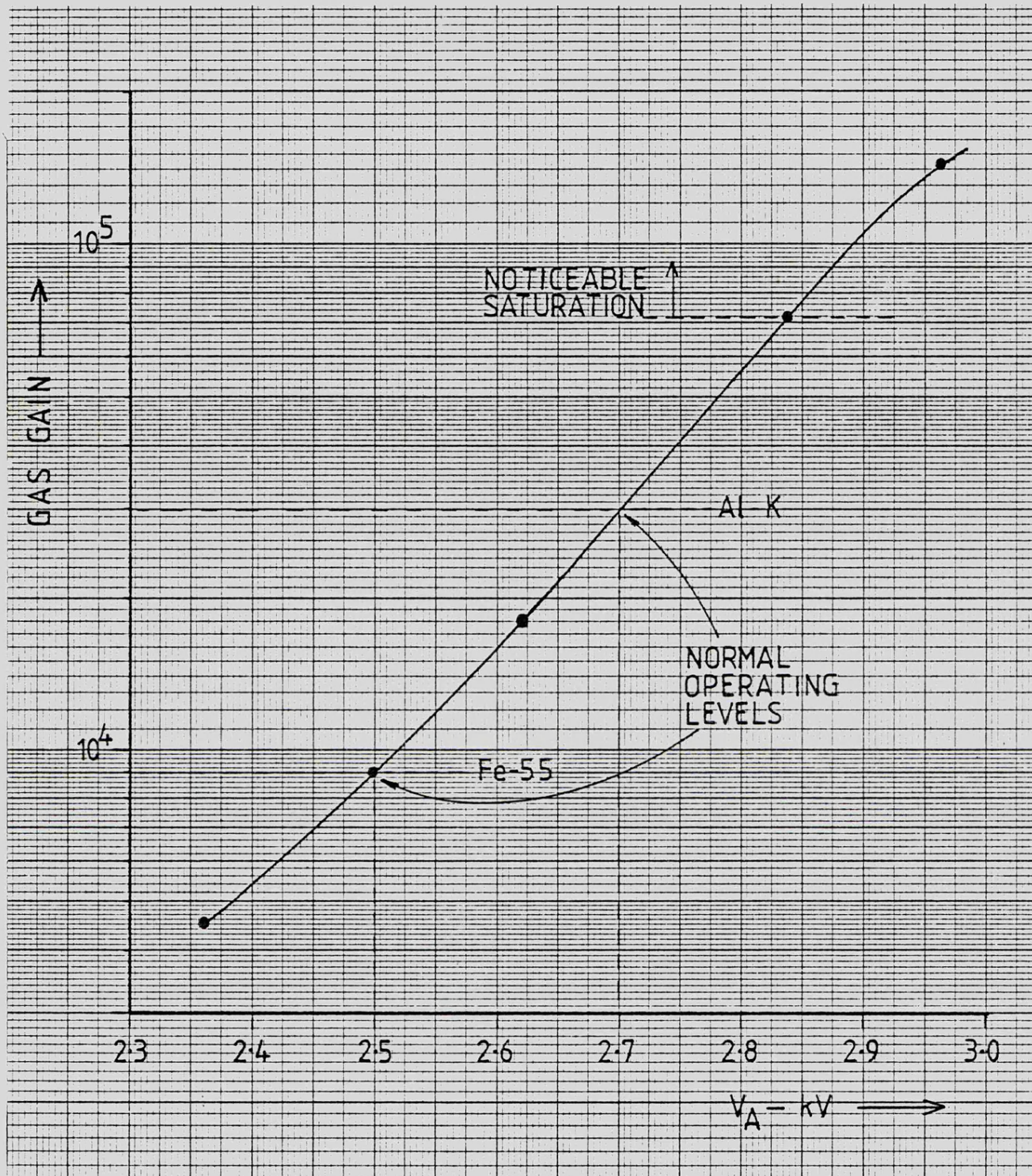


FIG 5,3 — GAS GAIN VARIATION WITH ANODE VOLTAGE

the 'cell' boundaries can be detected. The mid-point then identifies the avalanche wire position.

Another method used to locate wire positions was found to be less sensitive, but is briefly mentioned here.

Observation of the gas gain across the 'cell' gave a reasonably good indication of its boundaries. Clearly, as the 'cell' boundary is crossed the avalanche wire becomes a sense wire of induced charge and there is a reversal of charge polarity. Diffusion effects in the boundary region tend to mask the changeover point, but the mid position, between the two points can be determined accurately. Fig. 5.4 enables this method to be compared with the former method. Agreement between the two methods is found to be extremely good.

It is interesting at this stage to note the variation in gas gain as the source traverses the three centre anodes with those anodes connected together. Fig. 5.5 shows the gain remaining near constant over the centre anode 'cell', but immediately increasing and remaining less constant beyond this region as chamber end effects become apparent (note vertical scale). Presumably the difference in gain from the two side wires ( $\sim 7\%$ ) is due to non-uniformity in wire diameter. This should not affect results given later where ratios of direct to induced pulses have been taken to eliminate energy dependence and gas gain variations.

With the positions of the central anode wires established, the induced charge in wires A' and B could be examined experimentally. Measurements of  $-v_B/v_A$  for various positions of the  $^{55}\text{Fe}$  X-ray beam,  $x_0/s$ , are shown in Fig. 5.6. The filter time constants used were  $10\mu\text{s}$  and comparison is made with a theoretical curve drawn for  $T/T_0 = .15$  ( $\equiv T = 10\mu\text{s}$  at  $V_a = 2.5\text{kV}$  and  $\mu = 1.5 \text{ cm}^2/\text{Vs}$ ).

The curves compare favourably over the range  $x_0/s = -.3$  to

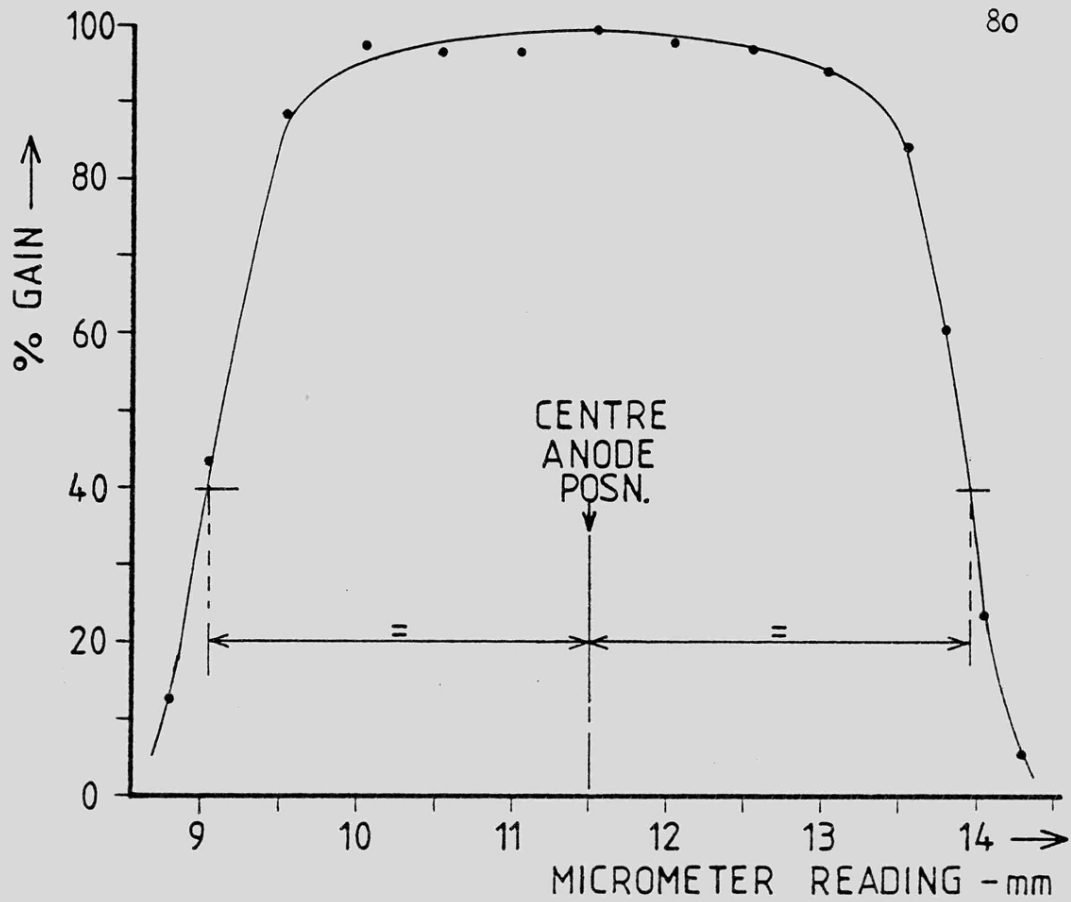


FIG 5,4(b) - GAIN VARIATION ACROSS A SINGLE WIRE

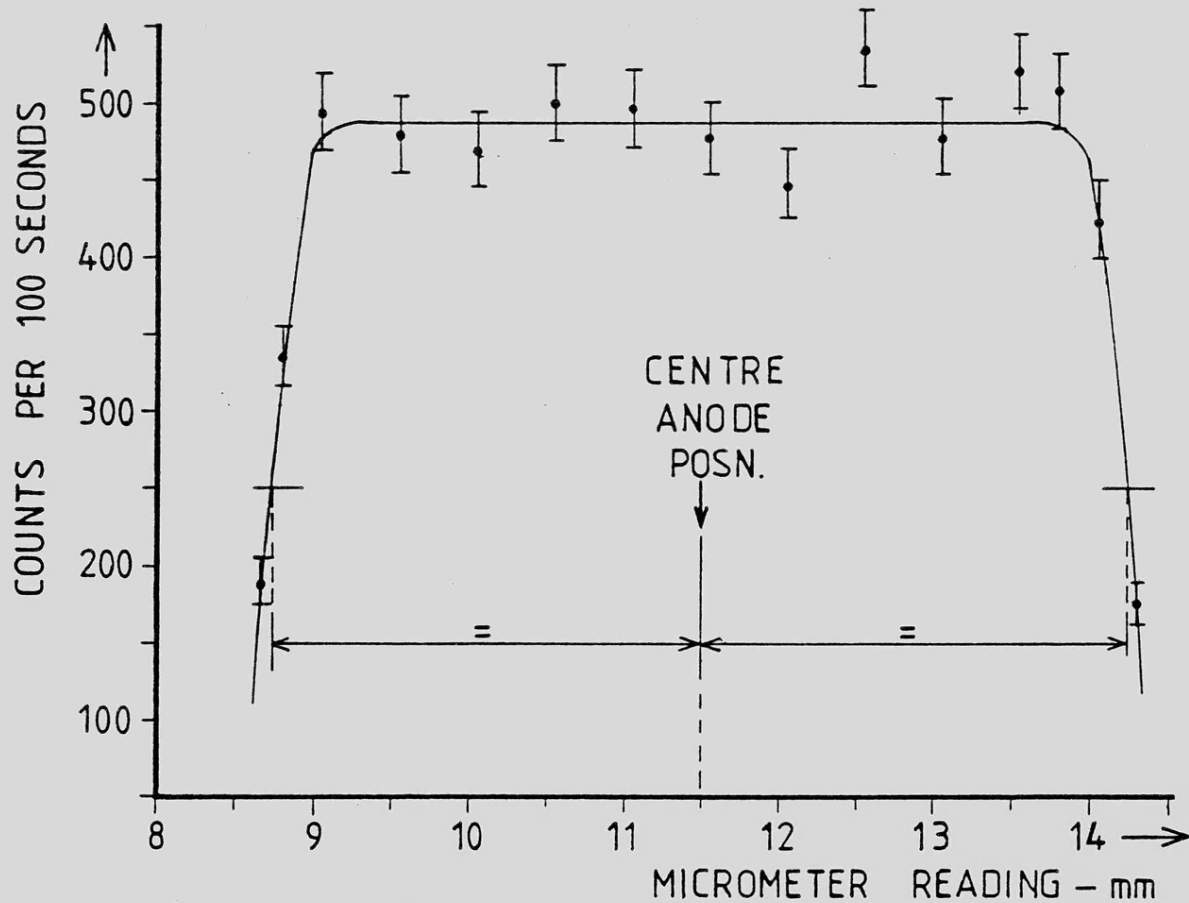


FIG 5,4(a) - CHANGE IN COUNT RATE ACROSS THE CENTRE WIRE

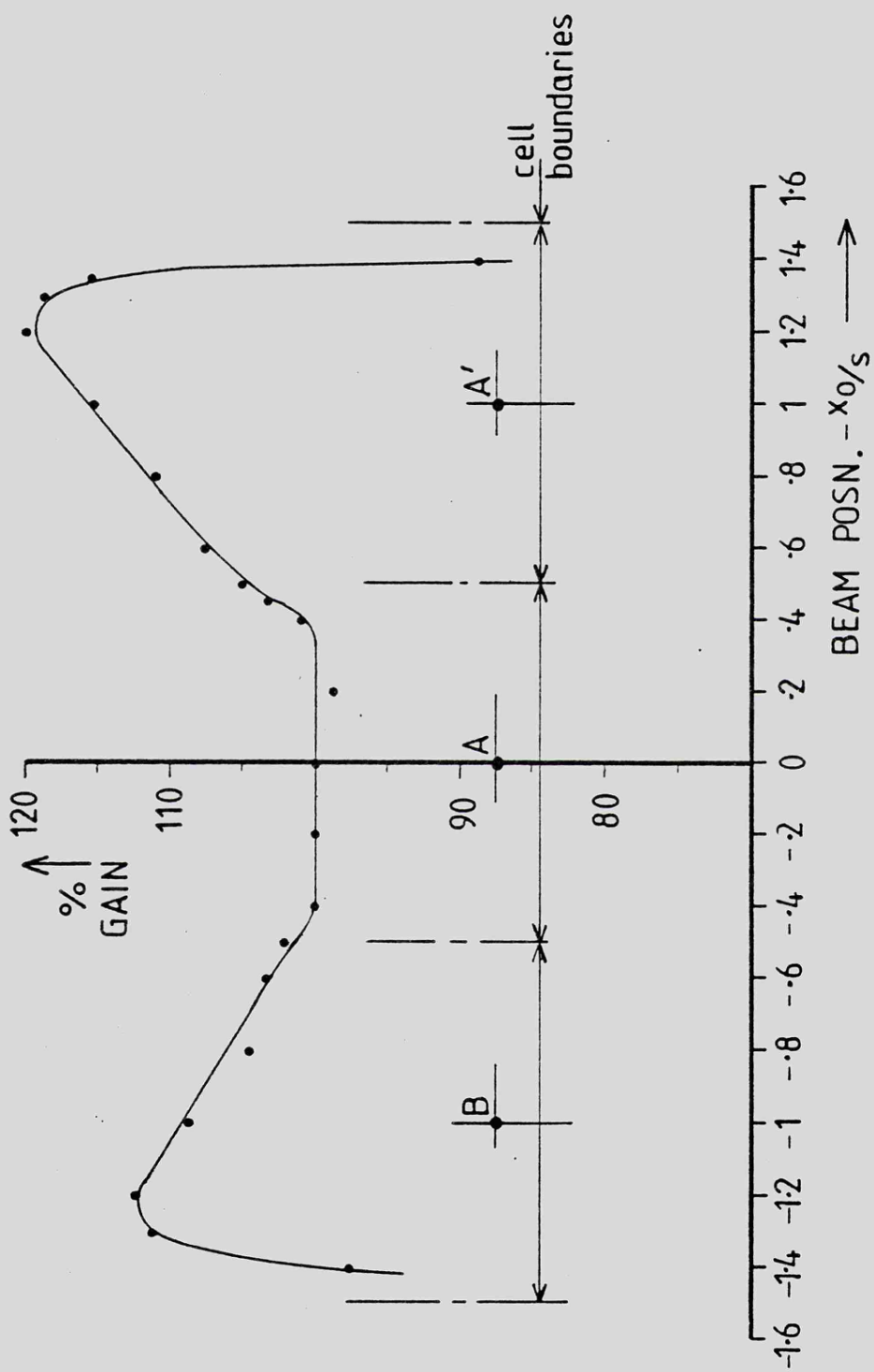


FIG 5,5 - GAIN VARIATION OVER  
CENTRAL THREE ANODES

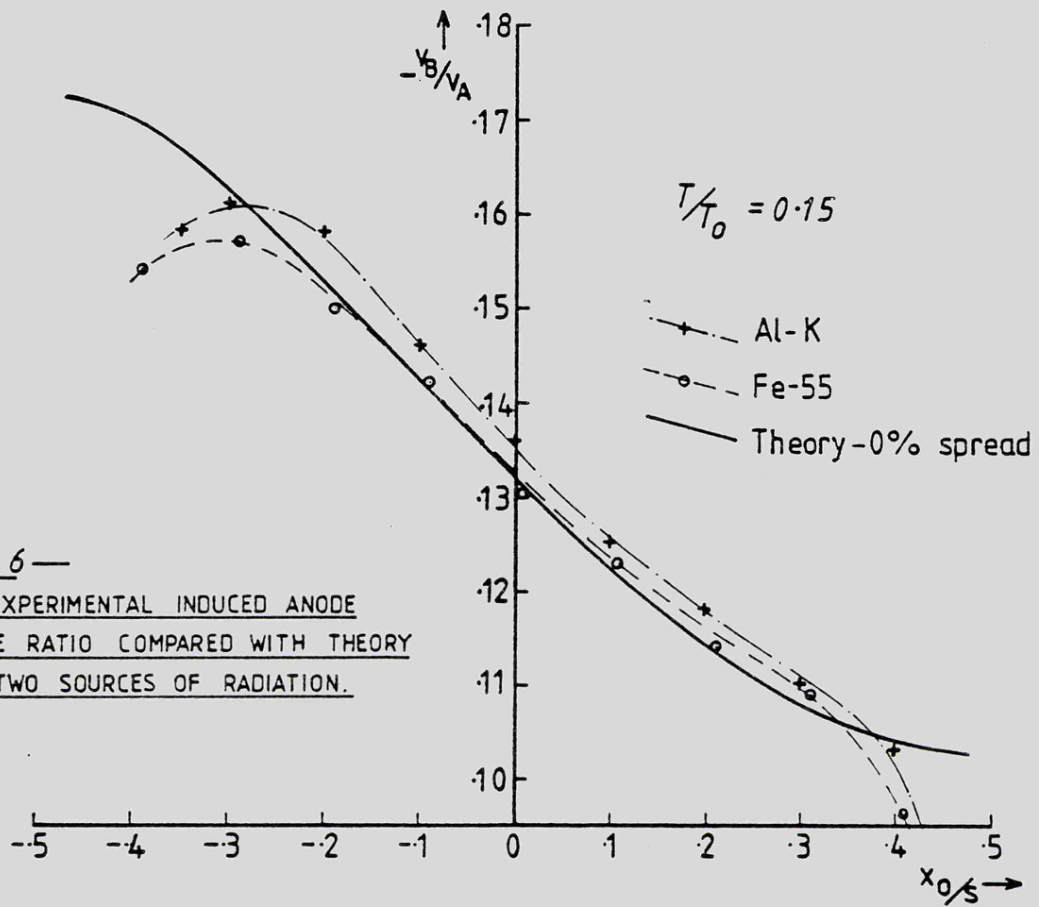


FIG 5.6—

THE EXPERIMENTAL INDUCED ANODE  
PULSE RATIO COMPARED WITH THEORY  
FOR TWO SOURCES OF RADIATION.

+0.3 but beyond these points the experimental curve falls off rapidly, accompanied by a severe degradation of the energy spectrum photopeak resolution. Providing the predicted field pattern near the 'cell' boundary remains undistorted, and there is no reason to suspect otherwise, then this fall off must be attributable to the effects of imperfect collimation, to the extent of initial ionisation and also to electron diffusion. The .004in. slit collimator provides a beam width of about 200 $\mu$ m. at the anode plane which increases to 273 $\mu$ m. at the bottom cathode. This alone is unlikely to cause trouble except beyond  $x_0/s = .48$ . The extent of initial ionisation is determined by the range of photoelectrons produced. For 5.9keV X-rays in argon, the mean photoelectron range has been estimated as 59 $\mu$ m.<sup>(33)</sup>, which in this instance may be neglected. Diffusion effects are more likely to be troublesome and an account of this is given later in section 5.9.

For each electron diffusing into a neighbouring cell, the anode of that cell, which previously was a sense anode, will collect an avalanche, which for 6keV radiation is approximately 1/200 times the size of the total avalanche. Now, since the total avalanche was about ten times the size of the induced charge, it becomes clear that 20 stray electrons will completely negate the induced positive charge. Hence the experimental curve of Fig. 5.6 becomes very sensitive to lost electrons.

The spread due to collimation and initial photoelectron range can be greatly reduced by using 1.5keV incident radiation from the sealed aluminium source, whereby absorption will take place very close to the upper window. Fig. 5.6 shows these results alongside those for <sup>55</sup>Fe. It is possible that some lateral shift in the collimator position of about 100 $\mu$ m. has unwittingly occurred whilst using the Al source. (Unfortunately the sealed aluminium source was available for only a

short time and it has not since been possible to repeat these results.) If this were the case, then the two experimental curves would be almost superimposed and there would be little difference in the upper turnover point, where a reduction in angular spread due to absorption nearer the window, would be most influential. This would indicate that diffusion is mostly responsible for angular spreading, and that initial photo-electron range and collimator spread are only minor contributors.

### 5.5 Beyond the Cell Boundary

Moving the  $^{55}\text{Fe}$  source beyond .5s provides a convincing demonstration of the angular localisation effect. Within the transition region .4s to .6s, the avalanche transfers to anode A', with a simultaneous reduction in induced charge on anode B. From .6s to 1.4s there is again good agreement with theoretical predictions (Fig. 5.7).

### 5.6 The Position Signal

Utilising the information from both sense anodes provides a more sensitive, more linear response when the quantity  $r = (v_B - v_A) / (v_B + v_A) + \text{constant}$  is plotted against  $x_0$ . The response is also symmetrical about  $x_0 = 0$  and independent of X-ray energy. The constant is a dc voltage added after division to prevent the output of the electronics passing through zero at  $x_0 = 0$ . The output would otherwise have been incompatible with the multichannel analyser.

The resulting linearity is demonstrated in Fig. 5.8(a) where the centroid of the distribution  $r$  is plotted against the  $^{55}\text{Fe}$  X-ray source position. The error bars signify the accuracy to which the centroid of  $r$  could be read. By this method useful positional information could be obtained over 70% of the cell width with acceptable linearity.

### 5.7 Resolution

An estimate of the positional resolving power is of importance

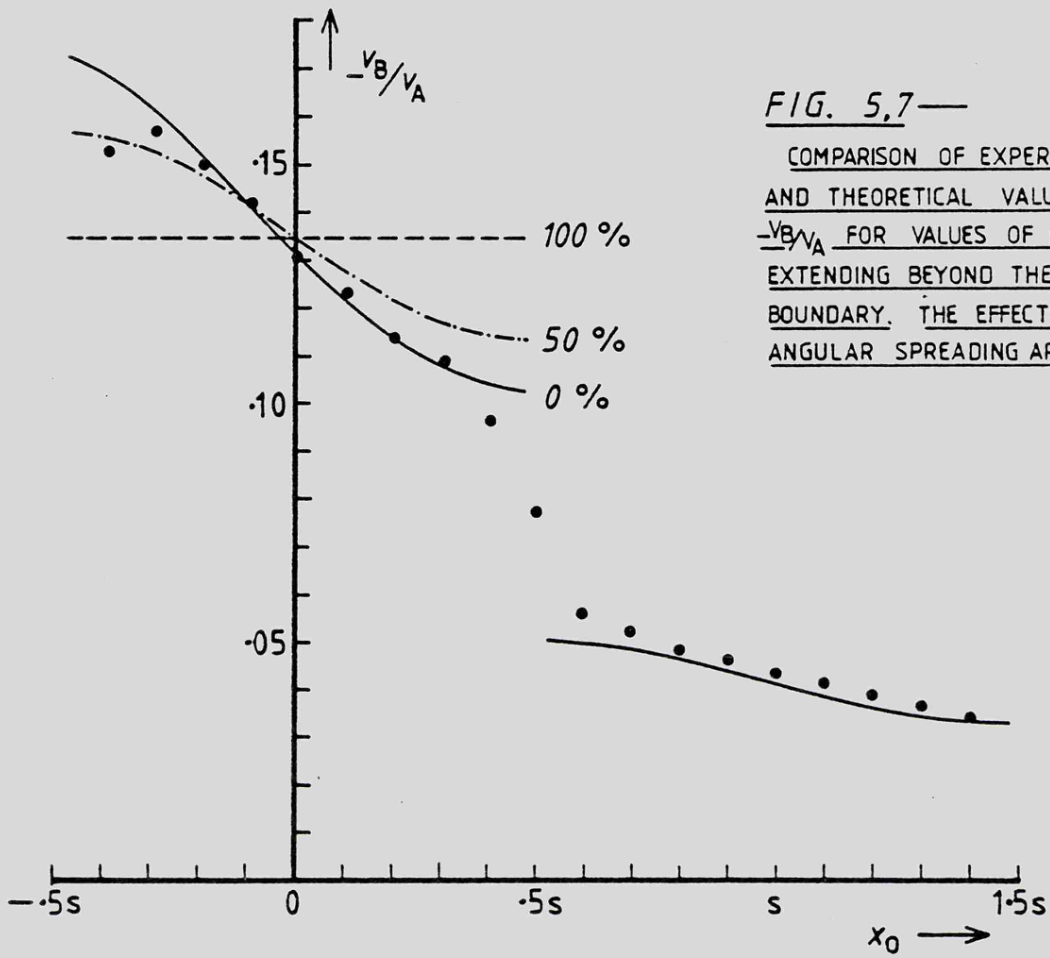
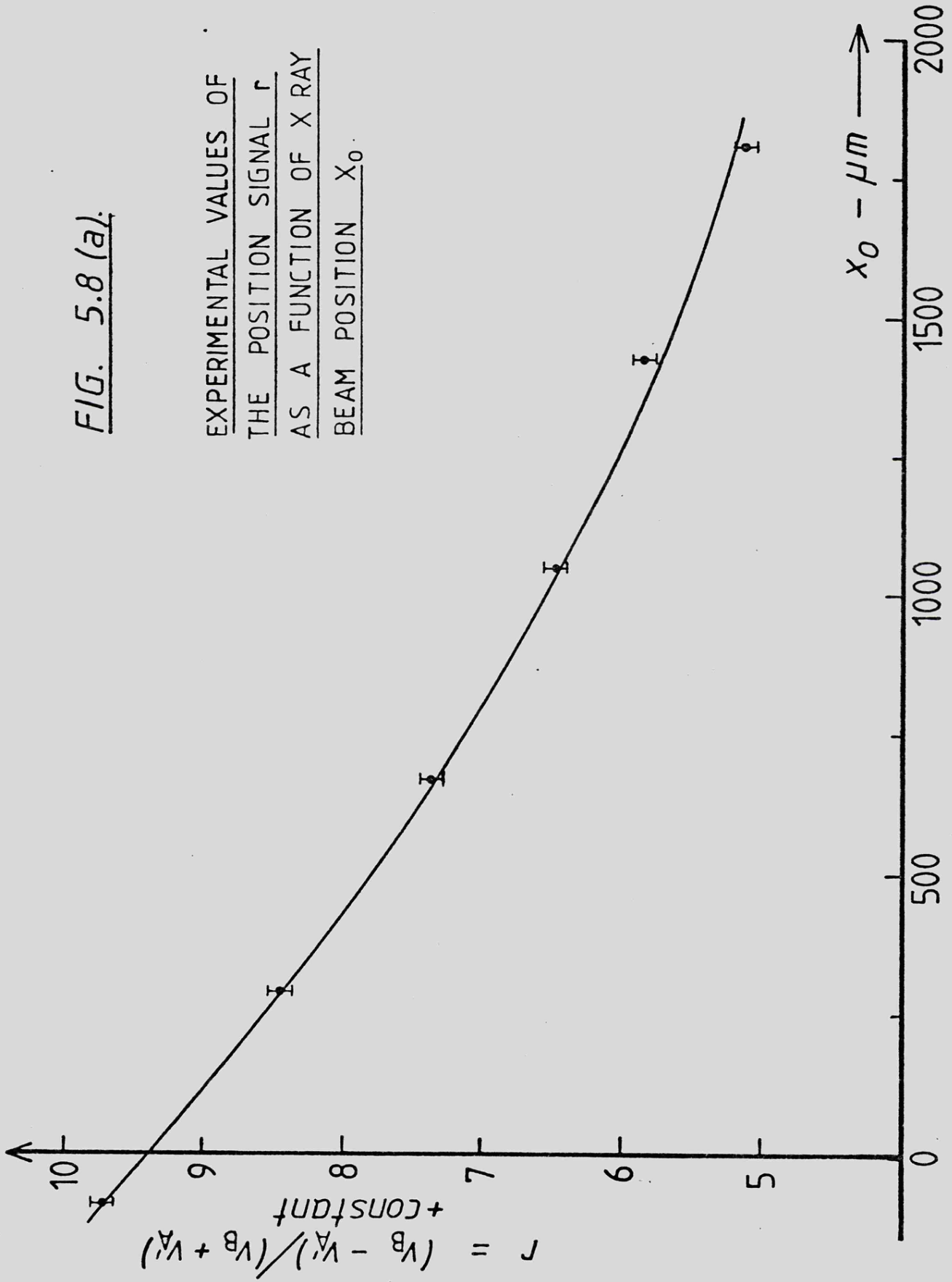


FIG. 5.7—

COMPARISON OF EXPERIMENTAL  
AND THEORETICAL VALUES FOR  
 $-v_B/v_A$  FOR VALUES OF  $x_0$   
EXTENDING BEYOND THE CELL  
BOUNDARY. THE EFFECTS OF  
ANGULAR SPREADING ARE SHOWN.

FIG. 5.8 (a).

EXPERIMENTAL VALUES OF  
THE POSITION SIGNAL  $r$   
AS A FUNCTION OF X RAY  
BEAM POSITION  $x_0$ .



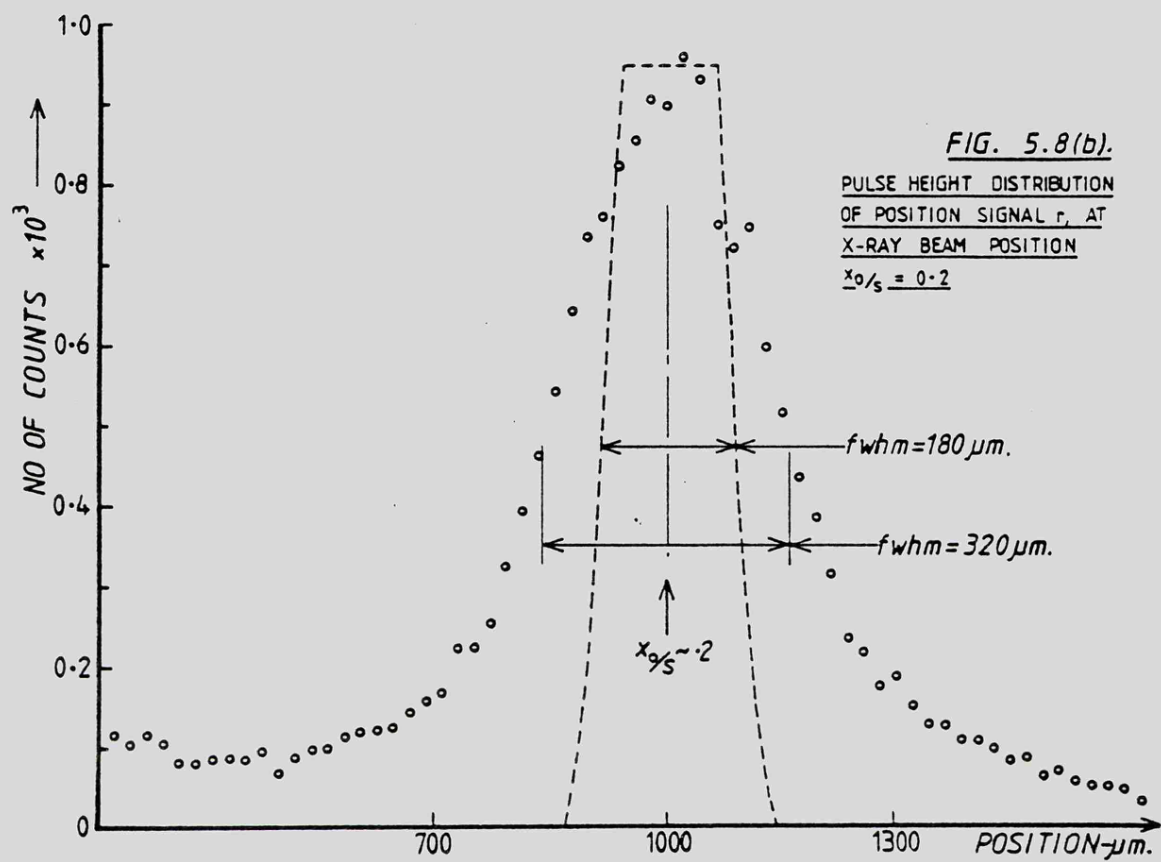
if the instrument is to be considered for use as a position sensitive detector. This may be obtained from the pulse height distribution of the position signal  $r$ , shown in Fig. 5.8(b) for an X-ray beam position  $x_0/s = .2$ . The theoretical contribution due to the collimator has been computed (see Appendix 1) for the collimator situation given in section 4.4 and assuming a mean-free-path for absorption of 5.9keV X-rays in argon/10% methane of 2.3 cm. This contribution is shown superimposed on the pulse height distribution, but for ease of illustration, the two curves are not normalised in area.

The full-width at half-maximum of the positive signal is  $320\mu\text{m}$ , the calibration for the x-axis being taken from the experimental measurements of the centroid of  $r$  (section 5.6). There are several contributions to this resolution. Firstly, the fwhm of the collimator distribution is  $180\mu\text{m}$ . Secondly, by replacing the chamber anode signals by precision pulses, the electronic noise contribution was measured as  $60\mu\text{m}$  fwhm. The remaining contribution  $260\mu\text{m}$  must be comprised of other factors within the chamber, one of which is probably angular jitter in the centroid of the electron cloud arriving at the anode, due to statistical fluctuations in the shape of the initial 200 electron group. Another factor must be due to initial absorption in the central non-linear region of the chamber (section 5.9).

By regarding field imperfections, statistical jitter and to some extent, the electronic noise, as being fundamental and unavoidable, but considering the collimator distribution to be due to the experimental method, a resulting spread of  $264\mu\text{m}$  fwhm is potentially achievable, which in terms of wire spacing  $s$ , amounts to an rms resolution better than  $s/40$ .

### 5.8 Increased Gas Gain

Proportional counters and chambers become non-proportional when

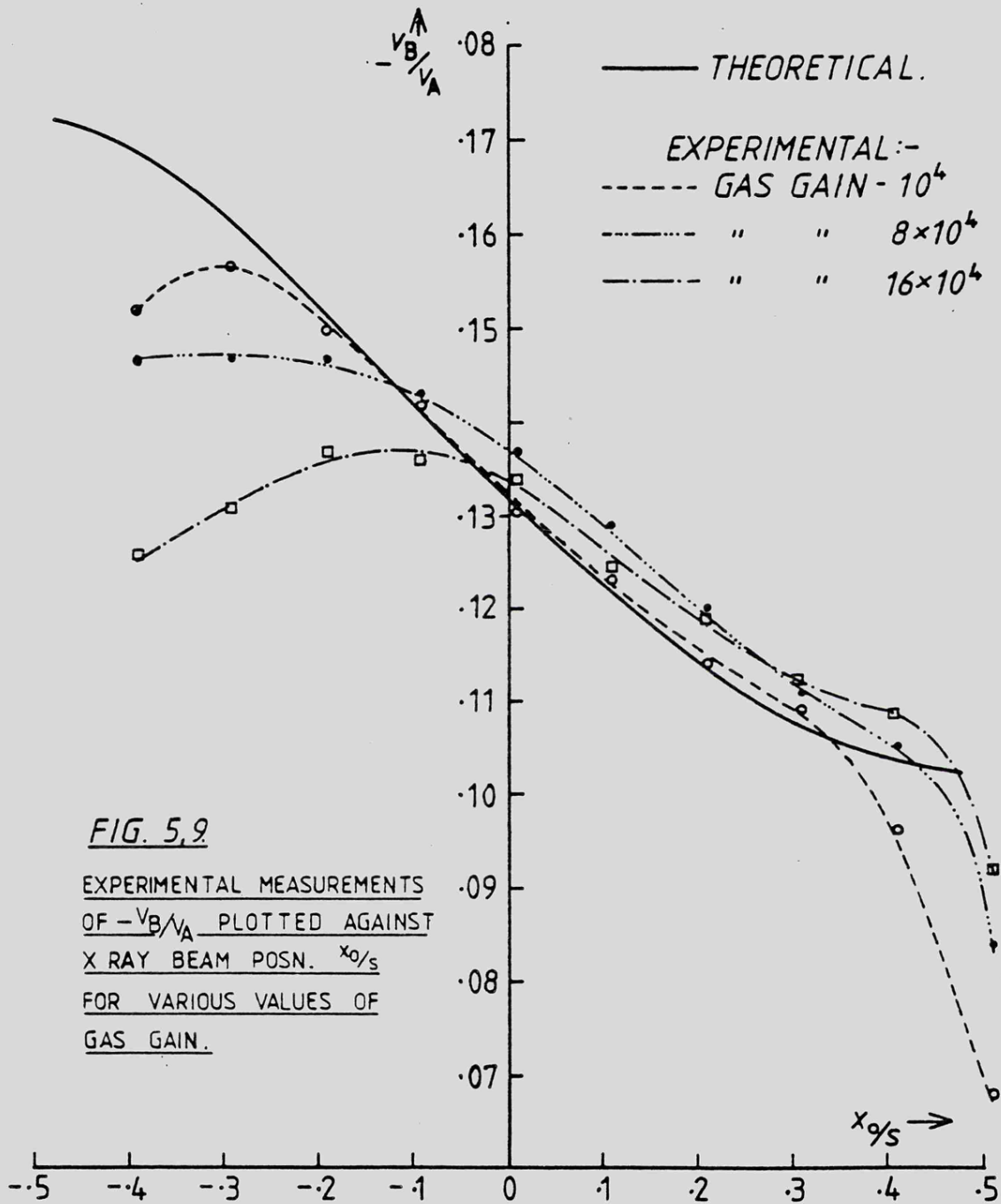


the gas gain is increased to such a point that high concentrations of positive ions in the multiplication region seriously reduce the local field and modify the field distribution. The expected result of this is a defocussing action upon the electron group causing it to spread around the anode. This is in contrast to the normal situation in a proportional chamber where the change from linear to coaxial field near the anode plane introduces a strong focussing action. Further spreading around the anode may be due to the increased production of ultra-violet photons<sup>(63)</sup>, which, unaffected by the field, will broaden the avalanche. The effect of increasing the gas gain upon the localised avalanche has been examined experimentally and is shown in Fig. 5.9 where  $-v_B/v_A$  is plotted against the beam position of the 6keV source for three values of gas gain,  $10^4$ ,  $8 \times 10^4$ , and  $16 \times 10^4$ . The latter of these is well beyond the saturation region (see Fig. 5.3). The gradual levelling-off of the curves is noticeable as the gain is increased and comparison with the theoretical curves for various assumed rectangular distributions around the anode wires (Fig. 3.3), indicates a spread of between 50% and 100% at the highest gain. The persistence of the localisation phenomenon, however, is indeed surprising.

### 5.9 Discussion

The measurements presented so far have shown to some extent the degree of angular localisation which can be achieved providing the gas gain is within normal operating regions. The results agree remarkably well with theory, but although it is clear that spread is between 0% and 50% of the anode wire circumference and is probably nearer to 0%, it is difficult to draw any further conclusions at this stage. Nevertheless, useful positional information can be obtained over at least 70% of the cell width by using the position signal  $r$ .

The results have been taken with a system shaping network of



10 $\mu$ s differentiating and 10 $\mu$ s integrating time constants. Similarly, good agreement with theory exists at other time constants in the range 0.5 to 50 $\mu$ s but in the interest of space, these are not presented here. It is noticeable however that the slope of  $-v_B/v_A$  increases rapidly with time constant, but appreciable assymetry occurs above 10 $\mu$ s.

It is convenient that with typical low noise charge sensitive preamplifiers with uncooled single field-effect transistor front-ends, and 10<sup>8</sup> $\Omega$  detector bias resistors, the noise minimum occurs at about 10 $\mu$ s time constant. This is shown in Fig. 5.10 where the theoretical amplifier noise performance curves of Smith and Cline<sup>(64)</sup> are reproduced. (The noise contribution of a 10<sup>8</sup> $\Omega$  bias resistor has been superimposed). A choice of time constant of 10 $\mu$ s for the present system with 10<sup>8</sup> $\Omega$  bias resistors is therefore near optimum.

Probably the greatest limitation of the chamber, which has not so far been mentioned and is not accounted for in the theory, is the increased spreading of the avalanche which will occur when absorption takes place near the anode plane. The simple theoretical model assumes that X-rays are all absorbed close to the upper or lower cathodes, where the stream lines are running parallel to one another. Positional information will however be degraded when absorption occurs in the non-linear region of the chamber. Fig. 5.11 shows the equipotential pattern near the centre of the present chamber and the non-linearity is becoming quite marked below  $y/s \sim .3$ . The non-linear central region therefore occupies  $\sim 15\%$  of the chamber depth. The non-linear region is only slightly affected by the anode radius ( $r_a/s$ ) but its depth could be made much less significant by increasing the ratio of chamber depth to anode wire spacing  $h/s$ . For an absorption mean-free path  $\mu \gg d$  (the chamber depth) the 15% non-linear region also represents the percentage of events occurring in this region, but this percentage may be

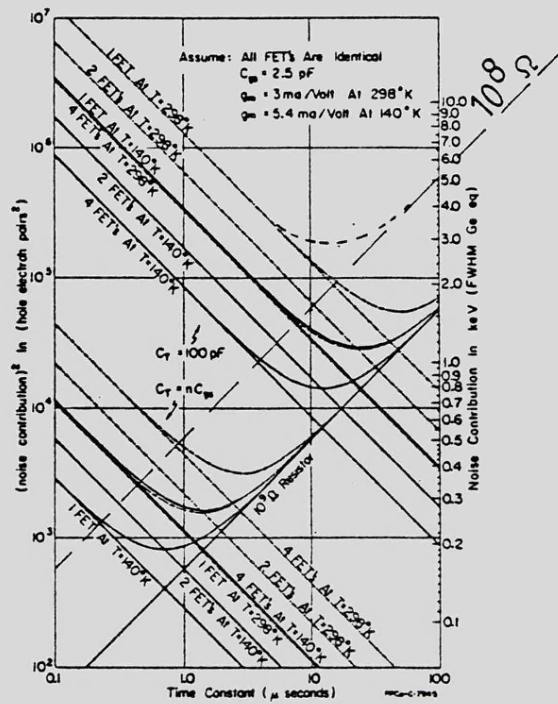


FIG 5-10

THEORETICAL PREAMPLIFIER NOISE  
VS. TIME-CONSTANT CHARACTERISTICS  
FOR EQUAL SINGLE DIFFERENTIATING  
AND INTEGRATING TIME-CONSTANTS

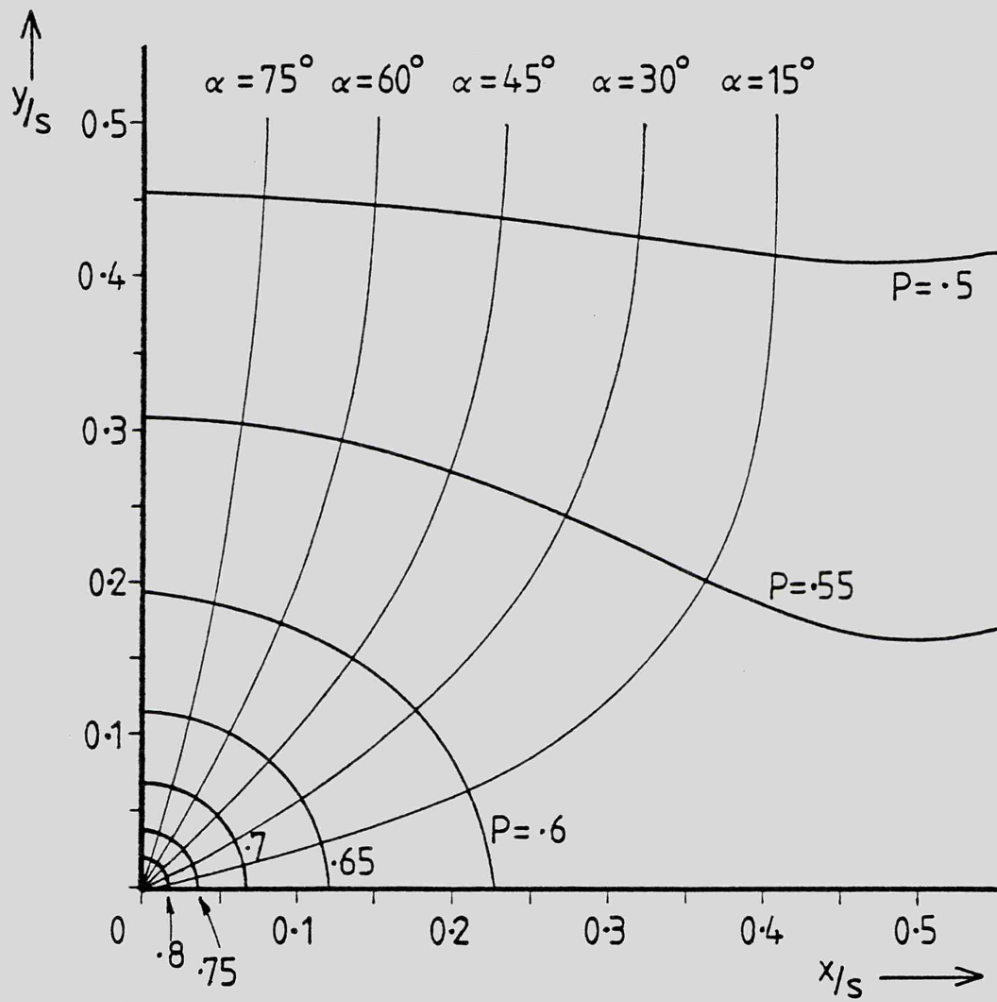


FIG. 5,11 — FIELD PATTERN NEAR THE  
CENTRE OF THE CHAMBER  
 $h/s = 2.22$        $r_0/s = 2.5 \cdot 10^{-3}$

reduced by using low energy radiation of shorter mean-free-path where almost total absorption takes place above the non-linear region.

Experimental attempts to avoid the non-linear region by using the aluminium source (1.5keV) to encourage absorption near the upper cathode have shown little improvement, presumably because electron overspill tends to overshadow the effect, particularly between  $x/s = .3$  and  $x/s \approx .5$ .

The curves of  $-v_B/v_A$  depart from the theoretical curve at  $x_0 = .4s$  (=2 mm.) by about 10% and this would correspond to a mean overspill of 2 electrons into the neighbouring cell. Since there are some 200 electrons in the initial cloud, this gives an indication that the diameter of the cloud, just before it is deflected inwards by the field lines, is about 1mm.

It is useful now to obtain some estimate of the radius of the diffused electron group at  $y = .4s$  (= 2 mm.) after it has travelled 9 mm. under the influence of a linear field  $E$  V/cm.

From Fig. 5.11  $E = (.5 \times 2500)/.9 = 1388$  V/cm.

According to Einstein's formula<sup>(33)</sup>, the rms radius of an electron group  $\sigma_x$ , having started as a point source and travelled a distance  $d$  cm. through a uniform field  $E$ .V/cm. with a drift velocity  $W$  cm/s, is given by

$$\sigma_x = (2 D \tau)^{1/2}$$

where  $\tau = \frac{d}{W} = \frac{d}{\mu E}$  s.,

$D$  is the diffusion coefficient,

and  $\mu$  is the electron mobility.

may be written in terms of the 'characteristic energy'  $\epsilon_k$  :

$$\sigma_x = (2 D/\mu \cdot d/E)^{1/2} \text{ cm.},$$

where

$$\epsilon_k = D/\mu.$$

Inserting actual values,  $E = 1388 \text{ V/cm.}$ ,  $d = .9 \text{ cm.}$

$$\epsilon_K \approx 2.4\text{eV at } 1.83\text{Vcm}^{-1}\text{ torr}^{-1}$$

(determined theoretically<sup>(51)</sup> for A/10%CH<sub>4</sub> )

The rms radius, therefore, after transverse diffusion is ,

$$\underline{\sigma_x \approx .5\text{mm.}}$$

CHAPTER 6THE INDUCED CATHODE PULSE - EXPERIMENTAL RESULTS IN P106.1 Experimental Conditions

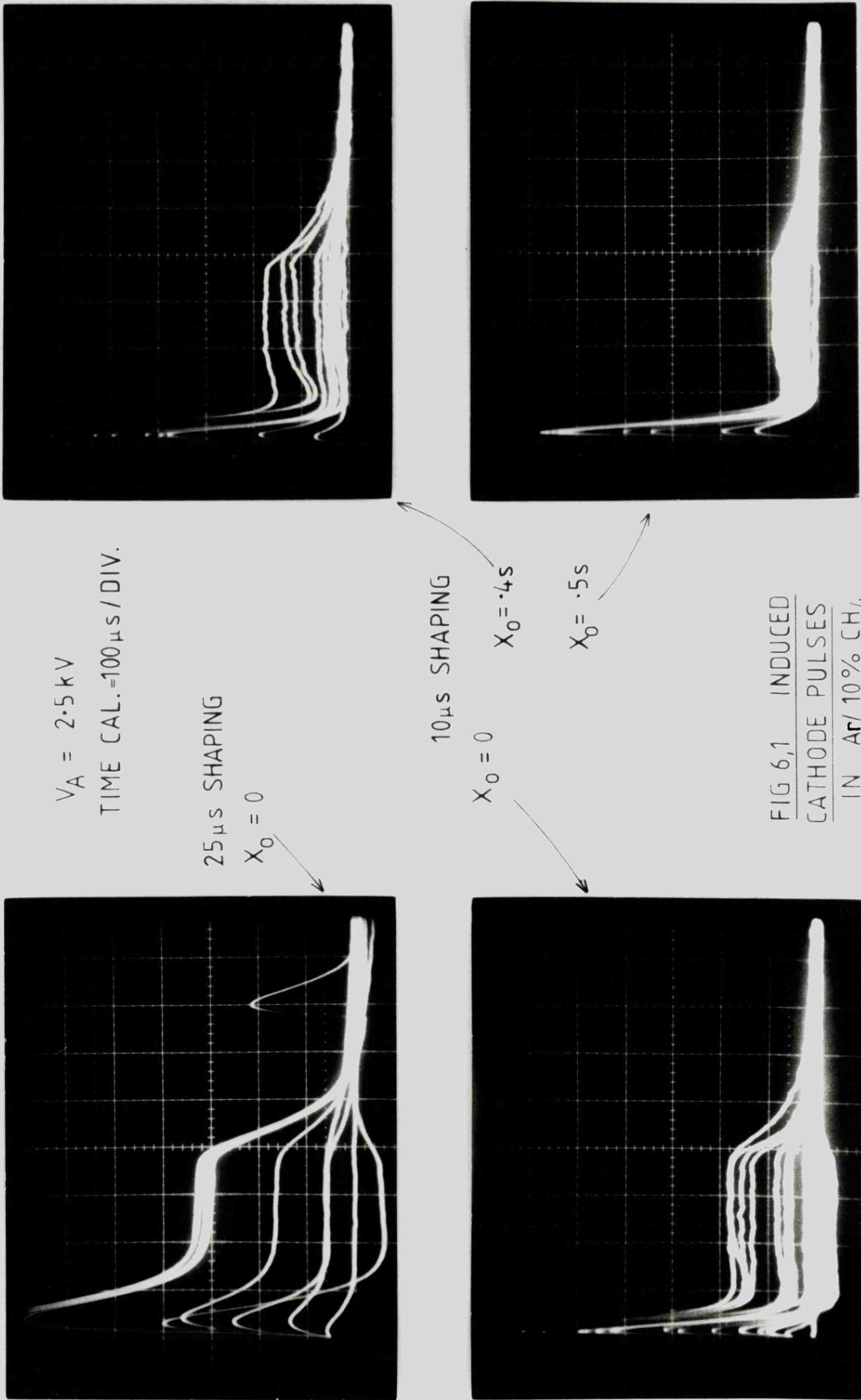
The chamber geometry for these experiments remained the same as that described in section 5.1, but the electrical configuration was modified to that described in section 4.2.2(b). The flow gas was argon/10% methane at atmospheric pressure and room temperature. Measurements were taken with the .004" slit collimator.

6.2 Cathode Pulse Shapes

It would be expected from the isometric plots of section 3.7, that induced cathode pulses would be similar in shape to the induced anode pulses. Here the extensive linear field region results in a pulse shape, after differentiation, having a region of constant amplitude, which remains until the positive ions are finally collected at the cathodes. The photographs of Fig. 6.1 show that this is indeed so, but rather more information is revealed about the half of the chamber in which initial absorption takes place.

Considering first the upper half of the chamber, and considering only those events which occur at  $x_0 = 0$ , it can be seen from Fig. 3.5 that after the initial fast rise in P the gradient quickly reduces to a constant positive value. Conversely, in the lower half of the chamber, although the initial gradient is much the same, this quickly reduces to a constant negative value. The effect is shown clearly in the photographs where pulses due to events in the lower half of the chamber actually pass through zero as the gradient goes negative.

Similar results at  $x_0 = 0$  and  $T = 25\mu s$ . are also shown in Fig. 6.1, but it is interesting to note the pulse shape, as  $x_0$  is



increased to .5. The effect of the more devious positive ion route is indicated in the plateau region, which is no longer constant. This is an extreme condition where the positive ions spend some time travelling almost parallel to the cathodes before turning directly towards them.

When the photographs of Fig. 6.1 were taken, the source of radiation was  $^{55}\text{Fe}$ , but by using the Al-K source it is possible to observe the effects of unilateral absorption. The photo. of Fig. 6.2(a) shows pulses from the bottom cathode after  $25\mu\text{s}$  shaping with the Al-K source irradiating the top of the chamber at  $x_0 = 0$ . The pulses are solely due to positive ions moving away from the bottom cathode.

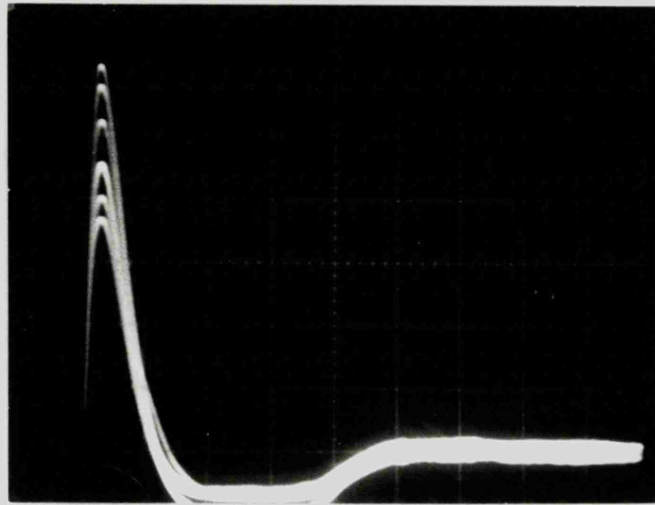
Fig. 6.2(b) shows two simultaneously occurring pulses from the top and bottom cathodes after  $10\mu\text{s}$  shaping, for an event occurring in the upper half of the chamber. The photograph was taken whilst the  $^{55}\text{Fe}$  source was situated above the central anode.

### 6.3 Spectra of Cathode Pulse Heights

The photographs of Fig. 6.2(b) shows that for each chamber event two different induced cathode signals are generated. The signal in the top cathode channel has a different pulse height and pulse shape from that in the lower cathode channel, and this difference depends upon the chamber depth at which initial absorption takes place. The pulse height spectrum from each cathode therefore can be expected to show two peaks, which are farthest apart when the X-ray source is located above the avalanche anode, A. Under this condition the positive ion drift path is either directly towards the sensing cathode, if absorption occurs above the anode, or vice versa. The peaks should also draw closer together as the source approaches the mid-position between anodes. Under these conditions, the early part of the induced pulse is due to positive ion motion close to the x-axis, which therefore has a similar influence

$V_A = 2.7 \text{ kV}$ 

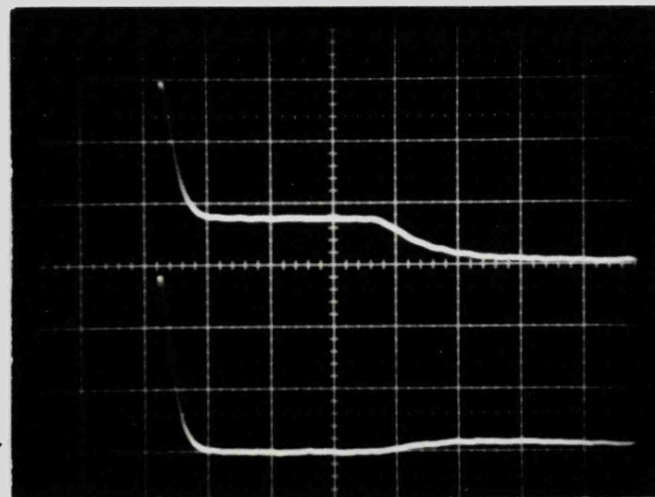
SOURCE - Al-K

LOWER  
CATHODE

(a)

TIME CAL. — 100  $\mu\text{s}$  / DIV
 $V_A = 2.5 \text{ kV}$ 

SOURCE - Fe55

UPPER  
CATHODE →LOWER  
CATHODE →

(b)

FIG 6,2 - INDUCED CATHODE PULSES SHOWING EFFECTS OF UNILATERAL ABSORPTION

upon both cathodes.

Fig. 6.3 is a reproduction of the pulse height spectrum taken from the top cathode channel, with the  $^{55}\text{Fe}$  source situated above A. The two photopeaks are clearly distinguishable, and each has an accompanying escape peak which is to some extent camouflaged by the background continuum. The lower amplitude photopeak, due to events in the lower half chamber, contains about  $1/1.58$  of the counts in the upper photopeak, which is consistent with a ratio of  $1/1.6$  calculated from the ratio of X-ray intensities,  $I_y/I_0 = e^{-\lambda y}$ , for a linear absorption coefficient  $\lambda = 1/2.3 \text{ cm.}^{-1}$ . Each of these photopeaks with its associated escape peak, of course, represents the energy spectrum that one would normally find when observing anode pulses. The photopeak resolution measured as 19%, is almost the same as that from the anodes.

Fig. 6.4 shows the pulse height spectrum taken from the lower cathode under the same conditions as for Fig. 6.3. Here the lower amplitude peak is due to events in the upper chamber and therefore contains the larger number of counts.

As the beam position was increased towards  $x_0/s = .5$ , the photopeaks blended together. In Fig. 6.5, taken at  $x_0/s = .3$ , it became apparent that the spatial resolution was inadequate, but by taking the ratio  $v_c/v_c'$ , energy dependent terms were cancelled out and a much improved spatial resolution was achieved. This is evident at  $x_0 = .4s$  in Fig. 6.6 where the two distributions are still quite separate. In Fig. 6.6, although some broadening of the distributions of  $v_c/v_c'$  is occurring at  $x_0 = .4s$  (and this increases further towards  $.5s$ ), it should be noted that 180 channels have been offset and the peaks are actually extremely sharp. At  $x_0 = 0$ , the resolution is around 3% fwhm and this degrades to 5% fwhm at  $x_0 = .4s$ . Projecting this distribution width on to Fig. 6.7 (discussed below), an equivalent spread at  $x_0 = .4s$

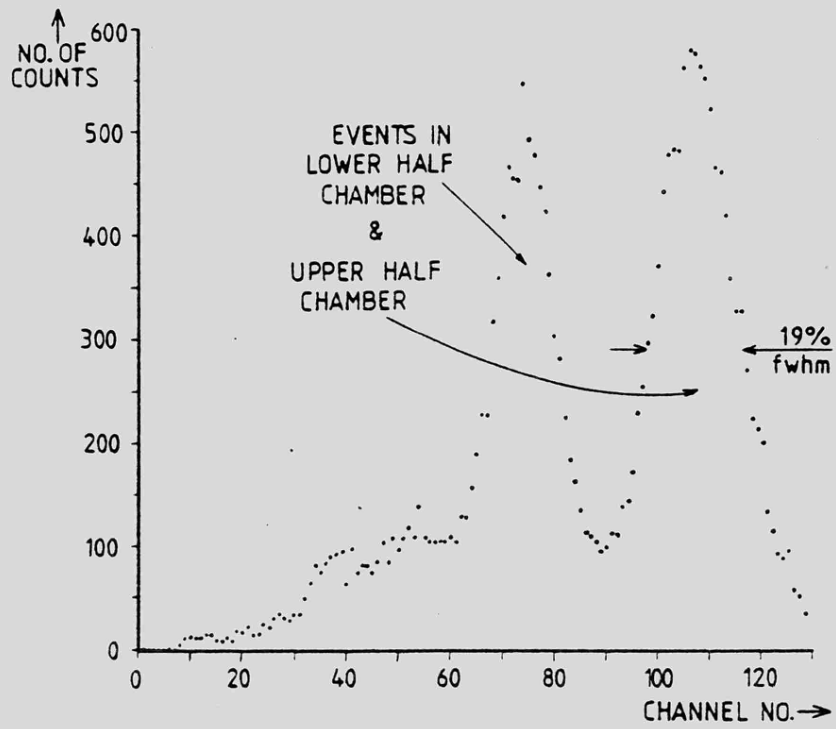


FIG 6.3 — PULSE HEIGHT SPECTRUM FROM  
UPPER CATHODE —  $x\alpha_s = 0$

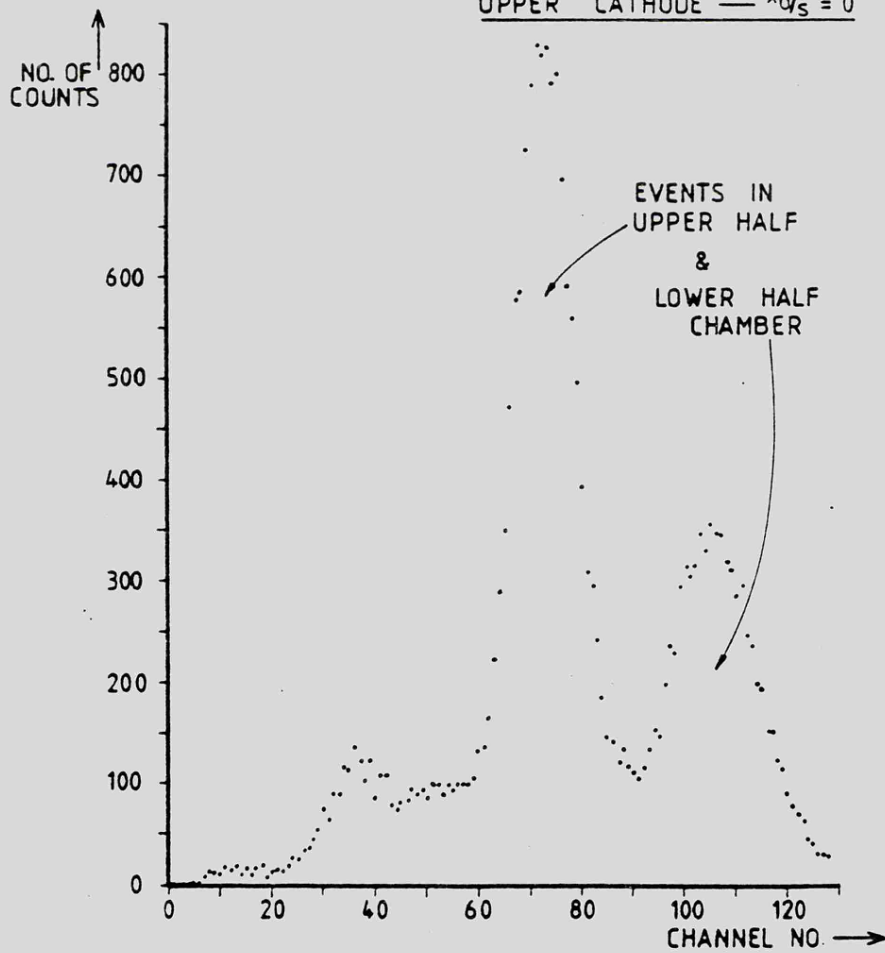


FIG 6.4 — PULSE-HEIGHT SPECTRUM FROM  
LOWER CATHODE —  $x\alpha_s = 0$

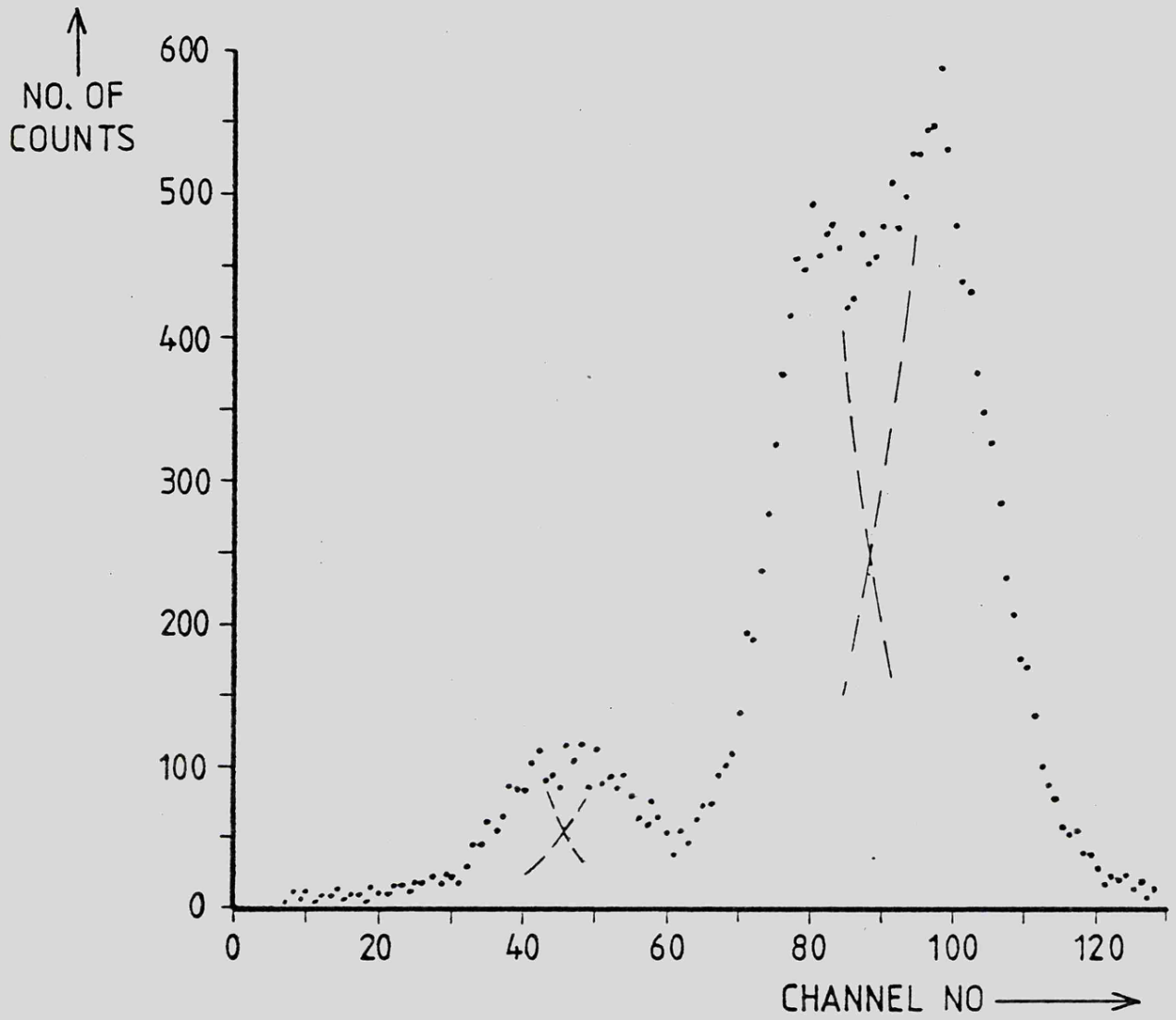


FIG 6,5 — PULSE HEIGHT SPECTRUM FROM  
UPPER CATHODE —  $x_0/s = 0.3$

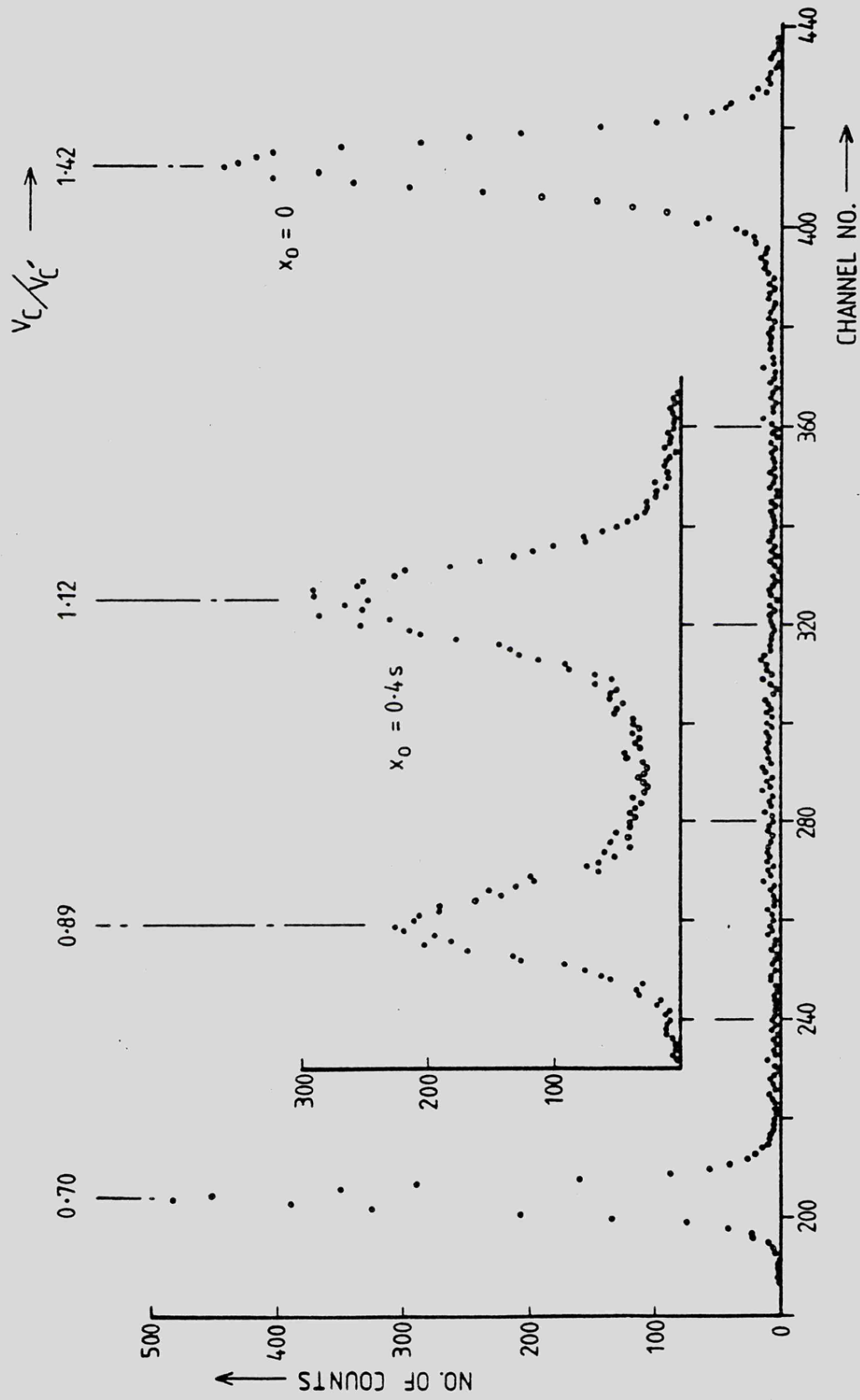


FIG. 6,6 — SPECTRA OF THE RATIO OF CATHODE SIGNALS  $-V_C/V_C'$

of .06s fwhm is obtained which in non-normalised terms is 300 $\mu$ m fwhm or 127 $\mu$ m rms.

In practice simply taking the ratio  $v_c/v_c'$  did not account for mismatching in the signal processing system, and although well matched preamplifiers ( $\sim 1\%$ ) were used, any mismatch was eliminated by reversing the cathode connections to the preamplifiers. This produced two ratios R and R'. Thus at the output of the charge preamplifiers with feedback capacitors  $C_1$  and  $C_2$ ,  $R = (q_1/C_1)/(q_2/C_2)$  and  $R' = (q_2/C_1)/(q_1/C_2)$ . The ratio  $q_1/q_2$  was then calculated as  $\sqrt{R/R'}$ , independent of the electronic system gains.

#### 6.4 Traversing the Chamber

The theoretical predictions of chapter 3 for cathode pulse ratios are again reproduced in Fig. 6.7 for three values of standard deviation of an assumed Gaussian positive ion distribution. They are compared here with the experimental results for  $v_c/v_c'$  obtained as the source was moved across the centre anode cell. The experimental points taken with an  $^{55}\text{Fe}$  source, lie quite accurately along the curve representing  $\sigma_\alpha = 33^\circ$ , except beyond  $x_0/s = .4$  where the divergence between the experimental and theoretical curves becomes apparent.

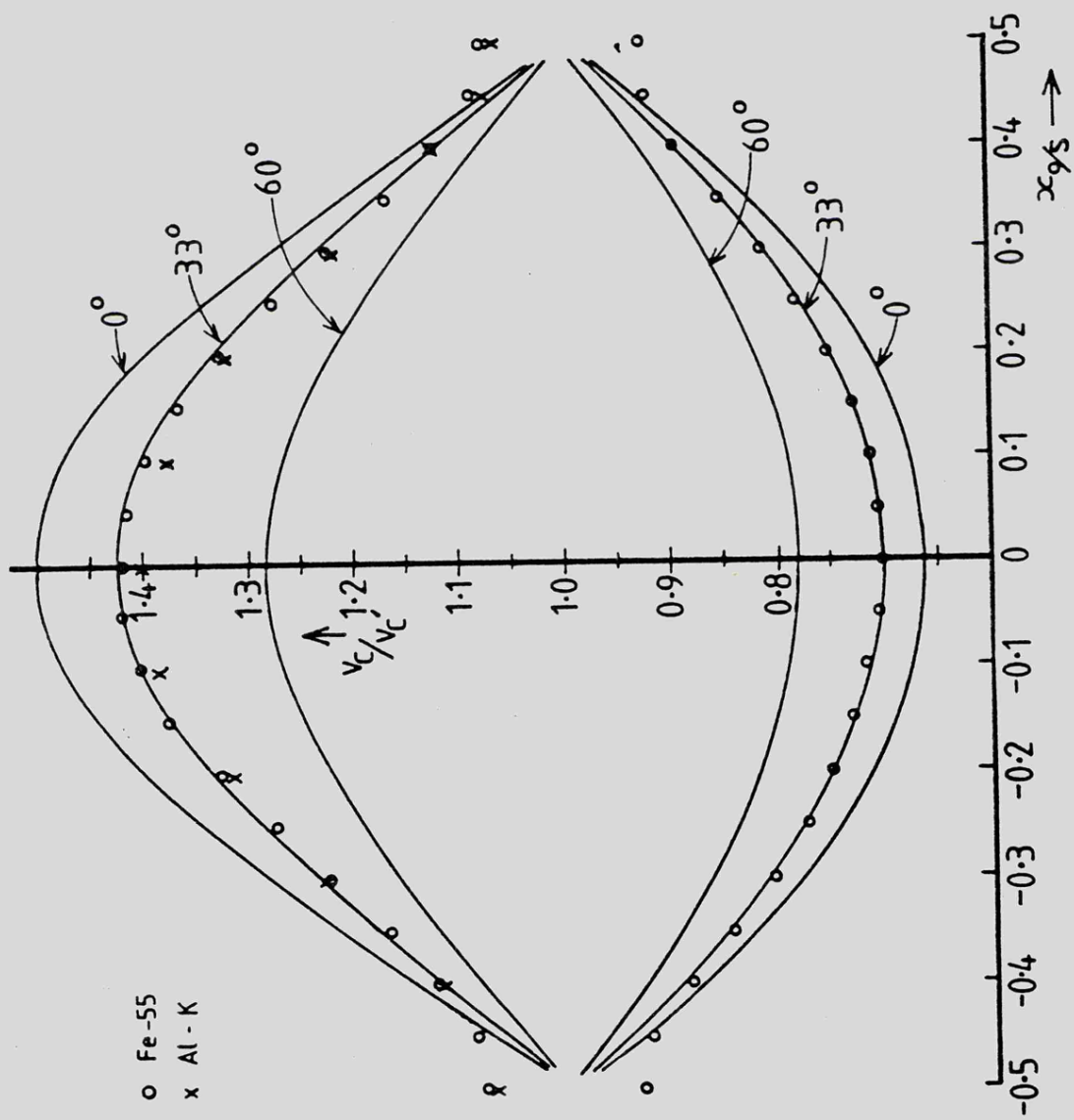
Theoretical predictions are also compared with experimental results in Fig. 6.8 for 25 $\mu$ s shaping. The experimental points no longer quite fit the curve for  $\sigma_\alpha = 33^\circ$ , but would suggest that a slightly greater angular spread was occurring. Since conditions within the chamber had not changed, it is more likely that there is a time dependent parameter, namely the positive ion mobility  $\mu$ , which has not been accounted for in the calculations.

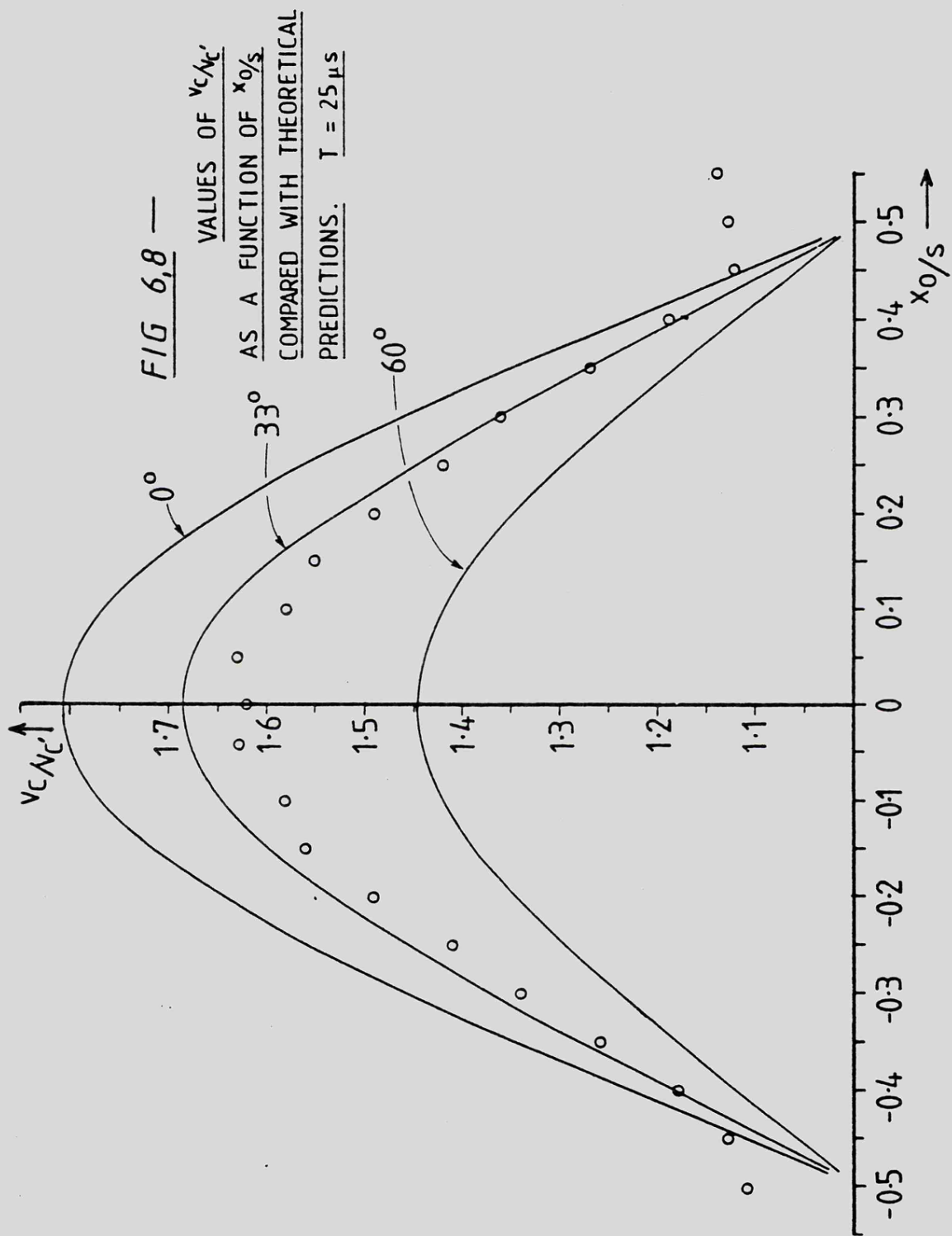
### 6.5 Discussion

#### 6.5.1 Experimental limitations

It is unfortunate, but not surprising, that experiment and

FIG 6.7 —  
 VALUES OF  $V_c/V_c'$   
 AS A FUNCTION OF  $x_0/s$   
 COMPARED WITH THEORETICAL  
 PREDICTIONS.  $T = 10 \mu s$





theory fail to agree in the region  $.4 < x_0/s < .5$ . In fact agreement is rather better than was anticipated from the work with induced anode pulses, and the problems associated with electron loss into the neighbouring cell do not arise here. For this reason, it is perhaps easier to utilize information from the cathodes, where polarity reversal does not occur and signals are about three times larger than corresponding induced anode signals, but an important limitation would be the lack of sensitivity of  $v_c/v_c'$  in the region  $x_0/s = 0$ .

The departure from theoretical predictions near  $x_0/s = .5$  is now more fully accounted for mainly in terms of electron diffusion and collimator beam width. For the condition  $v_c/v_c' = 1$  to be realised, it is necessary for the positive ion cloud to travel precisely along the rectangular field line ( $\alpha = 0^\circ$ ) which follows the x-axis before turning towards the cathode at  $x_0/s = .5$ . From previous estimates (chapter 5) it is found that the rms sum of noise, initial photoelectron range, and collimator beam width may be neglected in comparison with the diffusion contribution which amounts to .5 mm. rms.

Normally, since the position of the centroid of the distribution  $v_c/v_c'$  is recorded, any angular jitter due to the above effects will be accounted for in the width of the distribution and will not affect the centroid position, but near  $x_0/s = .5$  an imbalance will occur because field lines do not cross the x-axis. The x-axis then sharply intercepts the diffused cloud and distortion may be expected when the extent of angular jitter reaches the  $\alpha = 0^\circ$  field line, i.e. beyond  $x_0 = .4s = 2$  mm.

The above argument that diffusion is mainly responsible for the distortion near  $x_0 = .5s$ , is further supported by comparing the results with the aluminium source, where absorption takes place near the upper window and the collimator beam width is accordingly reduced. The results are much the same as for  $^{55}\text{Fe}$  and can be seen in Fig. 6.7

### 6.5.2 The choice of mobility value

The main purpose of repeating the cathode pulse ratio measurements at 25 $\mu$ s shaping, was to examine the constancy of the positive ion mobility. It is normal<sup>(66)</sup> for the rare gas positive ions in their parent gas to move with almost constant mobility. In fact, over the range of field strengths normally encountered in proportional chambers, one would expect the mobility to increase slightly as the ions move towards the lower field region, but certainly by not more than 20%. However this is not reflected in the results which show a tendency for  $\mu$  to reduce slightly rather than increase. From the experiment, it can be deduced that the mobility remains nearly constant with no indication of charge exchange, at least up to the time-to-maximum of the 25 $\mu$ s shaped cathode pulse (i.e. theoretically 36 $\mu$ s). In practice the times-to-maximum of the induced pulses are in reasonably good agreement with theory (Fig. 6.9), which is further evidence that  $\mu = 1.6\text{cm}^2/\text{Vs}$  is a suitable choice for mobility.

### 6.5.3 The angular spread

It is possible, from the assessment of diffusion (.5 mm. rms) to obtain a rather crude estimate of the angular spread. The standard deviation of the angular distribution  $\sigma_{\alpha}$  may be obtained from the relationship  $\alpha = \pi/2 (1 - 2x_0/S)$  given in chapter 3 (Eqn. 13). Thus  $\sigma_{\alpha} = 18^{\circ}$ . This is in disagreement with value of  $\sigma_{\alpha}$  obtained by curve fitting in Fig. 6.7 and Fig. 6.8 and the suggestion is that other contributing factors have not been identified, one of which could well be additional spread during the avalanche process. A further explanation could be that, contrary to the above argument, the choice of  $\mu = 1.6\text{cm}^2/\text{Vs}$  is inaccurate, but this is not likely;  $\mu$  would have to be reduced to near  $1.3\text{cm}^2/\text{Vs}$  to account for such an anomaly.

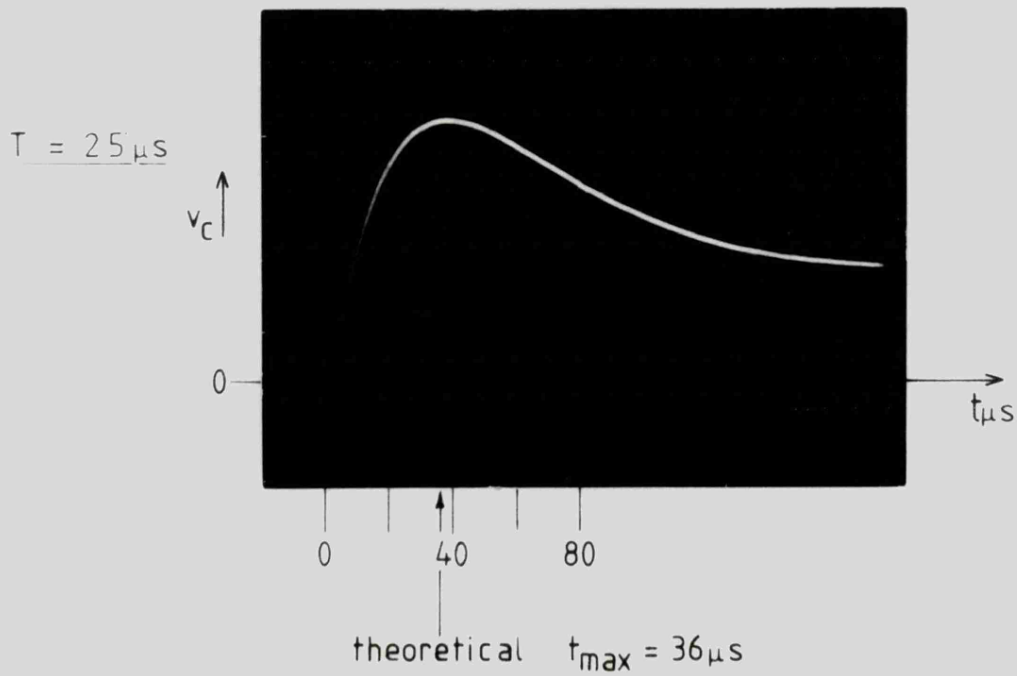
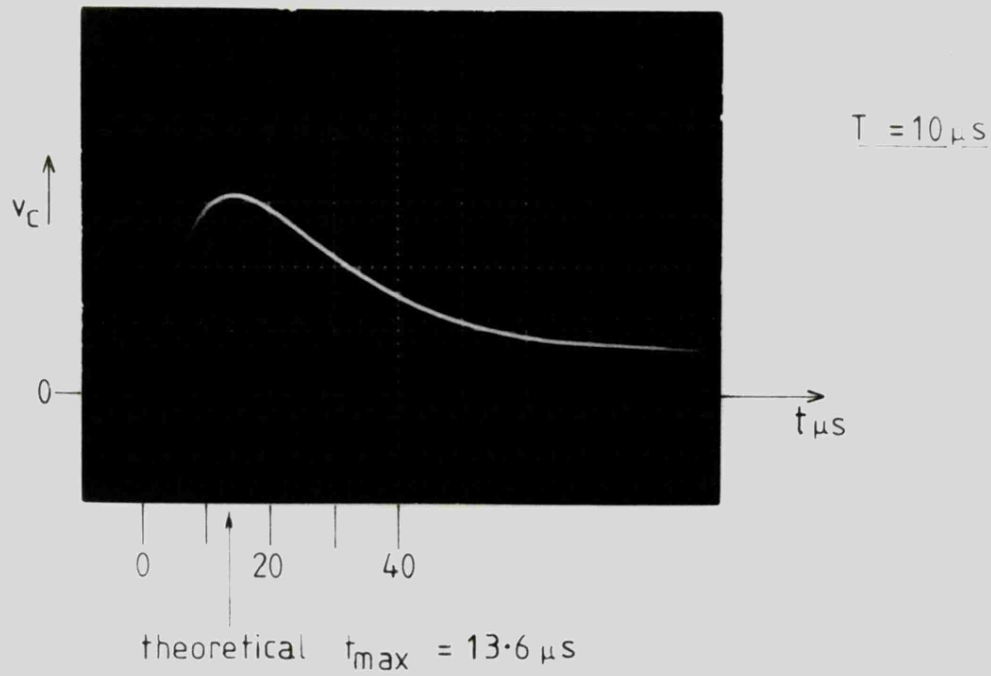


FIG 6,9—

INDIVIDUAL CATHODE PULSES TAKEN FROM THE TOP CATHODE, AFTER SHAPING, FOR AN EVENT IN THE UPPER HALF CHAMBER.

#### 6.5.4 Resolution

It is fortunate that the position resolving capability of the method is hardly limited by diffusion, because the cathodes sense the centre of charge and provided that diffusion gives rise to a symmetrical spread at the anode, this does not greatly affect the induced pulses at the cathodes. Diffusion, however does affect the slope of the ratio  $v_c/v_c'$  but the spread in this ratio of  $127\mu\text{m}$  rms, determined in section 6.4, must be due to those effects which actually affect the position of initial absorption, such as the mean photoelectron range (discussed in section 5.4), and the spread due to the collimator ( $\sim 76\mu\text{m}$ . rms). The effects of amplifier noise and other electronic imperfections are also partly responsible.

CHAPTER 7EXPERIMENTAL RESULTS IN OTHER GASES7.1 Introduction - Choice of Gas Mixtures

It was considered that much useful information could be obtained by applying this study of induced charges to proportional chambers filled with less common gas mixtures than P10. The choice of gases was, however, partly limited by the technique of flowing the gas, and the cost involved. On this basis xenon, costing several pounds per litre was completely ruled out, only to be used in sealed systems, but neon mixtures, costing about one pound per five litres were considered a possibility provided that due care was taken to avoid excessive usage. Krypton, also fairly expensive, nowadays suffers the added disadvantage of being intrinsically radioactive and is troublesome in low count rate systems where a low background count is important. Since time and space further impose limitations on the number of gas mixtures to be studied, it was decided to consider just two rare gases, argon and neon, with admixtures of methane and carbon dioxide.

Neon being a much lighter gas than argon, is inefficient in this depth of chamber ( $\sim 2$  cm.) for the detection of 6keV radiation, but is quite suitable as a detection medium for the 1.5keV X-radiation of the aluminium source. Combinations of 90% Ne with 10% CH<sub>4</sub> and also with 10% CO<sub>2</sub> were studied and also 90% Ar with 10% CO<sub>2</sub> to complement previously reported studies with 90% Ar 10% CH<sub>4</sub>.

The amount of diffusion in the noble gases is known to reduce considerably with the addition of polyatomic impurities, and as diffusion has been the subject of some discussion in previous chapters and clearly represents a major limitation in the behaviour of proportional chambers,

a mixture of argon and 75% methane has also been studied.

For convenience the linear absorption coefficient has been calculated from mass absorption coefficient data<sup>(70)</sup> at the two energies of X-radiation and these are shown with the mean-free-path for absorption in Table 7.1.

TABLE 7.1

X-ray energy	1.5keV		6keV	
	ABSORPTION COEFFICIENT cm <sup>-1</sup>	MEAN-FREE- PATH cm.	ABSORPTION COEFFICIENT cm. <sup>-1</sup>	MEAN-FREE PATH cm.
Ar/CH <sub>4</sub> 90/10	1.74	.6	.434	2.3
Ar/CH <sub>4</sub> 25/75	.66	1.52	.073	13.8
Ar/CO <sub>2</sub> 90/10	2.01	.498	.44	2.27
Ne/CH <sub>4</sub> 90/10	2.19	.456	.044	22.7
Ne/CO <sub>2</sub> 90/10	2.57	.388	.051	19.6

The measurements are presented mostly in diagrammatical form and are divided into two categories:

7.2 Induced anode signals.

7.4 Induced cathode signals.

The results will be only briefly described in these sections and will be discussed respectively in sections 7.3 and 7.5.

## 7.2 Induced Anode Signals.

### 7.2.1 Measurements in Ar/75%CH<sub>4</sub> (P.75.)

The experimental measurements in P.75 were taken at a gas gain of 10<sup>4</sup> with an anode-cathode voltage of 3.54kV. Experiments showed that under these conditions and with <sup>55</sup>Fe as a radiation source there were no obvious signs of gain saturation, and the energy spectrum photopeak had a resolution of 17% measured at the centre anode. Amplifier time constants of 10μs were used. Chamber and collimator dimensions and all

other conditions remained the same as those used for the P.10 studies in chapter 4.

In order to estimate the mobility of positive ions in P.75, experimental results are compared in Fig. 7.1 with theoretical predictions for assumed mobilities of  $\mu = 2.3 \text{ cm}^2/\text{Vs}$  and  $\mu = 2.8 \text{ cm}^2/\text{Vs}$ . It should be noted that the value of  $\mu$  affects only slightly the crossover point, but does affect the slope of the theoretical curve. Since the slopes are quite well matched it may therefore be assumed that the choice of  $\mu$  value of 2.3 is reasonably good, but the insensitivity of the slope of these curves to fairly large changes in  $\mu$  indicates that this can only be an order of magnitude estimate. The crossover point is similarly insensitive to small changes in anode voltage and time constant. Consequently the near constant vertical offset of about 4% has most likely occurred in the division process.

The divider is able to determine the quantity  $(v_B - v_A') / (v_B + v_A')$  and it has already been mentioned that this provides a symmetrical response with improved linearity. Divider output spectra are plotted for a few positions of the source in Fig. 7.2 and from these some estimation of the spatial resolution may be obtained.

#### 7.2.2 Measurements in Ne/10% CH<sub>4</sub>

It was not possible to obtain statistically meaningful information from Ne/CH<sub>4</sub> using the <sup>55</sup>Fe source owing to the long mean-free-path for absorption of 5.9 keV radiation and the consequential reduction in detection efficiency. Al-K radiation was therefore used for all experiments with this mixture. The gas gain was maintained at  $3 \times 10^4$  by an anode-cathode potential of 2.25kV.  $-v_B/v_A$  has been plotted against  $x_0/s$  in Fig. 7.3 and compared with the theoretical prediction assuming mobility values  $\mu = 4\text{cm}^2/\text{Vs}$  and  $\mu = 1.7\text{cm}^2/\text{Vs}$  for equal time constants of 10 $\mu$ s. The slope is best matched to some mobility

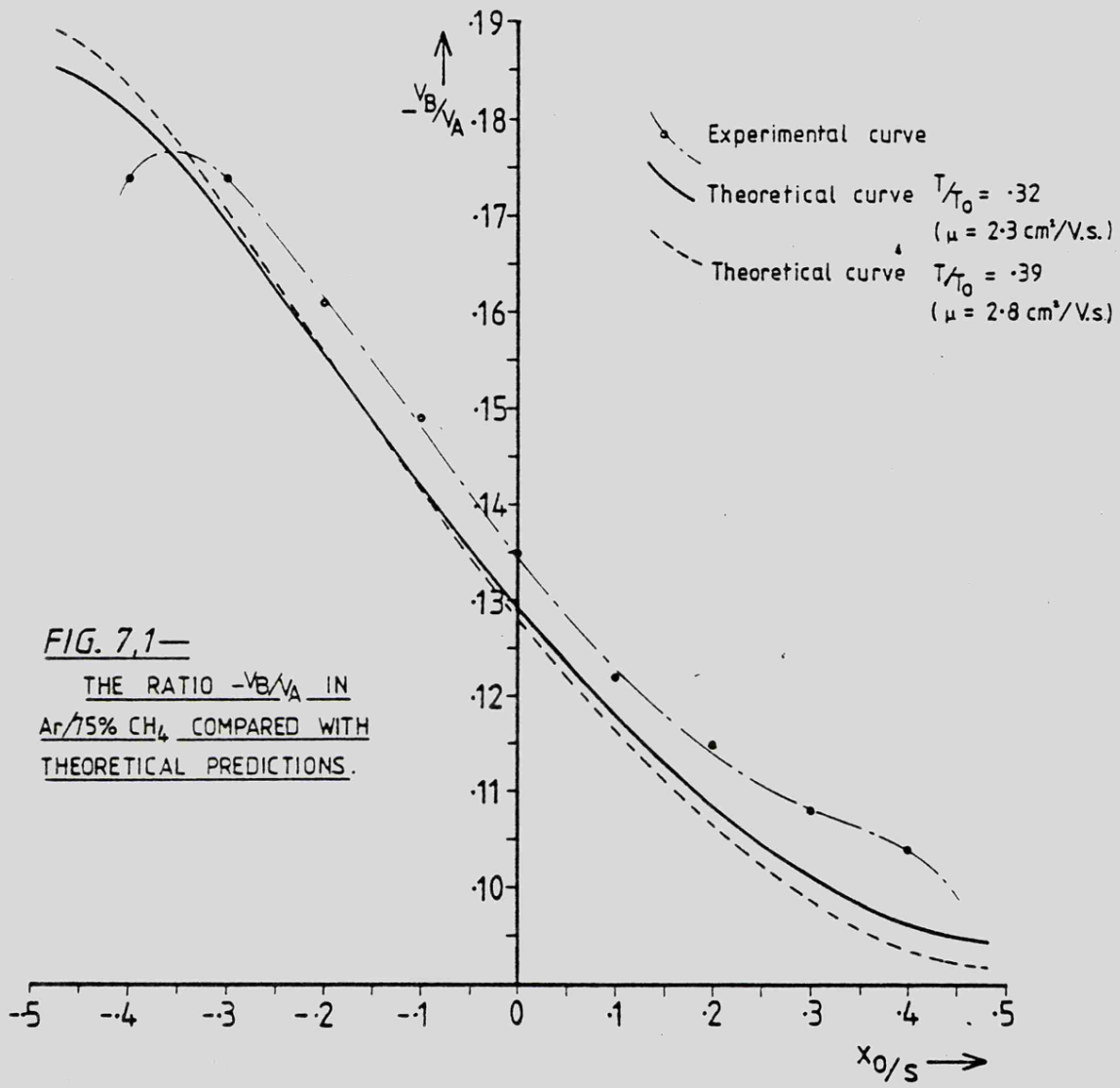
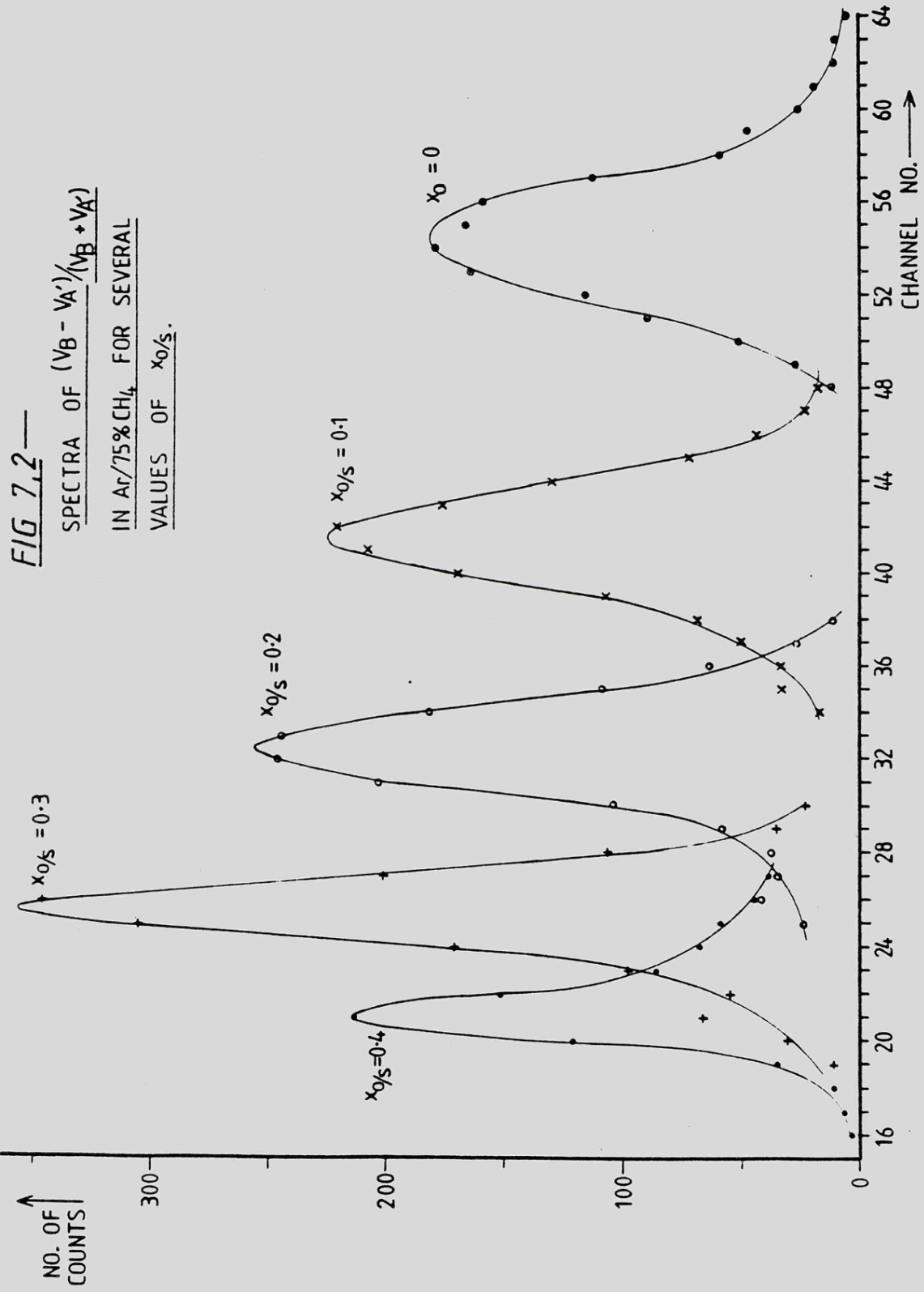
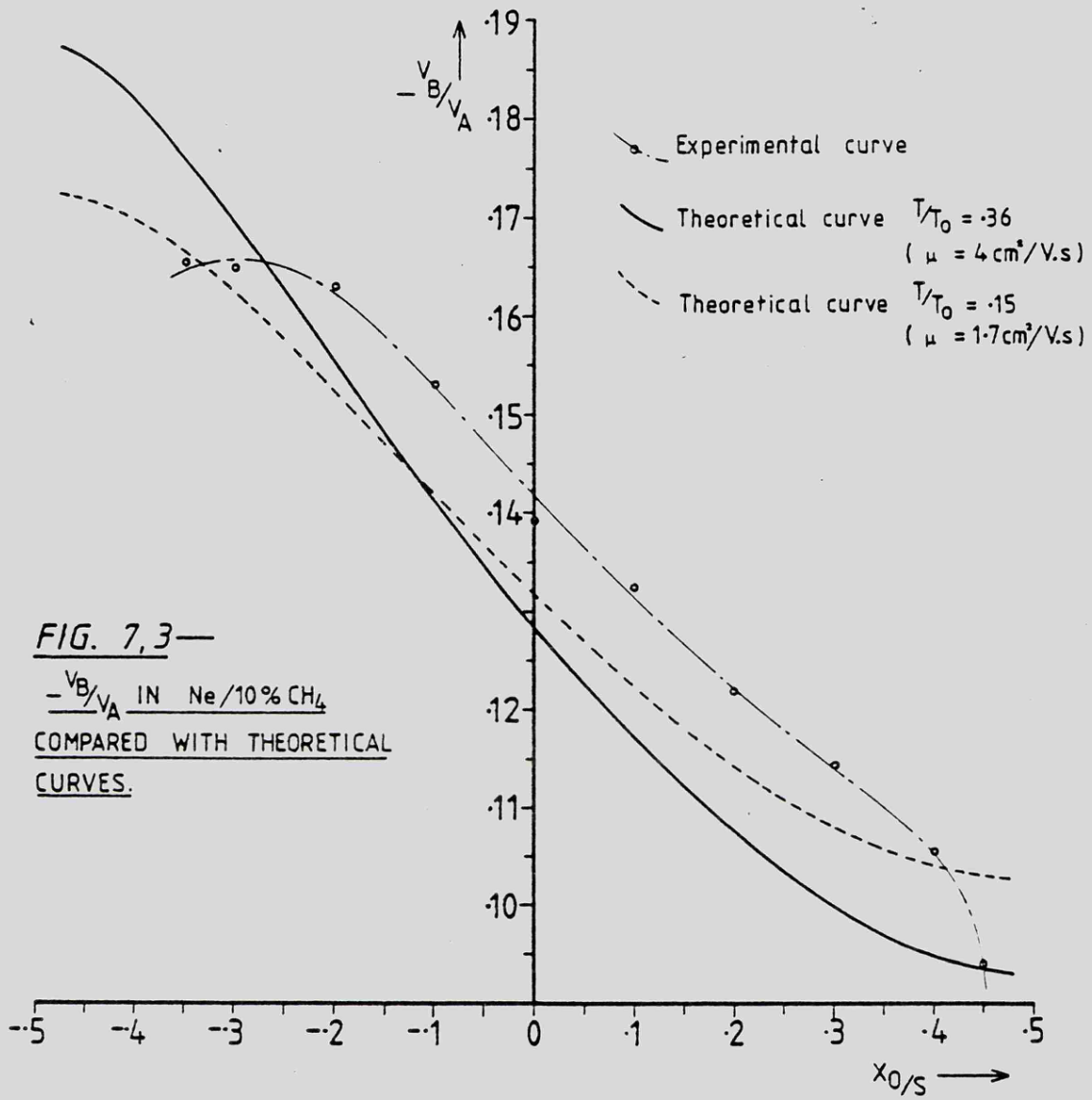


FIG. 7.1—

THE RATIO  $-v_B/v_A$  IN  
Ar/15% CH<sub>4</sub> COMPARED WITH  
THEORETICAL PREDICTIONS.





value between those used, possibly  $3\text{cm}^2/\text{Vs}$ . The plot of  $(v_B - v_A')/(v_B + v_A')$  is not shown here, but relevant data have been extracted and used for comparison in section 7.3.

### 7.2.3 Measurements in Ne/10% CO<sub>2</sub>

Measurements in Ne/10% CO<sub>2</sub> are plotted in Fig. 7.4. It was necessary to use an anode-cathode potential of 2.45kV to achieve a gain of  $3 \times 10^4$ . Conditions are otherwise the same as those in section 7.2.2. The Al-K source was again used because of the long mean-free-path at 6keV.

The experimental curve is compared with theoretical curves for assumed mobility values of  $4\text{cm}^2/\text{Vs}$  and  $1.53\text{cm}^2/\text{Vs}$ . It can be estimated that a mobility value nearer to  $3\text{cm}^2/\text{Vs}$  would be a better choice.

### 7.2.4 Measurements in Ar/10% CO<sub>2</sub>

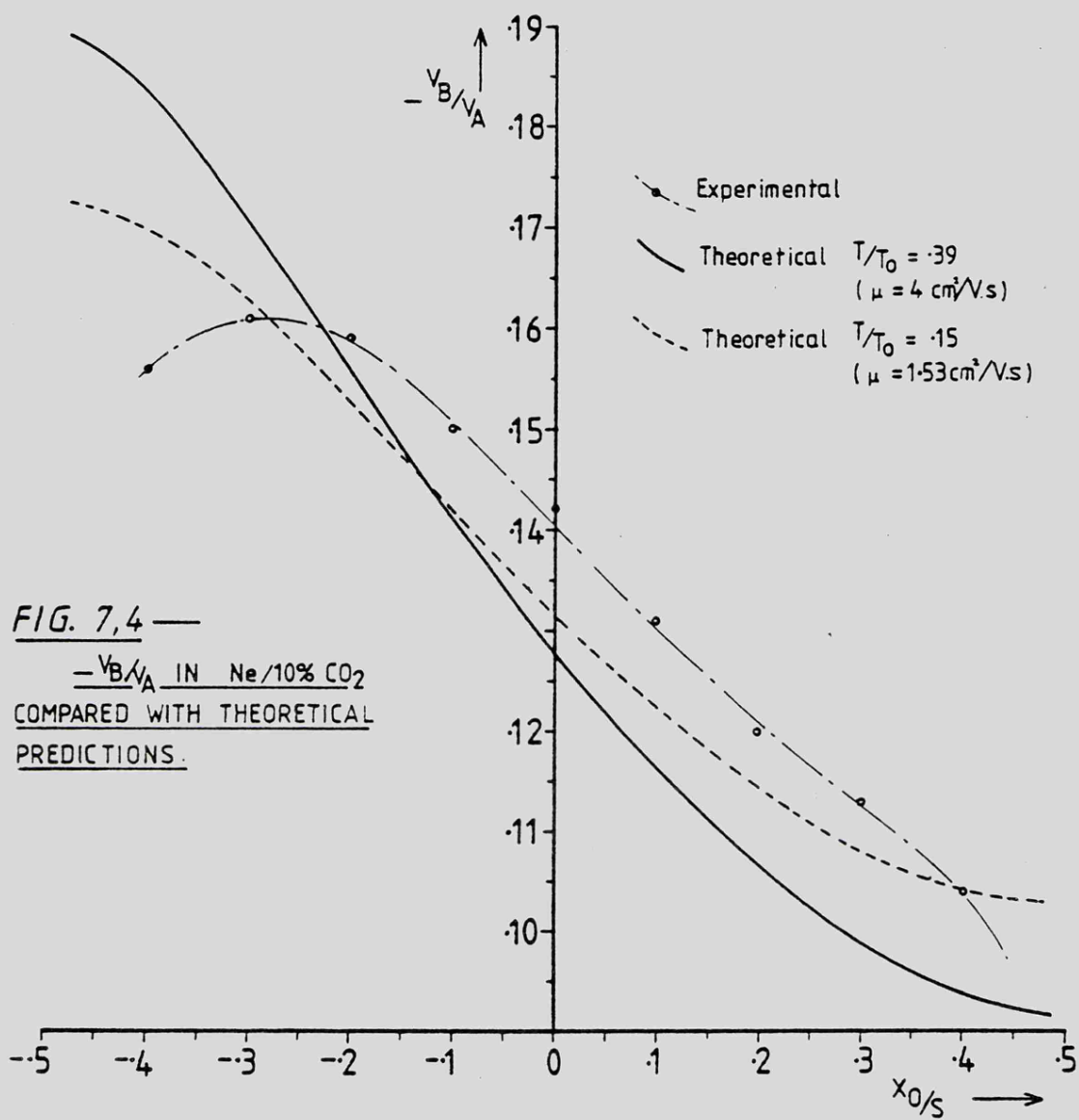
It was possible again to use the  $^{55}\text{Fe}$  source for these measurements, and results are shown in Fig. 7.5 where they are compared with theoretical curves which assume mobilities of 1.5 and  $3.2\text{cm}^2/\text{Vs}$ . The value of anode-cathode voltage was 2.5kV for a gas gain of  $10^4$  and the time constants were  $10\mu\text{s}$ . It appears that a suitable choice for mobility would be  $2.3\text{cm}^2/\text{Vs}$ .

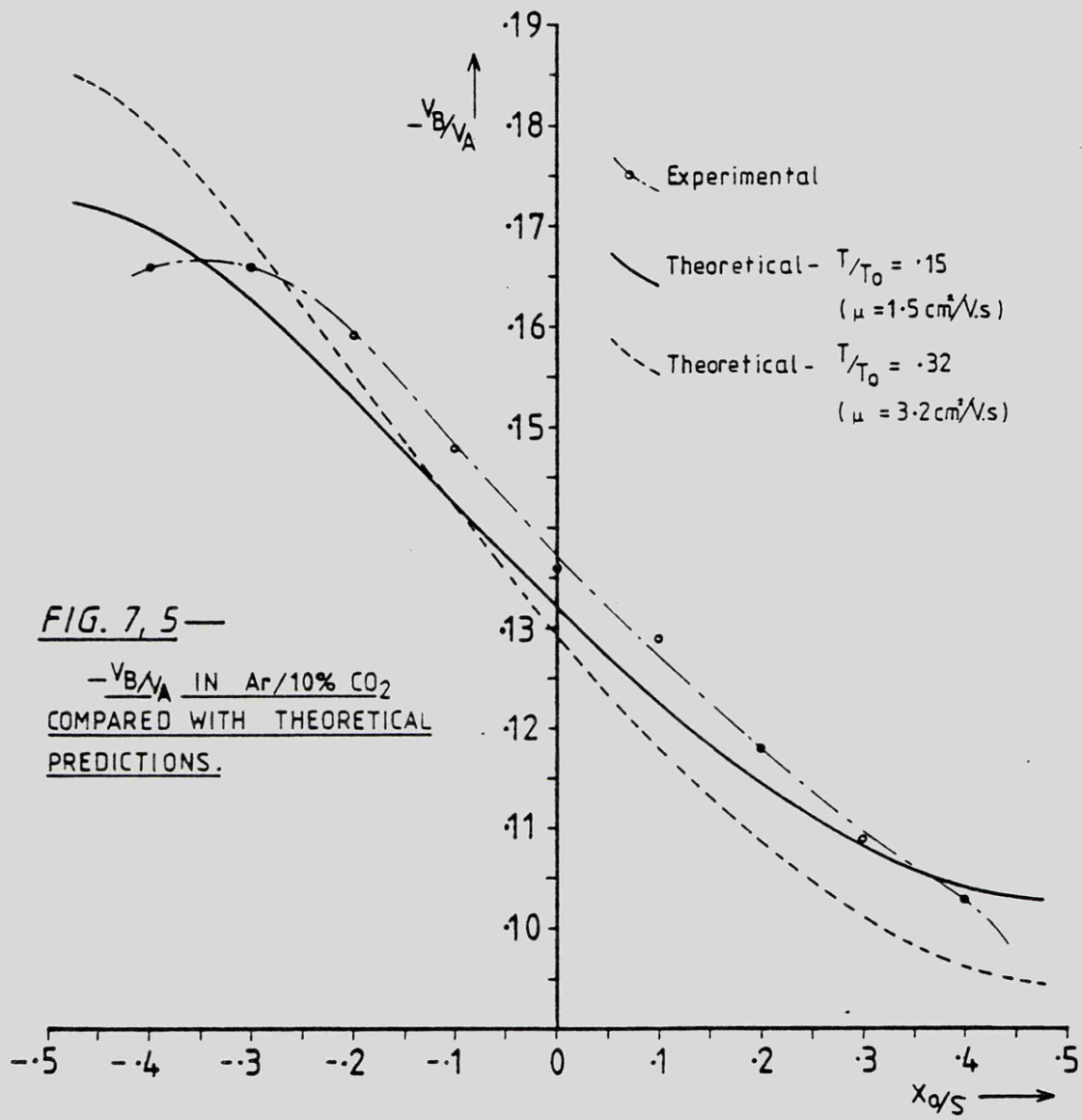
## 7.3 Discussion - Induced Anode Signals

### 7.3.1 Limitations

Not too much emphasis should be placed on the accuracy of the positive ion mobility estimates; matching of the slopes is very difficult particularly with such severe end-effect limitations. The theoretical curves were also calculated for zero angular spread, and since some angular spread must be occurring, then the mobility estimates must be on the high side.

Measurements near the extremes of the cell, particularly near  $x_0/s = - .5$  are subject to greater inaccuracy than those within the bounds  $\pm .3$  owing to a decrease in resolution of the energy spectrum





photopeak. It was found, however, that the worst case repeatability was within 5%, but for  $-.3 < x_0/s < +.3$  repeatability was within 2%.

### 7.3.2 Comparison of gas mixtures

From the above argument, it may be concluded that positive ion mobilities in the five gas mixtures are as shown in Table 7.2.

TABLE 7.2

GAS MIXTURE	MOBILITY $\text{cm}^2/\text{Vs}$
Ar/10%CH <sub>4</sub>	1.5
Ar/75%CH <sub>4</sub>	2.3
Ne/10%CH <sub>4</sub>	3
Ne/10%CO <sub>2</sub>	3
Ar/10%CO <sub>2</sub>	2.3

Comparing these mobility values with Gott and Charles'<sup>(62)</sup> figures, and with Brown'<sup>(66)</sup>, there is no indication of charge transfer in P10 or the two neon mixtures although there may be some evidence of transfer in P75 and Ar/10%CO<sub>2</sub>.

From the shapes of the experimental curves and the point at which premature turnover occurs at the upper extreme (i.e. the point at which electron loss into the neighbouring cell becomes apparent), it is possible to conclude that there is considerably less diffusion in P.75 than in P.10 and also that in Ar/10%CO<sub>2</sub> there seems to be less diffusion. In Ne/10%CO<sub>2</sub> rather more diffusion is apparent than for P.10.

Spectra of  $(v_B - v_A')/(v_B + v_A')$  similar to those of Fig. 7.2 have been obtained for each gas mixture and from these the fwhm at position  $x_0/s = .2$  has been measured and is given in Table 7.3.

Possible contributors to this spread have already been suggested in section 5.7, and the collimator contribution was thought to be the largest. For this reason, absorption mean-free-paths have been listed

also in Table 7.3 for the particular source used. The longer mean-free-path will of course cause larger collimator spreads. With this in mind, it is interesting that Ar/75%CH<sub>4</sub> and Ar/10%CO<sub>2</sub> prove to be the better of the five gas mixtures in terms of both diffusion and resolution of the position signal r.

TABLE 7.3

GAS MIXTURE	FWHM RESOLUTION - $\mu\text{m}$	SOURCE	MEAN-FREE-PATH - cm.
Ar/10%CH <sub>4</sub>	320	<sup>55</sup> Fe	2.3
Ar/75%CH <sub>4</sub>	312	<sup>55</sup> Fe	13.8
Ne/10%CH <sub>4</sub>	453	Al-K	.456
Ne/10%CO <sub>2</sub>	504	Al-K	.388
Ar/10%CO <sub>2</sub>	240	<sup>55</sup> Fe	2.27

#### 7.4 Induced Cathode Signals

##### 7.4.1 Photographs of induced cathode pulses

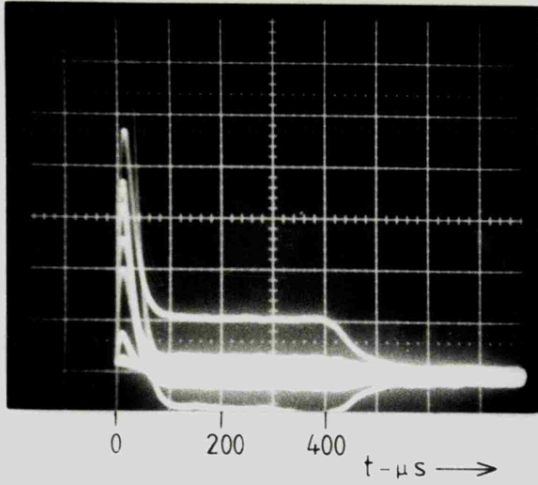
The photographs in Fig. 7.6 are of induced cathode pulses in the four gas mixtures after 10 $\mu\text{s}$  shaping in the amplifiers. In each case, the source was situated above the centre anode and the anode voltage and other conditions were identical to those specified in section 7.2. A comparison of positive ion collection times may now be made and by the same argument as that in section 5.2, the mobility of each mixture may again be estimated. These are as follows:

$$\text{Ar/10\%CO}_2 \quad - \quad \mu = 1.77 \text{ cm}^2/\text{Vs}$$

$$\text{Ne/10\%CO}_2 \quad - \quad \mu = 2.73 \text{ cm}^2/\text{Vs}$$

$$\text{Ar/75\%CH}_4 \quad - \quad \mu = 2.00 \text{ cm}^2/\text{Vs}$$

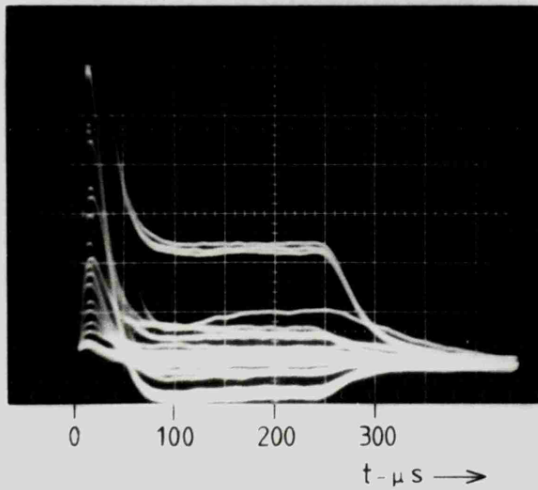
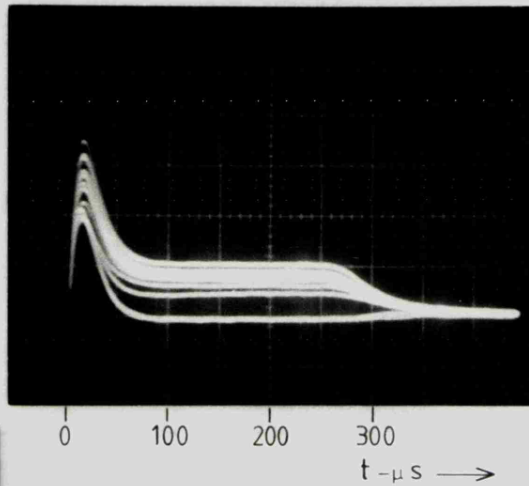
$$\text{Ne/10\%CH}_4 \quad - \quad \mu = 3.28 \text{ cm}^2/\text{Vs}$$



Ar/10%CO<sub>2</sub>

SOURCE Fe-55

Ne/10%CO<sub>2</sub>  
SOURCE AL-K



Ar/75%CH<sub>4</sub>

SOURCE Fe-55

Ne/10%CH<sub>4</sub>  
SOURCE AL-K

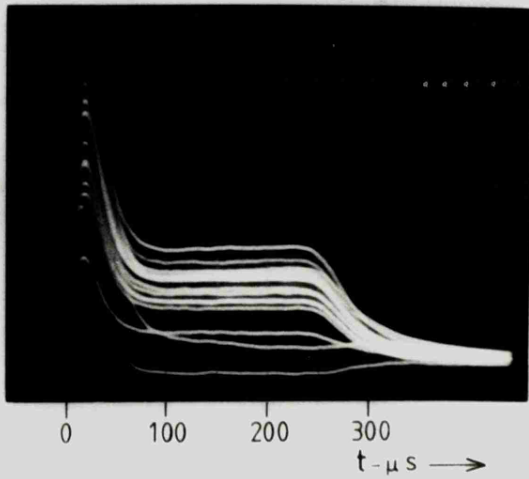


**FIG 7,6** —  
INDUCED CATHODE PULSES  
AFTER 10 μs SHAPING IN SOME  
GAS MIXTURES.

#### 7.4.2 Induced cathode signals in Ar/75%CH<sub>4</sub>

Experimental points are plotted in Fig. 7.7 for the ratio  $v_C/v_C'$  at several positions of the <sup>55</sup>Fe source,  $x_0/s$ . The shaping was 10 $\mu$ s and the e.h.t. was set to 3.54kV for a gas gain of 10<sup>4</sup>. For comparison, theoretical predictions are shown for angular spreads of 0<sup>o</sup> and 60<sup>o</sup>, and for  $T/T_0 = .32$  which corresponds to an assumed mobility of 2.3 cm<sup>2</sup>/Vs.

As in the case of P.10 the results are in reasonably good agreement with theory and one can roughly estimate the angular spread as being 33<sup>o</sup>.

It was expected, from anode signal measurements in this gas mixture, that diffusion would be rather less than in P.10. This is indeed evident in Fig. 7.7 where at  $x_0/s = .45$ , experimental points have not departed so much from the theoretical curve.

#### 7.4.3 Induced cathode signals in Ne/10%CH<sub>4</sub>

Experimental conditions here were the same as those in section 7.2.2 (i.e.  $V_a = 2.25$ kV.  $T = 10\mu$ s, source Al-K).

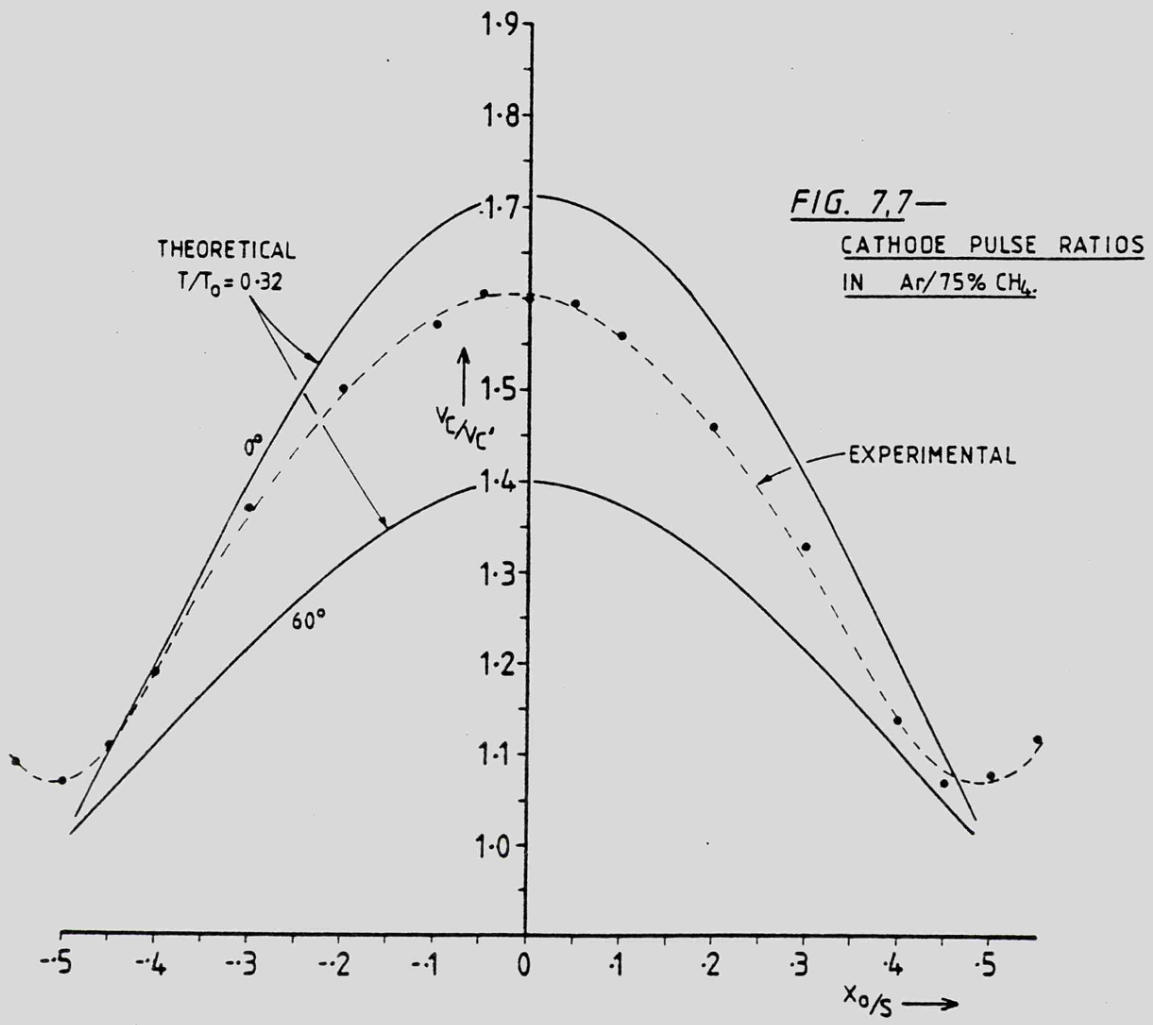
The dotted curve of Fig. 7.8 is drawn through experimental points, and is compared with theoretical curves for  $T/T_0 = .36$  at

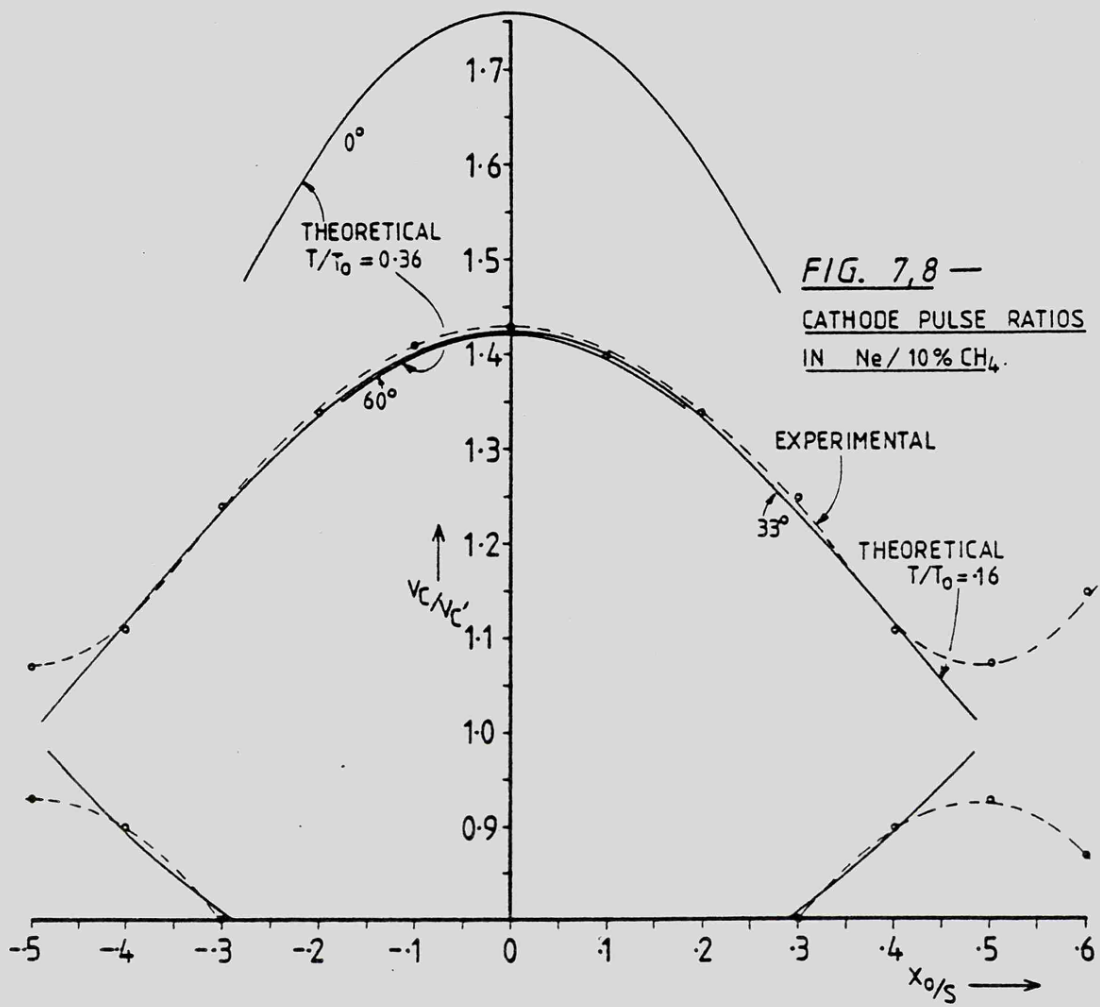
$\sigma_\alpha = 0^o$  and 60<sup>o</sup>, corresponding to  $\mu = 4$  cm<sup>2</sup>/Vs. It is clear that unless the angular spreading corresponds to  $\sigma_\alpha = 60^o$ , then the assumed mobility is much too high. If it is assumed that  $\mu \simeq 1.8$  cm<sup>2</sup>/Vs and that  $\sigma_\alpha = 33^o$ , then experiment and theory are in good agreement, but since the agreement near  $x_0/s = .5$  is worse than P.10, it is likely that angular spreading exceeds  $\sigma_\alpha = 33^o$  and it may be concluded that

$$1.8 \leq \mu \leq 4 \text{ cm}^2/\text{Vs}.$$

#### 7.4.4 Induced cathode signals in Ne/10%CO<sub>2</sub>

Again, experimental conditions remained the same as in section 7.2.3 (i.e.  $V_a = 2.45$ kV,  $T = 10\mu$ s, source Al-K.)





Similar disagreement with theory may be seen here in Fig. 7.9 where the experimental curve is compared with theoretical predictions for  $T/T_0 = 0.4$  ( $\mu \sim 4 \text{ cm}^2/\text{Vs}$ ). Similar conclusions to those for Ne/10%CH<sub>4</sub> may also be drawn, except that the two lower theoretical curves now assume a  $\mu$  value of  $1.6 \text{ cm}^2/\text{Vs}$ . Hence  $1.6 \leq \mu \leq 4 \text{ cm}^2/\text{Vs}$ .

#### 7.4.5 Induced cathode signals in Ar/10%CO<sub>2</sub>

In many ways Ar/10%CO<sub>2</sub> behaves similarly to Ar/10%CH<sub>4</sub> as a chamber gas. From Fig. 7.10 it can be seen that agreement with the theoretical curve at  $10\mu\text{s}$  ( $T/T_0 = .16$ ,  $\mu = 1.6$ ,  $V_a = 2.5\text{kV}$ ) is good. The lower diffusion in this mixture is evident near  $x_0/s = .5$  where the proximity of the experimental curve to the x-axis at  $v_c/v_c' = 1$  is closer than for P.10.

Similarly good agreement may be seen at  $T/T_0 = .4$  ( $25\mu\text{s}$ ) and  $T/T_0 = .08$  ( $5\mu\text{s}$ ), indicating that the ionic mobility remains constant over this time range.

In calculating the three theoretical curves, a standard deviation  $\sigma_\alpha = 33^\circ$  for the angular spread has been assumed. It may well be, however, that there is rather less angular spread, in which case similar agreement between experiment and theory could be achieved by assuming a lower value for  $\mu$ .

#### 7.5 Discussion - Induced Cathode Signals

The major objective in obtaining the experimental results of section 7.4 has been to determine the usefulness of the particular gas mixture as a position sensitive detection medium and in order to do this it has been necessary to make some assessment of the angular spreading of the electron cloud around the anode due mainly to diffusion and also to other effects previously discussed. Since at the cathodes the effective centre of charge is detected it is expected that the shapes of the curves of  $v_c/v_c'$  will generally not be sensitive to diffusion,

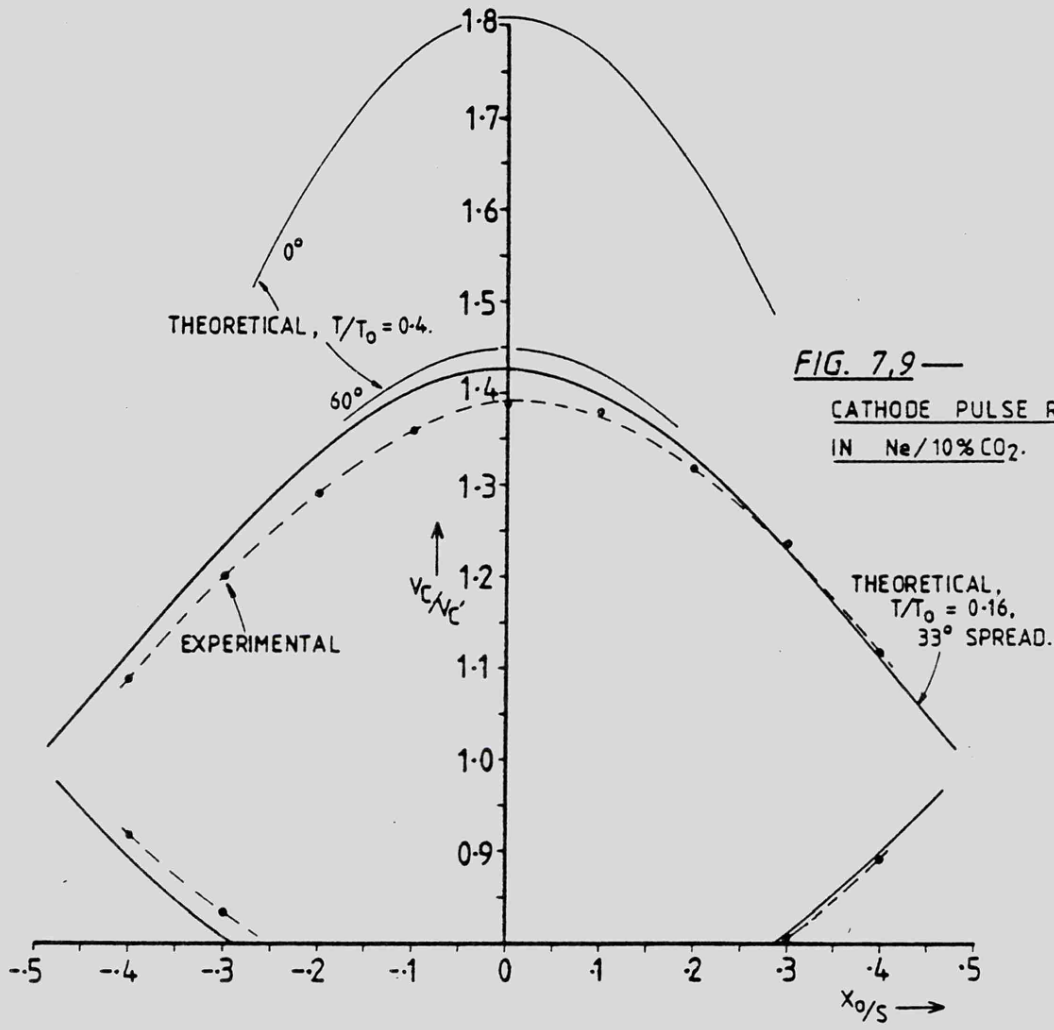


**FIG. 7.9**—  
**CATHODE PULSE RATIOS**  
**IN Ne/10% CO<sub>2</sub>.**

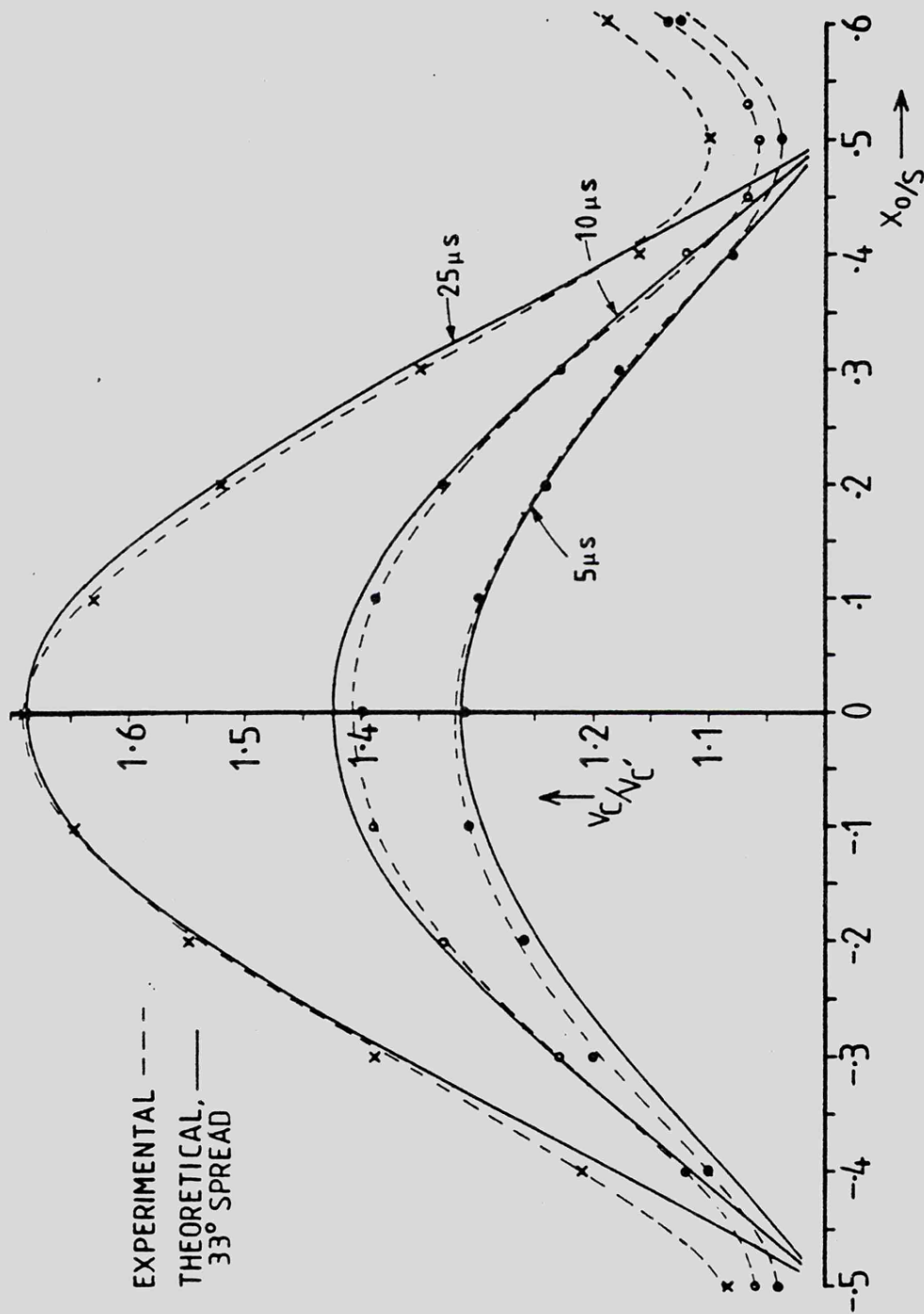


FIG. 7.10 — CATHODE PULSE RATIOS IN Ar/10% CO<sub>2</sub> FOR A RANGE OF FILTER NETWORK T VALUES.

but in the region  $x_0/s = .5$  diffusion and other effects prevent the ratio  $v_c/v_c'$  from ever reaching unity (see section 6.5.1). Experimental behaviour in this region then gives some indication of the amount of diffusion occurring, and from the measurements it is again clear that Ar/75%CH<sub>4</sub> and Ar/10%CO<sub>2</sub> are more favourable than the other gas mixtures in this respect.

Unlike the theoretical predictions for anode ratios, those for the cathode induced signals are much more sensitive to  $T/T_0$  (where  $T_0 = s^2/\mu V_a$ ) and hence to  $\mu$ . This is particularly apparent in the results for the neon mixtures where it seems likely that a value for  $\mu$  of 4cm<sup>2</sup>/Vs is rather high, unless there is a large amount of angular spreading. In the case of Ne/CH<sub>4</sub> the region around  $x_0/s = .5$  certainly indicates greater spreading than for P.10, but unfortunately, for Ne/CO<sub>2</sub>, the Al-K source was not available to investigate this region in more detail. Cursory investigations indicated that less diffusion was occurring than in P.10, but more work needs to be done here.

For the argon mixtures, good agreement with theory exists if the mobility figures given by Gott and Charles<sup>(62)</sup> are assumed and if an angular spread of 33° is used. It is difficult to draw further conclusions from this work until more basic data on positive ion mobilities and on the nature of positive ions under changing field conditions, become available.

CHAPTER 8CHAMBER GEOMETRY8.1 Introduction

As with radiation detectors generally, changes in chamber geometry are not easily effected and are extremely time consuming. For this reason it has not been possible to make changes to the outer dimensions of the chamber, but only to the anode wire radii and to their spacing. In each case, time has permitted only three different conditions to be investigated, but this has been sufficient to observe trends and limitations.

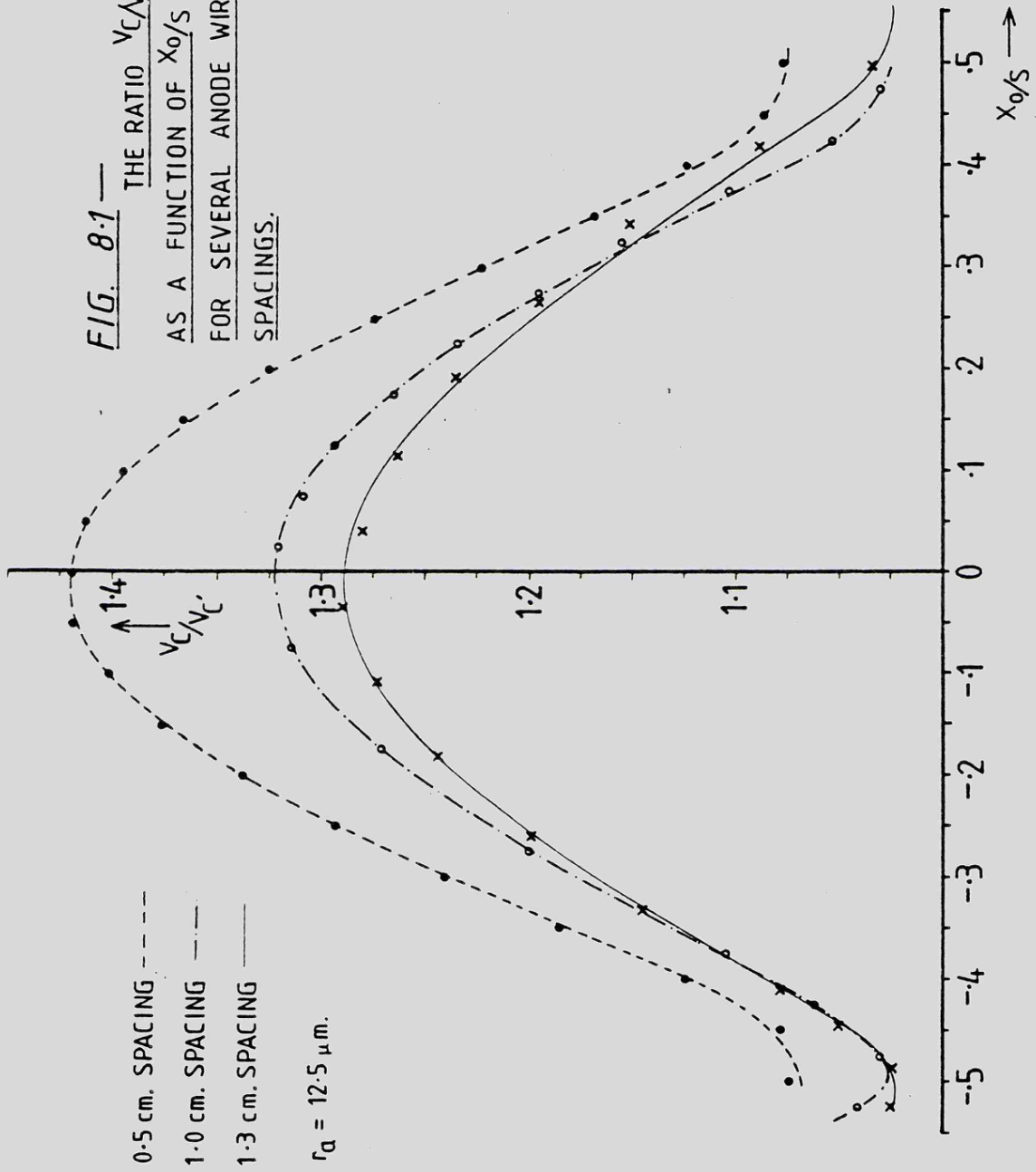
In the results that follow, the limitations imposed by the theoretical model (chapter 3) have often been grossly violated, and there has been little point in making comparisons with theory.

In each case the gas mixture was P.10 and the source of radiation was  $^{55}\text{Fe}$ . A shaping network time constant of  $10\mu\text{s}$  was used throughout.

8.2 Effects of Varying the Anode Wire Spacing8.2.1 Induced cathode signals

In Fig. 8.1 the ratio of induced cathode pulses  $v_c/v_c'$  is shown as a function of the X-ray beam position  $x_0/s$  for anode spacings of .5 cm. ( $h/s = 2.22$ ), 1.0 cm. ( $h/s = 1.11$ ) and 1.3 cm. ( $h/s = .85$ ). The wire diameter in each case was  $25\mu\text{m}$ . Where 1 cm. spacing was used, the anode plane consisted of five 1 cm. spaced wires with two wires either side at 0.5 cm. spacing. The two outer wires were of  $125\mu\text{m}$  stainless steel as used previously. Where the anode spacing was increased to 1.3 cm., only five equally spaced wires were used. At this spacing the operating voltage was low and there were no signs of

FIG. 8.1—  
 THE RATIO  $V_C/V_C'$   
 AS A FUNCTION OF  $X_0/S$   
 FOR SEVERAL ANODE WIRE  
 SPACINGS.



electrical breakdown so that the larger diameter outer wires were no longer necessary. Of course, at these latter spacings, the approximation to an infinite anode plane was becoming less realistic.

At 1.3 cm. spacing, the anode-cathode voltage required for a gas gain of  $10^4$  was 1750V., and at 1 cm. spacing  $V_a$  was 1950V. The measurements for 0.5 cm. spacing have been obtained at  $V_a = 2500V$ , and although they have previously been given, they are reproduced here for comparison.

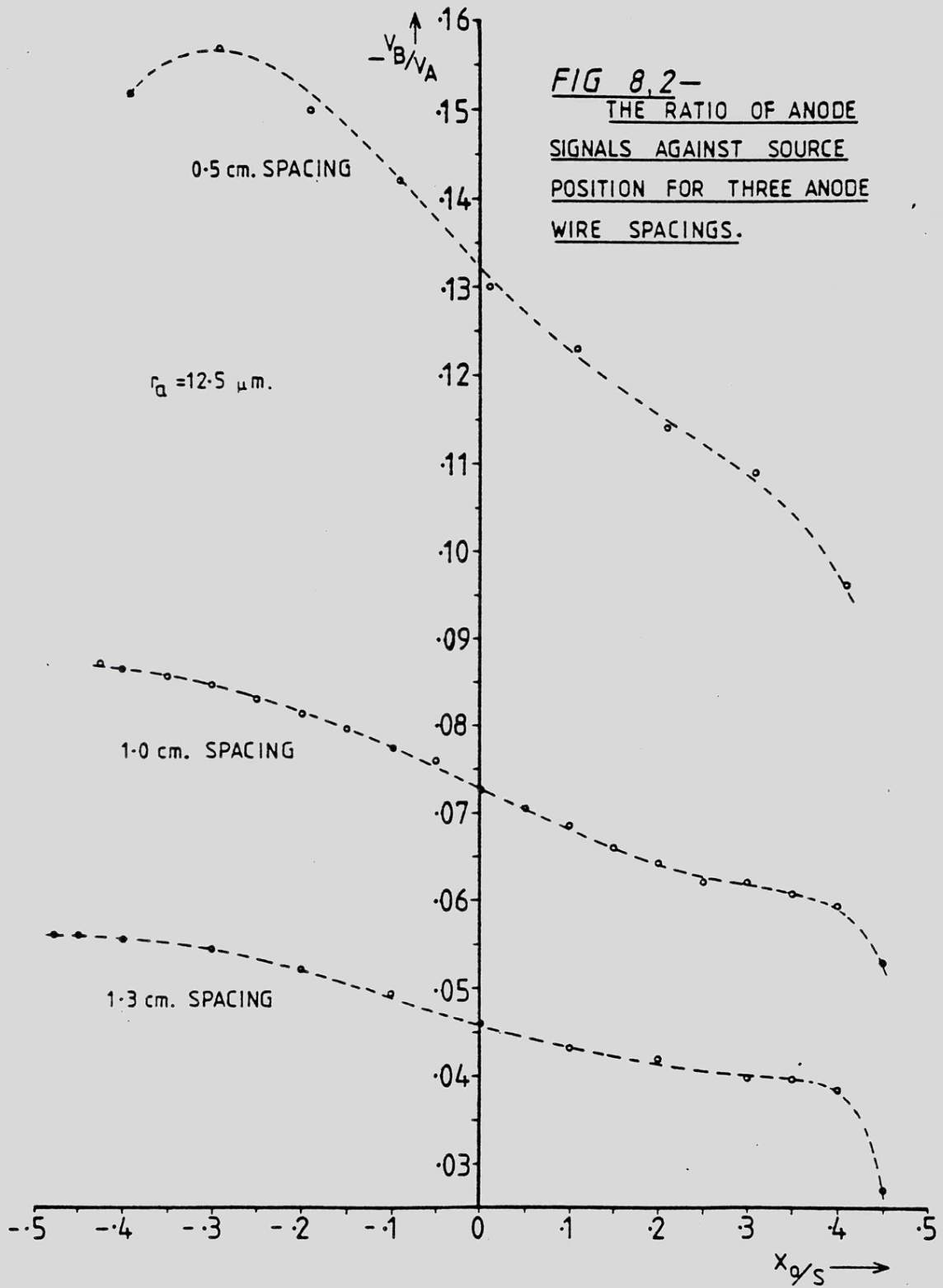
Fig. 8.1 shows that the sensitivity of  $v_c/v_c'$  to changes in  $x_0/s$  does not reduce appreciably as the spacing is increased and it would appear that positional information is still available at 1.3 cm. spacing. It must be remembered, however that the position of the centroid of the distribution of  $v_c/v_c'$  is plotted and no account is taken of the width of the distribution. In practice it is found that this width increases as the spacing is increased and the resolving power is accordingly reduced. This will be illustrated later when considering ratios of induced anode signals.

### 8.2.2 Induced anode signals

The ratio  $-v_B/v_A$  of anode signals is plotted in Fig. 8.2 for the three anode wire spacings. It is surprising to note that worsening end effects at the larger wire spacings tend to increase the useful working region of the cell. This was also noticeable to a lesser extent in Fig. 8.1. The slope of  $-v_B/v_A$  falls off as the spacing is increased, but perhaps more serious is the fall-off in induced signal amplitude which at 1.3 cm. spacing is only 1/3 that at .5 cm. spacing. However, with low noise amplification, this is not troublesome.

### 8.3 Effects of Varying Anode Wire Diameter

With a constant anode wire spacing of 1 cm., the wire diameter has been changed from 25 $\mu$ m. to 20 $\mu$ m. and 15 $\mu$ m. The anode wires were of



gold plated tungsten as previously used. It was necessary to adjust the anode-cathode voltage to ensure that the gas gain remained at  $10^4$ , and the anode voltages for the above wire diameters were 1950, 1850 and 1720 volts respectively. In all other respects the chamber and external conditions remained the same.

Fig. 8.3 shows the ratio  $-v_B/v_A$  as a function of  $x_0/s$  for each anode diameter. The theoretical curve for  $r_a = 10\mu\text{m.}$ ,  $V_a = 1850\text{V}$  and  $T/T_0 = .028$  is shown for comparison, but good agreement is not expected. The spread of the avalanche now becomes particularly noticeable in the upper non-linear region of the curves as it engulfs more of the smaller diameter anodes.

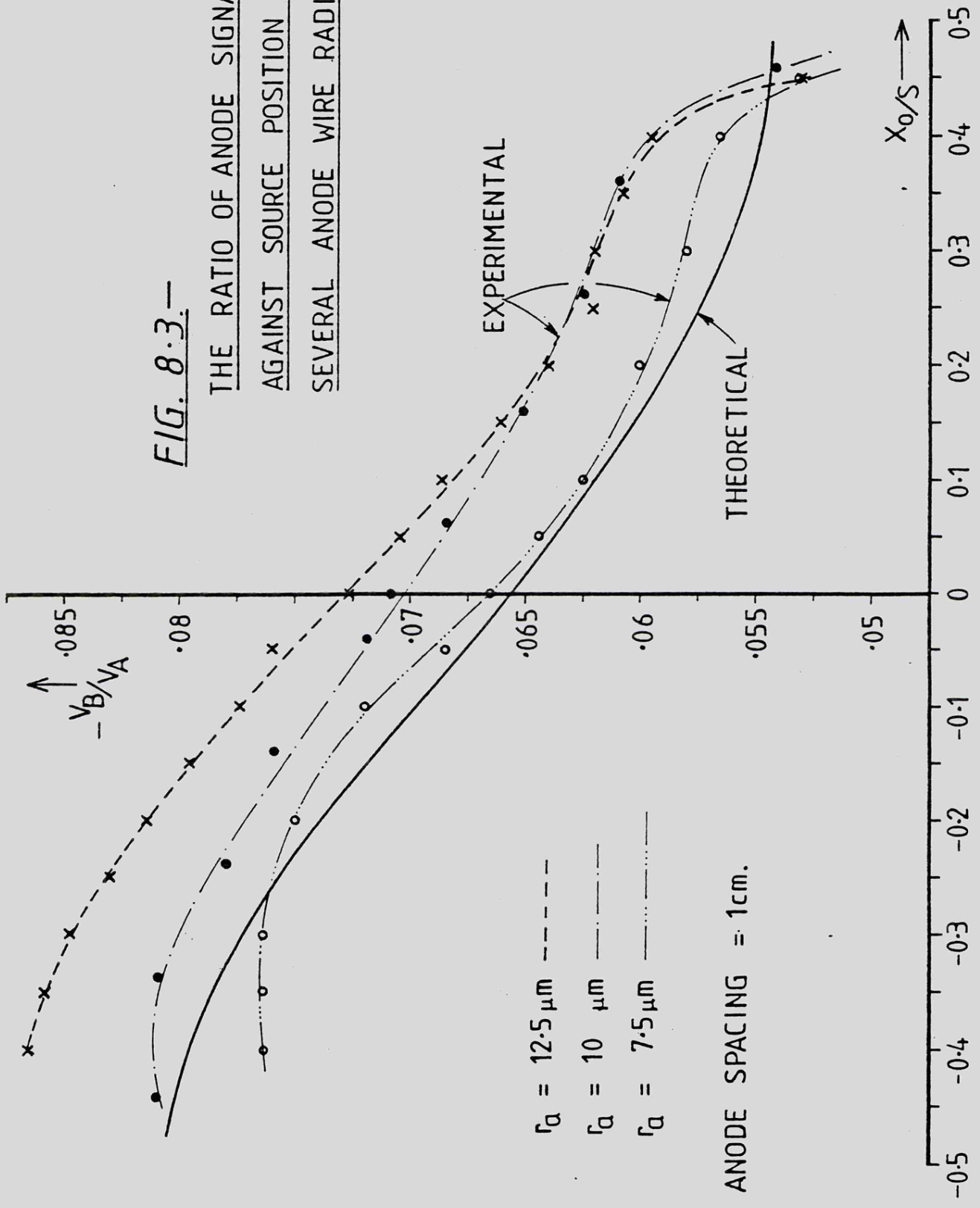
#### 8.4 Resolution

The resolution, as it is affected by geometrical changes can best be observed from the spectra of the position signal,  $r = (v_B - v_A') / (v_B + v_A') + \text{Const.}$  These are given in Fig. 8.4 for three conditions,  $s = 1 \text{ cm. } r_a = 12.5\mu\text{m.}$ ,  $s = 1.3 \text{ cm. } r_a = 12.5\mu\text{m.}$  and  $s = 1 \text{ cm. } r_a = 7.5\mu\text{m.}$

The resolution in each case has been estimated from the fwhm of the spectrum at  $x_0/s = .2$ , calibrated in position by experimental measurement of the centroid of  $r$  as a function of  $x_0$ , as in section 5.7. It was found that increasing the wire spacing from .5 cm. to 1 cm. with constant anode diameter of  $25\mu\text{m.}$ , degraded the resolution from  $320\mu\text{m.}$  (see section 5.7) to  $590\mu\text{m.}$  and increasing the spacing still further to  $1.3\text{cm.}$  resulted in a much more severe degradation to  $1120\mu\text{m.}$

Reducing the anode wire diameter from  $25\mu\text{m.}$  to  $15\mu\text{m.}$  at a constant anode spacing of 1 cm. resulted in only a slight degradation from  $590\mu\text{m.}$  to  $640\mu\text{m.}$  The  $180\mu\text{m.}$  collimator contribution and other smaller contributions may reasonably be neglected at these larger fwhm values.

FIG. 8.3.—  
THE RATIO OF ANODE SIGNALS  
AGAINST SOURCE POSITION FOR  
SEVERAL ANODE WIRE RADII.



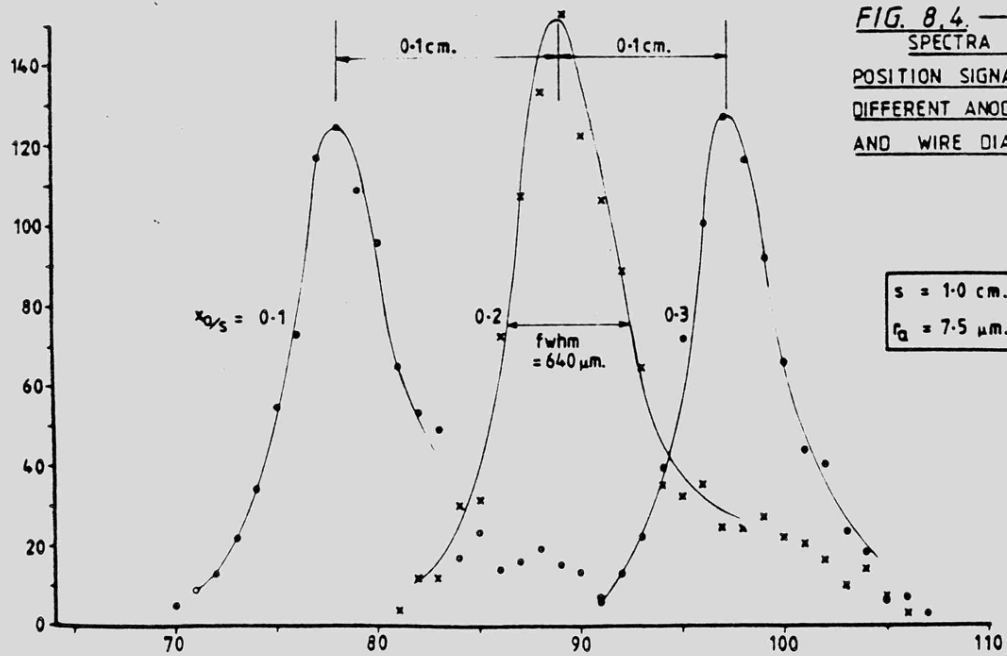
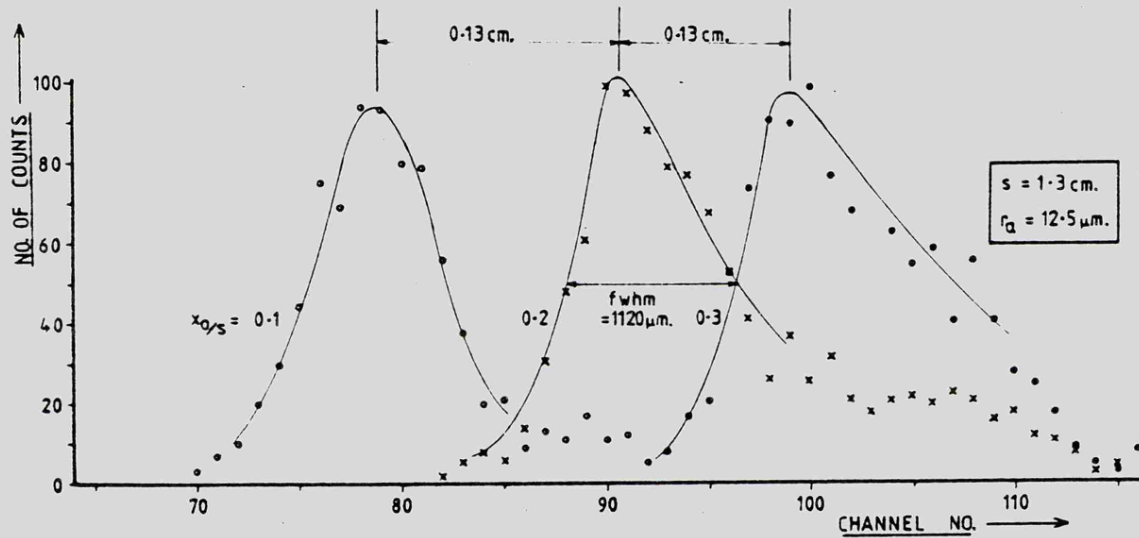
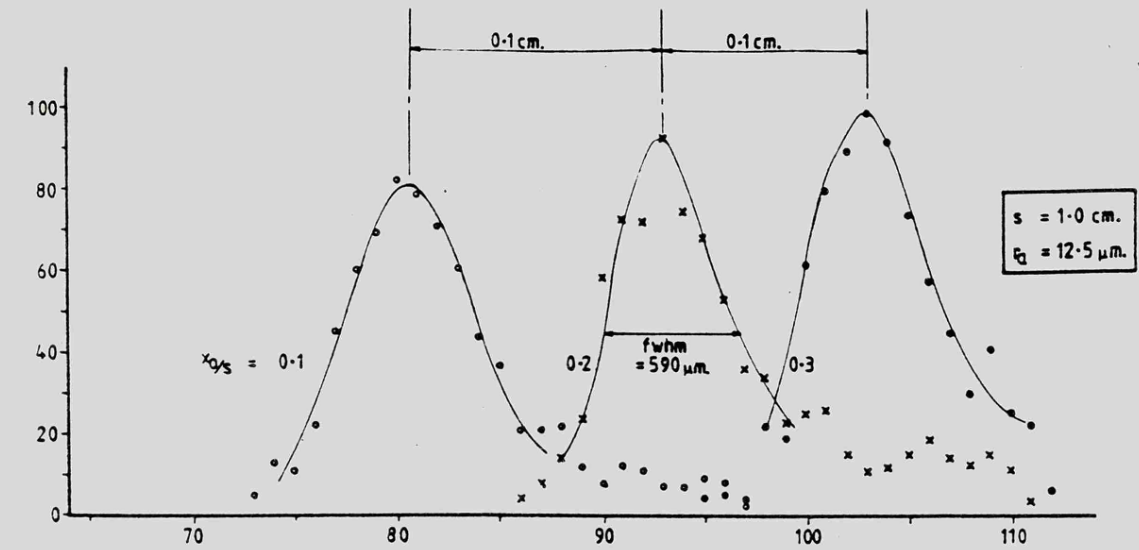


FIG. 8.4. —  
SPECTRA OF THE  
POSITION SIGNAL  $r$ , FOR  
DIFFERENT ANODE SPACINGS  
AND WIRE DIAMETERS.

### 8.5 The Single Wire Chamber

A single wire chamber was constructed with the same dimensions as previous chambers, but with only one central 25 $\mu$ m. diameter anode wire. The value of  $V_a$  required for  $10^4$  gas gain was 1600 volts.

Of course, only cathode induced pulses could be observed here, but it was found that the resolution was so poor, that from the spectrum of  $v_c/v_c'$ , it was only just possible to discern the two peaks when the source was in a central position. Presumably, now, an almost radial field extended well out towards the cathodes, and the position of the localised avalanche depended very much on the depth at which absorption took place. No results are therefore recorded with the present source, but it may be of interest to repeat this at some later date with the Al-K source or with a heavier gas (e.g. xenon) in a sealed chamber.

### 8.6 Discussion

The foregoing has shown that increasing the wire spacing in this shallow chamber has the undesirable effect of degrading the resolution, but this is to be expected with such a long mean-free-path for absorption, as the field becomes more nearly radial and non-linear. The results are encouraging in that positional information is still available over a cell width of 1.3 cm., and this could probably be extended further were a low energy source used. Alternatively a chamber of greater depth, with a larger extent of uniform field, should yield improved resolution.

It would appear that, with the present  $^{55}\text{Fe}$  source, 1 cm. spacing of 25 $\mu$ m. anode wires certainly represents the experimental maximum.

Results presented here were not intended to be fully exhaustive, but merely to provide a foundation for further work which

clearly now needs to be done, and it seems that more work with an Al-K source would be particularly productive.

CHAPTER 9CONCLUDING DISCUSSION9.1 Summary

It has been the intention throughout this work to provide as much basic information as possible about this recently discovered and interesting phenomenon of angular localisation. Often, for this reason, only the surface has been uncovered to expose a foundation for new areas of research, and no attempt has been made at this stage to apply these findings to practical situations.

In summary, it has been found that, because of a strongly localised avalanche, positional information can be extracted from a simple multiwire chamber, with few external components, by two methods:

First, induced signals from the two anodes on either side of the avalanche anode may be used to determine the position of incoming radiation. This method is particularly useful in locating the position of radiation entering the chamber in the immediate vicinity of the avalanche anode, and in fact 70% of the cell width can be utilised but with reducing sensitivity near the extremes.

Secondly, induced signals from the two cathodes also provide information regarding the position of incoming radiation, but this is rather insensitive in the region above the avalanche anode yet is increasingly sensitive towards the extremes of the cell. In fact this method provides information over about 90% of the cell width.

In argon/10% methane, the angular spread has been estimated as  $33^\circ$  and the resolution appears to be  $\sim s/40$  under favourable conditions.

Some experimental work with other gases indicates that there

is rather less diffusion in argon/75% methane and in argon/10% carbon dioxide than in P.10, and that these provide better resolution as position sensitive detection media.

Variations in the chamber geometry have been investigated and it was found that at anode spacings up to 1.3 cm. useful positional information was still available. A single wire chamber has also been briefly investigated and shows promise as a position sensitive detector, but work on this was limited by presently available experimental facilities.

Changes in anode wire diameter show that there is evidence of greater spreading around the smaller diameter wires, but the spatial resolution is not unduly degraded. Similar observations have also been reported by Okuno et al<sup>(63)</sup>, whilst working with a segmented cathode, coaxial proportional counter designed for angular distribution measurements.

In general it has been found that experimental results have agreed well with theoretical predictions, and where serious disagreement has occurred it has usually been possible to recognise the cause. In the case of geometrical variations, however, the conditions demanded by the theoretical model have sometimes been grossly violated and comparison with theory has not been possible. Work is now proceeding with a new theoretical model<sup>(67)</sup> which may be applied to conditions where  $h$  is not necessarily much greater than  $s$  and where any radius of wire may be used, even different radii in the same chamber.

## 9.2 Major Experimental Limitations

### 9.2.1 Cell boundaries

It has been found that at positions of  $x_0$  where the anode signals yield insensitive information, the cathode signals are most sensitive, and vice versa, and it should not be too difficult to

electronically combine this information to provide sensitive detection over about 90% of the cell. Unfortunately, mainly because of electron diffusion, the remaining 10% at the mid position between anodes is an area devoid of any information. For minimum ionising radiation, chambers could be stacked and electronically interlaced to avoid this region, but for radiation of a totally ionising nature, this area represents a fundamental limitation which can only be avoided by increasing the wire spacing to a distance greater than the region of interest.

#### 9.2.2 Positive ion mobility

Throughout the work, comparison of experimental results with theoretical predictions has been hampered by a lack of knowledge of positive ion mobility in the various gas mixtures and this has prevented an accurate determination of the amount of angular spreading. Clearly there is a great need for basic data to supplement that of Brown<sup>(66)</sup> and Schultz et al<sup>(69)</sup>, which may be applied under conditions of varying field and for gas mixtures of the types commonly used in radiation detectors.

#### 9.2.3 Diffusion

Estimates of electron diffusion are always difficult to provide, mainly because of a lack of consistent experimental data on  $\epsilon_K$  values in typical counter gas mixtures. It is understandable, however, when one considers that electron transport coefficients for gas mixtures are so dependent upon the component quantities of the mixture and also upon minute traces of impurity<sup>(51)</sup>, that such data has not been forthcoming.

#### 9.2.4 Radioactive sources

Most of the work presented here has been carried out with  $^{55}\text{Fe}$  as the radiation source and occasionally it has been possible to make use of a sealed Al-K source of low energy X-rays. There are still some areas of this work which could be more thoroughly investigated using a

1.5keV source and these are discussed in section 9.3.

### 9.3 Future Research

Inevitably in this research project time has not permitted all loose ends to be tied up, and also several areas of research, not originally conceived, have now come to light. These are discussed below.

#### 9.3.1 Count rate limitations

There will necessarily be some limit on the count rate up to which multiwire chambers operating in the localised avalanche mode can operate. This limit will be imposed by the chamber rather than the electronics, which, with recovery times of a few tens of microseconds could well operate at rates up to at least 20,000 p.p.s. The positive ion collection time is likely to be the main limiting factor. For the present chamber collection times of between 250 $\mu$ s, and 400 $\mu$ s, depending on the filling gas mixture, have been measured and it is expected therefore that space charge limitations would begin to take effect at count rates > 2500 p.p.s. Hopefully some experimental work can be done on this in the near future.

#### 9.3.2 Further work with the Al-K source

The limited work carried out with Ar/75%CH<sub>4</sub> as a filling gas has been particularly interesting because of the apparently low diffusion which occurs. It would be appropriate now to continue this work with the 1.5keV source and thereby take advantage of the resulting reduction in collimator spread.

Similarly, as mentioned in Sections 8.5 and 8.6, the 1.5keV source could very usefully be employed in chamber geometries with wider spaced anodes and particularly in single wire chambers, where it is imperative that absorption should take place near the cathode to avoid the effects of the radial field.

### 9.3.3 Greater chamber depths

The requirement imposed by the theoretical model that  $h \gg s$ , has not been fully satisfied at any time during this work, where  $h/s$  has usually been equal to 2.22. Better results may be obtained with deeper chambers having a larger linear field region, although any improvement may be offset by increased diffusion over longer drift paths.

### 9.3.4 Use of heavier gases

Cost considerations have ruled out the use of xenon and krypton in flow chambers, and since lighter gases have been investigated the work could now be extended towards the use of mixtures containing heavier gases. This will be a large undertaking requiring the use of specially designed, sealed chambers, but the work is essential if X-radiation up to 30keV is to be efficiently detected.

### 9.3.5 Rise time and crossover detection

It has been noticed that the rise time, and hence the crossover time of a doubly differentiated induced pulse, is to some extent dependent upon  $x_0$ , and also, so far as the induced cathode pulses are concerned, upon whether absorption takes place above or below the anode plane. The photograph in Fig. 9.1 was taken, of the induced cathode pulses after singly integrating and doubly differentiating with equal time constants of  $10\mu s.$ , using the original chamber filled with P.10. The two distinct crossover times represent absorption above and below the anode plane with the  $^{55}\text{Fe}$  source at  $x_0 = 0$ . Further work is presently under way in the Physics Department to investigate rise time effects more fully.

## 9.4 Applications

The most obvious application of angular localisation is to X-ray imaging or position-sensitive detection of particles by inter-anode interpolation. Some other less obvious applications are now

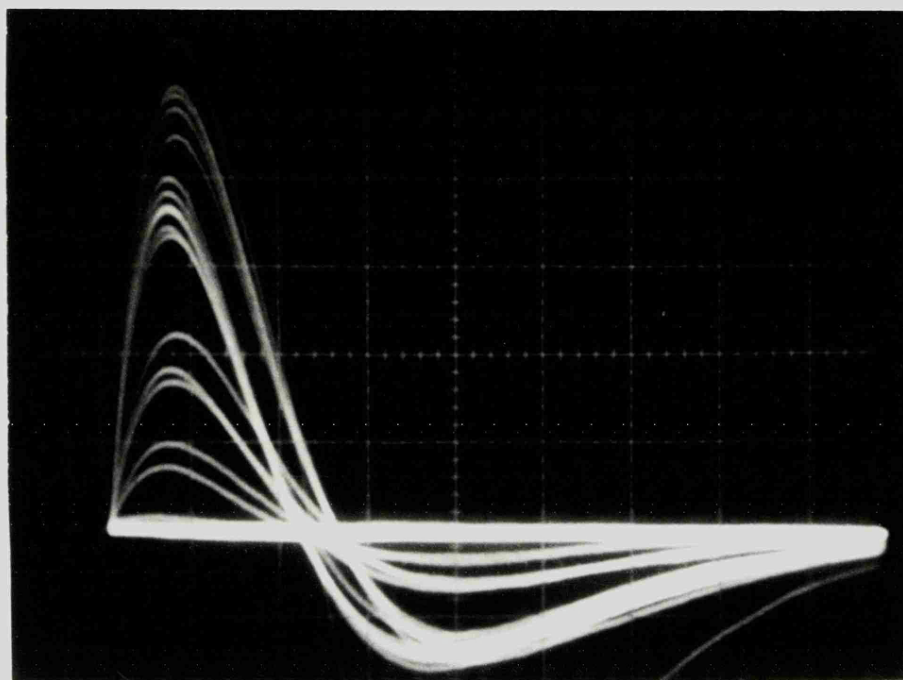


FIG. 9.1—

THE INDUCED CATHODE PULSE  
AFTER BIPOLAR SHAPING.

Fe-55 SOURCE POSITION  $x_0=0$ .

$T = 10\mu s$

TIME CAL. —  $10\mu s/\text{division}$

GAS — P.10.

briefly suggested.

#### 9.4.1 Background reduction

During experimental work with induced cathode pulses the possibility of using angular localisation for background reduction was briefly investigated and a description follows:

An  $^{55}\text{Fe}$  source mounted directly above the avalanche anode produces two peaks in the spectrum of  $(v_c - v_c')/(v_c + v_c')$  due to absorption above and below the anode plane. These peaks move towards one another as  $x_0$  is changed, but are always individually distinguishable. If the avalanche totally surrounds the anode wire then  $v_c = v_c'$  and the pulse height spectrum reduces to a single central peak. It is likely that something near to this latter situation exists when distributed ionisation occurs, possibly with delta-ray production, due to background radiation.

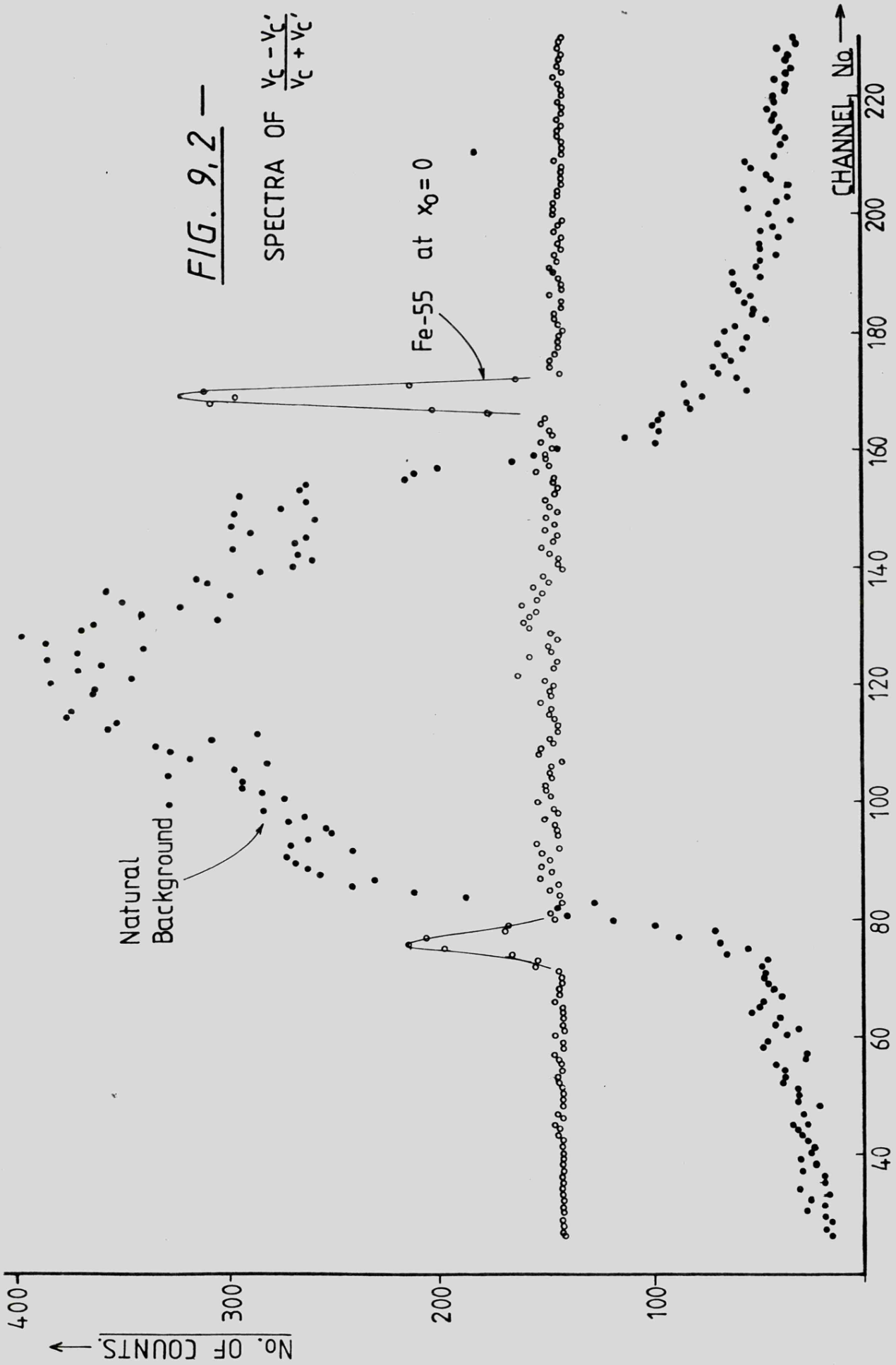
The principle is seen more clearly in Fig. 9.2 where spectra of  $(v_c - v_c')/(v_c + v_c') + K$  ( $K$  is a constant voltage added to ensure that the quantity is always positive) for naturally occurring background and for collimated X-rays at  $x_0 = 0$ , are shown. A single channel analyser, with upper and lower levels set just within the X-ray peaks, could now be arranged to reject most of the background without affecting too much the X-ray acceptance.

Practically, however, it would be unreasonable to use a collimated beam of X-rays and so the curve of Fig. 9.3 has been determined experimentally to show the effect of using a single channel analyser on spectra of the type shown in Fig. 9.2 but with an X-ray beam unrestricted by collimation.

The background reduction is not outstanding, but in conjunction with some amplitude rejection above and below 6keV, much improved results are possible.

FIG. 9.2 —

SPECTRA OF  $\frac{V_C - V_C'}{V_C + V_C'} + K$



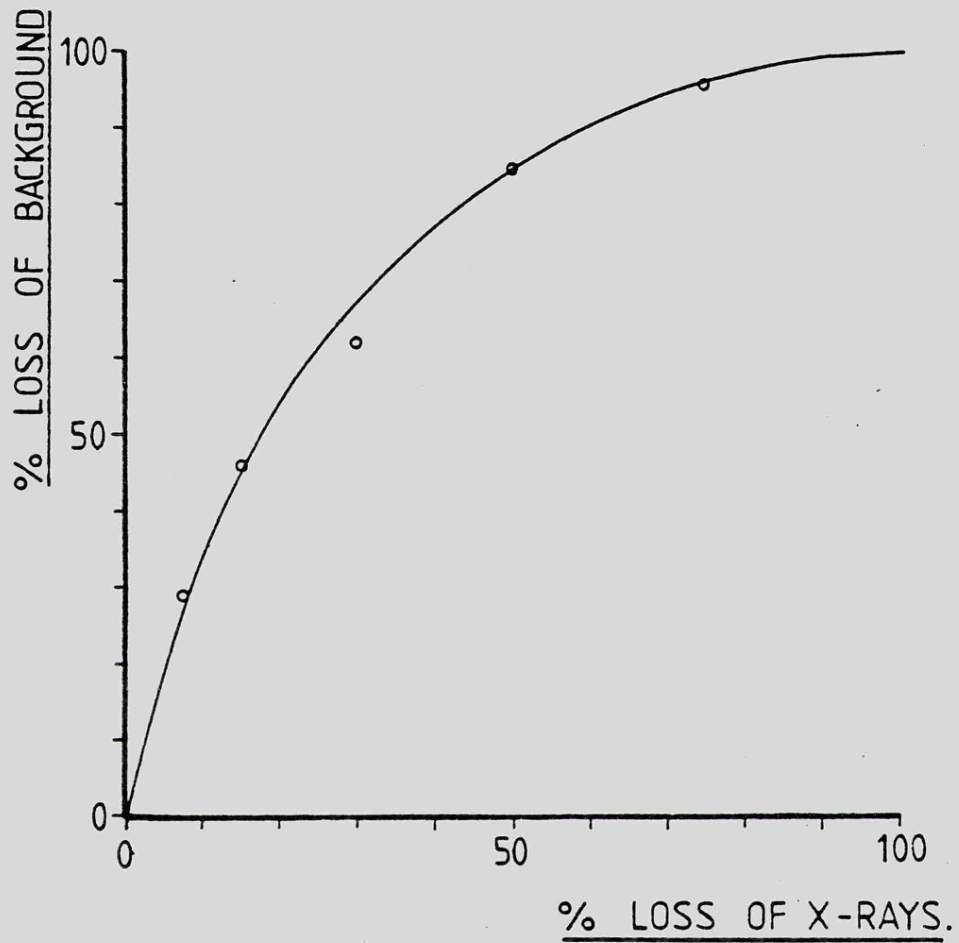


FIG. 9.3. —

EXPERIMENTAL CURVE TO SHOW THE  
EFFECTS OF DISCRIMINATING AGAINST  
BACKGROUND UPON AN UNCOLLIMATED  
SOURCE OF 6 keV. X-RAYS.

#### 9.4.2 Left-right discrimination

The induced signals on the anodes on either side of an avalanche anode may be used to effectively determine from which side electrons are drifting. The polarity of the difference signal indicates which sense anode is the more positive and therefore, on which side of the avalanche anode the avalanche is localised. This method has been used<sup>(55)</sup> to overcome the left-right ambiguity which occurs in drift chambers.

#### 9.4.3 Absorption depth discrimination

The ratio of induced cathode signals  $v_c/v_c'$  may also be used to discriminate between events occurring above and below the anode plane. The ratio is always greater than unity for absorption above the anode plane and less than unity for absorption below the anode plane.

Rise time measurement may also be used for absorption depth discrimination purposes<sup>(71)</sup>. From the photograph in Fig. 9.1 one can visualise how a crossover detector might be used to effectively provide discrimination between upper and lower events.

#### 9.4.4 X-Ray imaging

Multiwire chambers have probably found their most important application as X-ray imaging detectors in biology, medicine and X-ray astronomy. In biology and medicine, they take over from scintillation cameras in detecting X-rays and low energy  $\gamma$ -rays and may be used to provide large area, rapid readout. In X-ray astronomy they have replaced slow scanning techniques and facilitated the rapid accumulation of data during costly flight programmes.

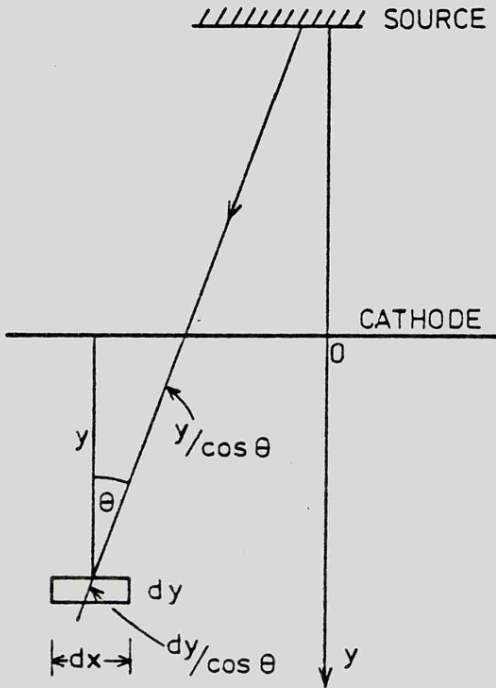
Angular localisation techniques offer similar resolution capabilities to multiwire chambers and drift chambers and in the latter case offer a much improved time resolution. It is hoped now that these techniques may be further developed to provide a larger sensitive area

of detection. With the promise of reduced complexity of external electronic circuitry which offers a great advantage in economy and reliability, so important in the above fields, this must surely be a worthwhile area for continuing research.

\*\*\*\*\*

APPENDIX I

THE CHAMBER RESPONSE DUE TO A SLIT COLLIMATOR.



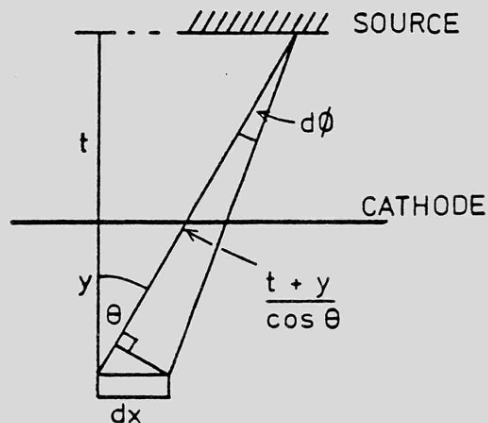
In determining the response of the chamber due to the collimated source, two effects have been considered. Firstly the effect of linear absorption in the chamber and secondly the geometrical arrangement of the source collimator and chamber with respect to one another. No account is taken of the third dimension along the collimator slit, but with high aspect ratio of collimator slit length to slit width, this effect may be ignored.

Consider a small section of chamber of width  $dx$  and thickness  $dy$  and infinite depth.

The X-ray path length within the strip =  $dy/\cos \theta$   
 and the probability of an interaction within the strip,

$$= e^{-\lambda y/\cos \theta} \cdot \lambda dy/\cos \theta$$

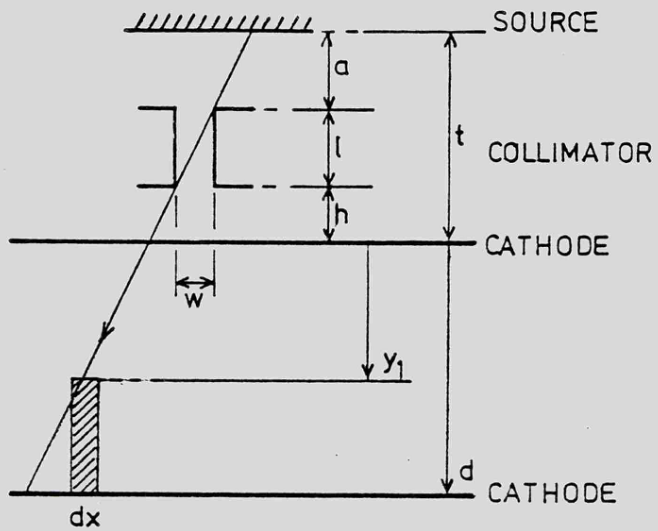
where  $\lambda$  is the linear absorption coefficient.



The angle subtended by  $dx$  at the source =  $d\phi = dx \cos \theta$ .  $\frac{\cos \theta}{t+y}$

$$= \frac{dx \cos^2 \theta}{t+y}$$

The general equation for the number of interactions,  $n$  in the strip of width  $dx$  and height  $(d - y_1)$  may now be written,



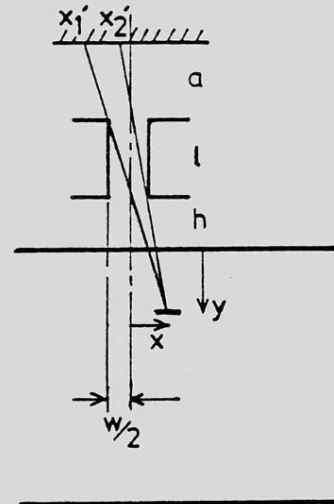
$$n = B \int_{y_1}^d \int_{x_1'}^{x_2'} \frac{dx \cos^2 \theta}{t+y} \cdot e^{-\lambda y / \cos \theta} \cdot \lambda \frac{dy}{\cos \theta} dx'$$

where  $B$  = no. of emissions per unit angle from the source.

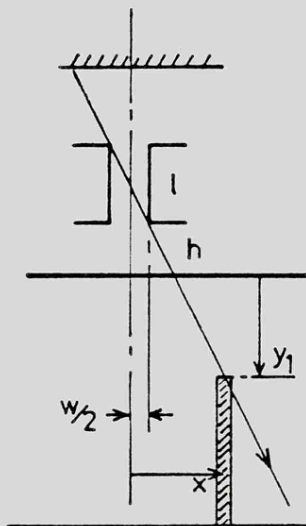
The equation may be evaluated in two parts representing the two regions  $x \geq w/2$  and  $-w/2 \leq x \leq w/2$ , by integrating within the limits shown. For  $x \geq w/2$  it can be simply shown that

$$x_1' = w/2 - (a + l) \cdot \frac{x - w/2}{h + y}$$

$$x_2' = -w/2 - a \left( \frac{x + w/2}{l + h + y} \right) \quad x_1' \geq x_2'$$



$$y_1 = (x - w/2) \frac{l}{w} - h$$

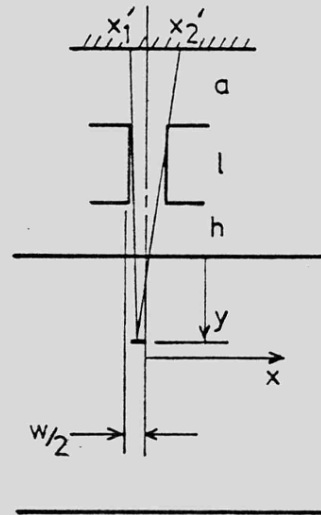


For  $-w/2 \leq x \leq w/2$ ,

$$x'_1 = \frac{w}{2} + a \left( \frac{w/2 - x}{\ell + h + y} \right)$$

$$x'_2 = \frac{-w}{2} - a \left( \frac{x + w/2}{\ell + h + y} \right)$$

$$y_1 = 0$$



APPENDIX 2

ANGULAR LOCALISATION OF PROPORTIONAL CHAMBER AVALANCHE -

E.Mathieson and T.J.Harris

Reprinted from Nature, Vol. 272, No. 5655, p. 709, 20 Apr. 1978.

(Reprinted from Nature, Vol 272, No. 5655, pp. 709-710, April 20, 1978)

© Macmillan Journals Ltd., 1978

## Angular localisation of proportional chamber avalanche

CHARPAK<sup>1</sup> points out in his review on multi-wire proportional chambers, that despite previous considerations<sup>2</sup> there is some evidence that the discharge in a proportional chamber does not necessarily spread uniformly round the wire. We have been examining in some detail avalanche localisation in proportional chamber operation during the past year or so, and give here a brief quantitative account of some of our findings. These were initially rather unexpected.

The most striking evidence of avalanche localisation is obtained from observations of the charges induced on neighbouring wires. These form particularly sensitive probes for examining the avalanche position, and chamber geometry and operation are not disturbed in any way. The situation is shown schematically, but not to scale, in Fig. 1, where A is the particular wire at which avalanche occurs and B is an adjacent wire at the same potential. A and B are connected to charge-sensitive amplifiers, of conversion gain  $1/C$ , followed by pulse shaping networks. A positive ion of charge  $q$  starting at time  $t = 0$  at the surface of wire A, at angular position  $\alpha$ , will drift away from A along the field line defined by  $\alpha$  with velocity proportional to the local field value. The induced charges  $q_B$  and  $q_A$  may then be calculated by standard electrostatic theory as a function of the position of  $q$  and hence as a function of  $t$ . As in the creation of the positive ion charge  $q$ , an equal negative, electron charge  $-q$  must have been deposited at  $t = 0$  on wire A, the charge-sensitive amplifier output voltages are  $-q_B/C$  and  $(-q_A - q)/C$ . The pulse heights  $v_B$  and  $v_A$  from the pulse shaping networks may thus be calculated as a function of the starting angular position  $\alpha$ . These calculations may be extended to describe the effect on  $v_B$  and  $v_A$  of an initial angular distribution of positive ion charge.

The important experimental observation, Fig. 2, is that the observed ratio  $-v_B/v_A$  depends strongly upon the  $x$ -coordinate of a finely collimated soft X-ray beam, showing that the angular distribution of the positive ions round the wire is non-uniform and that the angular centroid of the distribution depends on the direction from which the initiating electrons have drifted. For normal chamber geometry the field lines near the cathode have equation  $x = s(1 - 2\alpha/\pi)/2$  independent of  $y$ , where  $s$  is the anode wire spacing. Thus

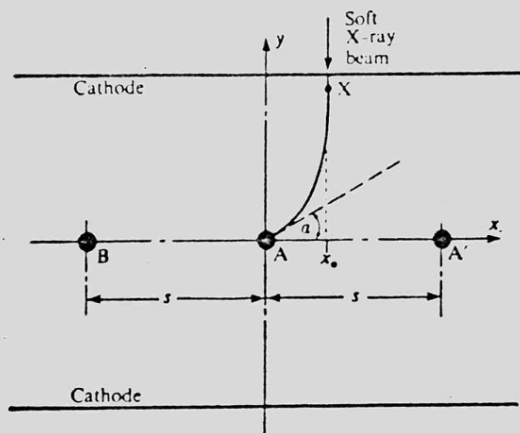


Fig. 1 Schematic diagram of conventional multi-wire proportional chamber. The angular position of the avalanche on wire A is obtained from measurement of the induced charge signal on wire B.

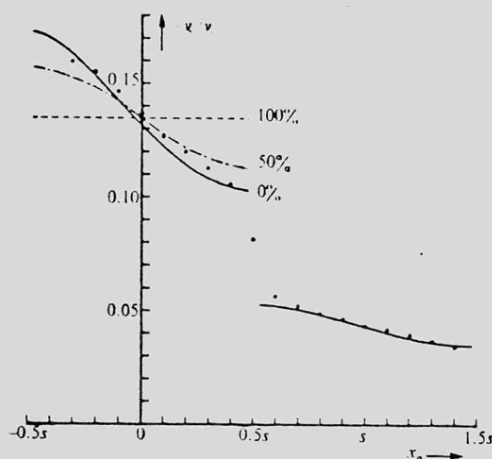


Fig. 2 Experimental measurements of the ratio of pulse heights  $-v_B/v_A$  in the charge-sensitive pulse shaping systems connected to wires B and A, plotted against X-ray beam position  $x_0$ . The curves are theoretical predictions for rectangular distributions spreading round 0%, 50% and 100% of the anode wire circumference.

for absorption of a soft X-ray photon at the point X, coordinate  $x_0$  in Fig. 1, the initial electrons drift along the field lines indicated and, ignoring diffusion, the angular centroid of the resultant avalanche at the wire A is  $\alpha = \pi(1 - 2x_0/s)/2$ .

Figure 2 shows experimental measurements of  $-v_B/v_A$  plotted against  $x_0$ , the  $x$ -coordinate of an X-ray beam of energy 5.9 keV and collimated width 0.2 mm. The chamber cathode-anode separation was 11 mm, the anode wire separation,  $s$ , 5 mm and the diameter of the anode wires 25  $\mu\text{m}$ . The chamber gas was argon/10% methane at atmospheric pressure. The pulse shaping networks consisted of passive, single RC integrating and differentiating circuits of equal time constant, 10  $\mu\text{s}$ . The full curve is the result of calculations using the model described above, with zero angular spread. Also indicated on Fig. 2 are the theoretical predictions for rectangular positive ion distributions spreading round 50% and 100% of  $2\pi$  (that is, a completely uniform spread). If  $x_0$  exceeds  $s/2$  then the avalanche switches over to the next wire A'. It is interesting that the wire B can still sense to some extent the avalanche position on A'. This is shown by the non-zero slope of the lower set of experimental results representing  $-v_B/v_A$ . The full curve is again the theoretical prediction, with zero angular spread.

Such measurements show the surprising degree to which angular localisation of the avalanche occurs, despite the diffusion which must occur during electron drift. Possible extensions of imaging MWPC operation are suggested as a result of these investigations (such as positional interpolation between anode wires). A detailed report of this experimental and theoretical work and of similar investigations on cathode-induced signals is being prepared.

E. MATHIESON  
T. J. HARRIS  
G. C. SMITH

Physics Department,  
The University,  
Leicester, UK

Received 16 December 1977; accepted 1 February 1978.

1. Charpak, G. *Nature* 270, 479-482 (1977).
2. Charpak, G., Rohm, D. & Steiner, H. *Nucl. Instrum. Meth.* 80, 13-14 (1970).

APPENDIX 3

INDUCED CATHODE SIGNALS IN MULTIWIRE CHAMBERS -

T.J.Harris and E.Mathieson.

Paper read at 3rd Int. Conf. on "Drift and Proportional Chambers",  
Dubna, U.S.S.R., June 1978.

Induced cathode signals in multi-wire chambersAbstract

Experimental measurements have been made of the ratio of the signals induced on the cathodes of a symmetric multi-wire proportional chamber under X-ray irradiation. Because of angular localisation of the avalanche at the anode wire this ratio is expected to depend strongly on the lateral position of the X-ray beam. The predictions of a simple theoretical model are in good agreement with the experimental results.

T. J. Harris  
E. Mathieson

Physics Department  
Leicester University  
Leicester  
England

1. Introduction It has become clear recently<sup>1-5</sup> that for a localised ionising event, i.e. soft X-ray photon absorption, the resulting avalanche at a proportional chamber anode wire may exhibit a correspondingly high degree of angular localisation. This localisation influences markedly the induced charges on neighbouring anode wires and on the cathodes. The effect may have considerable implications on the position-sensitive performance for soft X-rays of proportional chambers. In preliminary investigations of two aspects of this new mode of extracting positional information, rms resolution orthogonal to the anode wire direction better than  $150 \mu\text{m}$  has been achieved<sup>4,5</sup>.

This present paper describes some experimental measurements on the signals induced on the two cathodes of a symmetric multi-wire chamber as a function of the lateral position of a collimated soft X-ray beam. These experimental results are compared with the predictions of a theoretical model<sup>6</sup>.

2. Theoretical considerations Fig. 1 is a schematic of a conventional multi-wire chamber with anode wire spacing  $s$  and anode-cathode separation  $h$ . The anode wires are perpendicular to the  $x$ - $y$  plane with the particular wire at which avalanche occurs at the origin. The X-ray beam is parallel to the  $y$ -axis and has  $x$ -coordinate  $x_0$ .

For normal chamber geometry there is a considerable fraction of the volume in which the field is very nearly uniform. Thus from a localised ionising event well away from the anode plane, at coordinate  $x_0$ , the electrons drift along a field line and result in an avalanche whose centre-of-charge has an angular position at the anode wire surface  $\alpha$  given by  $\alpha = \pi(1-2x_0/s)/2$ . Positive ions from the avalanche drift back along the field lines; from a knowledge of the ion mobility,

chamber geometry and chamber voltage it is therefore possible to calculate the time development of the induced charge  $q_c(t)$  at a chamber cathode. The appropriate formulae have been developed in Ref. 6.

If, as in the present case, the cathode is connected to a charge-sensitive pre-amplifier, of conversion gain  $1/C$ , then the pre-amplifier output is  $-q_c/C$ . Finally, if the amplifier pulse-shaping system has impulse response  $h(t)$ , then the final output signal of the system may be obtained from the convolution integral of  $-q_c(t)/C$  and  $h(t)$ . The peak height  $v_c$  of the signal may be calculated in this way (see Ref. 5).

In the present system a single differentiating filter and a single integrating filter of time-constant  $T$  was used. It has already been shown, in Ref. 5, that in the calculation of the position of the positive inducing charge there emerges a natural unit of time  $T_0 = s^2/\mu V_a$  where  $\mu$  is the ion mobility (assumed constant in the present report) and  $V_a$  is the chamber voltage. The normalised filter time-constant  $T/T_0$  is found to be an important system parameter.

3. Experimental arrangement The measurements presented below were taken with a small, symmetric chamber with eleven anode wires, with  $s = 5$  mm and  $h = 11$  mm. The operating gas was argon/10% methane at atmospheric pressure. Well-matched signal processing systems were attached to each cathode, with the value of  $T$  in each shaping amplifier  $10 \mu s$ . A dividing circuit yielded pulses of height  $v_c/v'_c$ , the ratio of the pulse heights in the two cathode channels, Fig. 2. The effect of different sensitivities in the two channels could be eliminated by interchanging the signal processing systems.

The position of the 5.9 keV X-ray beam could be set to within  $10 \mu m$ ; the geometry and height of the collimator resulted in a beam width at the anode plane of  $200 \mu m$ .

In the measurements presented below the chamber was operated at 2.5 kV, resulting in a gas gain of approximately  $10^4$ .

4. Results A spectrum of the ratio of cathode signals, for  $x_0 = 0$  is shown in Fig. 3(a). The two peaks represent absorption events occurring above the anode plane at  $\alpha = +90^\circ$  and below the anode plane at  $\alpha = -90^\circ$ , the ratio of intensities being closely in accord with the attenuation over 11 mm of 5.9 keV X-rays in the chamber gas. As  $x_0$  is increased from zero the maximum value of  $\alpha$  decreases; the two distributions approach each other as shown in Fig. 3(b), for  $x_0 = 0.40$  s.

If one assumes that absorption occurs in the essentially uniform field regions of the chamber, i.e. that the coordinate  $x_0$  of the X-ray beam uniquely defines  $\alpha$ , then the theoretical model outlined above can be employed to calculate  $v_c/v'_c$ . Further, a simple extension of the calculations allows an initial angular distribution of the positive ions at the anode wire surface to be taken into account. The experimental results are compared with theoretical predictions in Fig. 4 where the value  $T/T_0 = 0.16$  has been used, corresponding to  $\mu = 1.6 \text{ cm}^2/\text{Vs}$ . The high degree of angular localisation is very evident in these results. The curve passing closely through the experimental results represents a gaussian initial angular distribution with standard deviation  $33^\circ$ . This is very similar to a value  $30^\circ$  estimated recently by Charpak<sup>4</sup> for a similar geometry chamber ( $h = 8$  mm compared with 11 mm in the present work).

5. Discussion The main purpose of this brief paper has been to present preliminary measurements of the degree to which angular localisation occurs in the avalanche process in proportional chambers and counters. There appears to be fairly satisfactory agreement between theoretical model and experimental results, as represented by Fig. 4.

Presumably the divergence near  $x_0 = s/2$  is partly due to the finite beam width and partly to departure from the uniform field assumption.

A very rough estimate of the effect of diffusion may be made by considering the initial electron group to drift from cathode to anode in a uniform field. If this were the case then the rms radius of the electron group would be  $\sigma_x = \sqrt{(2Dh/v)}$  where  $D$  is the diffusion coefficient and  $v$  the drift velocity. Substituting approximate numerical values  $D \sim 10^{-2} \text{ cm}^2/\mu\text{s}$  and  $v \sim 5 \text{ cm}/\mu\text{s}$  then for  $h = 1 \text{ cm}$  we have  $\sigma_x = 0.65 \text{ mm}$ . The finite beam width  $200 \mu\text{m}$  then yields a resultant of about  $0.68 \text{ mm}$ . From the relationship between  $x_0$  and  $\alpha$  given above we can thus estimate  $\sigma_\alpha \sim 25^\circ$ . This is reasonably close to the experimental value  $33^\circ$  obtained above.

There are of course several aspects to be examined critically, in detail, before real confidence can be placed on the quantitative evaluation of  $\sigma_x$ . The numerical result clearly depends upon the assumed figure for positive ion mobility  $\mu$ . In reality ionic mobility is field dependent<sup>8</sup> and further, due to charge exchange, the actual nature of the ion may change with time. Thus  $\mu$  is actually a rather complicated function of field and time. A series of measurements are therefore being made over a range of time constants  $T$  in an effort to examine this situation in more detail. Measurements are also being made for a range of gas mixtures.

#### References

1. C.J.Borkowski and M.K.Kopp I.E.E.E.Trans. on Nuclear Science NS24 No 1 (1977) 287.
2. G.Charpak Nature 270 (1977) 479.
3. E.Mathieson, T.J.Harris and G.C.Smith Nature 272 (1978) 709.
4. G.Charpak, G.Peterson, A.Policarpo and F.Sauli Nucl.Instr. & Meth. 148 (1978) 471.
5. T.J.Harris and E.Mathieson Nucl.Instr. & Meth. (in the press)

6. E.Mathieson and T.J.Harris Nucl.Instr. & Meth. (in the press)
7. R.Gott and M.W.Charles Nucl.Instr. & Meth. 72 (1969) 157.
8. S.C.Brown Basic data of plasma physics  
M.I.T. Press, Boston, 1966.

Figure Captions

Figure 1 Schematic of symmetric multi-wire chamber, anode wire spacing  $s$  and anode-cathode separation  $h$ . The narrow X-ray beam is parallel to the  $y$ -axis with  $x$ -coordinate  $x_0$ . The field line shown intersects the anode wire surface at an angle  $\alpha$  to the  $x$ -axis where  $\alpha = \pi(1-2x_0/s)/2$ .

Figure 2 Schematic of signal processing system.

Figure 3 Spectra of the ratio of cathode signals  
a)  $x_0 = 0$  , b)  $x_0 = 0.40 s$

Figure 4 Values of  $v_c/v'_c$  plotted as a function of  $x_0/s$ . The continuous curves are theoretical predictions representing gaussian initial positive ion angular distributions with standard deviations  $0^\circ$ ,  $33^\circ$  and  $60^\circ$ .

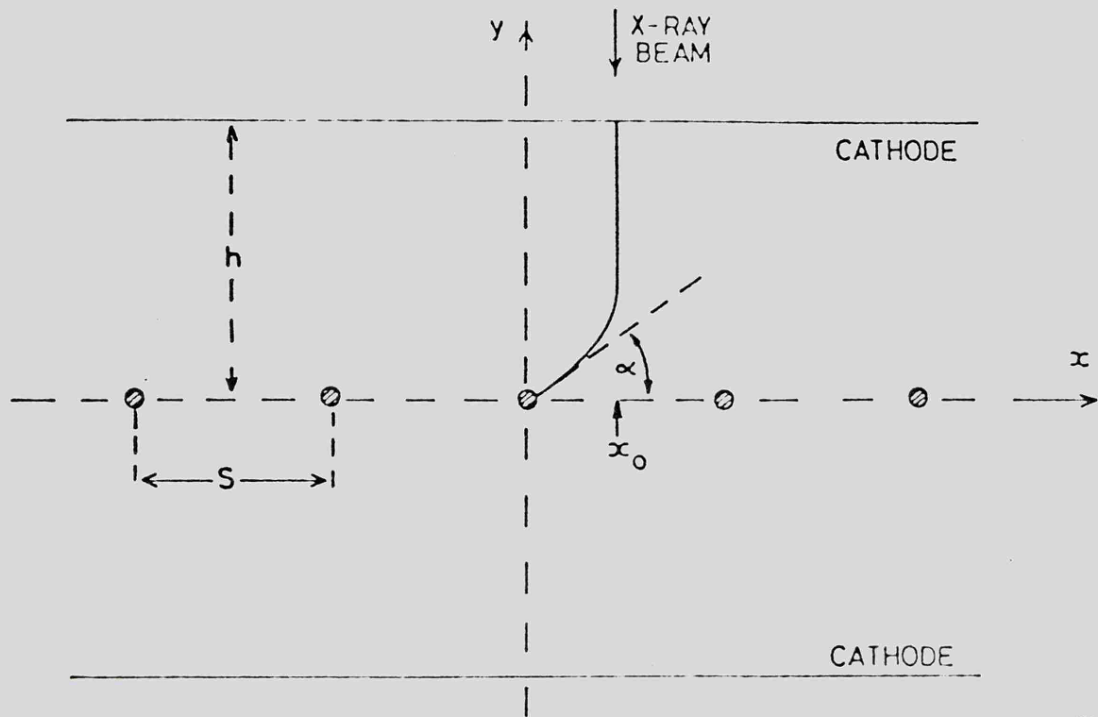


FIG. 1

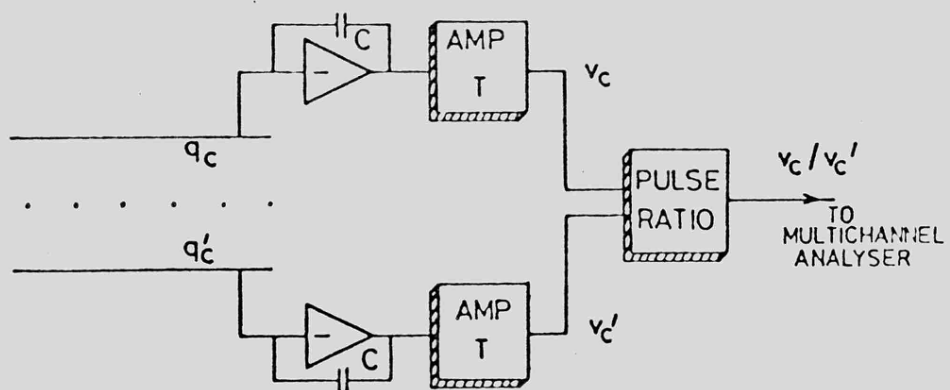


FIG. 2

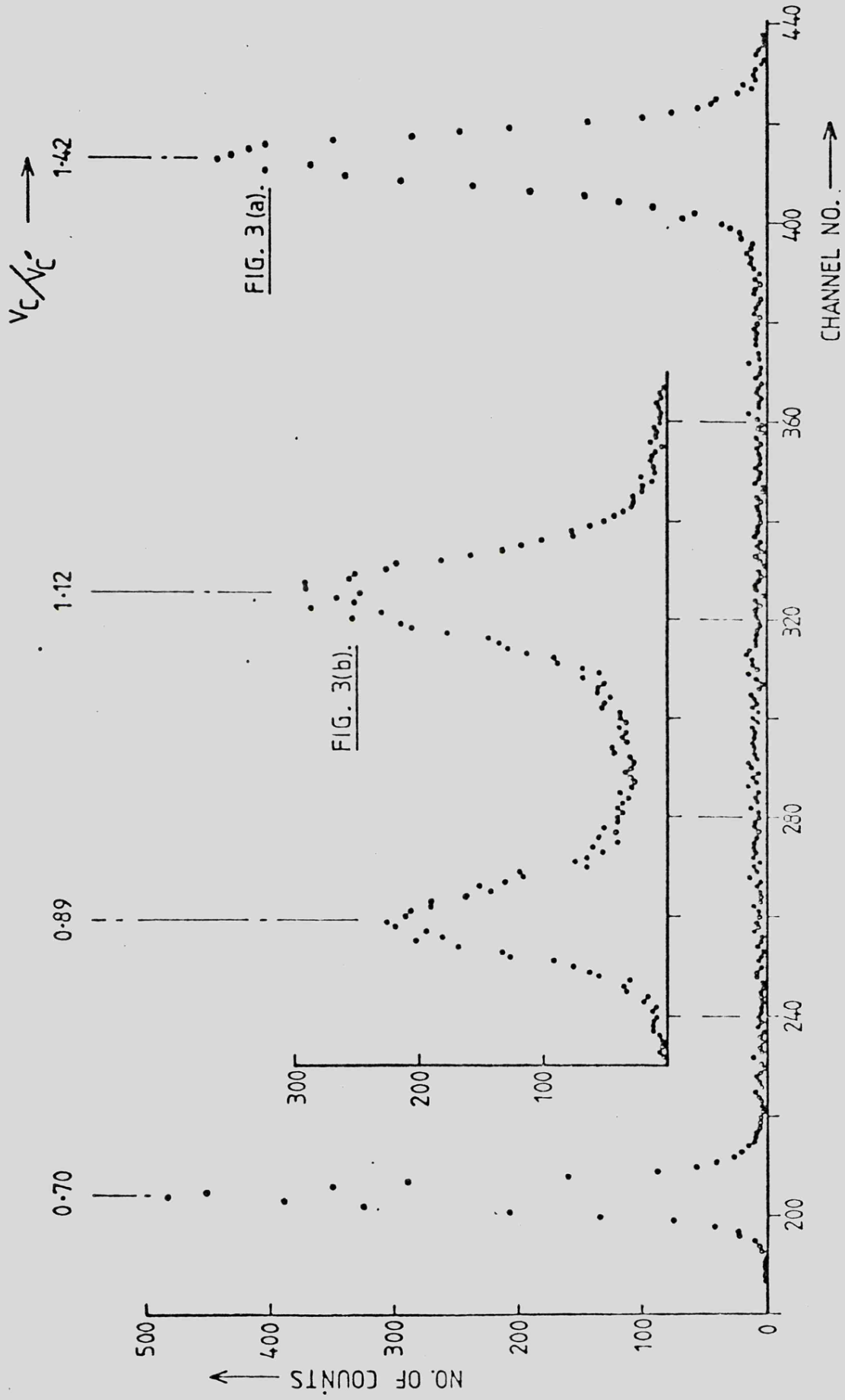
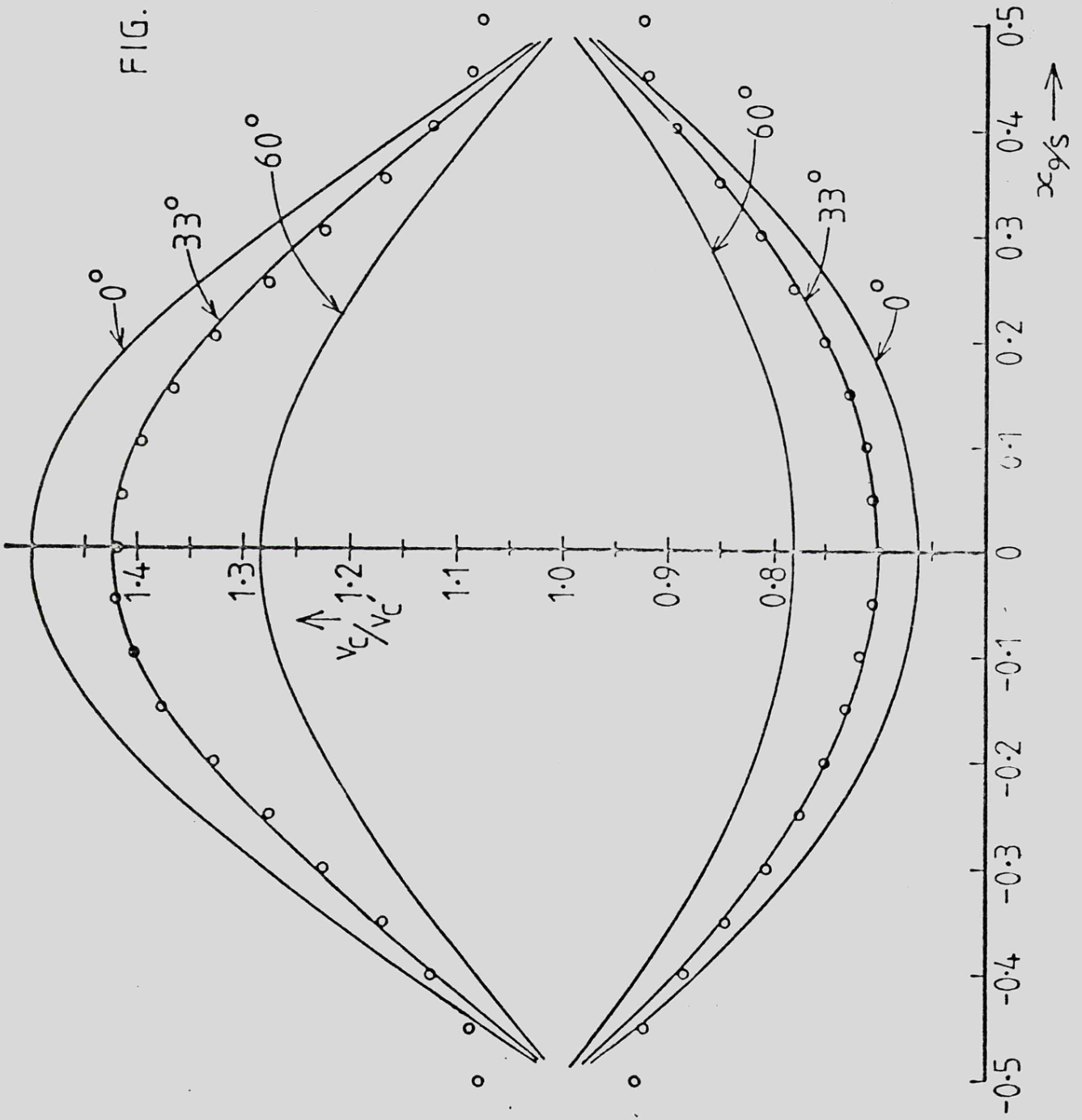


FIG. 4.



APPENDIX 4

ANGULAR LOCALISATION OF PROPORTIONAL CHAMBER AVALANCHE -

T.J.Harris and E.Mathieson

Reprinted from Nucl. Instr. and Meth., 154(1978)183.

## ANGULAR LOCALISATION OF PROPORTIONAL CHAMBER AVALANCHE

T. J. HARRIS and E. MATHIESON

*Physics Department, The University, Leicester, England*

Received 23 January 1978

Experimental evidence has been obtained which demonstrates that, under certain conditions, the avalanche at an anode wire of a proportional chamber may exhibit a high degree of angular localisation. One anode wire of a conventional multi-wire chamber has been employed to sense the angular position of the avalanche at an adjacent anode wire. Comparisons are made between these experimental measurements and the predictions of a theoretical model. Further experimental measurements are presented to demonstrate the feasibility of using this localisation effect to obtain positional interpolation between anode wires of an imaging chamber.

### 1. Introduction

During various experimental investigations in this department on imaging multi-wire proportional chambers it was noted that under certain conditions, apparently anomalous pulse heights and pulse shapes were obtained. These particular observations suggested that, surprisingly and contrary to previous description<sup>1)</sup>, the avalanche at an anode wire may be to some degree angularly localised. Other workers have also recently considered this possibility<sup>2)</sup>. The measurements and calculations described in this paper were undertaken to examine quantitatively this concept of a localised avalanche. A brief preliminary report of some of this work has already been given<sup>3)</sup>.

The situation can be briefly described as follows. Suppose initially that positive ions originate at a specific point on the anode wire surface. Then the trajectory of those ions can be followed and hence, in principle, the time development of the induced charge signal at any chamber electrode can be calculated. The final output signal, after filter circuits and amplification, thus depends in some predictable way upon the point or origin of the positive ions. Now if an avalanche results in a non-uniform distribution of positive ions around the anode wire then the output signal from the chosen electrode will depend upon the shape and position of this distribution as well as upon the avalanche magnitude. If one further assumes that the angular centre-of-charge of a non-uniform avalanche defines the field line along which the centroid of the initial electrons have drifted then a relationship is established between position of X-ray absorption and magnitude of induced charge signal. The validity of this theoretical prediction can be examined experimentally.

The present paper describes measurements of the induced charge signals at neighbouring anode wires. These form particularly convenient and sensitive probes for examining the avalanche position and of course chamber geometry and operation is not disturbed in any way. Possible extensions of imaging MWPC operation are suggested as a result of these investigations. Measurement and calculation of the induced charge signals at chamber cathodes will be described in a separate report.

### 2. Basic description of system

Fig. 1 is a schematic of a conventional, symmetric multi-wire proportional chamber with anode wire spacing  $s$  and anode-cathode separation  $h$ . The anode wires are perpendicular to the  $x$ - $y$  plane, with the particular wire, A, at which avalanche occurs at the  $x, y$  origin. In the measurements described below the induced charge signals on an adjacent wire, B, were examined as a function of the  $x$ -coordinate of a finely collimated soft X-ray beam.

With normal chamber geometry the field at the surface of an anode wire is very accurately radial and further, provided  $s$  is small compared with  $h$ , the field at the cathode surface is nearly uniform. This means that a set of equidistant field lines starting at the cathode end as equiangular field lines at the anode. Hence electrons produced in an ionising event occurring far from the anode plane (strictly speaking at the cathode surface) drift along a field line and result in an avalanche whose centre-of-charge has an angular position directly proportional to the  $x$ -coordinate of the event. The angular width of the distribution must depend upon the initial size of the electron group and upon the diffusion during drift.

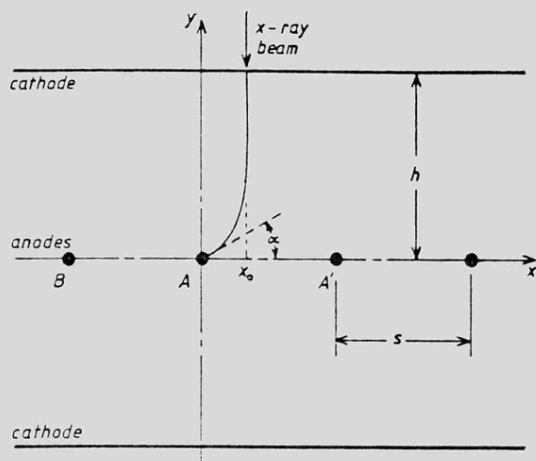


Fig. 1. Schematic diagram of conventional multi-wire proportional chamber. The induced charge signal on wire B depends upon the angular position of the avalanche on wire A.

Positive ions from the avalanche drift back along the field lines. From a given initial distribution of positive ions, and assuming a constant ion mobility, the time development of the induced charge at a neighbouring anode wire, or at a cathode, may be calculated. The appropriate formulae are given in the next section.

### 3. Theoretical considerations

Application of standard electrostatic theory shows that for the chamber geometry represented in fig. 1, provided  $r_a \ll s$  (where  $r_a$  is the anode wire radius) and  $s \ll h$ , then the field can be described by the complex potential  $W$  given by

$$W = V_a \frac{\pi h/s - \log 2 \sin \pi z/s}{\pi h/s - \log 2\pi r_a/s}$$

here  $V_a$  is the potential of the anode wires, the cathodes being earthed, and  $z = x + jy$ . It follows from the above expression that a field line originating at the anode wire A has equation

$$\tanh \pi y/s = \tan \alpha \tan \pi x/s,$$

where  $r_a \cos \alpha$ ,  $r_a \sin \alpha$  are the cartesian coordinates of the intersection of the field line with the surface of the anode wire. For regions well away from the anode plane, i.e. where  $y \gg s$ , the field line equation reduces to

$$x = \frac{s}{2} \left( 1 - \frac{\alpha}{\pi/2} \right), \quad \text{independent of } y,$$

showing the linear relationship between lateral position  $x$  of the field line near the cathode and the angular position  $\alpha$  at the anode surface (fig. 1).

A positive ion starting at the anode surface of wire A at angular position  $\alpha$  drifts along the field line with velocity  $\mu E$ , where  $\mu$  is the (constant) positive ion mobility and  $E$  is the field intensity.  $E$  may be obtained from the above expression for complex potential

$$E = \frac{V_a}{s} \frac{s/h}{1 - s/\pi h \log 2\pi r_a/s} \left\{ \frac{\cosh 2\pi y/s + \cos 2\pi x/s}{\cosh 2\pi y/s - \cos 2\pi x/s} \right\}^{1/2}$$

Thus the coordinates  $(x, y)$  of the ion as a function of time  $t$  can be calculated progressively, numerically, by solving simultaneously the equations

$$\frac{1}{s} \left\{ \left( \frac{dx}{dt} \right)^2 + \left( \frac{dy}{dt} \right)^2 \right\}^{1/2} = \frac{\mu E}{s}$$

and

$$\frac{dy}{dx} = \tan \alpha \left\{ \frac{\cosh \pi y/s}{\cos \pi x/s} \right\}^2$$

with the initial conditions  $x = r_a \cos \alpha$ ,  $y = r_a \sin \alpha$  at  $t = 0$ .

It should be especially noted that when  $E$  is substituted in the velocity expression there emerges a natural unit for time,  $s^2/\mu V_a = T_0$ , say. It is thus very convenient during calculations to normalise time to this unit. It will also be noticed that all distances can be conveniently expressed as multiples of the anode wire spacing  $s$ .

The position of a positive ion having been calculated as a function of time, it is possible to calculate the charge induced on one of the anode wires using the following formulae. Let  $Q$  be the positive ion charge, at position  $x, y$ . Then, assuming as before that  $r_a \ll h$ , the charge  $q_k$  induced on the  $k$ th anode wire is given by

$$q_k = -Q \sum_{n=-l}^{n=l} C_n L_n \quad l \gg k$$

where

$$L_n = \log \left\{ \frac{\cosh \pi(x - ns)/2h + \cos \pi y/2h}{\cosh \pi(x - ns)/2h - \cos \pi y/2h} \right\}^{1/2}$$

In this formula  $C_n$  is the solution vector of the matrix equation

$$P_m = \sum_n C_n L_{nm}$$

where

$$L_{nm} = \log \left\{ \frac{\cosh \pi(m-n)s/2h + 1}{\cosh \pi(m-n)s/2h - 1} \right\}^{1/2}, \quad m \neq n,$$

$$L_{mm} = \log(4h/\pi r_a)$$

and

$$P_m = 0, \quad m \neq k, \quad P_k = 1.$$

## ANGULAR LOCALISATION

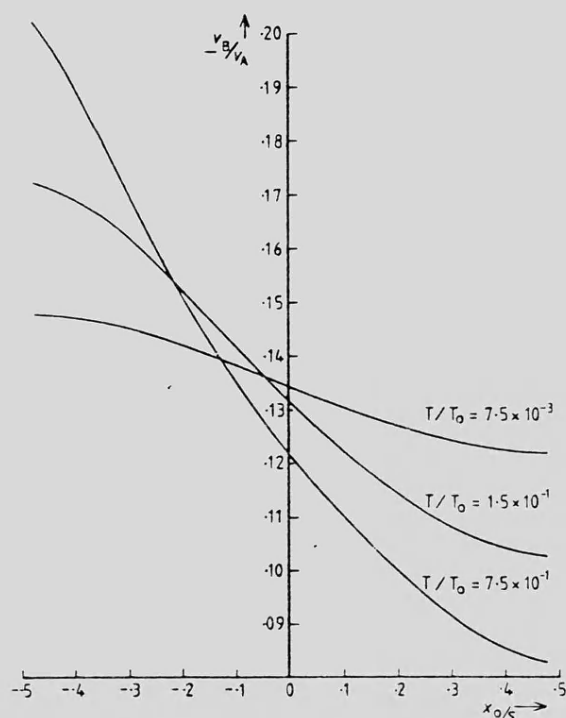


Fig. 2. Theoretical values of the ratio of pulse heights,  $-v_B/v_A$ , in the charge-sensitive pulse shaping systems connected to wires B and A, plotted against  $x_0 = (1 - 2\alpha/\pi)s/2$ . Curves are shown for several values of normalised time constant  $T/T_0$ . The calculations are for zero angular spread.

If, as in the measurements described below, the  $k$ th wire is connected to a charge-sensitive pre-amplifier of conversion gain  $1/C$ , then the pre-amplifier output is a voltage signal  $v(t) = -q_k/C$ . Finally, if the amplifier-pulse shaping system has impulse response  $h(t)$  then the final output signal of the system connected to the  $k$ th anode wire may be obtained from the usual convolution integral

$$v_0(t) = \int_0^t v(t') h(t-t') dt'.$$

The peak height  $v_B$  of the signal may thus be calculated. In the present work a single differentiating filter and a single integrating filter of equal time constant  $T$  was used so the  $h(t) = e^{-tT}(1-t/T)/T$ .

In order to remove the dependence on positive ion charge magnitude  $Q$  the output signal amplitude  $v_B$  from the 'sense' wire B ( $k = -1$ ) was compared with the output signal amplitude  $v_A$  from an identical processing channel connected to the 'avalanche' wire A ( $k = 0$ ). The signal  $v_A$  can of course also be calculated using the formulae

above, with  $k = 0$ , and remembering that the avalanche wire collects at  $t = 0$  a real negative (electron) charge  $-Q$ . Thus for the A wire pre-amplifier  $v(t) = (-Q - q_k)/C$ , and clearly the ratio  $-v_B/v_A$  does not contain  $Q$ . Using the formulae given above the theoretical ratio  $-v_B/v_A$  has been calculated as a function of  $\alpha$  the angular position of origin of positive ion charge at the anode wire A. The calculations are easily extended to take into account an initial angular distribution of ion charge round the wire. In the present case a uniform distribution spreading round a fraction  $f$  of  $2\pi$  has been assumed. As  $f$  increases, the dependence of  $-v_B/v_A$  upon the angular position  $\alpha$  of the centre-of-charge becomes weaker; clearly when  $f = 1$  the ratio  $-v_B/v_A$  becomes independent of  $\alpha$ .

If X-ray absorption occurs well away from the anode plane then angular position  $\alpha$  results from electrons generated at linear position  $x_0 = (1 - 2\alpha/\pi)s/2$ . Fig. 2 shows theoretical values of  $-v_B/v_A$ , for  $f = 0$ , plotted therefore as a function of  $x_0$ , for various values of normalised shaping circuit time constant  $T/T_0$ .

#### 4. Experimental arrangement

The measurements presented below were taken with a small multi-wire chamber, internal dimensions  $8\text{ cm} \times 12\text{ cm}$ , with  $11\text{ mm}$  between anode plane and each cathode plane. There were eleven anode wires, the central nine being  $25\text{ }\mu\text{m}$  diameter gold-plated tungsten and the two outer wires  $125\text{ }\mu\text{m}$  diameter stainless steel. The central five wires were spaced at  $5\text{ mm}$  and, in order to control the field at the anode edges, the outer three on each side were spaced at the reduced value  $2.5\text{ mm}$ . The cathodes were of aluminised melinex  $12\text{ }\mu\text{m}$  thickness. The operating gas, argon plus  $10\%$  methane at atmospheric pressure, could flow on both sides of the cathodes, there being separate gas-containing melinex windows.

In practice it was convenient to operate the anode at ground potential with the cathodes at negative HT. Each of the central three anode wires, B, A and A' of fig. 1, was directly coupled to a low-noise charge-sensitive pre-amplifier, Ortec type 118A, and also grounded through a  $100\text{ M}\Omega$  resistor. All other anode wires were directly grounded. The main amplifiers had single differentiating and single integrating shaping networks of equal time constant which could be varied in the range  $0.5\text{ }\mu\text{s}$  to  $10\text{ }\mu\text{s}$ . In all the measurements described below  $10\text{ }\mu\text{s}$  was employed.

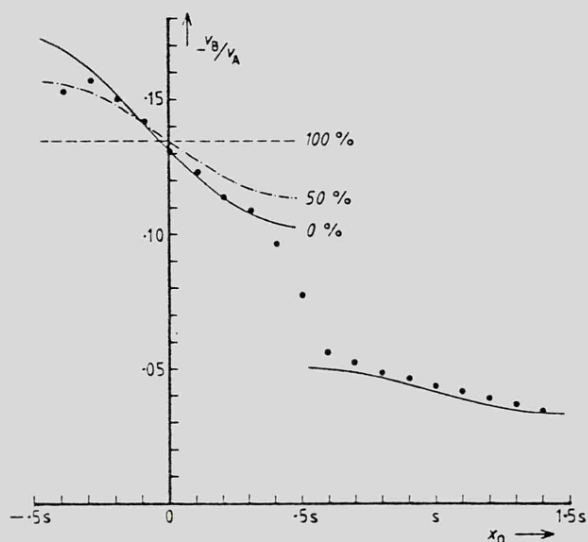


Fig. 3. Experimental measurements of  $-v_B/v_A$  plotted against X-ray beam position  $x_0$ . The curves are theoretical predictions, at  $T/T_0 = 0.15$ , for rectangular distributions spreading round 0%, 50% and 100% of the anode wire circumference.

Collimated X-radiation at 5.9 keV was obtained from an  $^{55}\text{Fe}$  source and a slit collimator, both mounted on a carriage which could be traversed, by means of a micrometer screw, across the chamber in a direction perpendicular to the anode wires. The position of the X-ray beam,  $x_0$  in fig. 1, could be set to within  $10\ \mu\text{m}$ ; the geometry and height of the collimator resulted in a beam width at the anode plane of  $200\ \mu\text{m}$ .

## 5. Results

1) Experimental measurements of  $-v_B/v_A$ , for various positions of the X-ray beam, are shown in fig. 3. For these measurements the chamber was operated at  $V_a = 2.5\ \text{kV}$ . If one takes for positive ion mobility in  $\text{Ar}/10\% \text{CH}_4$  the value<sup>4)</sup>  $\mu = 1.5\ \text{cm}^2/\text{Vs}$  then for the present operating conditions the characteristic time  $T_0 = s^2/\mu V_a$  has the value  $66.7\ \mu\text{s}$ . With pulse shaping time constant  $T = 10\ \mu\text{s}$  the normalised value becomes  $T/T_0 = 0.15$ . The theoretical curves for  $T/T_0 = 0.15$  are shown in fig. 3 for rectangular distributions spreading round 0% and 100% of the wire circumference. The sharpness with which the avalanche is localised is convincingly demonstrated by these measurements.

In comparing the experimental results with the predictions of the simple model it must be remembered that in reality the X-rays are not all absorbed close to the upper (or lower) cathode. In

fact at an X-ray energy of 5.9 keV, in argon/10% methane at atmospheric pressure, the absorption mean free path is about 2.3 cm. Thus at each value of  $x_0$  a range of  $\alpha$  values is possible from 0 to  $(1 - 2x_0/s)\pi/2$ . The weighting to be given to the lower values of  $\alpha$  (absorption events close to the anode plane) depends upon the ratio  $s/h$ . This effect of finite absorption depth can be included in the model but for simplicity it has been omitted in the present, initial discussions involving measurements taken with rather coarse collimation.

2) If  $x_0$  exceeds  $s/2$  then the avalanche switches over to the next wire  $A'$ . It is interesting to note that the wire B can still sense to some extent the avalanche angular position on  $A'$ . This is shown by the non-zero slope of the lower set of experimental results representing  $-v_B/v_A'$ . The full curve is the theoretical prediction, with zero angular spread. The range over which transition occurs from the upper branch to the lower branch, in the region  $x_0 = s/2$ , is dependent mainly upon the width of the collimated X-ray beam.

3) The measurements shown in fig. 3 were taken at a gas gain of about  $10^4$ . It is interesting to note the effect of increasing the gas gain. This is shown in fig. 4 where experimental values of  $-v_B/v_A$  have been plotted versus  $x_0$  for various

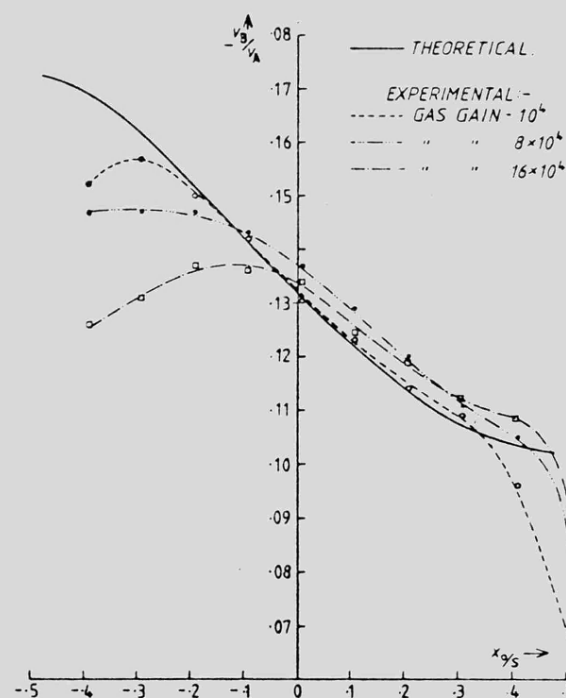


Fig. 4. Experimental measurements of  $-v_B/v_A$  plotted against X-ray beam position  $x_0$  for various values of gas gain.

## ANGULAR LOCALISATION

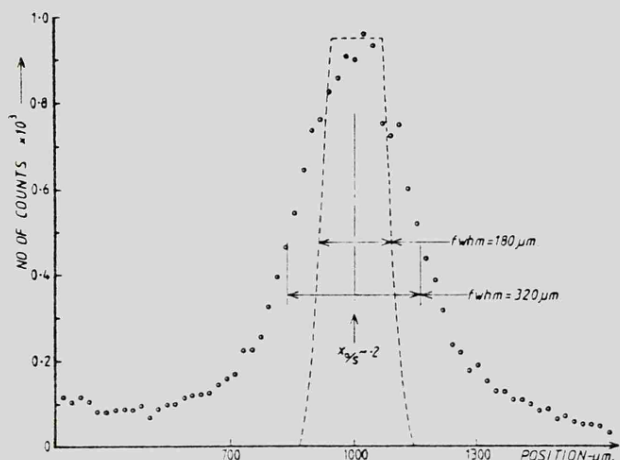


Fig. 5. Pulse height distribution of position signal,  $r = (v_B - v_A') / (v_B + v_A') + \text{constant}$ , for X-ray beam position  $x_0/s = 0.2$ . The additional constant merely ensures that  $r$  remains positive. The dashed, trapezium-shaped curve indicates the theoretical contribution from the collimator (the two curves have not been normalised in area).

values of gas gain up to about  $16 \times 10^4$  ( $V_a = 3$  kV). There is indeed a tendency for the avalanche to spread further round the wire as the gain increases, but the effect is surprisingly small until the highest gains are reached. The chamber has become markedly non-proportional to energy by about  $7 \times 10^4$  but the degree of avalanche spread has not changed significantly by then.

## 6. Position-sensitive detection

The experimentally observed relationship between induced charge signal  $v_B$  and the position  $x_0$  suggests the possibility of deriving positional information at a resolution not limited by the anode wire spacing. To demonstrate this possibility a circuit was constructed to obtain from induced charge signals from the two wires B and A' in fig. 1, a signal proportional to the quantity  $r = (v_B - v_{A'}) / (v_B + v_{A'}) + \text{constant}$ . Fig. 5 shows the pulse height distribution of this position signal  $r$  for the X-ray beam at position  $x_0/s = 0.2$ . The horizontal axis has been calibrated in position by experimental measurements of the centroid of  $r$  as a function of  $x_0$  (fig. 6).

The full-width at half-maximum of the position signal is  $320 \mu\text{m}$ . There are several factors contributing to this width, the most obvious being the rather wide incident beam width,  $180 \mu\text{m}$ . A second much smaller factor is the contribution due to pre-amplifier noise, amounting to approximately  $60 \mu\text{m}$ . The remainder,  $\approx 260 \mu\text{m}$ , must be re-

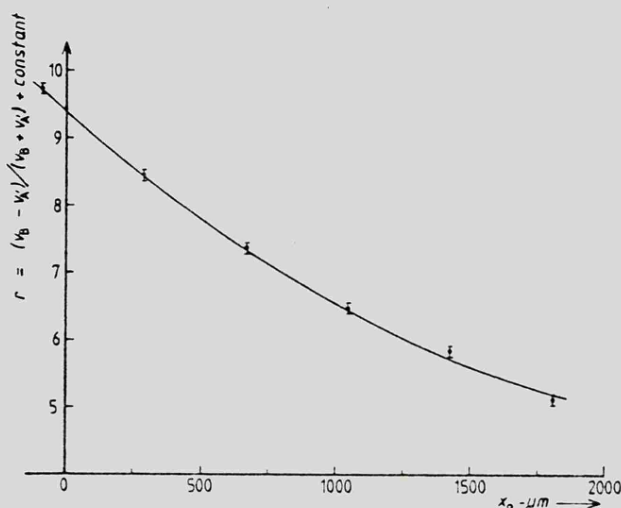


Fig. 6. Experimental values of position signal  $r$  plotted against X-ray beam position  $x_0$ .

garded as fundamental in the sense that it arises from the geometry of the initial positive ion distribution. Part of this width presumably represents angular jitter in the centroid of the initiating electron group at the anode wire. Another part must be due to the finite depth of X-ray absorption, already discussed in section 5 (1).

It is not suggested, of course, that the present system can be immediately employed for positional interpolation between anode wires. The major factor preventing this is that at present only about 70% of the inter-wire spacing can be explored in this way. Outside these limits the avalanche switches over to one of the 'sense' wires. However the potentially good r.m.s. resolution,  $\approx s/40$ , and the useful linearity in the workable region as demonstrated by fig. 6, encourage one to explore further this new mode of extracting positional information from a MWPC.

## 7. Conclusions

The measurements presented in this paper show that the avalanche at the anode of a proportional chamber is strongly angularly localised, even at gas gains high enough to cause serious non-proportionality. The equivalent width of the initial distribution of positive ions immediately after the avalanche is certainly less than 50% of the wire circumference.

Since the centroid of the distribution is determined by the field line along which the initiating electrons have drifted, a system sensitive to the angular position of the avalanche may also yield

T. J. HARRIS AND E. MATHIESON

information on the original interaction position. The possibility has been demonstrated of positional interpolation between anode wires. For soft X-rays this would imply considerably improved resolution over present MWPC systems, or increased anode wire spacing could be tolerated with welcome reduction in electrical breakdown problems. In view of this we are now examining induced charge signals, at anode wires and cathodes, in a chamber of increased anode wire spacing. We are also examining avalanche angular localisation in different operating gases. Preliminary results with

25% argon/75% methane are rather similar to those presented above for 90% argon/10% methane.

#### References

- 1) G. Charpak, D. Rohm and H. Steiner, Nucl. Instr. and Meth. **80** (1970) 13.
- 2) G. Charpak, Nature **270** (1977) 479.
- 3) E. Mathieson, T. J. Harris and G. Smith, Nature **272** (1978) 709.
- 4) R. Gott and M. W. Charles, Nucl. Instr. and Meth. **72** (1969) 157.

APPENDIX 5

INDUCED CHARGES IN A MULTIWIRE PROPORTIONAL CHAMBER -

E.Mathieson and T.J.Harris.

Reprinted from Nucl. Instr. and Meth., 154(1978)189

## INDUCED CHARGES IN A MULTI-WIRE PROPORTIONAL CHAMBER

E. MATHIESON and T. J. HARRIS

*Physics Department, The University, Leicester, England*

Received 23 January 1978

Formulae are presented and developed to allow the calculation of induced charges at individual anode wires or at the cathode of a conventional multi-wire chamber.

### 1. Introduction

In a report recently submitted to this journal it has been shown that under certain conditions, the avalanche at an anode wire of a multi-wire chamber may be highly localised. Experimental evidence was obtained by examining the signals induced in the anode wire adjacent to the 'avalanche' wire. The purpose of this present brief note is to justify and collate various theoretical formulae quoted in that report, and to be quoted in further work, on induced charges in a symmetric multi-wire proportional chamber.

Expressions for the charge induced on a grounded electrode may, in principle, be obtained by application of the following theorem due to Maxwell<sup>1</sup>, expressed here in terms appropriate to the present applications. "If a conductor raised to unit potential produces at an external point a potential  $P$  then a unit charge placed at that point will induce on the conductor, if at zero potential, a charge  $-P$ ." For convenience a proof of this theorem has been included in an appendix.

In the expressions developed below, the anode wires are perpendicular to the  $x$ - $y$  plane, the central wire of the system coinciding with the origin. It is assumed that both the anode wire length and the lateral width of the anode plane are large compared with the anode-cathode separation. The anode wire spacing is denoted by  $s$ , the anode-cathode separation by  $h$  and the anode wire radius by  $r_a$ . The positive inducing charge of unit magnitude is situated at  $(x, y)$  and the induced charge at the electrode of interest is  $-P$ . If, as is usually the case, the electrode is connected to a charge-sensitive pre-amplifier of conversion gain  $1/C$  then the output voltage of the pre-amplifier is  $P/C$ .

### 2. Induced charge at connected anode wires

This is the simplest case to consider since, provided  $s \gg r_a$  and  $h \gg s$ , the potential and field lines

in a symmetric multi-wire chamber may be described by the complex potential  $W$  given by<sup>2</sup>):

$$W = -K \log \sin \pi z/s + V_0.$$

Here  $z = x + jy$  and  $K$  and  $V_0$  are real constants determined by the electrode potentials.

The potential  $P$  is obtained as the real part of  $W$  when the anode wires are at unit potential and the cathodes are grounded. Applying these conditions we obtain

$$1 = -K \log \pi r_a/s + V_0$$

and

$$0 = -K (\log 1/2 + \pi h/s) + V_0.$$

Substituting the values obtained for  $K$  and  $V_0$  into the expression for  $W$  we find after some manipulation

$$P = \frac{\pi h/s - \log \{2(\cosh 2\pi y/s - \cos 2\pi x/s)\}^{1/2}}{\pi h/s - \log 2\pi r_a/s}.$$

It must be noted that if the unit positive inducing charge was produced as a result of an avalanche at one of the anode wires then a real charge  $-1$  would have been collected at the anode. The charge-sensitive pre-amplifier output voltage would then be  $(P-1)/C$ .

### 3. Induced charge at individual anode wire

This rather clumsy situation is best approached by first considering the mapping function

$$w = u + jv = je^{\pi z/2h}.$$

A single line charge at the origin in the  $z$ -plane maps into a line charge at the point  $(0, 1)$  in the  $w$ -plane, and the zero potential cathode planes at  $y = \pm h$  map into the  $u$ -axis. The complex potential  $W$  is therefore given, from simple image theory, as

$$W = -C_1 \{ \log(w-j) - \log(w+j) \}$$

where  $C_1$  is a constant determined by the line charge magnitude. In the  $z$ -plane the complex po-

tential expression becomes

$$W = C_1 \log \coth \pi z/4h$$

and after some manipulation this becomes

$$W = C_1 \log \left\{ \frac{\cosh \pi x/2h + \cos \pi y/2h}{\cosh \pi x/2h - \cos \pi y/2h} \right\}^{1/2} + jC_1 \varphi,$$

where  $\tan \varphi = -\sin(\pi y/2h)/\sinh(\pi x/2h)$ .

For  $x, y \ll h$ ,  $W = C_1 \log(4h/\pi r) - jC_1 \theta$  where  $r = (x^2 + y^2)^{1/2}$  and  $\tan \theta = y/x$ .

The potential  $P$  due to an array of  $(2l+1)$  line charges, not necessarily of equal magnitude, at regular spacing  $s$ , is therefore given by

$$P = \sum_{n=-l}^l C_n L_n,$$

where

$$L_n = \log \left\{ \frac{\cosh \pi(x-ns)/2h + \cos \pi y/2h}{\cosh \pi(x-ns)/2h - \cos \pi y/2h} \right\}^{1/2}.$$

The constants  $C_n$  are determined by the potentials of the wires. Provided  $r_a \ll s$ , the wire surfaces are represented by equipotential cylinders coaxial with the line charges. Thus the potential of the  $m$ th wire is given by

$$P_m = \sum C_n L_{nm},$$

where

$$L_{nm} = \log \left\{ \frac{\cosh \pi s(m-n)/2h + 1}{\cosh \pi s(m-n)/2h - 1} \right\}^{1/2}, \quad n \neq m,$$

$$L_{mm} = \log(4h/\pi r_a).$$

Now if we wish to calculate the charge induced on the  $k$ th wire, say, then to apply the original theorem we place  $P_k = 1$  and  $P_m = 0$  for  $m \neq k$ . Thus the constants  $C_n$  are obtained as the solution vector of the matrix equation

$$P_m = \sum C_n L_{nm},$$

with the input vector  $P_m$  as given above. The charge induced on the  $k$ th wire is then

$$-P = -\sum C_n L_n.$$

#### 4. Induced charge at cathode

This case can be treated in a straightforward manner by noting that a suitable complex potential may be chosen as

$$W = -K \log \sin \pi z/s - jE_0 z + V_0$$

where  $K$ ,  $E_0$  and  $V_0$  are real constants determined by the electrode potentials.

If the cathode at  $y = +h$  is at unit potential and the anode wires and the other cathode are at zero potential then

$$1 = -K (\log 1/2 + \pi h/s) + E_0 h + V_0,$$

$$0 = -K \log(\pi r_a/s) + V_0,$$

$$0 = -K (\log 1/2 + \pi h/s) - E_0 h + V_0.$$

The second of these equations is true provided that  $E_0 r_a \ll V_0$ . This condition is equivalent to  $r_a/h \ll V_0$  and substitution of normal values shows that it is adequately satisfied.

By solving for  $K$ ,  $E_0$  and  $V_0$  and substituting in the expression for  $W$  we find, after some manipulation, that the real part  $P$  is given by

$$P = \frac{y}{2h} - \frac{\log 2\pi r_a/s - \log \{2(\cosh 2\pi y/s - \cos 2\pi x/s)\}^{1/2}}{2(\pi h/s - \log 2\pi r_a/s)}.$$

#### 5. Time development of induced charge

Since in reality the inducing charge is not stationary in position, the induced charge will develop with time. Although this aspect is not the main point of the present note, for completeness two useful formulae are included here. These derive from the expression for the complex potential  $W$  for anode potential  $V_a$  and cathode potentials zero.

$$W = V_a \frac{\pi h/s - \log 2 \sin \pi z/s}{\pi h/s - \log 2\pi r_a/s}.$$

If the positive ion was created at the anode wire surface, on the wire at the  $(x, y)$  origin, at position  $(r_a \cos \alpha, r_a \sin \alpha)$  then the ion drifts along the field line given by

$$\tanh \pi y/s = \tan \pi x/s \tan \alpha.$$

The velocity of drift is  $\mu E$  where  $\mu$  is the positive ion mobility and  $E$  is the local field value given by

$$E = \frac{V_a/h}{1 - s/\pi h \log 2\pi r_a/s} \left\{ \frac{\cosh 2\pi y/s + \cos 2\pi x/s}{\cosh 2\pi y/s - \cos 2\pi x/s} \right\}^{1/2}.$$

#### Appendix

The relationships between the charges  $q_i$  and the potentials  $v_i$  of a system of  $n$  conductors may be conveniently expressed in terms of configuration coefficients  $c_{ij}$ . Thus

$$q_i = \sum_{j=1}^n c_{ij} v_j.$$

## INDUCED CHARGES IN A MWPC

Suppose we wish to calculate the charge  $q_1$  induced on conductor 1 by unit charge placed on conductor 2, all other conductors (including 1) being grounded. Then  $q_1 = c_{12} v_2$  and  $1 = c_{22} v_2$ . Hence  $q_1 = c_{12}/c_{22}$ . To calculate the ratio  $c_{12}/c_{22}$  consider now the case that conductor 1 is raised to unit potential, conductor 2 is insulated and uncharged, and all other conductors are grounded. Let  $P$  be the potential to which conductor 2 rises. Then  $0 = c_{21} + c_{22}P$  or  $c_{21}/c_{22} = -P$ . But, by

Green's reciprocal theorem,  $c_{21} = c_{12}$ . Thus  $q_1 = -P$ .

The conductor 2 may be physically very small; that is, we may regard a positive ion mathematically as conductor 2.

## References

- <sup>1)</sup> J. C. Maxwell, *A treatise on electricity and magnetism* (Third Edition), Vol. 1, Ch. III, Section 86 (Oxford University Press, London, 1892).
- <sup>2)</sup> E. Weber, *Electromagnetic fields* (Wiley, New York, 1950).

APPENDIX 6

MODULATION OF ANODE SIGNALS IN MULTIWIRE PROPORTIONAL CHAMBERS -

E.Mathieson and T.J.Harris.

Reprinted from Nucl. Instr. and Meth., 157(1978)563.

## MODULATION OF ANODE SIGNAL IN MULTIWIRE PROPORTIONAL CHAMBERS

E. MATHIESON and T. J. HARRIS

*Physics Department, The University, Leicester, LE1 7RH, England*

Received 9 May 1978

In the detection of soft X-rays with a multiwire proportional chamber the angular localisation of the anode avalanche may cause dependence of the final output signal on X-ray absorption position. Two distinct mechanisms may occur; variation of gas gain due to the non-radial field and variation in the time development of the anode induced charge. Simple theoretical estimates show that the magnitudes of these two effects may be comparable and non-negligible.

### 1. Introduction

It has become apparent fairly recently that the avalanche at the anode of a proportional chamber or counter may exhibit a high degree of angular localisation<sup>1-4</sup>). Charpak<sup>1)</sup> has pointed out that, in a multiwire proportional chamber, because of the field variation round the wire this localisation effect will result in a variation of gas gain. Marked modulation of chamber gain with the position of a collimated X-ray beam has already been noted experimentally by Charpak<sup>1)</sup> and also by Smith and Wells<sup>5)</sup>.

There are in fact two mechanisms whereby the chamber signal can be modulated by the angular localisation of the avalanche. The first is the variation in gas gain with angular position of the avalanche as outlined above. The second effect arises because of the way in which the time development of the resultant anode charge depends upon the initial angular position of the positive ions. The magnitude of this second, induced charge effect will depend fairly strongly upon the time characteristics of the signal processing system.

The purpose of this present paper is to develop theoretical estimates of the magnitudes of these two effects and to compare their relative importance.

### 2. Angular variation in gas gain

A section of a conventional symmetric multiwire chamber is shown schematically, but not to scale, in fig. 1. For anode wire radius  $r_a$  small compared with anode wire spacing  $s$ , the field may be described<sup>4)</sup> to a good approximation by the expression

$$E = \frac{V_a/h}{1 - s/\pi h \log 2\pi r_a/s} \left( \frac{\cosh 2\pi y/s + \cos 2\pi x/s}{\cosh 2\pi y/s - \cos 2\pi x/s} \right)^{\frac{1}{2}},$$

where  $V_a$  is the anode voltage, both cathodes being earthed, and  $h$  is the anode-cathode separation.

In the close neighbourhood of the anode wire at the co-ordinate origin the field is very nearly radial; the expression above reduces to the simpler form

$$E = \frac{C_a V_a}{r} \left[ 1 - \frac{\pi^2}{3} \left( \frac{r}{s} \right)^2 \cos 2\alpha \right],$$

where

$$C_a = \frac{s/\pi h}{1 - s/\pi h \log 2\pi r_a/s}.$$

Here  $r = (x^2 + y^2)^{\frac{1}{2}}$  and  $\alpha = \tan^{-1} y/x$ . Thus at constant radius  $r$  the fractional change in field from its maximum value at  $\alpha = \frac{1}{2}\pi$  to its minimum value at  $\alpha = 0$  is  $\frac{1}{3}\pi^2 (r/s)^2$ . For radii within which gas amplification occurs, this fractional change is a fairly small quantity compared with unity,  $\sim 10^{-2}$ .

The gas gain  $M$  may be expressed in the usual manner in terms of the ionisation probability  $\alpha_g$  by the expression

$$\log M = \int_{r_a}^{r_0} \alpha_g dr.$$

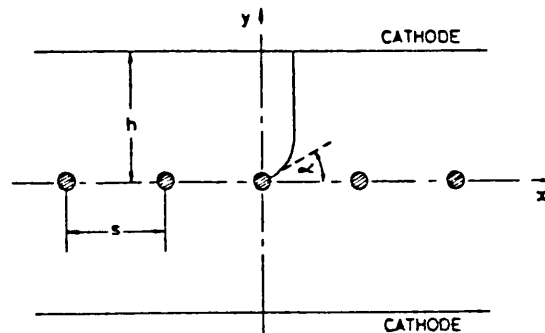


Fig. 1. Schematic of symmetric multiwire chamber with anode wire spacing  $s$  and anode-cathode separation  $h$ .

Here  $r_0$  is the critical radius at which the field becomes great enough for multiplication to commence. This critical radius may be expressed in terms of the critical voltage  $V_0$  above which the chamber gain exceeds unity. At voltage  $V_0$  the critical field value is just reached at the anode wire surface and, if we assume that at this radius the field is strictly radial, then

$$C_2 V_0 / r_a = (C_2 V_a / r_0) [1 - \frac{1}{2} \pi^2 (r_0/s)^2 \cos 2\alpha].$$

This quadratic equation may be solved for  $r_0$  to yield, as the acceptable solution

$$r_0 \approx r_a \frac{V_a}{V_0} \left[ 1 - \frac{1}{2} \pi^2 \left( \frac{V_a}{V_0} \right)^2 \left( \frac{r_a}{s} \right)^2 \cos 2\alpha \right],$$

It is necessary in obtaining an expression for gas gain to assume a functional dependence of  $\alpha_s$  upon electric field  $E$ , and for the present purpose the simple form developed in the work of Rose and Korff<sup>6</sup> is convenient. This expression may be written

$$\alpha_s = (KE)^{\frac{1}{2}},$$

where  $K = \text{constant}$ .

Thus

$$\alpha_s \approx (KC_s V_a)^{\frac{1}{2}} r^{-\frac{1}{2}} \left[ 1 - \frac{1}{2} \frac{\pi^2}{3} (r/s)^2 \cos 2\alpha \right],$$

where  $\frac{1}{2} \pi^2 (r/s)^2 \ll 1$ . With this expression for  $\alpha_s$ , and using the value for  $r_0$  obtained above, the definite integral for  $\log M$  may be evaluated. The result, simplified by using again the fact that  $(r_a/s)^2$  is very small compared with unity, may be written

$$\log M = \log M_0 - \log M_0 \left\{ \left( \frac{V_a}{V_0} \right)^{\frac{1}{2}} - 1 \right\}^{-1} \times \\ \times \frac{\pi^2}{30} \left( \frac{r_a}{s} \right)^2 \left[ 6 \left( \frac{V_a}{V_0} \right)^{\frac{1}{2}} - 1 \right] \cos 2\alpha,$$

where

$$\log M_0 = 2(KC_s r_a V_a) [(V_a/V_0)^{\frac{1}{2}} - 1].$$

The expression for  $M_0$ , which represents the gas gain in a purely radial field, is of course in the form obtained originally by Rose and Korff.

It can be seen that the fractional change in gain from the radial field value is then

$$\Delta M \approx - \frac{\log M_0}{(V_a/V_0)^{\frac{1}{2}} - 1} \left( \frac{V_a}{V_0} \right)^{\frac{1}{2}} \frac{\pi^2}{5} \left( \frac{r_a}{s} \right)^2 \cos 2\alpha,$$

where it has been assumed for simplicity that  $(V_a/V_0)^{3/2} \gg 1$ . To the extent that the Rose and Korff

expression for  $\alpha_s$  is correct, then the above formula predicts that, for a given chamber,  $\Delta M$  should vary approximately as  $(V_a/V_0)^{3/2}$ .

As a typical numerical example, if  $V_a/V_0 = 4$ ,  $M_0 = 10^4$ ,  $r_a = 10 \mu\text{m}$  and  $s = 2 \text{ mm}$  then for  $\alpha = \frac{1}{2}\pi$  and  $0$ ,  $\Delta M = \pm 1.4\%$ . If  $s = 1 \text{ mm}$  then  $\Delta M = \pm 5.8\%$ .

### 3. Variation in induced charge

The time development of the charge induced on the anode wires by the drifting positive ions depends upon their initial angular position. Relevant formulae for induced charges in a multiwire chamber have been developed in ref. 4 and the method of calculating the waveform in the signal processing channel has been described in ref. 3. To summarise the situation briefly, suppose the anode wires are connected to a charge-sensitive preamplifier of conversion gain  $1/C$ , and that positive ions, charge  $q$ , have reached position  $x, y$  following an avalanche in which electron charge  $-q$  has been collected by the anode. Then the preamplifier output voltage is given by

$$v(t) = - \frac{q}{C} \left\{ 1 - C_2 \frac{\pi h}{s} \left[ 1 - \frac{s}{\pi h} \log \left( 2 \cosh \frac{2\pi y}{s} - 2 \cos \frac{2\pi x}{s} \right)^{\frac{1}{2}} \right] \right\},$$

where  $C_2$  has been defined above.

The positive ion position may be calculated, numerically, by integrating, along the field line  $\tanh \pi y/s = \tan \pi x/s \cdot \tan \alpha$ , the equation

$$\left\{ \left( \frac{dx}{dt} \right)^2 + \left( \frac{dy}{dt} \right)^2 \right\}^{\frac{1}{2}} = \mu E$$

employing the simplified initial conditions at  $t = 0$  that  $x = r_a \cos \alpha$ ,  $y = r_a \sin \alpha$ . In reality there must be a finite initial angular spread; this can be simply included in a calculation, see ref. 3, but in the present case the maximum magnitude of the effect, i.e., zero angular spread is required. The ions are not all produced at the actual surface of the anode wire, but calculations with the present model show that the waveforms are very insensitive to the initial radial position of the ions. In the above expression  $\mu$  is the positive ion mobility. For the present calculation  $\mu$  has been assumed constant, a particular field dependence, if known experimentally, could be simply accommodated.

The final output waveform from the pulse shap-

## MODULATION OF ANODE SIGNAL

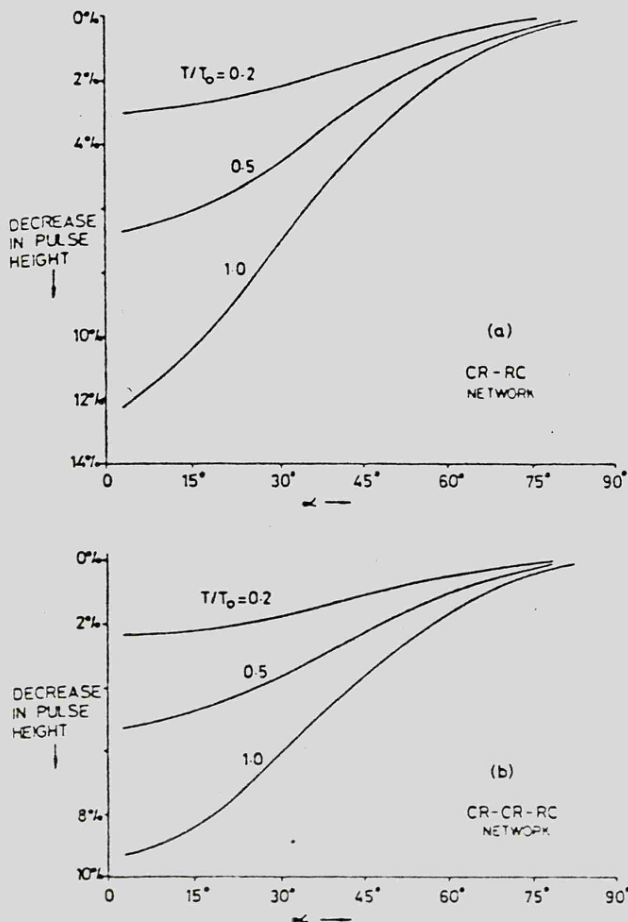


Fig. 2. Output pulse height dependence on initial positive ion angular position  $\alpha$ . The ordinate is the percentage decrease from the value at  $\alpha = \frac{1}{2}\pi$ . (a) CR-RC network of time constant  $T$ . (b) CR-CR-RC network of time constant  $T$ .

ing network may be calculated from the convolution integral

$$v_0(t) = \int_0^t v(t') h(t-t') dt',$$

where  $h(t)$  is the impulse response of the network. Two pulse shaping networks have been considered here; single differentiation with single integration and double differentiation with single integration, in each case with equal time-constants. As explained in ref. 3, it is particularly convenient to express time normalised to the unit  $T_0 = s^2/\mu V_a$ . Typically  $T_0$  falls within the range 1–50  $\mu s$ .

Fig. 2 shows the predicted variation in final out-

put pulse height as a function of initial positive ion angular position  $\alpha$ . The ordinate is the percentage decrease from the value at  $\alpha = \frac{1}{2}\pi$ . Fig. 2a represents the CR-RC network and fig. 2b the CR-CR-RC network. The parameter  $T/T_0$  is the ratio of network time constant  $T$  to the characteristic time  $T_0$ .

#### 4. Discussion

The predicted variations described above are, of course, only estimates. In the discussion of gas gain, space charge and photoionisation effects have been ignored and a particular, restricted, theory has been adopted. In fact no one theory is adequate to cover the whole operating range of proportional chambers. In the induced charge calculations it has been assumed that the positive ions are all formed at the anode wire surface and that there is no angular spread in the avalanche. Despite these restrictions and simplifications it is clear nevertheless that either type of variation might be of serious magnitude. If localised events are being detected and electron diffusion is small then the observed energy resolution may be markedly inferior to that of a single-wire coaxial counter unless attention is paid to minimising both effects. The induced charge variation can be made arbitrarily small by employing a filter time constant sufficiently small compared with  $T_0 = s^2/\mu V_a$ . The gas gain variation increases rather rapidly with anode voltage, probably as fast as or faster than  $(V_a/V_0)^3$ . It is not yet clear how much this effect might be smoothed out by an increase in angular spread with gas gain. Experimental examinations of these modulation effects are at present being attempted.

#### References

- 1) G. Charpak, G. Petersen, A. Policarpo and F. Sauli, Nucl. Instr. and Meth. 148 (1948) 471.
- 2) E. Mathieson, T. J. Harris and G. C. Smith, Nature 272 (1978) 709.
- 3) T. J. Harris and E. Mathieson, Nucl. Instr. and Meth. 154 (1978) 183.
- 4) E. Mathieson and T. J. Harris, Nucl. Instr. and Meth. 154 (1978) 189.
- 5) G. C. Smith and A. A. Wells, private communication.
- 6) M. E. Rose and S. A. Korff, Phys. Rev. 59 (1941) 850.

APPENDIX 7

EVALUATION OF THE INITIAL ANGULAR WIDTH  
OF THE AVALANCHE IN A PROPORTIONAL CHAMBER -

E.Mathieson and T.J.Harris

Reprinted from Nucl. Instr. and Meth., 159(1979)483.

## EVALUATION OF THE INITIAL ANGULAR WIDTH OF THE AVALANCHE IN A PROPORTIONAL CHAMBER

E. MATHIESON and T. J. HARRIS

*Physics Department, Leicester University, Leicester, England*

Received 18 July 1978 and in revised form 26 October 1978

Experimental measurements have been made of the ratio of the signals induced on the cathodes of a symmetric multi-wire proportional chamber under X-ray irradiation. Because of avalanche angular localisation this ratio depends strongly on the lateral position of the X-ray beam. It is shown how a simple theoretical model may be employed with these measurements to evaluate the width of the initial angular distribution of the positive ions in the avalanche.

### 1. Introduction

The recent independent work of several groups<sup>1-4</sup>) has shown that, for a localised ionising event, the resulting avalanche at a proportional counter or chamber anode wire may exhibit a considerable degree of angular localisation. Analysis and experiment show that this localisation influences significantly the induced charges on neighbouring anode wires or potential wires and on chamber cathodes. The effect has important implications on the position-sensitive performance of proportional chambers. Borkowski and Kopp<sup>1</sup>) have employed the effect to adjust electronically the effective aperture of a multiwire chamber by discriminating between photons absorbed above and below the anode plane. Fischer et al.<sup>2</sup>), Walenta<sup>3</sup>) and Breskin et al.<sup>6</sup>) have shown that it is possible to solve the left-right ambiguity problem with high precision. Charpak et al.<sup>3</sup>) and Harris and Mathieson<sup>7</sup>) have shown, by somewhat different methods, that as a consequence of the localisation, rms resolution orthogonal to the anode wire direction better than  $150\ \mu\text{m}$  may be achieved.

The present paper describes the way in which a quantitative measure of the angular spread of the avalanche may be obtained. Experimental measurements of the ratio of the signals induced in the two cathodes of a symmetric multiwire chamber, as a function of the position of a collimated X-ray beam, are compared with the predictions of a simple theoretical model. A preliminary announcement<sup>8</sup>) of this method for evaluating the avalanche angular spread was submitted to the 3rd International Conference on *Proportional and drift chambers*, Dubna, June 1978.

### 2. Theory

Fig. 1 is a diagram, not to scale, of a conventional multiwire chamber with anode wire spacing  $s$  and anode-cathode separation  $h$ . The anode wires are perpendicular to the  $x$ - $y$  plane with the particular wire at which avalanche occurs at the origin. The X-ray beam is parallel to the  $y$ -axis and has coordinate  $x_0$ .

For conventional chamber geometry there is a considerable fraction of the volume in which the field is very nearly uniform. Thus from a localised ionising event well away from the anode plane, at coordinate  $x_0$ , the electrons drift along a field line and result in an avalanche whose centre-of-charge has an angular position at the anode wire surface given by  $\alpha = \frac{1}{2}\pi(1 - 2x_0/s)$ . Positive ions from the avalanche then drift back along the field lines. It is therefore possible, from a knowledge of positive

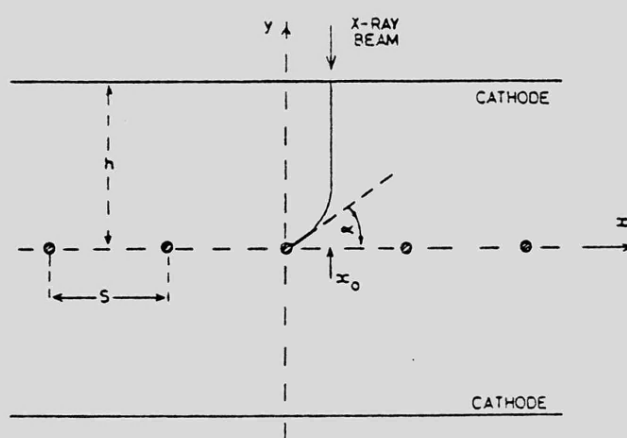


Fig. 1. Schematic of a symmetric multiwire chamber. The finely collimated X-ray beam is parallel to the  $y$ -axis with  $x$ -coordinate  $x_0$ . The field line shown intersects the anode wire surface at an angle  $\alpha$  to the  $x$ -axis where  $\alpha = \frac{1}{2}\pi(1 - 2x_0/s)$ .

ion mobility, chamber geometry and chamber voltage, to calculate the time development of the induced charge  $q_c(t)$  at the chamber cathode as a function of  $x_0$ . The appropriate formulae have already been developed by Mathieson and Harris<sup>9</sup>.

Briefly, the positive ion drift back along the field line

$$\tanh \pi y/s = \tan \pi x/s \cdot \tan \alpha,$$

with velocity  $\mu E$  where  $\mu$  is the positive ion mobility and  $E$  is the local field value given by

$$E = \frac{V_a/h}{1 - s/\pi h \log 2\pi r_a/s} \left( \frac{\cosh 2\pi y/s + \cos 2\pi x/s}{\cosh 2\pi y/s - \cos 2\pi x/s} \right)^{\frac{1}{2}}$$

Here  $V_a$  is the anode-cathode voltage and  $r_a$  is the anode wire radius. The initial positive ion position is assumed to be  $(r_a \cos \alpha, r_a \sin \alpha)$ . If the positive ions have charge  $q_0$  and have reached position  $(x, y)$  then the cathode induced charge  $q_c(t)$  is given by  $q_c(t) = -q_0 P(x, y)$  where

$$P(x, y) = \frac{y}{2h} -$$

$$\frac{\log 2\pi r_a/s - \log [2(\cosh 2\pi y/s - \cos 2\pi x/s)]^{\frac{1}{2}}}{2(\pi h/s - \log 2\pi r_a/s)}.$$

For interest, an isometric plot of  $P(x, y)$  is shown in fig. 2.

If, as in the present case, the cathode is connected to a charge-sensitive amplifier, of conversion gain  $1/C$ , then the amplifier output is  $v(t) = -q_c(t)/C$ . The final output from the pulse shaping system may be obtained from the convolution integral

$$v_0(t) = \int_0^t v(t') h(t-t') dt',$$

where  $h(t)$  is the impulse response of the system. The peak height  $v_c$  of the output signal may be calculated in this way.

In the present system a single differentiating

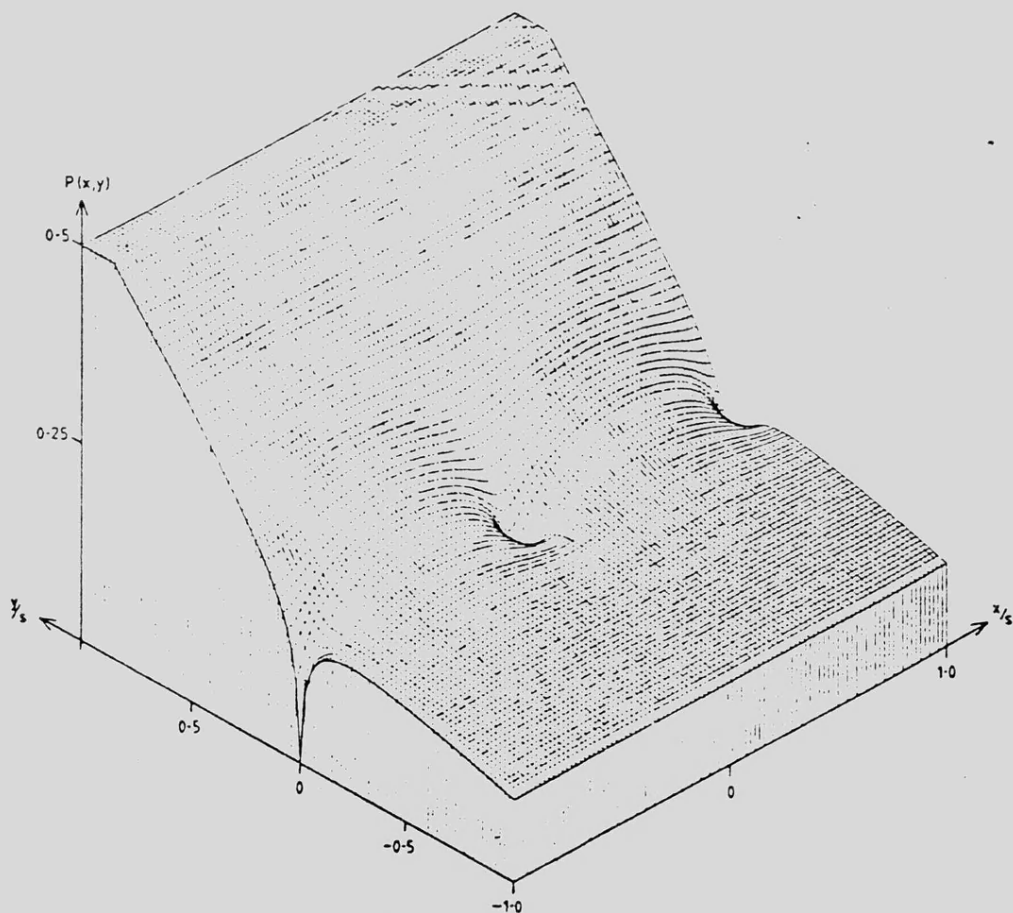


Fig. 2. Isometric plot of the charge induced on a cathode as a function of the position  $(x/s, y/s)$  of the inducing charge. This example was plotted for the parameters  $h/s = 2.22$ ,  $r_a/s = 5 \times 10^{-3}$ .

## ANGULAR WIDTH OF THE AVALANCHE

filter and a single integrating filter of equal time constant  $T$  was used so that  $h(t) = e^{-t/T}(1-t/T)/T$ . It has already been shown, in ref. 7, that in calculations of the position of the positive inducing charge there emerges a natural unit of time  $T_0 = s^2/\mu V_s$ . The normalised filter time constant  $T/T_0$  is found to be an important system parameter.

In the numerical evaluations of  $v_0(t)$  and  $v_c$  it is a comparatively simple task to extend the calculations to describe the effect of an initial angular distribution of positive ions at the anode wire surface. For the present considerations a gaussian angular distribution  $\rho(\alpha')$  was chosen. That is

$$\rho(\alpha') = \frac{q_0}{\sqrt{2\pi\sigma_x^2}} e^{-(\alpha'-x)^2/2\sigma_x^2},$$

where  $\rho(\alpha')d\alpha'$  represents the initial positive ion charge in the angular range  $d\alpha'$ ,  $\alpha$  is the initial angular centre-of-charge and  $\sigma_x$  is the standard deviation of the distribution.

In addition to angular spread there must be some radial spread in the initial positive ion distribution; the ions are not all produced at the actual surface of the anode wire. However calculations with the present model show that the ratio of cathode signals is very insensitive to the initial radial position of the ions.

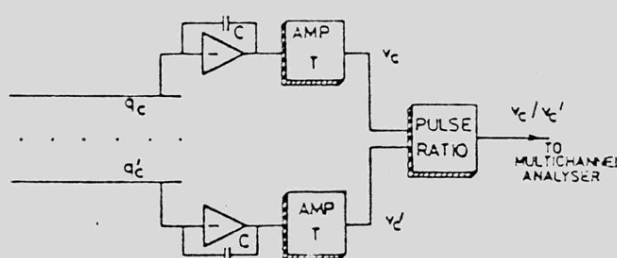


Fig. 3. Schematic of signal processing system. The amplifiers each have single differentiating and integrating circuits of time constant  $T$ .

### 3. Experiment arrangement

The measurements presented here were taken using a symmetric chamber, with plane cathodes, with  $s = 5$  mm,  $h = 11$  mm and  $r_s = 25 \mu\text{m}$ . Argon/10% methane at atmospheric pressure was the filling gas and the chamber was operated at a gain of about  $10^4$ .

Well-matched signal processing systems were attached to each cathode, with the value of  $T$  in each shaping amplifier  $10 \mu\text{s}$ . A dividing circuit yielded pulses of height  $v_c/v'_c$ , the ratio of pulse heights in the two cathode channels, fig. 3. The effect of different sensitivities in the two channels could be eliminated by interchanging the signal processing systems.

The position of the 5.9 keV X-ray beam could

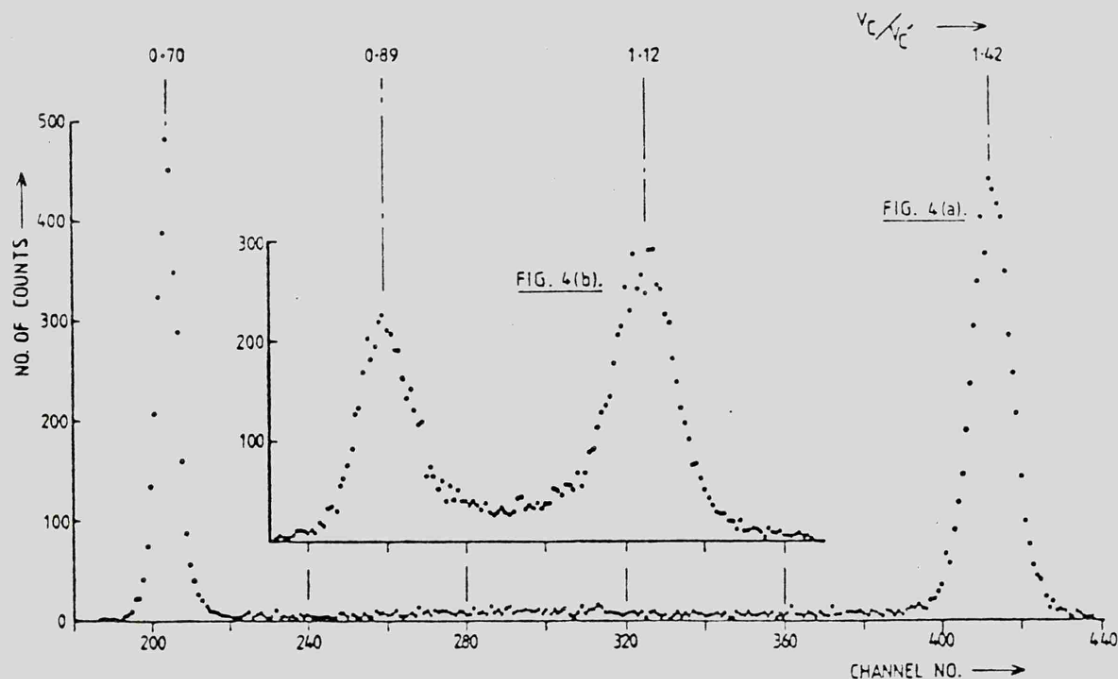


Fig. 4. Spectra of the ratio of cathode signals; (a)  $x_0 = 0$ , (b)  $x_0 = 0.40$  s.

be set to within  $10\ \mu\text{m}$  while the geometry and height of the collimator resulted in a beam width at the anode plane of  $200\ \mu\text{m}$ .

#### 4. Results

Spectra of the pulse heights from the ratio circuit are shown in fig. 4, for  $x_0 = 0$  in (a) and for  $x_0 = 0.4\ \text{s}$  in (b). In fig. 4a the two peaks represent absorption events occurring above the anode plane at  $\alpha = +90^\circ$  and below the anode plane at  $\alpha = -90^\circ$ , the ratio of the two intensities being closely in accord with the attenuation over 11 mm of 5.9 keV X-rays in the chamber gas. As  $x_0$  is increased from zero the maximum value of  $\alpha$  decreases; the two distributions approach each other as shown in fig. 4b.

If one assumes that absorption occurs in the essentially uniform field regions of the chamber, that is that the coordinate  $x_0$  of the X-ray beam uniquely defines  $\alpha$ , then the theoretical model outlined above can be employed to calculate  $v_c/v_c'$ . The experimental results are compared with theoretical predictions in fig. 5 where the value  $T/T_0 = 0.16$  has been used corresponding to  $\mu = 1.6\ \text{cm}^2/\text{Vs}$  (10). The high degree of angular localisation is very evident in these results. The curve passing closely through the experimental results represents a Gaussian initial angular distribution with standard deviation  $\sigma_\alpha$  equal to  $33^\circ$ .

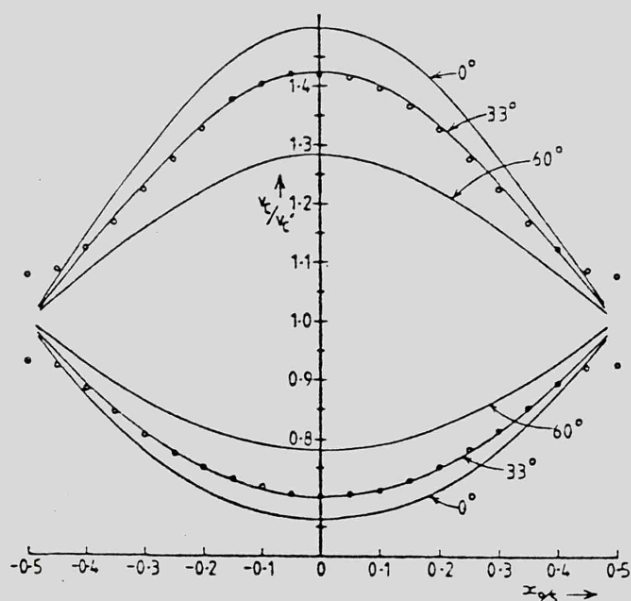


Fig. 5. Values of  $v_c/v_c'$  plotted as a function of  $x_0/s$ . The continuous curves are the theoretical predictions for gaussian initial positive ion distributions with standard deviations  $0^\circ$ ,  $33^\circ$  and  $60^\circ$ .

#### 5. Discussion

The main purpose of this present paper has been to show how a value for the width of the initial angular distribution of the avalanche, in a particular case, may be derived from the cathode signals. There appears to be fairly satisfactory agreement between the theoretical model and experimental results, as represented by fig. 5. The divergence near  $x_0 = \frac{1}{2}s$  is presumably due partly to the finite beam width and partly to departure from the uniform field assumption.

A rough estimate of the effect of electron diffusion may be made by considering an initial electron group to drift to the anode through a distance  $d$  in a uniform field. If the group had initially negligible size then the rms radius of the electron group would be  $\sigma_e = \sqrt{2Dd/v}$ , where  $D$  is the diffusion coefficient and  $v$  is the drift velocity. Substituting approximate numerical values  $D \approx 10^{-2}\ \text{cm}^2/\mu\text{s}$  and  $v \approx 5\ \text{cm}/\mu\text{s}$  then for  $d \approx \frac{1}{2}h \approx 0.5\ \text{cm}$  we have  $\sigma_e = 0.45\ \text{mm}$ . Taking into account the finite range of the initial photoelectron,  $\sim 60\ \mu\text{m}$ , and the finite beam width,  $200\ \mu\text{m}$ , a resultant spread of about  $0.50\ \text{mm}$  is obtained. From the relationship between  $x_0$  and  $\alpha$  given above we can thus estimate  $\sigma_\alpha$  as about  $18^\circ$ . This admittedly rather crude estimate suggests that electron diffusion is the main but not the sole contributor to the width of the initial positive ion angular distribution (in argon/methane at gas gains of the order  $10^4$ ).

The numerical result for  $\sigma_\alpha$  clearly depends upon the assumed figure for positive ion mobility  $\mu$ . In reality ionic mobility is somewhat field dependent<sup>11)</sup> and further, due to charge exchange, the actual nature of the ion may change with time. Thus  $\mu$  is actually a rather complicated function of field and time. There is clearly a need for further basic data on ionic mobilities. The present measurements are being extended to cover a range of time constants  $T$ , in an effort to examine the situation in more detail, and also to cover a range of gas mixtures.

#### References

- 1) C. J. Borkowski and M. K. Kopp, IEEE Trans Nucl. Sci. NS-24 (1977) 287.
- 2) J. Fischer, H. Okuno and A. H. Walenta, IEEE Trans. Nucl. Sci. NS-26 (1978) 794.
- 3) G. Charpak, G. Peterson, A. Policarpo and F. Sauli, Nucl. Instr. and Meth. 148 (1978) 471.
- 4) E. Mathieson, T. J. Harris and G. C. Smith, Nature 272

## ANGULAR WIDTH OF THE AVALANCHE

- (1978) 709.
- <sup>5)</sup> A. H. Walenta, Nucl. Instr. and Meth. **151** (1978) 461.
- <sup>6)</sup> A. Breskin, G. Charpak and F. Sauli, Nucl. Instr. and Meth. **151** (1978) 473.
- <sup>7)</sup> T. J. Harris and E. Mathieson, Nucl. Instr. and Meth., **154** (1978) 183.
- <sup>8)</sup> T. J. Harris and E. Mathieson, 3rd Int. Conf. on *Drift and proportional chambers*, Dubna (June 1978) (to be published).
- <sup>9)</sup> E. Mathieson and T. J. Harris, Nucl. Instr. and Meth. **154** (1978) 189.
- <sup>10)</sup> R. Gott and M. W. Charles, Nucl. Instr. and Meth. **72** (1969) 157.
- <sup>11)</sup> S. C. Brown, *Basic data of plasma physics* (M.I.T. Press, Cambridge, 1977).

REFERENCES

1. E.Rutherford and H.Geiger, Proc.Roy.Soc.A., 81(1908)141.
2. B.Rossi and H.Staub, 'Ionisation Chambers and Counters', McGraw Hill 1949
3. B.Rossi and H.Staub, 'Ionisation Chambers and Counters', P.97 McGraw Hill 1949
4. G.Charpak, R.Bouclier, T.Bressani, J.Favier and Č.Zupančič, Nucl. Instr. and Meth.,62(1968)262.
5. G.Charpak, R.Bouclier, T.Bressani, J.Favier and Č.Zupančič, Nucl. Instr. and Meth., 65(1968)217.
6. G.Charpak, D.Rahm and H.Steiner, Nucl. Instr. and Meth., 80(1970)13.
7. G.Charpak, G.Fischer, A.Minten, L.Naumann, F.Sauli, G.Flügge, Ch.Gottfried and R.Tirler, Nucl. Instr. and Meth. 97(1971)377.
8. J.E.Bateman, M.W.Walters and R.E.Jones, Nucl. Instr. and Meth. 135(1976)235.
9. S.Parker, R.Jones, J.Kadyk, M.L.Stevenson, T.Katsura, V.Z.Peterson and D.Yount, Nucl. Instr. and Meth. 97(1971)181.
10. S.N.Kaplan, L.Kaufman, V.Perez-Mendez and K.Valentine, Nucl. Instr. and Meth. 106(1973)397.
11. P.F.Christie, E.Mathieson and K.D.Evans, J.Phys.E. 9(1976)173.
12. C.J.Borkowski and M.R.Kopp, Rev. Sci. Instr. 46(1975)951.
13. G.Charpak, Nucl. Instr. and Meth. 156(1978)1.
14. A.R.Faruqi, Nucl. Instr. and Meth. 156(1978)19.
15. R.Allemand, J.Bourdel, E.Roudaut, P.Convert, K.Ible, J.Jacobe, J.P.Cotton and B.Farnoux, Nucl. Instr. and Meth. 126(1975)29.
16. J.Alberi, J.Fischer, V.Radeka, L.C.Rogers and B.Schoenborn, Nucl. Instr. and Meth. 127(1975)507.
- 17.

18. J.W.Stumpel, P.W.Sanford and H.F.Goddard, J.Physics.E, 6(1973)4,397.
19. S.Rappaport, R.Petre, M.Kayat, K.Evans, G.Smith, A.Levine, Astrophys. J.Lett. (submitted 30 Dec. 1977).
20. A.Levine, R.Petre, S.Rappaport, G.C.Smith, K.D.Evans and D.Rolf, Astrophys. J.Lett. (submitted 8 Sept. 1978).
21. K.H.Lauterjung, J.Pokar, B.Schimmer and R.Stäudner, Nucl. Instr. and Meth. 22(1963)117.
22. W.R.Kuhlmann, K.H.Lauterjung and B.Schimmer, Nucl. Instr. and Meth. 40(1966)109.
23. R.Bock, H.H.Duhm, W.Melzer, F.Pühlhofer and B.Stadler, Nucl. Instr. and Meth. 41(1966)190.
24. S.Kalbitzer and W.Melzer, Nucl. Instr. and Meth. 56(1967)301.
25. A.Doehring, S.Kalbitzer and W.Melzer, Nucl. Instr. and Meth. 59(1968)40.
26. R.B.Owen and M.L.Awcock, IEEE. Trans. Nucl. Sci. N. 15(1968)290.
27. LeCroy Research Systems - Charge Sensitive Preamplifier Data, TRA510 and TRA1000.
28. G.Charpak, Nature 270(1977)479.
29. W.R.Kuhlmann, K.H.Lauterjung, B.Schimmer and K.Sistemich, NIM 40(1966)118.
30. C.J.Borkowski and M.R.Kopp, Rev. Sci. Instr. 39(1968)1515.
31. E.Mathieson and T.J.Harris, Nucl. Instr. and Meth. 88(1970)81.
32. T.J.Harris and E.Mathieson, Nucl. Instr. and Meth. 96(1971)397
33. T.J.Harris - MSc. Thesis, Leicester, 1972.
34. H.Becker, S.Kalbitzer, D.Rieck and C.A.Wiedner, Nucl. Instr. and Meth. 95(1971)525.
35. E.Mathieson, Nucl. Instr. and Meth. 97(1971)171.
36. E.Mathieson, K.D.Evans, W. Parkes and P.F.Christie, Nucl. Instr. and Meth. 121(1974)139.

37. E.Mathieson, K.D.Evans, K.Cole and R.Everett, Nucl. Instr. and Meth. 126(1975)199.
38. A.Rindi, V.Perez-Mendez and R.I.Wallace, Nucl. Instr. and Meth. 77(1970)325.
39. R.Grove, K.Lee, V.Perez-Mendez and J.Sperinde, Nucl. Instr. and Meth. 89(1970)257.
40. D.M.Lee, S.E.Sobottker and H.A.Thiessen, Nucl. Instr. and Meth. 104(1972)179.
41. E.R.Flynn, S.Orbesen, N.Stein and H.A.Thiessen, Nucl. Instr. and Meth. 111(1973)67.
42. E.Beardsworth, J.Fischer, S.Iwata, M.J.Levine, V.Radeka and C.E.Thorn, Nucl. Instr. and Meth. 127(1975)29.
43. C.J.Borkowski and M.R.Kopp, IEEE Trans. Nucl. Sci. NS17(1970)340.
44. F.Sauli, Invited paper, Wire Chamber Conf. Vienna, Feb. 1978.
45. A.Breskin, G.Charpak, C.Demierre, S.Majewski, A.Policarpo, F.Sauli and J.C.Santiard, Nucl. Instr. and Meth. 143(1977)29.
46. G.Charpak, G.Petersen, A.Policarpo and F.Sauli, Nucl. Instr. and Meth. 148(1978)471.
47. G.Charpak, Z.Harjduk, A.Jeavons, R.Stubbs and R.Khan, Nucl. Instr. and Meth. 122(1974)307.
48. E.Mathieson - Notes on 'Binning' - Internal Communication.
49. T.Bressani, G.Charpak, D.Rahm and C.Zupančič, Proc. Dubna Mtg. Apr. 1969.
50. J.Saudinos, J.C.Duchazeaubeneix, C.Laspalles and R.Chaminade, Nucl. Instr. and Meth. 111(1973)77.
51. N.S. El Hakeem - PhD. Thesis, Leicester, 1979.
52. A.H.Walenta, J.Heintze and B.Schurlein, Nucl. Instr. and Meth. 92(1971)373
53. G.Charpak and F.Sauli, Nucl. Instr. and Meth. 107(1973)371.

54. A.Breskin, G.Charpak and F.Sauli, Nucl. Instr. and Meth. 151(1978)473.
55. A.H.Walenta, Nucl. Instr. and Meth. 151(1978)461.
56. J.Heintze and A.H.Walenta, Nucl. Instr. and Meth. 11(1973)461.
57. G.C.Smith - E.Mathieson, Private Communication, 1977.
58. C.J.Borkowski and M.R.Kopp, IEEE Trans. Nucl. Sci. NS24 no. 1(1977)287.
59. J.Fischer, H.Okuno and A.H.Walenta, IEEE Trans. Nucl. Sci. NS26(1978)794.
60. J.C.Maxwell - 'A Treatise on Electricity and Magnetism'(Third edition) Vol. 1, Ch.111, Sec. 86, Oxf.Univ.Press, London 1892.
61. E.Weber - 'Electromagnetic Fields', Wiley, New York, 1950.
62. R.Gott and M.W.Charles, Nucl. Instr. and Meth. 72(1969)157.
63. H.Okuno, J.Fischer, V.Radeka and A.H.Walenta, paper read at Nucl. Sci. Symposium, Washington D.C., Oct. 1978.
64. K.F.Smith and J.E.Cline, IEEE Trans. Nucl. Sci. NS13(1966)468.
65. A.Einstein, 'Investigations on the Theory of Brownian Movement', Methuen, London (1926) 70.
66. S.C.Brown - 'Basic Data of Plasma Physics' M.I.T.Press, Cambridge, 1977.
67. E.Mathieson - Internal Communication, April 1979.
68. G.Charpak and F.Sauli, Nucl. Instr. and Meth. 113(1973)381.
69. G.Schultz, G.Charpak and F.Sauli, Rev.Physique Appl. 12(Jan.1977)67.
70. U.Gastaldi, Nucl. Instr. and Meth. 157(1978)441.
71. C.J.Borkowski and M.R.Kopp, IEEE Trans. Nucl. Sci. NS24, no. 1, (Feb.1977)287.
72. W.N.McDicken, Nucl. Instr. and Meth. 54(1967)157.

## INDUCED CHARGES IN X-RAY PROPORTIONAL DETECTORS

A thesis submitted to the University of Leicester by Trevor J. Harris.

### ABSTRACT

A brief description is given of gas proportional detectors, with emphasis on the development and behaviour of multiwire proportional counters (MWPC's). In particular, the behaviour of MWPC's as position sensitive detectors is discussed and a description given of the various techniques employed in obtaining and processing positional information.

A theoretical analysis of a recently discovered phenomenon, known as angular localisation of the electron avalanche, is presented and a study is made of induced charges, due to this avalanche, on nearby anodes and cathodes. Formulae are developed which allow the calculation of the induced charges, and theoretical predictions are given of how the effect may be used to provide position signals.

An experimental system is described from which evidence has been obtained that a high degree of angular localisation does indeed exist. Comparisons are made between these experimental measurements and the predictions of the theoretical model. Various fundamental limitations are discussed which indicate the feasibility of using the localisation effect for positional interpolation between anode wires.

The experimental work is extended to observe the effects of using several common counter gas mixtures and also of varying the chamber geometry.

Finally some applications are discussed and suggestions are made for future research.

## INDUCED CHARGES IN X-RAY PROPORTIONAL DETECTORS

A thesis submitted to the University of Leicester by Trevor J. Harris.

### ABSTRACT

A brief description is given of gas proportional detectors, with emphasis on the development and behaviour of multiwire proportional counters (MWPC's). In particular, the behaviour of MWPC's as position sensitive detectors is discussed and a description given of the various techniques employed in obtaining and processing positional information.

A theoretical analysis of a recently discovered phenomenon, known as angular localisation of the electron avalanche, is presented and a study is made of induced charges, due to this avalanche, on nearby anodes and cathodes. Formulae are developed which allow the calculation of the induced charges, and theoretical predictions are given of how the effect may be used to provide position signals.

An experimental system is described from which evidence has been obtained that a high degree of angular localisation does indeed exist. Comparisons are made between these experimental measurements and the predictions of the theoretical model. Various fundamental limitations are discussed which indicate the feasibility of using the localisation effect for positional interpolation between anode wires.

The experimental work is extended to observe the effects of using several common counter gas mixtures and also of varying the chamber geometry.

Finally some applications are discussed and suggestions are made for future research.